Development of a Robust Microfluidic Electrochemical Cell for Biofilm Study in Controlled Hydrodynamic Conditions

Thèse

Mirpouyan Zarabadi

Doctorat en chimie
Philosophiæ doctor (Ph. D.)

Québec, Canada

Development of a Robust Microfluidic Electrochemical Cell for Biofilm Study in Controlled Hydrodynamic Conditions

Thèse

Mirpouyan Zarabadi

Sous la direction de :

Jesse Greener, directeur de recherche
Steve Charette, codirecteur de recherche

Résumé

Le domaine de la bioélectrochimie a actuellement un grand impact sur les nouvelles biotechnologies, notamment les dispositifs médicaux aux points de service et la détection bioélectrochimique. D'autre part, les systèmes émergents de bioénergie offrent de nouvelles opportunités pour se passer des produits pétroliers classiques grâce à des approches alternatives plus durables sur le plan environnemental. En tant que telle, la branche de la bioélectrochimie traitant des systèmes énergétiques est sur le point d'avoir un impact incontestable sur les concepts d'énergie verte et de bioénergie. Pour faciliter ces études et d'autres, les systèmes bioélectrochimiques (BES), qui utilisent des composants biologiques tels que des bactéries (souvent appelées biocatalyseurs), sont de plus en plus développés et miniaturisés pour une nouvelle série de biotechnologies.

Cette thèse porte sur la fabrication et la fonctionnalité d'un « système microfluidique électrochimique à trois électrodes » pour l'étude de biofilms de différentes bactéries (électroactives et non-électroactives) à l'aide de différentes techniques électrochimiques. Ces biofilms ont été largement étudiés par des techniques électrochimiques et d'imagerie microscopique (microscopie optique et électronique). Cette thèse pourra potentiellement ouvrir la voie à une nouvelle vague de développements de biocapteurs électrochimiques, tout en offrant des avancées scientifiques spécifiques dans les études de biocapacité de biofilm, de biorésistance, de pH du biofilm, de dépendance nutritionnelle de l'activité du biofilm et de la cinétique de respiration bactérienne.

Abstract

The area of bioelectrochemistry is currently making the greatest impact in new biotechnology, including point of care medical devices and bioelectrochemical sensing. On the other hand, emerging bioenergy systems offer new opportunities to move away from conventional petroleum products toward more environmentally sustainable alternative approaches. As such, the branch of bioelectrochemistry dealing with energy systems is poised to have an undoubtable impact on green-energy and bioenergy concepts. To facilitate these and other areas of study, bioelectrochemical systems (BESs), which use biological components such as bacteria (often referred to as biocatalysts) are increasingly being developed and miniaturized for a new round of biotechnology.

This PhD thesis focuses on fabrication and functionality of a “three-electrode electrochemical microfluidic system” for biofilm studies of different bacteria (electroactive and non-electroactive) using different electrochemical techniques. They were broadly studied by electrochemical and microscopic imaging (optical and electron microscopy) techniques. This thesis can potentially open the way for a new wave of electrochemical biosensor development, while offering specific scientific advances in studies of biofilm biocapacitance, bioresistance, biofilm pH, nutrient dependency of biofilm activity and bacterial respiration kinetics.

Table of contents

List of Figures

List of tables

List of abbreviations

AB	Agrobacterium
Ac	Sodium acetate
ATR	Attenuated total reflection
BES	Bioelectrochemical system
CA	Chronoamperometery
C_b	Biocapacitance
C-cyt	Cytochrome c
C_{dl}	Double layer capacitance
CE	Counter electrode
CLSM	Confocal laser scanning microscopy
CPE	Constant phase element
CV	Cyclic voltammetry
COV	Coefficient of variance
DET	Direct electron transfer
DIET	Direct interspecies electron transfer
EAB	Electroactive biofilm
EET	Extracellular electron transfer
E_f	Formal potential
EIS	Electrochemical impedance spectroscopy
EPS	Extracellular polymeric substance
ET	Electron transfer
Fc	Ferrocene
GFP	Green florescence protein
G_{OX}	Glucose oxidase
k_{cat}	Catalytic rate
K_M	Michaelis constant
$K_{M(app)}$	Apparent Michaelis constant
LB	Lysogeny broth
M3C	Microbial 3-electrode cell
MDC	Microbial desalination cell
MEC	Microbial electrolysis cell
MET	Mediated electron transfer
MFC	Microbial fuel cell
OD	Optical density
OMC	Outer membrane cytochrome c
Ox	Oxidized form
PDMS	Poly dimethyl siloxane
R_b	Bioresistance
R_{CT}	Charge transfer resistance
Re	Remolds number
RE	Reference electrode

Red	Reduced form
R_S	Solution resistance
SCE	Saturated calomel electrode
TCA	Tricarboxylic acid cycle
T_g	Glass transition temperature
WE	Working electrode
Z	Absolute impedance
Z'	Real impedance
Z''	Imaginary impedance
Z_d	Anomalous linear diffusion resistance

Acknowledgment

First of all, I would like to thank my thesis director, Professor Jesse Greener, for trusting me with this ambitious project and for giving me all the necessary resources for its accomplishment. Professor Greener, with his availability and critical sense, has a big part in the success of this project and working with him was a source of inspiration and motivation for me every day. He has allowed me immeasurable learning in 3 different scientific field (electrochemistry, microbiology and microfluidics) that will allow me to face future challenges.

I would also like to thank my co-director, Professor Steve Charette, for his support and help throughout these years of research. He was a great help to me in microbiology part of this thesis and was a key element in the success of this project. Without him and his generosity in providing and permission of using the microbiological instruments such as anaerobic glove box, these successes were not possible.

I would like to thank all the members of the Chemistry Department as well as the Biochemistry, Microbiology and Bioinformatics Department, especially Rodica Neagu-Plesu, Luc Trudel, Laurent Smith, Véronique Samson and Valérie Paquet who had huge impacts in success of my scientific projects.

My experience would have been incomplete without my colleagues from Greener's research team. I would like to thank Adnan, François, Eya, Mazeyar, Mohammad, Mehran, Farnaz, Erica, Jia and newcomers: Dirk, Gong and Tanver for making this difficult journey of research a little easier and making the laboratory great. I also want to thank all of summer interns, Arnaud Reitz, Julien, Mahdi, Sabrina, Maxim, Valérie, Germain, Brandon and Kimberly in lab during my research. I passed a great time and I learned several things by exchanging with you.

Finally, I would like to sincerely acknowledge my family. I thank you for your support and unconditional kindness.

Foreword

The following section lists the published works for each chapter including the contribution of each author.

Chapter 2. Zarabadi, M. P., Paquet-Mercier, F., Charette, S. J. and Greener, J. Hydrodynamic Effects on Biofilms at the Biointerface Using a Microfluidic Electrochemical Cell: Case Study of *Pseudomonas sp. Langmuir*, **2017**, 33(8), 2041-2049.

Contribution: M.P.Z., J.G., and S.J.C. formed the concepts of the project and planned the experiments. M.P.Z. fabricated flow channels, made microbiological and bacterial preparations, conducted all electrochemical experiments and analysis and some confocal laser scanning microscopy (CLSM) experiments and analysis. F.P.M. conducted ATR FT-IR and some CLSM experiments and analyzed them. The manuscript writing and editing was mostly done by J.G and M.P.Z. The manuscript was reviewed and edited by S.J.C.

Chapter 3. Zarabadi, M. P., Charette, S. J. and Greener, J. Flow-Based Deacidification of *Geobacter sulfurreducens* Biofilms Depends on Nutrient Conditions: a Microfluidic Bioelectrochemical Study. *ChemElectroChem*, **2018**, *5*, 3645-3653.

Contribution: M.P.Z., J.G., and S.J.C. formed the concepts of the project and planned the experiments. M.P.Z. fabricated flow channels, made microbiological and bacterial preparations, and conducted all electrochemical experiments and analysis. The manuscript writing and editing was mostly done by J.G. and M.P.Z. The manuscript was reviewed and edited by S.J.C.

Chapter 4. Zarabadi, M. P., Charette, S. J. and Greener, J. Toggling *Geobacter sulfurreducens* metabolic state reveals hidden behaviour and expanded applicability to sustainable energy applications, *Sustainable Energy & Fuels*, **2019**, DOI: 10.1039/C9SE00026G

Contribution: M.P.Z. and J.G. formed the concepts of the project and planned the experiments. M.P.Z. fabricated flow channels, made microbiological and bacterial preparations, and conducted all electrochemical experiments and analysis. The manuscript writing and editing was mostly done by J.G. and M.P.Z. The manuscript was reviewed and edited by S.J.C.

Chapter 5. Zarabadi, M. P., Couture, M., Charette, S. J. and Greener, J. A generalized kinetic framework for whole-cell bioelectrocatalysis in flow reactors clarifies performance enhancements, *ChemElectroChem*, **2019**, 6, 2715-2718.

Contribution: M.P.Z. and J.G. formed the concepts of the project and planned the experiments. M.P.Z. fabricated flow channels, made microbiological and bacterial preparations, and conducted all electrochemical experiments and analysis. The manuscript writing and editing was mostly done by J.G. and M.P.Z. The manuscript was reviewed and edited by M. C. and S.J.C.

Introduction

Electrochemistry is the branch of chemistry dealing with the combination of electrical and chemical effects. Among the most important applications, include electrical energy production during chemical reactions and chemical changes caused by applying a known electrical current or potential.[1] Other industrial applications include development of electro analytical sensors,[2] batteries,[3] and fuel cells[4] to technologies (the electroplating of metals,[5] electrochemical extraction[6] and corrosion).[7]

Bioelectrochemical processes can take place in an electrochemical energy conversion device. Bioelectrochemical systems (BES) include microbial electrolysis cells,[8] microbial fuel cells,[9] enzymatic biofuel cells[10] and microbial electrosynthesis cells.[11] Microbial fuel cell (MFC) technology generates electricity from organic compounds that may be sourced from organic waste, through the catalytic activity of microorganisms such as bacteria. In a chemical point of view, the MFC based technology therefore converts the energy stored in chemical bonds of organic compounds to electrical energy, through the catalytic reactions by microorganisms.

Microfluidics consists of channels with 10-1000 µm length scale in at least in one dimension. It can be used to accurately manipulate nanoliter sample volumes, making it an interesting technology to scale down and potentially automate culture-based platforms.[12] With the ability to run several low cost essays in parallel, microfluidics has the potential to revolutionize the ability to perform procedures such as high-throughput biological and chemical sensing, electrochemical and energetic analysis.

The introduction part of this PhD thesis demonstrates an overall literature review about BESs and microfluidics in the field of biosensing and bioconversion of energy.

Chapter 1. Background

1.1 Electrochemical cell

An electrochemical cell is used to control and monitor electrochemical reactions (a process in which electrons flow between two substances) by the input of electrochemical signals or create voltage and current from chemical reactions.[1] Generally, an electrochemical cell consists of two or three electrodes. Inert conducting materials such as platinum, gold and graphite are examples of typical electrode materials used in electrochemical cells.[1] The electrodes are usually placed in an electrolyte. Based on the goals of this project, electrochemists can determine the type of electrodes, electrolyte materials and cell structure and configuration for electrochemical measurement or energy applications.

1.1.1 Electrochemical cell configuration

The simplest electrochemical cell uses two electrodes, an anode and a cathode. In an electrochemical cell, the cathode is the electrode where current flows into while the anode is the electrode where the current flows out of. The cell potential is measured between the anode and cathode. Typically, this setup is used with energy storage or conversion devices like batteries, fuel cells and photovoltaic panels.[1] A simple equation, power (W) = potential (V) × current (I), gives power output from an electrochemical cell. By measurement of potential difference between anode and cathode, and calculation of current, and therefore cell power will be measurable. The readers refer to the section 1.2.2.2 for more information.

The 3-electrode cell setup is the most common electrochemical cell configuration used in electrochemistry. In this case, the current flows between the working electrode (WE) and the counter electrode (CE) and the potential difference between reference electrode (RE) and WE is controlled through a potentiostat.[13] This configuration allows the potential of an electrochemical reaction to be controlled, whereas no such control is provided in a 2-electrode setup. A reference electrode has a stable and well-defined electrochemical potential (at constant temperature) against which the applied or measured potential in an electrochemical cell is referred. Ag/AgCl in saturated KCl and saturated calomel electrodes (SCE) are the most well-known reference electrodes in electrochemistry laboratory.[13] In some electrochemical devices, such as miniaturized microfluidic electrochemical cells, it may not be possible to use a standard reference electrode. In such cases, a pseudo-reference electrode, generally a metal such as gold or silver, can be used. The most important challenge for a pseudo-reference electrode is stability and constancy of electrochemical potential during the measurements. This issue is addressed in this thesis.

1.1.2 Electrochemical techniques

Measurements in an electrochemical cell include (1) measuring the potential when the current is zero (potentiometric), (2) measuring the potential while controlling the current (galvanostatic), and (3) measuring the current while controlling the potential (potentiostatic). In galvanostatic measurements, the experiment is carried out by applying the controlled current between the WE and CE with a current source and monitoring the potential between the WE and RE. In a potentiostatic (voltammetry) experiment, a time-dependent potential is applied to a WE and the resulting current is recorded. A plot of current versus potential is called a voltammogram and it is the electrochemical equivalent of a spectrum in spectroscopy.[13]

Based on the main goals of this thesis, we only focus on voltammetry mode with three well-known electrochemical techniques. The cyclic voltammetry (CV), chronoamperometery (CA) and electrochemical impedance spectroscopy (EIS) are discussed in the following sections.

1.1.2.1 Cyclic voltammetry (CV)

In a cyclic voltammogram, a scan of electrochemical potential will be completed in both directions of negative and positive potential. Figure 1.1a shows a typical potential-excitation signal. In this example, we first scan the potential to more negative values, resulting in the following reduction reaction.

$$\mathrm{Ox} + \mathrm{ne}^- \longrightarrow \mathrm{Red} \qquad \text{(Eq. 1.1)}$$

When the potential reaches a predetermined switching potential, the electrochemical potential sweep direction will be reversed resulting toward more positive potentials. Because the reduced form of the analyte was generated on the forward scan, the reduced form of the analyte will be oxidized during the reverse scan.

$$\mathrm{Red} \longrightarrow \mathrm{Ox} + \mathrm{ne}^- \qquad \text{(Eq. 1.2)}$$

The resulting cyclic voltammogram provides an opportunity for measurement of the peak currents and peak potentials (Figure 1.1b). The separate peaks of reduction and oxidation reactions can be characterized by a peak potential and a peak current. For a reversible system, the anodic and cathodic peak currents are equal, and the half-wave potential, $E_{1/2}$, is midway between the anodic and cathodic peak potentials which is called formal potential ($E_f = \frac{E_{P(Anodic)} + E_{P(Cathodic)}}{2}$). Studies of the electrochemical behaviour of species generated at the surface of the electrode can be carried out with scanning the electrochemical potential in both oxidative and reductive directions.[1]

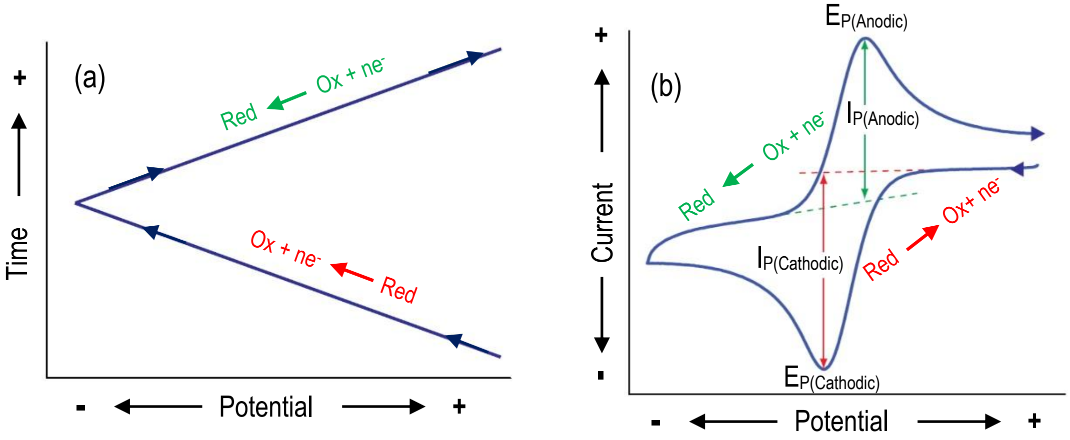

Figure 1.1 (a) One cycle of potential scanning showing the initial potential (more positive potential) to the switching potential (more negative potential) and then, coming back to initial potential value. **(b)** The resulting cyclic voltammogram showing the measurement of the peak currents and peak potentials.

1.1.2.2 Chronoamperometery (CA)

In chronoamperometery, a constant electrochemical potential is applied to the electrode and current as a function of time will be measured. At t = 0 and in presence of redox active species solution, the electrochemical potential is stepped to a value significantly more negative or positive than the E_f for the redox couple. Immediately after applying electrochemical potential, the electroactive species in the vicinity of the electrode are converted to Red or Ox.[1] With a known electrode area, measurement of either stoichiometric number of electrons involved in the reaction or diffusion constant for electroactive species is easily accomplished.

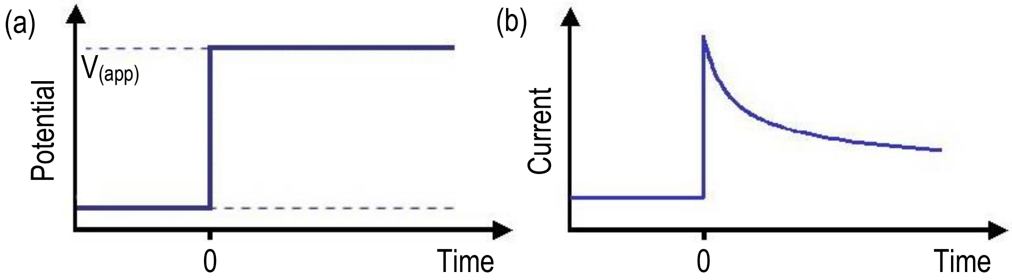

Figure 1.2 (a) Potential of the electrode versus time. At t = 0, a constant potential, $V_{(app)}$, is applied on the electrode and it is maintained constant during measurement. **(b)** Curve of chronoamperometery, which shows changes of current versus time.

1.1.2.3 Electrochemical impedance spectroscopy (EIS)

Electrochemical Impedance Spectroscopy (EIS) is a powerful technique for the characterization of electrochemical systems. At an applied electrochemical potential, with a sufficiently broad range of frequencies, the influence of physical and chemical phenomena can be isolated and distinguished. EIS has found widespread applications in the field of characterization of coatings, batteries, fuel cells, materials and corrosion studies.[14]

The fundamental approach of all impedance methods is to apply a small amplitude sinusoidal potential and measure the response (current or voltage). In a potentiostatic EIS experiment, a small AC amplitude sinusoidal excitation signal ($\Delta E \cdot \sin(\omega t)$), with a particular frequency ω, is superimposed on the DC polarization potential (E^0). As a result, the current response will be ($\Delta I \cdot \sin(\omega t+\varphi)$). The impedance of the system can be calculated using Ohm's law. The ratio of $E(\omega)$ to $I(\omega)$ results the impedance $Z(\omega)$. This impedance of the system is a complex quantity with a magnitude and a phase shift (φ) between the AC potential and the current response, which both depend on ω of the signal. The impedance of the system can be resulted by sweeping the frequency (typically between 100 KHz – 0.1 Hz) of the applied electrochemical potential.[16]

EIS results are usually represented by one of two plots. A Nyquist (complex) plot includes 2 parts of real and imaginary impedance. Nyquist representation gives an overview of the data, with the shape of the Z' (real impedance) vs. Z" (imaginary impedance) curve can make qualitative interpretations, but the frequency is shown. This problem is solved by the Bode plot, where the absolute value of impedance (|Z|) and the phase shifts (φ) are plotted as a function of frequency in two different plots giving a Bode plot. Figure 1.3 shows a typical Nyquist and Bode plot.

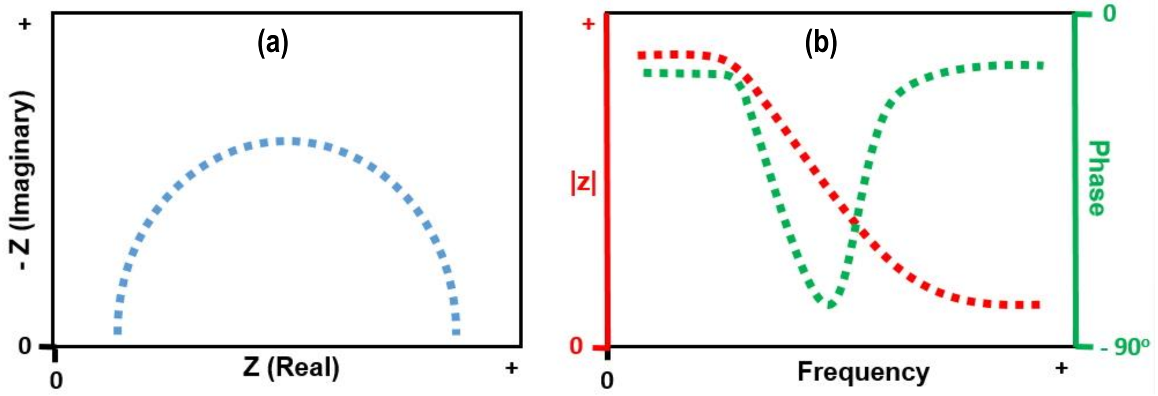

Figure 1.3 (a) Typical Nyquist plot based on Randles circuit model. **(b)** Typical Bode plot based on the same Randles circuit model.

An equivalent electrical circuit model should be used for analysing EIS data output. By fitting EIS data into an appropriate equivalent circuit model, physical electrochemistry parameters of the system can be extracted. As an example, one of the most common cell models is the Randles circuit model.[15] It includes a solution resistance (R_S), a double layer capacitance (C_{dl}) and a charge transfer resistance (R_{CT}) (see Figure 1.4). The charge transfer resistance is in parallel with the double layer capacitance. This simplified Randel's cell is the starting point for other more complex models for biological sensors, energy storage devices, fuel cells and corrosion studies. Figure 1.3 demonstrates an output EIS data, which can be fitted with a Randles circuit model. It should be considered that this is one of the simplest examples of an electrochemical system whereas typically, equivalent circuits can be much more complex. Based on Randles circuit, the semi-circle shape in Nyquist curve represents charge transfer resistance, therefore by the increasing diameter of the semi-circle curve indicates a higher charge transfer.

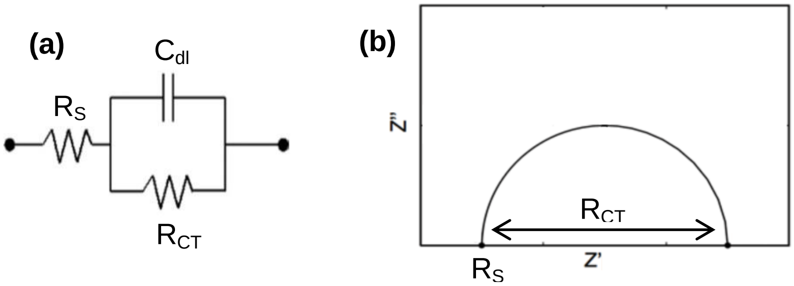

Figure 1.4 (a) Randles equivalent circuit (b) Nyquist curve of Randles circuit.

1.2 Bioelectrochemistry

The term "bioelectrochemistry" can be defined as the area of the science that utilizes electrochemical principles and techniques to investigate electrochemical processes of relevance to biological systems and biomaterials.[16] Bioelectrochemistry focuses on the structural organization and electron transfer (ET) functions of biointerfaces on electrode surfaces.[17] Applications include the development of devices such as electrochemical biosensors,[18] medical tools,[19] biofuel cells and other energetic applications.[20] Over the past 20 years, bioelectrochemistry has been proven to be a useful means to understand the electrochemical properties of biomolecules such as proteins, enzymes, lipids, nucleic acids and even whole cells such as bacteria. Also, it is a powerful tool for exploitation of biomolecules in biosensors and biofuel cell devices.[16]

Here, we will summarize some important topics in the field of bioelectrochemistry related to detection of certain analytes (proteins, bacteria and biomass) via various biosensors and also bioenergetic devices such as microbial fuel cells (MFC). This will include a discussion on how electrochemical biosensing occurs between biomass and the electrode surfaces in the case of both electroactive and non-electroactive species. Moreover, we will discuss the role of bioelectrochemistry in BES for energy applications. This section will finish with a discussion about ET kinetics between electroactive bacteria and the electrode surfaces.

1.2.1 Bioelectrochemical sensing

Development of electrochemical biosensors has grown rapidly over the last two decades. An electrochemical biosensor is generally defined as a transducer, which converts biological phenomena into quantifiable and processable signals.[21] Electrochemical techniques predominantly use functionalized electrodes to increase analyte selectivity and sensitivity over non-functionalized electrodes.[22] In any case, sensitivity can be improved by selection of right electrochemical technique such as CV and EIS.[23]

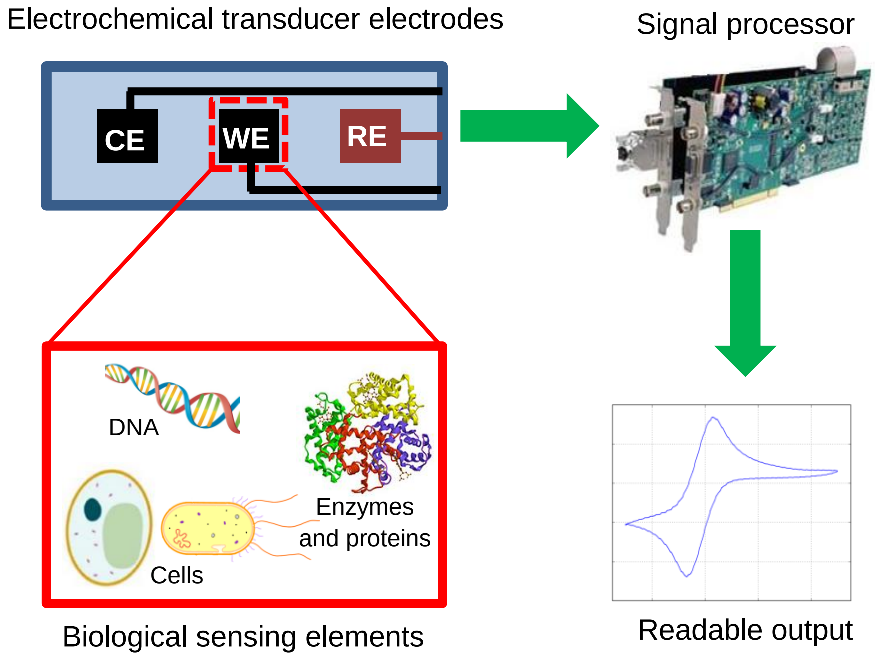

Figure 1.5 Scheme of an electrochemical biosensor. Biological sensing elements are coupled to working electrode. These traduce the signal to deliver a readable output.

The schematic of a typical electrochemical biosensor is shown in Figure 1.5, which consists of an electrochemical transducer device and a signal processor. The WE (in a 3-electrode configuration) is usually functionalized to increase binding with analytes, usually in solution. The mechanism for immobilization of the functional group(s) on the surface of the electrode and their interactions with the target molecules can change electrochemical properties of the electrode, resulting in a readable output in terms of current, potential, impedance, capacitance, conductance or other electrical parameters.[24] However, because of the sensitivity of the electrode surface, surface electrode changing (generally interfacial capacitance) can be used as an electrochemical biosensor for biomass detection, e.g. accumulation of bacteria,[25] neurotransmitters[26] and glucose.[27]

In the next section, we give an example for bioelectrochemical sensing based on CV and EIS techniques.

1.2.1.1 Biomolecule sensing with CV and EIS

One of the most well-known examples for electrochemical biosensing devices is the glucose sensor. There are several examples for different types of glucose sensors with different detection limits and electrochemical techniques.[28] The electrochemical biosensing based on glucose oxidase (G_{OX}) has attracted widespread interest owing to their importance in glucose monitoring and quantification. Three steps are involved for detection and measurement of glucose in a system. G_{OX} (Ox) reacts with glucose forming gluconolactone (Eq. 1.3). Then the reduced form can be re-oxidized by ferrocene (Fc) (Eq.1.4).[29] An oxidative electrochemical potential can oxidize Fc to Fc+ (Eq. 1.5) and by measurement of amount of oxidized Fc, the glucose concentration can be calculated.

1) G_{OX} (Ox) + glucose $\dashrightarrow$ G_{OX} (Red) + gluconolactone (Eq. 1.3)
2) G_{OX} (Red) + 2 Fc^+ $\dashrightarrow$ G_{OX} (Ox) + Fc (Eq. 1.4)
3) Fc $\longleftrightarrow$ $Fc^+ + e^-$ (measured) (Eq. 1.5)

Bioelectrochemical devices can be used in immunology, as well.[30] Immunosensors are anticipated to be one of the most important types of biosensors, with a wide range of applications in clinical diagnosis, food quality control, environmental analysis, detection of pathogens or toxins and forensics.[31]

EIS is another important electrochemical technique used in electrochemical biosensors.[32] In faradiac impedance measurements, the main parameter is the charge transfer resistance is modified by surface adhered species, usually by products of biochemical reactions. In this approach, a redox probe molecule is added to the analyte solution, which provides a faradaic current when an appropriate potential is applied to the electrode.[33] This procedure will be only applied when no electroactive biomolecules present in analyte. The interface blocking by surface products of biochemical reactions can change charge transfer resistance of redox probe molecules and it can be a function of blocking percentage of the surface. It should be considered that redox reactions within biomolecules reactions (electroactive proteins or enzymes) are assigned faradaic possess and can be interpreted with Randels equivalent circuit like redox probe in electrolyte solution.[33]

When a redox pair is absent from the analyte solution, (neither the presence of a redox probe nor an electroactive biomolecule) the impedance is termed non-faradaic[34] and depends on the conductivity of the supporting electrolyte and/or impedimetric electrode interfacial properties.[34] In the absence of a redox pair or if its charge transfer rate on the electrode is very slow, no faradaic process occurs, and subsequent electron transfer is not produced. In these cases, the interfacial capacitance changes are often studied.[35] The equivalent circuit for this type of EIS can be represented in different models. The formation of biochemical reaction products may be represented by an additional capacitor and/or resistor based on type of biomolecules, surface of electrode and analyte solution composition.[36]

EIS is used extensively to follow changes of R_{CT} in electrochemical cells. Blocking the electrode surface with the bulky biomolecules,[37] probing with electroactive species, or precipitation of insoluble materials due to the biochemical reactions[38] were the main processes observed by faradaic impedance spectroscopy. The changes of interfacial capacitance or resistance based on proposed equivalent model are the main processes in non-faradaic measurements.

1.2.1.2 Electrochemical sensing of planktonic and sessile bacteria

Bacteria can live either as free planktonic cells in bulk solution, or as sessile cells attached to a surface.[39] Bacterial biofilms are defined as bacterial populations encased in a protective extracellular polymeric matrix adherent to each other and/or to surfaces or interfaces.[40] The biofilm formation is regulated by different genetic and environmental factors. Genetic studies have shown that bacterial motility, cell membrane proteins, extracellular polysaccharides and signalling molecules play significant roles in biofilm formation, maturation and function.[41] The extracellular polymeric substance (EPS) has a significant role in biofilm formation. They comprise generally, a wide variety of proteins, glycoproteins, glycolipids and in some cases, extracellular DNA.[41] A complete biochemical profile of most EPS samples is still a challenge for biochemists.[42] The Figure 1.6 shows a general schematic of biofilm structure.

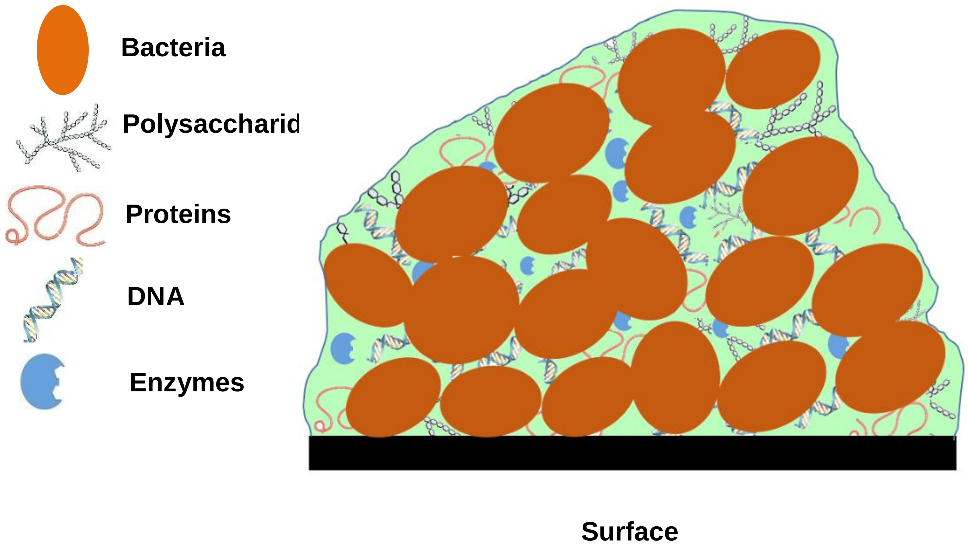

Figure 1.6 A schematic of a generic biofilm and composition of the EPS.

The identification and quantification of planktonic and sessile bacteria and their biofilms has become a key point in food safety, diagnostics and drug discovery.[43] For example, the detection of pathogenic bacteria in planktonic form in water and food samples plays a significant role in early detection for public and environmental health.[44] Generally, electrochemical biosensors are promising for bacterial detection due to portability, rapidity, sensitivity and ease of miniaturization.[45] CV was used to monitor the initial bacterial adhesion as well as subsequent biofilm maturation stage.[46] Like EIS, CV can be done either in presence or in absence of redox moieties for detection of biomass from bacterial growth. The cyclic voltammograms during bacterial attachment on the surface of the working electrode in an electrolyte solution contained potassium ferricyanide can be changed. As more bacterial cells attach to working electrode, the absolute value of anodic and cathodic currents decreases which confirms reduction of redox reactions of potassium ferricyanide species by blocking the surface of the electrode with biofilm biomass.[47]

The reversibility of the electrochemical reaction is observed by difference between the anodic and cathodic peak potentials (ΔE), increased with time. These results confirmed that the electrochemical potential of oxidation and reduction of $[Fe(CN)_6]^{3-/4-}$ were shifted toward higher and lower values, respectively which shows higher charge transfer resistance by increasing amount of grown biofilm on the surface of the electrode.[47]

Several studies have been reported on EIS for biofilm detection, which makes this technique extremely useful to detect bacterial and biofilm interactions. Based on the literature, impedance changes may be caused by two main reasons: changes of solution medium conductivity which is caused by metabolic by-products[48] or changes in the surface properties of the electrodes affecting the capacitance of the electrode/electrolyte interface due to bacteria presence.[49] We will also focus on EIS in faradaic and non-faradic modes for the detection of electrochemical biofilm detection and microbial growth (Chapter 2). Different studies have analyzed the relationship between microbial growth and relative changes in both the capacitive and the resistive parts of impedance showing that both components are indicative of bacterial growth.[50,51]

1.2.2 Bioelectrochemical systems (BES)

In a BES, the electrochemical interaction between microorganisms or enzymes and an electrode is mainly used for wastewater treatment.[52] The most common types of BES based on microorganisms includes microbial fuel cells (MFCs),[9] microbial electrolysis cells (MECs),[8] microbial 3-electrode cells (M3Cs),[53] and microbial desalination cells (MDCs).[54] These technologies rely on ability of some bacteria to transfer electrons from an oxidized electron donor, usually referred to as the nutrient, to an anode or working electrode. Such a bacteria-colonized electrode is then connected, through an external electrical circuit, to the cathode or counter electrode, where a reduction reaction takes place, thus completing a redox reaction.[55] BES applications span from electrical power generation and bioremediation, to the production of chemicals and biosensing tools.[56] The majority of scientific efforts have focused on the application of BESs for power-generation purposes.[52]

Based on the goals of this part of thesis, we only focus on energy producing BESs, which involves bacterial biofilms in MFC and M3C modes.

1.2.2.1 Electroactive bacteria

Generally, the electroactive bacteria are defined as being able to transport electrons through the cell membrane to or from the extracellular environment.[57] The biofilms of the electrogenic bacteria are called electroactive biofilms (EABs). The EABs have evolved to exchange electrons with insoluble extracellular minerals, a mechanism known as the extracellular electrons transfer (EET). Most of the knowledge about EET in microbes is derived from studies in bioelectrochemical systems. The ability of biofilms to exchange electrons with the electrode is derived from the metabolic interactions between EABs and solid minerals that can be used as an electron donor or electron acceptor in the environment, respectively.

Electroactivity has been reported in almost 100 microbial species.[58] It includes the extensively studied *Geobacter* sp.,[59] *Shewanella* sp.,[60] and *P. aeruginosa*[61] as well as certain Cyanobacteria.[62] Electroactive bacteria are catagorized amongst heterotrophic bacteria. A heterotroph is an organism that cannot produce its own food, relying instead on the intake of nutrients from external sources of organic carbon. The electroactive bacteria obtain energy from the oxidation of organic compounds and can respire via aerobic (an oxygen terminal electron acceptor) and anaerobic (a reducible electron acceptor instead of oxygen, such as Fe^{3+}) pathways.[52] In both cases, during respiration, nutrients are oxidized, liberating electrons which are transferred via a redox cascade, the tricarboxylic acid (TCA) cycle, and are finally transferred to an available terminal electron acceptor.[63]

In general, nutrients are organic materials, such as glucose, citrate, lactate and acetate.[9] Based on the type of bacteria and their metabolic ability to oxidize nutrient molecules, one or more nutrients can be digested by electroactive bacteria as a nutrient.[9] *Geobacter sulfurreducens* is known as a bacterial model for bioelectrochemical systems because of its importance in several biogeochemical processes and higher current output in comparison to other electroactive bacteria. However, the simple structure of enzymatic reactions in *G. sulfurreducens* does not allow digestion of macromolecules.[64]

The heme is an iron-containing compound within various proteins including c-type cytochromes. C-type cytochromes are a structurally diverse group of proteins, which are playing a key role in the transport of electrons across the electroactive bacterial cell.[65] The process of electron transfer through the cell membrane is often achieved by multiple heme-containing proteins, which exhibit a redox chain reaction.[66] Figure 1.7 demonstrates a simplified digestion cycle of an acetate molecule and the subsequent electron transfer from inside to outside of an electroactive bacterium (*G. sulfurreducens*).

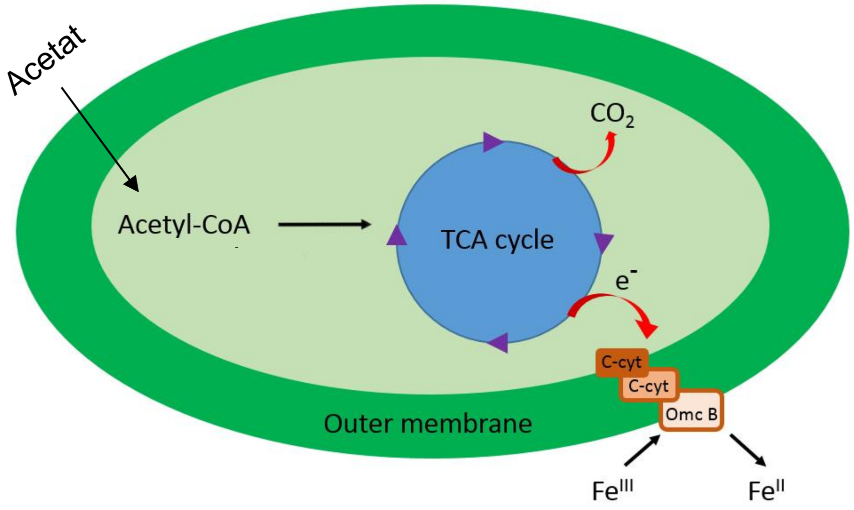

Figure 1.7 The simplified mechanism for acetate metabolism in *G. sulfurreducens* bacteria with Fe (III) serving as the electron acceptor. C-cyt and OmcB are c-type cytochrome and outer membrane c-type cytochrome, respectively. Higher electrochemical redox potentials toward outer membrane c-type cytochrome allow the electrons to pass through the membranes.

1.2.2.2 Microbial fuel cells (MFCs)

Conventionally, a MFC consists of two compartments, one containing an anode and the other a cathode, both separated by an ion-exchange membrane (see Figure 1.8).[9] EABs in the anodic chamber of an MFC oxidize organic matter, generating electrons and protons. In the absence of any other soluble electron acceptor the electrons are transported to the cathode through an external circuit. Usually, electrons reaching the cathode combine with protons that diffuse from the anodic chamber through an ion-exchange membrane (usually a proton exchange membrane, PEM) and oxygen provided from air to form water. Production of an electric current is made possible by keeping bacteria separated from oxygen and this requires an anaerobic anodic chamber.[9] If acetate in the anodic chamber and oxygen in the cathode compartment are the nutrient of electroactive bacteria and electron acceptor, respectively, the following reaction will be expressed:

$$CH_3COO^- + H_2O \longrightarrow 2CO_2 + 7H^+ + 8e^- \qquad \text{(Eq. 1.6)}$$

Anodic reaction: $E^{0'} = -0.21$ V

$$O_2 + 4H^+ + 4e^- \longrightarrow 2H_2O \qquad \text{(Eq. 1.7)}$$

Cathodic reaction: $E^{0'} = +0.82$ V

$$\Delta E = E^{0'}(\text{cathodic}) - E^{0'}(\text{anodic}) = 1.03 \text{ V}$$

Alternatively, in laboratory scale, many MFCs reduce ferricyanide ($[Fe(CN)_6]^{3-}$) to ferrocyanide ($[Fe(CN)_6]^{4-}$) in the cathode compartment. Because of fast redox reaction of ferri/ferro couple redox moieties, they are an appropriate candidate for electrochemical studies of EABs in MFCs.

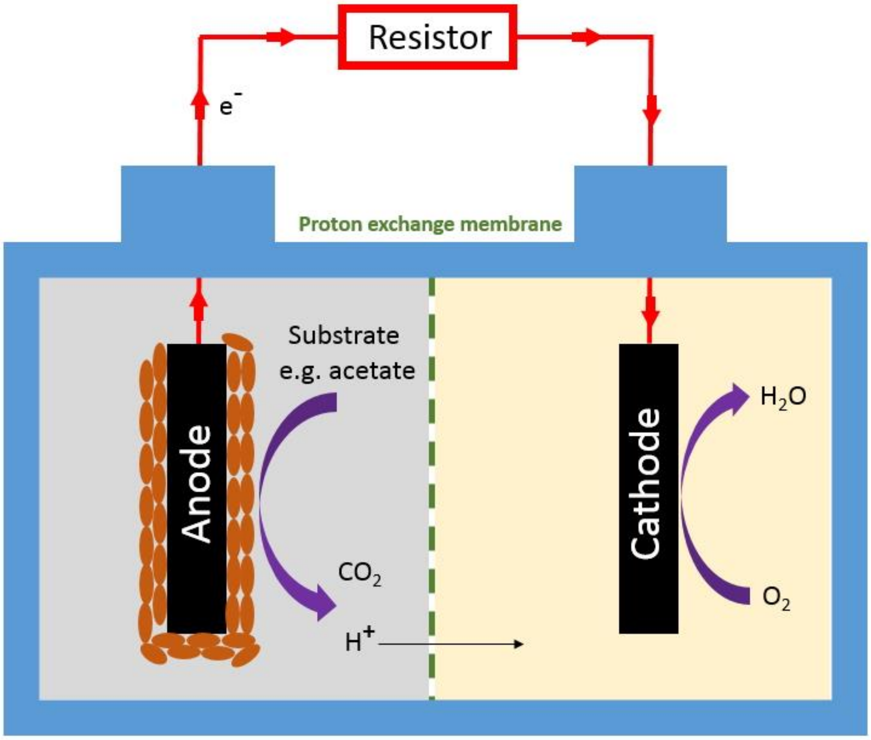

Figure 1.8 A conventional microbial fuel cell consisting of an anaerobic chamber (anode, left) and aerobic chamber (cathode, right), connected by proton exchange membrane (green dash line). The electrons passed through the external circuit reaching the cathode to form water. EABs are accumulated on the surface of anode electrode.

In general, electrons can be transferred from the bacterial cell to the anode surface through two extracellular electron transfer mechanisms. Direct electron transfer (DET), and mediated electron transfer (MET), which is based on dissolved redox species.[58] DET is facilitated by two processes. (1) Electron hopping between membrane-bound redox proteins and (2) direct conduction via “metal-like” nano wires.[67] The redox proteins are usually c-type cytochromes, which have evolved with sediment inhabiting metal reducing microorganisms such as, e.g., *Geobacter*[67] and *Rhodoferax*[68] species to aid in electron transfer to solid terminal electron acceptors of iron(III) oxides. This ET method is based on an electron hopping mechanism based on recent studies of some *Geobacter* strains. Hopping is defined as a redox conduction process in which electrons are transferred sequentially from one charge-localizing redox center (for example, the heme iron) to an adjacent one, such as along the heme chain of multi heme *c*-type cytochromes.[69] Conductive electron transfer is another DET process in which electrons are delocalized in the metal-like pili (nanowires), which are connected to the membrane-bound cytochromes proteins. These pili draw their conductivity via a pi-stacking between chains of aromatic amino acids, PilA (a protein of 150 amino acids).[70] These pili can grow as wide as 3–5 nm and as long as tens of micrometers, allowing the microorganism to reach more distant solid electron acceptors[71] and enhancing the conductivity of EABs by providing parallel ET pathways to hoping. The latter effect may allow the development of thicker electroactive biofilms by enhancing the electrical connection of cells in the upper biofilm layers to the support electrode.[72] Recent studies show direct conduction via nanowires is the most important electron transfer mechanism for *G. sulfurreducens.*[73]

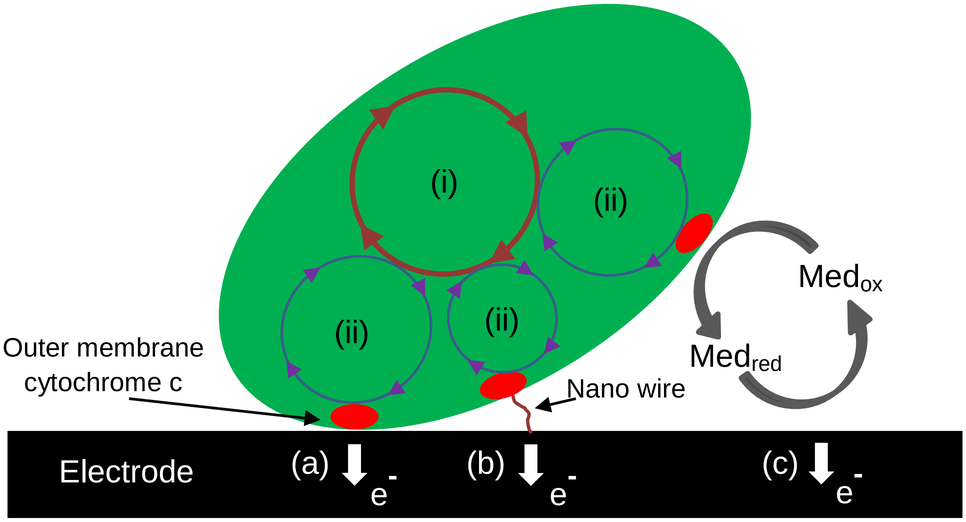

Figure 1.9 Shows direct electron transfer mechanism between electroactive bacteria and anode electrode surface by **(a)** outer membrane bound cytochromes and **(b)** electronically conducting nanowires **(c)** Shows MET mechanism with two proposed procedures: shuttling via outer membrane cytochromes and via periplasmic redox couples. (i) represents TCA cycle for bacteria and (ii) is internal electron transfer from TCA cycle to outer membrane cytochromes c.

The second method of ET is mediated via self-produced soluble redox molecules by the bacteria, which are capable of acting as electron shuttles between the bacteria and the electrode.[58] Shuttle molecules include molecules such as quinone, riboflavin and pyocyanin.[74,75] These mediators can divert electrons from the electron transport chain by entering outer cell membranes and/or periplasmic region (the space between the inner and outer membrane), becoming reduced, and then leaving in reduced state to transport electrons to the solid electrode. The oxidized mediators come back to cycle of redox reaction for electron transfer between bacteria and electrode.[58] Figure 1.9 demonstrates schematics of DET mechanism via membrane bound cytochromes, electronically conducting nanowires (pili) and MET mechanism via soluble mediators.

1.2.2.3 Microbial 3-electrode cells (M3Cs)

As discussed in section 1.1.1 and 1.1.2, a 3-electrode configuration can provide an opportunity for the study of interactions of electrode interfaces and electron transfer rate. Effective parameters in electron transfer kinetics such as biofilm pH[76] and nutrient availability[77] can be monitored.

In a M3C set up, the cathode and anode compartments of a MFC are replaced by a single electrochemical cell containing 3 electrodes (working, counter and reference electrode). An electrochemical potential is applied to a microbial colonized working electrode using a potentiostat. The working electrode is poised at a sufficiently positive potential and gains electrons from EAB, serving the role of the solid electron acceptor for natural biofilms. Hydrogen evolution occurs at counter electrode ($2H^+ + 2e^- \rightarrow H_2$). Evidence of a functioning M3C is easily observed via hydrogen bubble generation on counter electrode.[53] Figure 1.10 shows a conventional microbial 3-electrode cell.

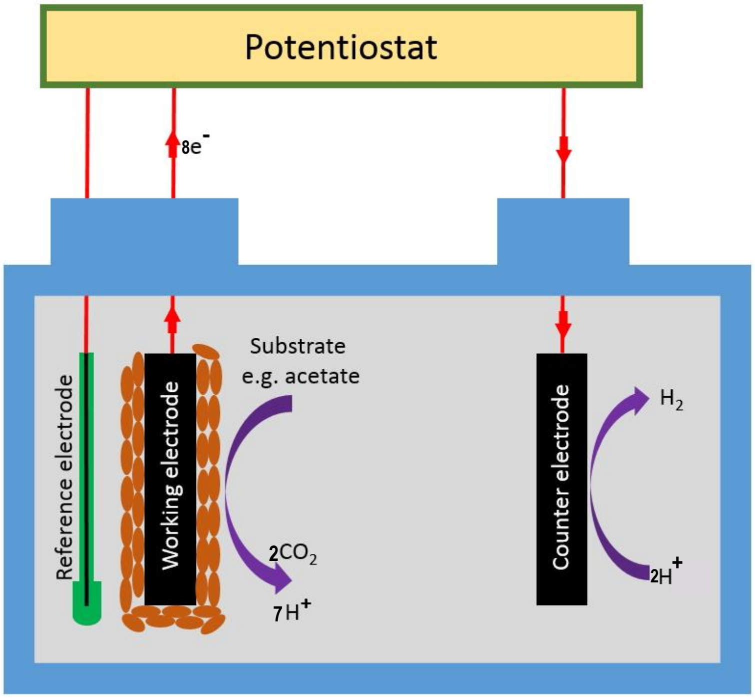

Figure 1.6 A microbial 3-electrode device connected to a potentiostat featuring an electroactive biofilm (brown ovals on the surface of working electrode) that is set up in a single-chamber electrochemical cell. Counter electrode supports a hydrogen evolution reaction.

1.2.2.4 Kinetic and environmental effects on EAB electrode respiration

Determining kinetic parameters involved in EET of EAB is crucial to properly understanding and controlling the biocatalytic processes.[78] In the case of EET in EABs, electron transfer steps from electroactive bacteria to the electrode can be complicated.[79] This includes the diffusion of nutrient molecules through the EAB, interfacial electron transfer (cell to cell), turnover rate of cytochromes in different EAB layers, counter ion mobility and interfacial EAB/electrode electron transfer.[80] In this thesis, we will focus on kinetics of nutrient utilization and rate of electron production by EABs in an electrode potential controlled mode.

The rate of nutrient utilization in microbial processes in EABs is frequently modeled using the Michaelis–Menten model. This relationship explicitly describes the rate at which bacteria oxidize the nutrient molecules and produce the reduced intracellular electron carrier. When the substrate oxidation in TCA cycle is rate-limiting for the entire process of metabolism and EET, the current density generated by EABs can be written as (Eq. 1.8) for a biofilm on the electrode:[78]

$$\mathrm{I} = \mathrm{I}_{\max}\frac{[\mathrm{S}]}{\mathrm{K}_{\mathrm{M(app)}}+[\mathrm{S}]} \qquad \text{(Eq. 1.8)}$$

where [S] (M) is the nutrient concentration in the medium, I (A) is the current obtained by EAB, I_{max} (A) is the maximum current achieved by EAB when [S] is in high concentration, and $K_{M(app)}$ (M) is the nutrient concentration at which the current is half of its maximum value which is called apparent Michaelis constant. In enzymology, the K_M constant is often considered a measure of the affinity between the enzyme and the substrate molecule and can have a similar meaning in whole-cell catalysis. In high concentration of nutrients in the medium of EAB, the nutrient is available in excess and the Michaelis–Menten equation will be $I = I_{max}$ assuming no limitations in electron transfer. A typical Michaelis–Menten curve based on current output of a bioelectrochemical system as a function of nutrient concentration for electroactive bacteria is shown in Figure 1.11(a).

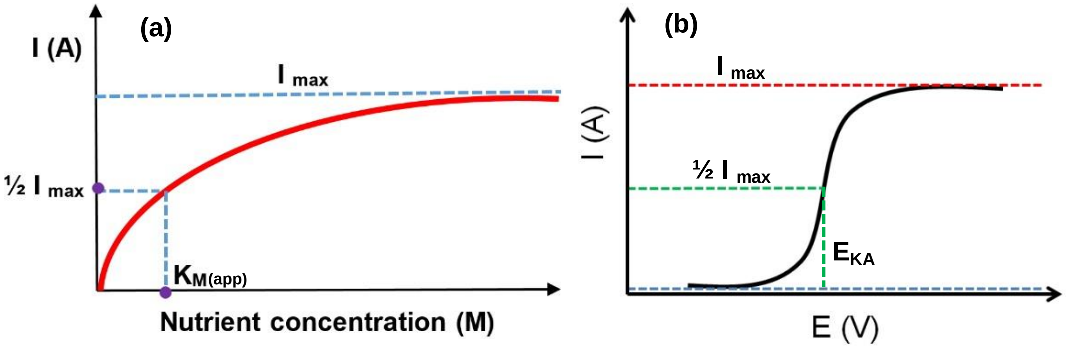

Figure 1.7 (a) A typical Michaelis–Menten curve based on current output of BES in function of nutrient concentration for electroactive bacteria, assuming non-limiting electron transport. **(b)** The Nernst–Michaelis–Menten curve for electroactive bacteria in high nutrient concentration (non-limiting nutrients).

Typically the Nernst and Michaelis–Menten equations (Figure 1.11b) are blended to create an electrochemically applicable equation to model the steady-state kinetics of an enzyme/electrode system.[81] Eq. 1.8 has a parameter (E_{KA}), can be defined based on the catalytic reactions of proteins that are being oxidized or reduced at the anode and mass transfer coefficients of reactants/products. This equation showed very good compatibility with EET of electroactive bacteria. Therefore, E_{KA} in case of EAB may be defined to the redox potential of proteins associated with respiration. Although, given the complex enzymatic processes occurring in an EAB electron transfer chain, because of similarity in kinetic processes of enzyme/electrode and bacteria/electrode systems, we can analyze them in a similar manner as is performed in enzyme electrochemistry.[82]

$$\mathrm{I} = \mathrm{I}_{\max}\left\{\frac{1}{1+\exp\left[-\frac{\mathrm{F}}{\mathrm{RT}}(\mathrm{E}-\mathrm{E}_{\mathrm{KA}})\right]}\right\} \qquad \text{(Eq. 1.9)}$$

Where R is the ideal gas constant (8.3145 $J.mol^{-1}.K^{-1}$), F is the Faraday constant (96 485 $C.mol^{-1}$), T is the temperature (K), and E_{KA} (V) is the potential at which I = 1/2 I_{max}. E_{KA} is related to the standard reduction potential of proteins associated with respiration. Therefore, the Nernst–Michaelis–Menten equation has been successfully used to model EABs' response to changes in anode or working electrode potentials.[82] Eq. 1.9 is relevant for either DET or MET mechanism.

Numerous factors affect BES performance and charge kinetics of EET in electroactive bacteria. Considered to be among the most important include electrode material, shape and roughness, substrate type and concentration, BES geometric design and operating conditions such as temperature, pH and salinity.[83]

The solution-phase pH (pH_s) around the biofilm can cause changes in the biofilm pH (pH_b), resulting in a significant impact on the current output from electroactive biofilm. The growth rates of *G. sulfurreducens* cultures utilizing fumarate as an electron acceptor were observed to be reduced at pH 6.4 and 6, and completely inhibited at pH 5.5.[76] The generation of protons by cells within an electrode-adhered *Geobacter* species biofilm, and their diffusion out of the biofilm, is predicted to result in the formation of a proton concentration gradient across the biofilm and a drop in the pH value is expected to occur close to the biofilm/electrode interface. This pH issue is discussed in Chapter 3 of this thesis.

1.2.2.5 Biocatalytic kinetic measurements in flow

The kinetics for immobilized enzymes may be different from those measured for the same enzyme in solution.[84,85] The kinetics of immobilized enzymes and those under flow are often referred to as the apparent kinetics. The Lilly-Hornby model (Eq. 1.10) was developed to account for changes to apparent enzymatic kinetics due to immobilized enzymes under flow conditions:[86]

$$P\,[A_0] = K_{M(app)}\,\mathrm{Ln}\,(1 - P) + \frac{C}{Q} \qquad \text{(Eq. 1.10)}$$

where P is the fraction of the substrate converted ($P = ([S]_i-[S]_f)/[S]_i$) to the product during the reaction, Q is the flow rate of the substrate ($L{\cdot}h^{-1}$), $[A_0]$ is the initial substrate concentration (M), *C* is the reaction capacity of the reactor ($mol{\cdot}h^{-1}$), and $K_{M(app)}$ is the apparent Michaelis constant (M). Comparing Eq. 1.10 to the equation of a line, P $[A_0]$ may be plotted against ln (1-P) resulting in a straight line with a slope of $K_{M(app)}$ and intercept on the P $[A_0]$ of C/Q. The reaction capacity of the reactor (C) can be defined in:

$$C = k_{cat}\,E\,\beta \qquad \text{(Eq.1.11)}$$

where k_{cat} (h^{-1}) is the turnover number (the maximum number of chemical conversions of substrate molecules per unit time), E is enzyme quantity (mol) and β is void fraction of the microreactor (V_v /V_s) ($V_{v,}$ is the void chamber volume and V_s is the reaction chamber volume).

Several studies on the heterogeneous kinetic parameters for an enzymatic reaction in a continuously operated micro reactor showed different behavior of enzymatic kinetic related to flow rate. In a continuous-flow system packed with immobilized micro beads at different flow rates, increasing flow rates can result in either increase[87] or decrease[88] of $K_{M(app)}$. By using the Lilly-Hornby equation, apparent Michaelis constant was calculated and the intercept of $K_{M(app)}$ vs. Q curve was revealed apparent Michaelis constant in zero-flow rate condition.

Until recently, the Lilly-Hornby had never been applied to whole-cell catalysis. Considering of EABs as immobilized biocatalysts, it is proposed in this thesis it may be possible to study the kinetics of bacterial respiration (linked to enzymatic reactions of nutrient digestion) by Lilly-Hornby model in microfluidic devices. In this thesis, respiration kinetic of electroactive bacteria (*G. sulfurreducens*) in a microfluidic electrochemical cell has been studied for the first time.

1.3 Microfluidics

Before the concept of “microfluidics” was introduced, microchannels had already been used, for example, glass or quartz capillaries for gas chromatography, inkjet printers and capillary electrophoresis, and flow reactors micromachined in metal.[89] The technology of microfluidics has experienced explosive growth after its debut in 1990s. Microfluidics is spreading into a wide range of scientific research areas due to the great need for miniaturized, portable and low-cost commercial devices[90] and due to certain unique phenomena that can be exploited at the microscale, which are discussed shortly. Microfluidic channels are defined as having at least one dimension with length in the range of 10-1000 µm. They are used for manipulations of liquids and gases in chemical, biological and medical applications.[91] The first-generation microfluidic chips were prepared in silica or glass, with polymer-based chips being introduced several years later.[89] Elastomeric materials such as poly dimethyl siloxane (PDMS) have emerged recently as excellent alternatives to the silicon and glass used in early devices.

This section begins with a brief introduction to microfluidics, principles, characteristics and benefits, followed by a description of the PDMS-based microfluidic technology (related to this thesis) fabrication, biofilms in microfluidic electrochemical cells and enzymatic kinetic studies in microchannels.

1.3.1 Principles, characteristics and benefits of microfluidics

Microfluidic channels consist of moulded or machined microscale channels to manipulate nanoliter sample volumes. It is an interesting technology for the scale-down and potential automation of culture-based platforms. Studies in microfluidic channels benefit from large surface-to-volume ratios, low thermal gradients, low reagent consumption, laminar fluid flow, and fast and complete reactions.[92] The reduction of reagent consumption through microchannels can reduce cost of reagents used in the experiments, specifically, when the reagents are expensive or only available in low quantity. The Reynolds number (Re), Eq 1.12[93] gives a quantitative measure of the flow, with Re values lower than 2100, being considered laminar.[93] In microchannels Re is routinely lower than 1.

$$\mathrm{Re} = \frac{\mathrm{d}\mathrm{v}\rho}{\mu} \qquad \text{(Eq. 1.12)}$$

where d is the hydraulic diameter (m) of the channel ((2ab/(a+b)), a=width, b=height of rectangular channel), v is the average velocity of the fluid ($\mathrm{m\cdot s^{-1}}$), ρ is the fluid density ($\mathrm{kg\cdot m^{-3}}$), and μ is the fluid viscosity in (Pa·s) or ($\mathrm{kg\cdot m^{-1}\cdot s^{-1}}$). A sketch of laminar and turbulent flow is shown at Figure 1.12.

Figure 1.8 A representation of laminar flow with separate flow layers (left) and a turbulent flow with crossed-mixed flow layers (right).

The low thermal mass and large surface to volume ratio facilitate rapid heat transfer, enabling rapid thermal stabilization and precise control of temperature.[94] The large surface to volume ratio is also an advantage in processes involving support-bound catalysts, biofilms or enzymes.[95] Small, controllable diffusion distances in microchannels can also allow enhance mass transfer despite the lack of convective mixing, which can improve efficiency and safety of chemical reactions when precisely controlled and monitored.[94] Also, contact time between the fluid and wall-supported catalysts is easily controlled and calculated in microfluidic devices.[96]

Microfluidics has been established in biological research areas, such as cell culture research,[97] polymerase chain reaction (PCR) diagnostic tools,[98] biofilm research[99] and even for synthesis of functional organ sub-systems.[100] Microfluidics has opened many new areas in electrochemistry, including hydrodynamic electrochemistry and miniaturization of energetic devices.[101] As is often the case with chemical and biological reactions, multiple products can be generated from a given set of reagents dependent on the local conditions of the reaction. With the control over these conditions granted by microfluidics, individual compounds that could be produced by a given reaction can thus be selectively produced with high degrees of precision. In regards to relative reaction times of microfluidic reactors and bulk reactors, there are a few fundamental considerations limiting the ability to make a direct comparison in all respects.[95] In industrial chemical processes, bulk reactions are often performed with more time than would be necessary to reach the equilibrium point of the reaction, in order to ensure that the desired reaction has reached completion everywhere within the reactor. Furthermore, chemical reactions in microfluidic devices can be performed with more inherent safety than before and with the ability to handle high pressures and temperatures and low volumes.[102]

Owing to the rapid response times programmed changes microreactor condition scan be easily optimized to perform high-throughput assays and combinatorial studies.[103] This can include mapping the reaction phase space, by varying reaction factors, such as temperature, reagent concentration, and residence time, then rapidly sampling product formation close to real-time.[103]

The shear stress is another important controllable parameter in flow cells. Shear stress is the tangential force applied to a surface by a flowing liquid. Fluid shear stress increases with fluid velocity and with viscosity, as calculated in Eq. 1.13:

$$\tau = \mu \frac{\partial v}{\partial z} \qquad \text{(Eq. 1.13)}$$

where μ is the liquid viscosity ($kg \cdot m^{-1} \cdot s^{-1}$) and $\frac{\partial v}{\partial y}$ (s^{-1}) is the velocity gradient perpendicular to the wall. This occurs because velocity of liquid flow layers continuously varies with distance from the wall, creating a parabolic velocity distribution in simple laminar microflows. Fluid velocity is the fastest at the center and due to the classic “no slip condition” velocity at the channel wall (y=0) is $v = 0$. Average velocity can be calculated with v = Q/A, where Q is flow rate and A is cross-sectional surface area. At y=0, the velocity gradient dv/dt results in a shear stress created by the fluid which is referred as the “wall shear stress” and the velocity gradient is usually called “wall shear rate”.[104] A schematic of flow profile and shear stress in a channel with laminar flow characteristic is demonstrated in Figure 1.13. The wall shear stress is usually the most critical parameter in determining a mechanical response by adhered cells.

Figure 1.9 (a) Side view of velocity profile and (b) shear rate distribution in a simple geometry with laminar flow.

In the last decade microfluidics has aided in detailing numerous biological responses to the application of hydrodynamic forces. These include changes to morphology (e.g., elongation and cell alignment in the direction of the flow), gene and protein expression and proliferation.[105] The impact of shear stress on cell behaviour can be different from cell to cell. For example, most of the responses to flow mentioned above are related to eukaryotic cells. Prokaryote cells, such as bacteria, can also be affected by hydrodynamic effects, such as shear stress, but are more specifically affected by related changes molecular mass transfer.

The shear stress can be evaluated using fluid dynamics methods. In a microfluidic device, in order to calculate the flow, thus the shear stress, the Navier-Stokes equation should be solved to find the velocity profile for the considered geometry. In the case of simple geometries such as a wide rectangular channel, the analytical solution is simple and can be found in the literature.[92] For instance, for a rectangular channel of dimensions h (height), w (width) and l (length) with $h < w < l$, the wall shear stress can be calculated according to the following equation:

$$\tau = \frac{6\eta Q}{h^2 w} \qquad \text{(Eq.1.14)}$$

where Q is the volumetric flow rate ($m^3 \cdot s^{-1}$), h and w are the height and the width of the channel (m), respectively. The shear stress calculation for complex geometries are usually performed using numerical simulations to estimate the shear stress or the shear rate.

1.3.2 Microfluidic fabrication and methods

The microfabrication can be categorized as either sequential or template-based. Sequential fabrication includes milling, printing and ablation. This approach has several advantages, such as straightforward formation of three-dimensional features and easy prototyping. Sequential methods can be useful, because of seamless design to prototyping workflow, however, as channels are created progressively, it is only efficient for small or low-density designs. In contrast, template-based fabrication techniques can include casting, injection moulding and hot embossing which create all features simultaneously in one step.[106] Template-based fabrication techniques, which we focus on here, have advantages including fast and accurate fabrication of replicate devices with complex features at market-relevant volume demands, but require special attention and the introduction of dedicated fabrication step.

Hot embossing is one example of template-based fabrication techniques, in which a heated microstructured template is contacted with a heated thermoplastic material, which then conforms to the template topography. In this method, the operational temperature is above the glass transition temperature (T_g) of the thermoplastic.[107] Hot embossing is similar to injection moulding, but in hot embossing complete melting of polymer is not required, thereby reducing energy consumption, cycle times and residual thermal stress.[108] Control of the conformation between the thermoplastic material and the template can also enable the formation of controllable three-dimensional features.[109] Another template-based approach is the casting of an elastomer against a mould. This work in microfluidics has focused on the elastomer poly-dimethyl siloxane (PDMS). PDMS is an excellent material for the fabrication of microchannel systems for use with biological samples in aqueous solutions.[110] Our approach to the fabrication of microfluidic templates for either PDMS casting or even embossing of thermoplastics[108] is based on photolithography, as discussed next.

1.3.2.1 Photolithography

Photolithography is the process of transferring geometric shapes from a high resolution two-dimensional mask to a photosensitive resist polymer adhered to a substrate (generally a silicon wafer or glass).[111] Depending on required resolution, the mask may be simply a laser-printed overhead transparency or a high-resolution print on thin polymer transparency film. There are two types of photosensitive resist polymer (photoresist), positive and negative. For positive photoresists, the resist is exposed with light wherever the underlying material is to be removed. In these photoresists, exposure to the light changes the chemical structure of the photoresist to become soluble in a developer solution, leaving behind an exact (positive) copy of the printed mask pattern. Exposure of a negative photoresist results in a photochemical reaction (usually cross-linking) rendering the exposed location insoluble to a developer solution. Therefore, the pattern remaining after development is the opposite (negative) of the photomask design. Generally, negative photoresists are very viscous enabling the formation of tall features, whereas the opposite is true for positive photoresists. Figure 1.14 shows the pattern differences generated from the use of positive and negative photoresists.

Generally, in channel based PDMS microfluidic devices a negative photoresist is used to achieve required channel heights. The moulds used for PDMS casting employ a wide variety of materials but generally a negative photoresist, such as SU-8 (used in this thesis), is the most common material used. Typically these are spin coated with many suitable formulations in SU-8 of varying viscosities being available for forming different layer thicknesses.

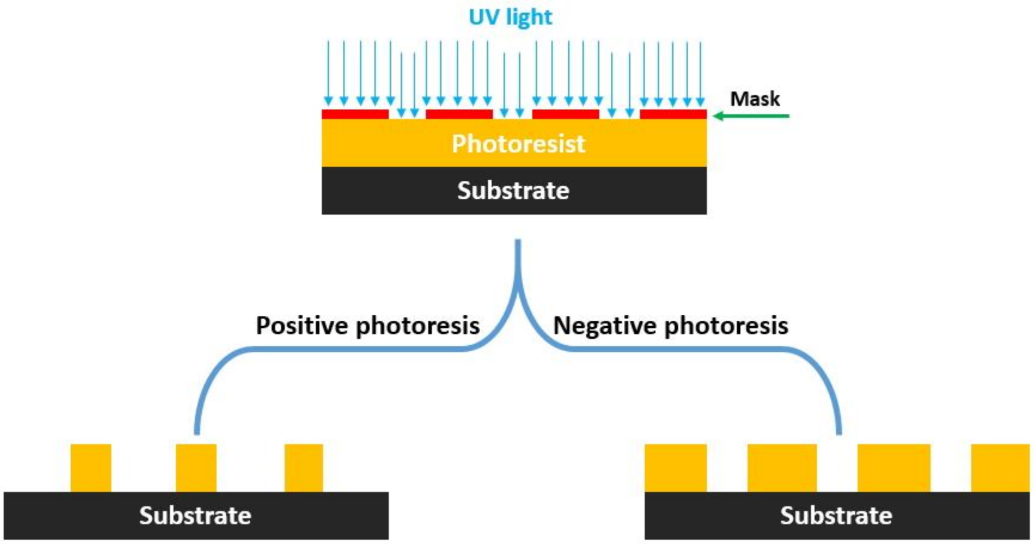

Figure 1.14 A schematic of positive and negative photoresist patterning. Based on which photochemical reactions occur during light exposure time, positive or negative features can be made on the substrate. Final mould will be ready after washing with the developer solution and cleaning removable portions.

1.3.2.2 Casting and bonding

The PDMS used in the work described here is supplied in two components, a viscous polymer base and a cross-linking agent. After combining the polymer and cross-linking agent and degassing any trapped bubbles the viscous solution conforms to the shape of the mould and solidifies, usually at a slightly elevated temperature of 70°C. The low surface free energy and elasticity of PDMS allow it to release from the mould without damage to itself or the mould.

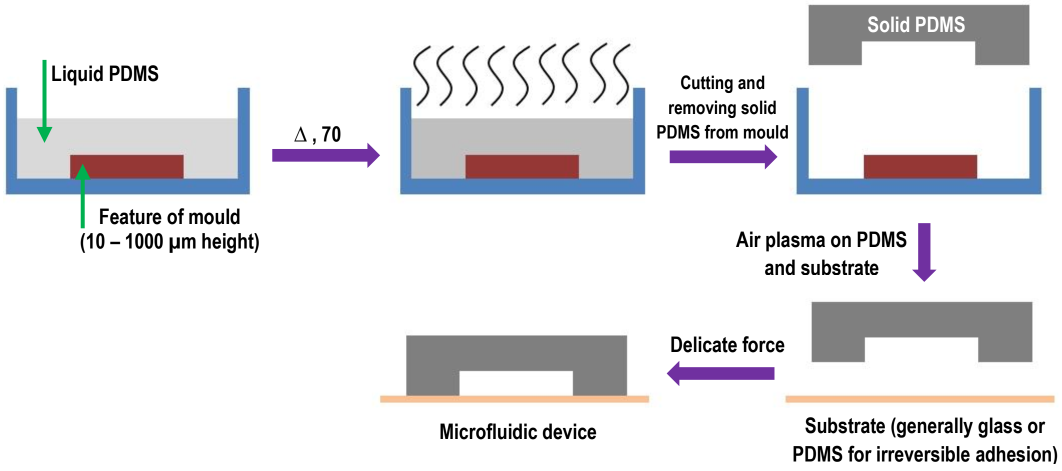

Figure 1.15 A schematic of PDMS baking and casting for microfluidic device fabrication

PDMS is easily demoulded from the smooth surfaces generated by photolithographic templates discussed above due to its elastomeric mechanical properties and low surface energy.[112] Another advantage of PDMS is that it can irreversibly seal to itself, or to certain planar surfaces, without distortion of the channels.[113] This is accomplished with exposure to a plasma gas of air or oxygen due to radical oxygen groups that transform Si-CH_3 to Si-OH at the expose PDMS-air interface. When the PDMS block is contacted by a glass slide or another plasma treated PDMS surface, Si-OH form a covalent connection (or bond) Si-O-

Si. Exposure to O_2-containing plasma gas also has the effect of temporarily decreasing the hydrophobicity, until mobile polymer chains reorganize to hide the Si-OH groups within the PDMS bulk. Adhesive silicone tapes or cellophanes can also seal the PDMS channels reversibly. In Figure 1.15, a flowchart of PDMS device fabrication is shown.

1.3.3 Bacteria and their biofilms studied with microfluidics

Bacterial biofilms are highly heterogeneous both in space and time.[99] Studying bacterial biofilms in microchannels has been demonstrated to help control their behaviour, enabling more accurate and repeatable studies into biocatalysts. Many studies have examined the hydrodynamic and environmental effects on biofilm development, such as shear stress,[114] quorum sensing signals,[115] and nutrient concentration.[116] By using microfluidics, precise control over both flow rate and chemical concentrations in the microchannel can provide information, such as real-time observation of biofilm formation, hydrodynamic effects and chemical components on biofilm formation.[117] The knowledge gained has significantly improved our understanding of underlying biofilm formation and function.

As a common characteristic of flow cells, the biofilms are always exposed to fresh nutrient medium with well-defined flow rates, while the batch reactors need periodic replacement of the medium because of continuous consumption of nutrients by electroactive bacteria.[118] In addition, the parallelization by multiple microfluidic channels can provide rapid assays of electrochemical activity for different bacterial strains.[119] Microfluidics promotes rapid response times and more precise control over different kinds of chemical components with different concentrations.

Microfluidic channels may be designed to study combined effects of several influencing factors on biofilm formation at the same time and providing more opportunities for bacterial cells to adhere and disperse.[120] As well, shear stress can act as an inhibitor of biofilm development, including causing a slow-down in maturation, maintaining biofilms in an early stage, as well as decreasing bacterial diversity in a biofilm.[121] Generally, shear stress can have contradictory influences on biofilm development; for example, both suppressing the development of a biofilm matrix, while at the same time providing more opportunities for new biofilm formation by increasing the residence time.[122]

Recently, the Greener group has identified certain practical challenges and their solutions, which should be addressed when studying biofilms in microchannels. First, using a new approach for attenuated total reflection Fourier transform infrared (ATR-FTIR) spectroscopy, growth assays could be conducted under different conditions.[123] It was noted that when the solid sealing surface was exposed to plasma gas during the device fabrication that deposited contaminants this could reduce lag phase and result in faster accumulation of biofilms.[124] A similar system also characterized the effect of semi-stable surface-adhered bubbles, which affected the production of extracellular biomolecules,[125] as well as high-resolution microscope studies which noted powerful effects on biofilm growth rate and patterning, indicating that careful attention to solution preparation and in-line bubble traps are required for accurate on-chip biofilm studies.[126] As well a solution to the widespread, yet often unaddressed problem of contamination of upstream fluidic components (connective tubing, nutrient source, etc.) was demonstrated that could avoid pre-digestion of nutrient molecules and related uncertainties in biochemical conditions growth medium.[127]

1.3.4 Biofilms in microfluidic electrochemical cells

As explained in the Section 1.2.1, EIS measurements are useful for monitoring changes to properties of the biointerface via changes to electrical properties, impedance and capacitance. This technique is generally used for demonstration and investigation of biofilm growth and can be conducted while under imposed shear stress of a microfluidic channel.[128] On the other hand, as explained in section 1.2.2, MFCs are two-electrode BES, which produce usable electric current via the oxidation of dissolved organic molecules. Microfluidic MFCs have some advantages. The anolyte and catholyte solutions in microfluidic MFCs can be separated without using any proton exchange membrane (PEM). This can happen with laminar flow characteristic in microfluidic channels.[129] The elimination of the membrane in MFCs can remove the membrane resistance from internal resistance of the system (R_{int}) and therefore, reduce the total internal resistance of the system.[130]

One the most important and significant characteristic of microfluidic MFCs is flow-induced performance improvement. This can be explained by higher mass transport of nutrients into low levels of biofilm layers (next to the electrode surface) in MFCs and washing out of by-products and H^+ of bacterial respiration[131] or higher rate of mass transfer of deprotonated buffer into the biofilm and mass transfer of protons and protonated buffer out of the biofilm.[132]

Examples of 3-electrode setups in microfluidic channels that are the most relevant for this thesis. This electrochemical configuration increases the number of applicable electrochemical techniques such as CV or EIS while the flow rate manipulates mass transfer of materials through biofilm. To our knowledge, the first report of a 3-electrode microfluidic electrochemical cell for studies of EABs is published in 2016.[133] A Y-shape microfluidic channel was used to make side-by-side co-flowing streams. This design can isolate the analyte stream against the working and counter electrodes and a KCl stream in contact with the calibrated reference electrode. This device enabled *in situ* measurements via electrochemical technique such as CV and monitoring the short- and long-term EAB response to addition of solutions containing toxic molecules with good repeatability.

1.4 Scope of thesis

As a whole, this thesis introduces a new 3-electrode microfluidic flow cell for *in situ* electrochemical measurement on both electroactive and non-electroactive biofilms. Characterization can be accomplished under tightly controlled conditions, including chemical concentrations and flow rates. The following chapters demonstrate applications of this new platform to study biofilm systems.

In Chapter 2, we use *in situ* electrochemical impedance spectroscopy (EIS) to characterize biofilm quantity and structure at the attachment surface under different hydrodynamic conditions. This work was conducted on a biofilm of *Pseudomonas sp*. bacteria during the growth and after maturation. Our hypothesis was that the biofilm layers directly at the electrode surface may not be strongly affected by shear forces compared to the more loosely attached outer layers, which would limit the effectiveness of mechanical removal as a method for controlling biofouling. This was indeed observed, however, some limited changes to biofilm structure of exposed layers at the attachment surface did appear to occur. Furthermore, we were able to control the position of the biofilm within the microchannel and make similar measurements on biofilms isolated to or away from the channel corners.

In Chapter 3, we successfully addressed a long-held assumption that observed improvements to current production from flow-through systems containing electroactive biofilms may be due to deacidification. Various published works hypothesized that such increases to pH could occur due to enhanced mass transfer of either acidic by-products out of the biofilm or deprotonated buffer molecules into the biofilm. Using a proven, but underused, approach to monitor pH changes via *in situ* cyclic voltammetry within the microchannel, it was shown that flow imposed tangentially against electrode-adhered *G. sulfurreducens* biofilms could modify the biofilm pH, but only for low acetate concentrations, which is not the case for most published studies. We put these interesting and unexpected results into context by considering the flow in enhancing deacidification and/or nutrient flux under elevated flow conditions.

In Chapter 4, we focused on the previously unaddressed limitations of EABs at low concentrations. Using the same three-electrode microfluidic platform used in the previous chapters, chronoamperometric measurements were made to give real-time respiration rates of an electrode-adhered *G. sulfurreducens* biofilm under highly nutrient limiting concentrations and varying flow conditions. In this chapter, we demonstrate a method to reversibly toggle between metabolic activity states on demand. This approach was used to make 3 separate fundamental discoveries: (1) the identification of a new pseudo-active metabolic state, (2) high molecular conversion efficiency at threshold concentrations compared to turnover concentrations, and (3) reductions in usable acetate concentrations to less than 50 times the thresholds obtained in static MFCs.

In Chapter 5 the kinetics of bacterial respiration were studied using the microfluidic electrochemical flow cell. Recent high-profile papers point to bacterial biofilms as an option for heterogeneous whole-cell catalysis, with potential to impact industry. Proof of the applicability of a flow-adapted version of the Michaelis-Menten model for enzymatic flow reactors is urgently required in order to accelerate advancements in the field. This approach shows the equation developed by Lilly and Hornby in 1966 is compatible with electroactive bacteria and can be used as a new means to translate improvements in biofilm catalysis under flow into standard parameters and concepts used in enzyme catalysis, thereby aiding rapid determination of biological kinetics in microfluidic systems. The new approach also brings a new variable, the device reactor capacity, which tentatively gives proof of that the involvement of increased numbers of enzymes (and bacteria) implicated in the catalytic process. Thus, we tentatively conclude that increases to mass transport of nutrients through the biofilm, are at the heart of increasing reaction efficiency compared to bulk reactors.

Chapter 2. Hydrodynamic effects on biofilms at the biointerface using a microfluidic electrochemical cell: case study of *Pseudomonas sp.*

Mir Pouyan Zarabadi[1], François Paquet-Mercier[1], Steve J. Charette[2,3,4], Jesse Greener[*,1]

[1]Département de Chimie, Faculté des sciences et de génie, Université Laval, Québec City, QC, Canada.

[2]Institut de Biologie Intégrative et des Systèmes, Pavillon Charles-Eugène-Marchand, Université Laval, Québec City, QC, Canada.

[3]Centre de recherche de l'Institut universitaire de cardiologie et de pneumologie de Québec, Québec City, QC, Canada.

[4]Département de biochimie, de microbiologie et de bio-informatique, Faculté des sciences et de génie, Université Laval, Québec City, QC, Canada.

Accepted manuscript online on 1 February 2017. Modifications on the numbering of the figures of the paper have been done in order to fit the sequence of the dissertation.

Published in *Langmuir* 33, 8, 2017, 2041-2049.

2.1 Résumé

La partie adhérée d'un biofilm devrait réagir différemment aux tensions environnementales que les parties dans la masse du biofilm en raison de la protection par les autres couches du biofilm et de la proximité de la surface de fixation. L'effet de la tension hydrodynamique sur la partie du biofilm adhérant à la surface a été vérifié à l'aide d'une cellule microfluidique spécialement conçue avec un système intégré de détection à trois électrodes. La mesure de la biocapacitance et la biorésistance de la couche du biofilm de *Pseudomonas sp.* liée à l'électrode a été réalisée lors de la croissance dans différentes conditions d'écoulement en utilisant la spectroscopie d'impédance électrochimique (EIS) *in situ*. Des changements distinctifs, mais réversibles, de la quantité et de la structure ont été observés à l'aide de l'EIS lors de l'application d'une contrainte de cisaillement élevée. Au contraire, la microscopie a révélé une déformation permanente du volume du biofilm, sous la forme de banderoles et d'ondulations. L'application de contraintes de cisaillement extrêmes a entraîné l'élimination complète de portions importantes des couches externes du biofilm, mais n'a pas modifié la quantité de biofilm présent à la surface. Cependant, la structure du biofilm restant s'est montrée susceptible de subir de nouveaux changements suite à l'application d'une contrainte de cisaillement directement aux couches de biofilm non protégées et adhérées à la surface.

2.2 Abstract

The anchoring biofilm layer is expected to exhibit a different response to environmental stresses than for portions in the bulk, due to the protection from other strata and the proximity to the attachment surface. The effect of hydrodynamic stress on surface-adhered biofilm layers was tested using a specially designed microfluidic bio flow cell with an embedded three-electrode detection system. In situ electrochemical impedance spectroscopy (EIS) measurements of biocapacitance and bioresistance of the electrode-bound layer of *Pseudomonas sp.* biofilms were conducted during growth under different shear flow conditions. Distinctive, but reversible, changes to the quantity and structure were observed using EIS during the application of elevated shear stress. In contrast, microscopy revealed permanent distortion to biofilm bulk, in the form of streamers and ripples. Application of extreme shear stresses, caused the complete removal of significant portions of biofilm outer layers, but did not change the quantity of biofilm at the attachment surface. The structure of the remaining biofilm, however, appeared to be susceptible to further changes following application of shear stress directly to the unprotected biofilm layers at the attachment surface.

2.3 Introduction

Biofilm formation enables the firm attachment of sessile bacteria to solid surfaces where they can develop an environmental niche. Tangential (shear) liquid flow can aid the bacteria by enhancing mass transfer of essential molecular species into the biofilm and preventing buildup of molecular byproducts. This has a pronounced impact on biofilm mechanical properties[134] and physical properties[135,136,137,138] but also on the metabolism,[139] growth kinetics,[140,141] and biochemistry[142,143] of the resident microorganisms. The impact of time-changing flow on biofilm properties is less understood.[144,145] The effect of fluidic conditions on the biofilm is complicated by the fact that flow against it is expected to affect outer layers disproportionately, whereas portions at the attachment surface remain relatively unperturbed.[146,147] For example, much of the biofilm resistance to elimination is linked to the surface attached portions, where highly attenuated molecular mass transfer of nutrients and oxygen may give rise to so-called "persister" cells.[148,149] Many biofilm species are also known to have structural features at the attachment surface due to localized anchoring points, resulting in mushroom-like structures.[150] These are critical features that allow limited convection through the interior of the biofilm.[147, 149] Biofilm structure and the influence of shear stress on it can be studied by optical microscopy, but the details at the attachment surface are hard to resolve due to interference from other strata. Confocal laser scanning microscopy can reject optical interference originating away from the attachment surface. However, even with fluorescent protein expressing bacteria, the extracellular polymeric material remains invisible and attempts to add fluorescent markers does not guarantee uniform results in space or time.[151] While, quantitative studies using high-resolution imaging are difficult to capture global properties, such measurements can add invaluable visual confirmation related to structural properties. Attenuated total reflection infrared (ATR-IR) spectroscopy has been successfully used to measure biofilm biomass and extracellular matrix materials within a few microns from the surface under flow conditions. Other surface techniques such as surface plasmon resonance spectroscopy and surface enhance Raman spectroscopy, can be valuable for biofouling studies, but require specific surface preparation.[152,153]

Electrochemical techniques have also been gaining favour as versatile approaches in studying bacteria attachment and biofilm development.[154,155,156,157] These approaches are also gaining attention in the microfluidics community,[133,158,159] thanks in part to their advances in microfabrication techniques.

Here we present a compact three-electrode system embedded in a microfluidic flow cell for studies of *Pseudomonas sp.* biofilms exposed to laminar flow conditions. Electrochemical impedance spectroscopy (EIS) produced Nyquist plots, which were subsequently analyzed using an accepted equivalence circuit for non-electroactive biofilms. This produced time-changing equivalent biofilm capacitance and resistance values, which helped assess biomass accumulation and structural changes as a function of growth time and hydrodynamic conditions. Parallel microscopy provided comparison with bulk biofilm properties, whereas ATR-IR and CLSM measurements were used to verify EIS observations regarding biofilm accumulation and structure at the biointerface.

2.4 Experimental section

2.4.1 Fabrication of a microfluidic flow cell

The graphite (GraphiteStore.com Inc., USA) working electrode (WE) and counter electrode (CE) were cut into 3 mm × 20 mm strips. A pseudo-reference electrode was made by electroless deposition of gold on a planar polystyrene substrate. The solution used for this included 10 mM of 99.999% chloroauric acid (Sigma-Aldrich, USA) as a gold source, with 18 mM D-glucose (Sigma-Aldrich, USA) as a reducing agent and 400 mM sodium bicarbonate (Sigma-Aldrich, USA) as a pH buffer in distilled water. After degassing, the solution was poured on a planar polystyrene substrate and was kept for 24 h at ambient temperature. The gold coated polystyrene was then rinsed with distilled water and cut into 5×20 mm strips.

Figure 2.1 shows the device fabrication steps. All three electrodes were placed in direct contact with the photoresist features on a silicon master mold (FlowJEM Inc., Toronto, Canada) using double-sided tape. Next, a 10:1 mixture of liquid polydimethylsiloxane (PDMS) and cross-linking agent Sylgard184 (Dow corning, Canada) was poured over the mold and left to cure for 4 h at 70 °C. This encased the three electrodes in PDMS except for the portion that was protected by the feature surface on the mold. Once cured, the PDMS device was carefully removed from the mold. As PDMS was excluded from flowing between the electrode and the channel feature on the mold, the surface of the electrodes could be exposed at the bottom of the microchannels after removing the double-sided tape. This resulted in a smooth transition from the PDMS portion of the microchannel to the electrodes. A portion of the PDMS device was then removed, exposing the electrodes for connection to the potentiostat. The sequential orientation of WE and CE relative to the flow direction in the microchannel is similar to other devices used for chemical sensing,[160] biofilm studies by voltammetry and EIS.[133,158,159] Two inlets were punched into the channel. The first (I_1) was at the far end, just before the gold reference electrode, and the second (I_2) just after the gold electrode (Figure 2.1 d). A third hold was punched at the opposite end of the channel as a device outlet (O). Cleaning and sterilization of channel and electrodes was conducted before sealing. Sterile cotton swabs dipped in 1M HCl were used for cleaning graphite electrodes and 70% ethanol for the PDMS channel surfaces and gold electrode. The time of exposure and applied scrubbing force did not visibly damage to the electrodes or swell of the PDMS, nor were any changes to the electrical conductivity detected after cleaning. A microscope glass slide (Fisher Scientific, USA) was cleaned by immersion in 70% ethanol for 5 minutes and then dried under clean N_2 gas stream in a laminar flow cabinet. The microfluidic electrochemical cell and microscope slide were placed into a plasma cleaning oven (PCD-001 Harrick Plasma, Ithaca, NY, USA) for 90 seconds exposure to sterile air plasma at 650 mtorr. This further sterilized both components and enabled surface activation of the PDMS for irreversible bonding. Sterile perfluoroalkoxy connective tubing (Hamilton Inc., Canada) was attached to inlets, which were in turn connected to 60 mL syringes (BD Scientific, NJ, USA) via connector assemblies (P-200x, P-658, IDEX, WA, USA). Syringe pumps (PHD 2000, Harvard Apparatus, Holliston, MA, USA) were used for liquid injection. The microfluidic channel and tubing were then rinsed with sterile distilled water for 1 hour at 1 mL·h^{-1} through inlets I_1 and I_2. Finally, electrical connections were made between the electrodes and the potentiostat.

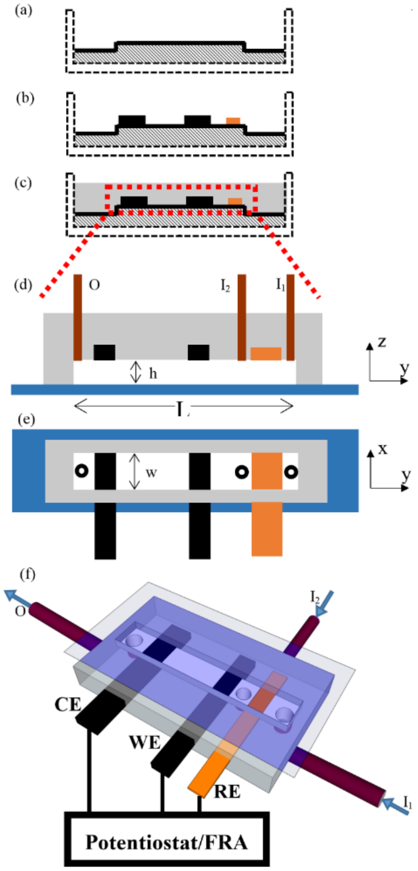

Figure 2.1 Device fabrication. **(a)** Cross-section view of the mold (diagonal cross-hatch) with a raised feature that defines the microchannel, which is fixed to the bottom of a container (dashed). **(b)** Two 3 mm wide graphite electrodes (black) and a 5 mm wide gold electrode (green) were placed on top of the mold channel feature. **(c)** PDMS (grey) with cross-linker were poured over the mold/electrode assembly. **(d)** Zoomed cross-section view from the marked region in (c) of the microfluidic device after removal from the mold with embedded electrodes and sealing to a glass microscope slide (blue). Device includes inlets (I_1, I_2), and outlet (O). Cleaning process described in text not shown. **(e)** Bird's eye view of the microfluidic electrochemical cell in (d). **(f)** Thee-dimensional rendering of the microfluidic device with embedded electrodes with connections of the working (WE), counter (CE) and gold pseudo-reference (RE) electrodes connected to a potentiostat with frequency response analyzer (FRA) and liquid connections. Electrode sizes are not to scale. Channel length, height and width were L=33 mm, h=300 µm and w=2 mm, respectively, as defined by the mold protrusion in (a). The axes x and y are perpendicular and parallel to the flow direction of the channel, respectively, and z is parallel with the channel vertical axis.

2.4.2 Bacteria and solution preparation

The bacterial strain used was *Pseudomonas fluorescens* CT07 tagged with a chromosomally integrated green fluorescent protein (GFP), known as *Pseudomonas* sp., strain CT07 in the literature.[161] The nutrient source used in this study was of the AB type, which consisted of 1.51 mM $(NH_4)_2SO_4$, 3.37 mM Na_2HPO_4, 2.20 mM KH_2PO_4, 179 mM NaCl, 0.1 mM $MgCl_2 \cdot 6H_2O$, 0.01 mM $CaCl_2 \cdot 2H_2O$, 0.001 mM $FeCl_3$ and 10 mM $Na_3C_6H_5O_7$ (trisodium citrate) as the carbon source. Liquid cultures were obtained by transferring and dispersing bacterial colonies from an agar-culture dish containing AB growth medium and to 3 mL of liquid AB growth medium. The pre-culture was ready for use after 18 h of incubation at 30 °C on orbital shaker operating at 300 rpm. This protocol was followed precisely to obtain inoculum solutions with similar bacterial activities from experiment to experiment. All chemicals were obtained from Sigma Aldrich, USA. Confinement solution was identical to the liquid nutrient solution except there was no carbon source. Growth medium and confinement solutions were sterilized in an autoclave at 120 °C in 20 psi pressure for 20 min.

2.4.3 Channel inoculation by laminar flow-templating

Following the method of flow templated biofilm growth developed elsewhere, we selectively grew biofilms in either the corners or the middle of the microchannel (Figure 2.2).[162] This was achieved by exposing the target areas in the microchannel to a so-called “template” flow, with flow rate Q_T. Templating solutions included the inoculant solution (1 hour) followed by the AB growth medium (70 h). Template flows were isolated to the target regions of the microchannel with the use of a co-flowing “confinement” flow, with flow rate Q_C. Due to the low Reynold’s numbers ($Re=7\times10^{-4}$) generated by typical flow rates ($Q_T+Q_C=1.2\ mL \cdot h^{-1}$) and the small channel dimensions, mass transfer between the two streams was strictly diffusion-limited. In these conditions, even co-flowing miscible streams could maintain an interface between them during the 60 s transit time through the microchannel. The choice of the templated growth region was facilitated by injecting the nutrient solution (Q_T=0.4 mL·h^{-1}) through either inlet I_1 (corner growth) or I_2 (middle growth) and the confinement solution (Q_C=0.8 mL·h^{-1}) through the remaining inlet (Figure 2.1).

2.4.4 Optical microscopy

Optical measurements were acquired using an inverted light microscope (IX73, Olympus, Canada with condenser NA = 0.9) with fluorescence and white light transmission illumination and 2× magnifications (numerical aperture 0.06). Images were captured using a monochrome CCD camera (Lumenera Infinity 3–1, Ottawa, Canada). Fluorescence images of GFP expressing bacteria were obtained from the same instrument with the use of an appropriate filter cube. Quantitative measurements of the total amount of biofilm were obtained by optical density (OD) from standard optical microscopy in a defined region of interest within the microchannel. This was based on average pixel intensities at time t ($I_{pixel,t}$) and the average background pixel intensity at t=0 ($I_{pixel,0}$) using the equation for optical density, OD = – log ($I_{pixel,t}/I_{pixel,0}$).[163] Structural heterogeneity was quantified by coefficient of variance COV = OD_{STD} / OD×100%, where OD_{STD} was the standard deviation in the OD within the biofilm-containing portions in the same field of view. To obtain imaging at the attachment surface without interference from out of plan biofilm segments, confocal laser scanning microscopy (CLSM) was conducted (FV1200, Olympus, Canada) with either 10× or 40× objectives. Excitation of the GFP was at 488 nm and emitted light was detected between 500 and 600 nm with 12-bit intensity resolution. In all cases images were analyzed using the Fiji bundle for ImageJ.

2.4.5 Electrochemical impedance spectroscopy (EIS)

Electrochemical impedance spectroscopy (EIS) was used to report on the complex electrical response of an electrode-adhered biofilm to imposed oscillations in the applied voltage. Experiments were recorded using a potentiostat (Solartron 1287

Electrochemical Interface, Solartron Electronic Group, UK) in combination with a frequency analyzer (Solartron 1260 Frequency Response Analyzer, Solartron Electronic Group, UK) with instrument control software (Zplot, Scribner Associates, Inc, USA). Data treatment and modeling was conducted via software (Zview, Scribner Associates, Inc, USA). For all experiments, the frequency range used was 0.1 Hz–10 kHz. The AC amplitude was 25 mV around a bias potential of 0 V versus Au. The difference in potential between Au pseudo-REs and an Ag/AgCl, KCl (3M) reference electrode was tested 5 separate times by cyclic voltammetry of ferricyanide-containing nutrient solution over a month. The difference in potential remained constant within detectability of the instrument (+/- 0.5 mV) at 360 mV. Separate experiments verified that this difference in potential remained constant as long as the chemical environment did not change, particularly the pH. As the growing biofilm on the WE was downstream of the RE, biofilm related changes to chemical environment near the RE were expected to be minimal (upstream diffusion was calculated to be many orders of magnitude lower than downstream convection). See supporting information for a discussion about the possible effects of RE exposure to biofilm growth in some experiments. All experiments were conducted with the same WE and CE graphite electrodes, which were cleaned with 1M HCl between experiments before re-use. A new RE was fabricated for each experiment.

2.4.6 Attenuated total reflection infrared spectroscopy (ATR-IR)

Infrared spectra were recorded using a Nicolet Magna 850 Fourier transform infrared spectrometer (Thermo Scientific, Madison, WI) with a liquid nitrogen cooled narrow-band MCT detector. In order to acquire spectra in attenuated total reflection (ATR) mode, a diamond ATR accessory was used (Golden Gate, Specac Ltd, London, UK). The probing surface of the diamond internal reflection element was 2×2 mm and is fixed in a tungsten carbide holder on the ATR accessory. The resulting spectra were treated using the GRAMS/AI 8.0 software (Thermo Galactic, Salem, NH). Intensity of each band of interest was measured by determining the maximum between a local linear baseline. See section 2.8.5 for more details.

2.5 Results and discussion

2.5.1 Flow templated biofilm growth

Laminar flow in microchannels enabled the application of steady, well-developed shear forces against wall-adhered biofilms. However, in rectangular cross-section microchannels, wall shear force can change drastically at the intersection between two walls (the microchannel corner), whereas it is nearly constant in the middle portion.[162] Our first goal was to identify how or if these differences in hydrodynamic conditions would affect EIS measurements during biofilm growth. This was conducted by templating biofilm growth against the WE surface in either the microchannel middle or the corners (Figure 2.2), as explained in the experimental section. The flow rate ratio between confinement and template flows was always $Q_C/Q_T = 2$, even for experiments where the total flow rate, $Q_{Tot} = Q_C+Q_T$ was changed. For typical flow rate $Q_{Tot} = 1.2\ \text{mL}\cdot\text{s}^{-1}$, we estimated the shear stress in the middle portion of the channel to be $\tau = 10.7$ mPa. This was based on the calculated shear stress in a rectangular channel, $\tau = 6\cdot\mu\cdot Q / (w\cdot h^2)$, where μ is the liquid-phase viscosity (1×10^{-3} Pa·s), Q is the total flow rate, and w and h are the channel width (2 mm) and height (300 µm), respectively.

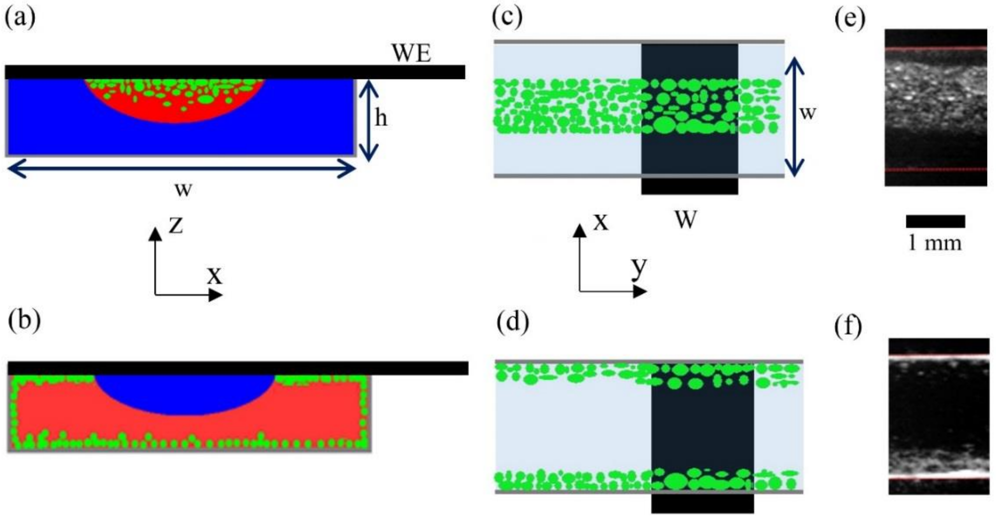

Figure 2.2 Schematic of biofilm growth (green) in the microchannel with width (w) and height (h) under middle (a and c) and corner (d and f) templating approaches. **(a)** Growth templating flow (red) confined to middle of WE (black) by a confinement flow (blue). The opposite configuration resulted in templating flow confinement to the WE within the microchannel corners **(b)**. Bird's eye view of the middle **(c)** and corner **(d)** confined biofilms against the embedded WE. Fluorescence microscopy images of a 27-h-old biofilm in the middle **(e)** and corner **(f)** of the microchannel with red lines superimposed to show the position of the side walls. Brightness was increased by 25% for visualization purposes. Parts (a) and (b) are in the y,z plane, whereas the other are in the x,y plane. By convention the y axis is in the direction of flow.

Optical microscopy was conducted in parallel with EIS to obtain complementary information on biofilm bulk properties. Growth in the corners and middle of the channel was first registered after 15 h and 24 h and continued until 30 and 50 h, respectively (Figure 2.3 a). Structural heterogeneity continuously diminished in time for biofilms in corners and middle portions of the microchannel until maturity was reached (Figure 2.3 b). After stabilization, structural heterogeneity was about 10 times greater for middle-templated biofilms. We associate this with the fact that biofilms grew thicker in the corners, which resulted in the merging of biofilm segments. In contrast, they remained isolated in the thinner films in the middle of the channels. As microscopy reported on the entire vertical cross-section of the biofilm, details of the biofilm at the surface were not revealed.

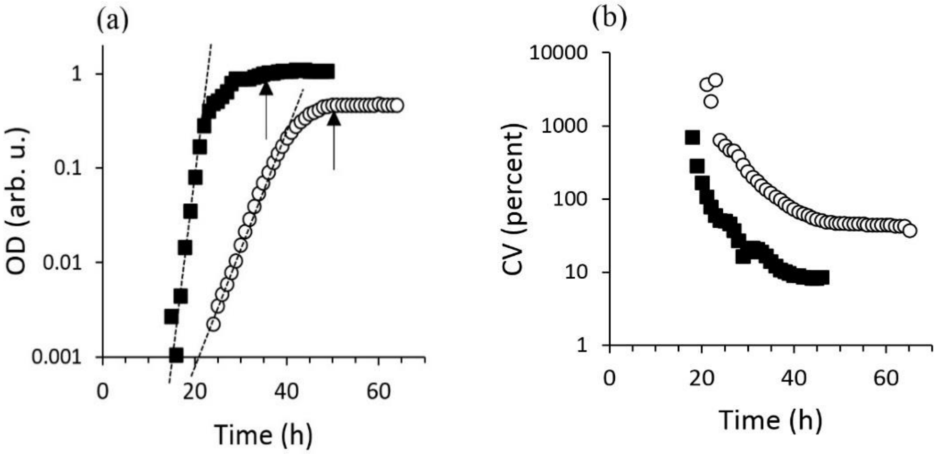

Figure 2.3 (a) Pseudomonas sp. growth kinetics visualized by a semi-log plot of OD versus time in channel corners (■) and middle (O). Trend lines show exponential growth period. Arrows point to the growth curve when OD was nearly constant. **(b)** Structural heterogeneity by coefficient of variance (COV) versus time for corners (■) and middle (O). All biofilms were Pseudomonas sp. grown with template solution consisting of AB medium containing 10 mM sodium citrate in device with same dimensions.

2.5.2 Electrochemical impedance spectroscopy on templated biofilms and verification

In order to study the biofilm directly adjacent to the attachment surface, EIS measurements were made in parallel with the optical measurements described above. The interaction between electric fields and charged molecular groups in the biofilm are known to affect the biofilm morphology.[164] Therefore, a single DC offset voltage of 360 mV versus Ag/AgCl was used (see section 2.8.1 for more details). At this offset voltage, we expected a slight net repulsion of Gram-negative bacteria from the electrode surface.[164,165] Measurements started 10 h after inoculation and were repeated at time intervals not exceeding 1 h^{-1}. Figure 2.4 shows selected Nyquist plots collected for corner and middle templated biofilms during two separate experiments. In total, Nyquist plots were acquired during four separate experiments conducted at different times for each biofilm templating growth configuration (corner or middle). While biofilms were observed to grow on the CE during the experiment, similar to other EIS studies,[157,159] there should be no effect on the measurements due to its role of supporting the small currents generated at the WE. See Section 2.8 for a discussion about the possible effects of RE exposure to biofilm growth in corner templated experiments.

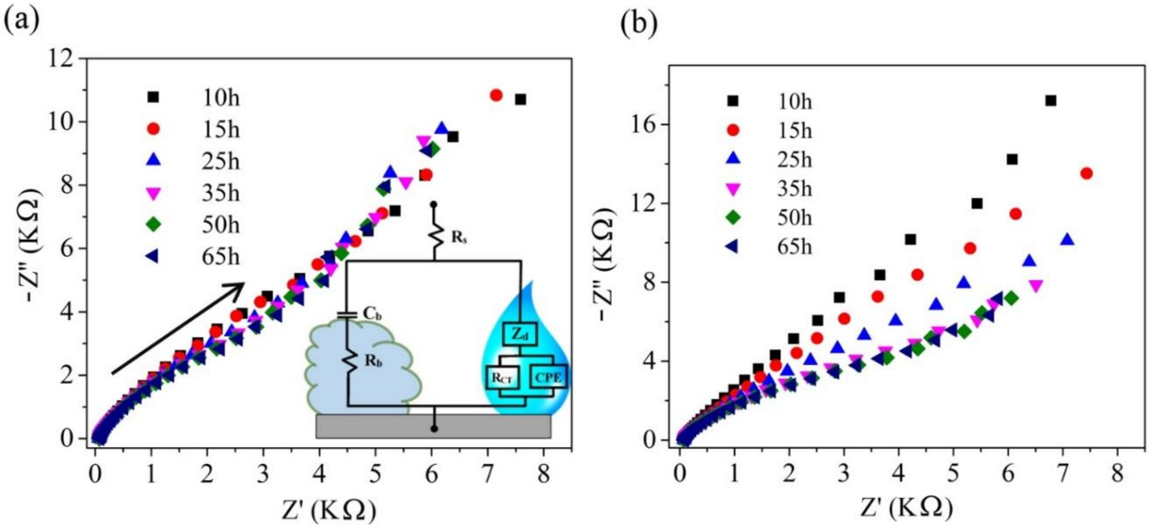

Figure 2.4 Representative measurements of time series Nyquist curves of biofilm growth in the middle **(a)** and the corner **(b)** of channel for different times after inoculation. Real and imaginary components of impedance are Z' and Z", respectively. Arrow in (a) points toward lower frequencies. Inset figure in (a) is the equivalence circuit schematic for a non-electroactive electrode-adhered biofilm used in this study. The biofilm portion (left branch) includes biocapacitance and bioresistance (C_b, R_b, respectively). Liquid-phase interactions at the electrode surface (right branch) include constant phase element (CPE), anomalous diffusion (Z_d) and charge transfer resistance (R_{CT}). Bulk solution resistance is represented by R_s.

To extract physical meaning from Nyquist curves, we used an equivalence circuit (Figure 2.4). This circuit was chosen due to its successful application to non-electroactive *Escherichia coli* biofilms in a Luria–Bertani (LB) growth medium in a previous report.[157] Elements included a solution-phase resistor (R_s) in series with a parallel circuit. The first branch of the parallel circuit included a resistor, R_b, in series with a capacitor, C_b, representing bioresistance and bio capacitance of the attached biofilm, respectively. These were the elements used to track biofilm development. On the second branch, elements for solution-phase contributions near the electrode were used. These included a parallel circuit consisting of a charge transfer resistance element (R_{CT}) and a constant phase element (CPE), in series with an anomalous diffusion element, Z_d. See section 2.8.2 for more information.

We fit the Nyquist plots using the selected equivalence circuit to obtain time-varying values for all fitted electrical components. Figure 2.5 shows trends for C_b and R_b, which relate to the biofilm. We noted the continuously decreasing R_b for both corner- and middle-templated biofilms for the entire experiment. This somewhat counter intuitive result has been observed previously in the first 24 hours after inoculation of an *E. coli* biofilm[157] and was attributed to a growing number of isolated colonies at the electrode surface. In electrical terms, this was considered as a circuit of parallel resistance elements (Figure 2.8), which should reduce R_b according to $1/R_b=1/R_1+1/R_2+...1/R_n$, as n increases. The observed increases to R_b after 24 h in the cited study were likely the result of a reduction in n due to merging of enlarged colonies. In the current study, a similar parallel resistor circuit is expected based on widely reported mushroom-shaped biofilms formed by *Pseudomonas sp.* in citrate-containing AB media.[121,166,167,168] To account for continuous decreases to R_b observed in this study, we note that n must continuously increase. This can be explained by three mechanisms. First, under similar experimental conditions in microchannels, it has been shown that *Pseudomonas sp.* biofilms continuously emit planktonic bacteria, which can seed uncolonized areas.[121] Second, coulombic repulsion between the WE and the biofilm at the applied potential used here should reinforce localized attachment structures by limiting biofilm/surface contact elsewhere. Third, displacement of the nutrient solution out of the original templated growth region due to accumulation of biofilm, causing templating area to become enlarged in time, further increased n (Figure 2.9).

The second tracked bioelectrical element was C_b. This is generally considered to be related to the amount of biofilm at the electrode surface. Biofilm accumulation, inferred from increases of C_b, was observed immediately after measurements started at 10 h for both corner- and middle-templated growth (Figure 2.5 b). This shows that EIS was more sensitive to early stages of biofilm accumulation compared to optical microscopy experiments conducted with the zoom and numerical aperture used here. The measured C_b continued to increase until 25 h and 20 h for corner- and middle-templated growth, respectively. Following this, the amount of biofilm decreased noticeably for corner templated biofilms, despite growing thicker in these regions. In order to verify that changes to C_b correlated to biofilm surface coverage, we conducted ATR-IR under similar conditions to the EIS experiments (see section 2.8.5 for more details). Results for the absorbance of the biofilm Amide II band demonstrated growth and a reduction in intensity over nearly the same time intervals as C_b (Figure 2.5 c). Former ATR-IR experiments on *Pseudomonas aeruginosa PAO1* bacteria also demonstrated similar behavior.[169,170] The reduction in intensity after initial growth was previously attributed to a restructuring event at the attachment surface, which was caused by the migration of bacteria away from surface, likely to maintain closer proximity to nutrient solution.[170] This is supported by CLSM measurements, which confirmed the preference for some bacteria to concentrate near the biofilm/liquid interface, independent of turbulent or laminar flow regimes.[171] For further validation, we conducted our own CLSM experiments to show that, after an initial growth phase marked by spreading of bacteria randomly across the surface, a reorganization process occurred which resulted in an interconnected network of localized biofilm colonies (Figure 2.5 d). See Supporting Information for more information about the time-varying trends to quantified measurements of structural heterogeneity from continuous CLSM imaging. In contrast to surface sensitive EIS, ATR-IR and CLSM measurements, regular microscopy revealed growth in overall biofilm OD until 30 h for corner growth and 50 h for middle growth (Figure 2.3). Therefore, the local biofilm accumulation at the electrode surface, and even subsequent restructuring, were both complete while the bulk accumulation of biofilm was still underway.

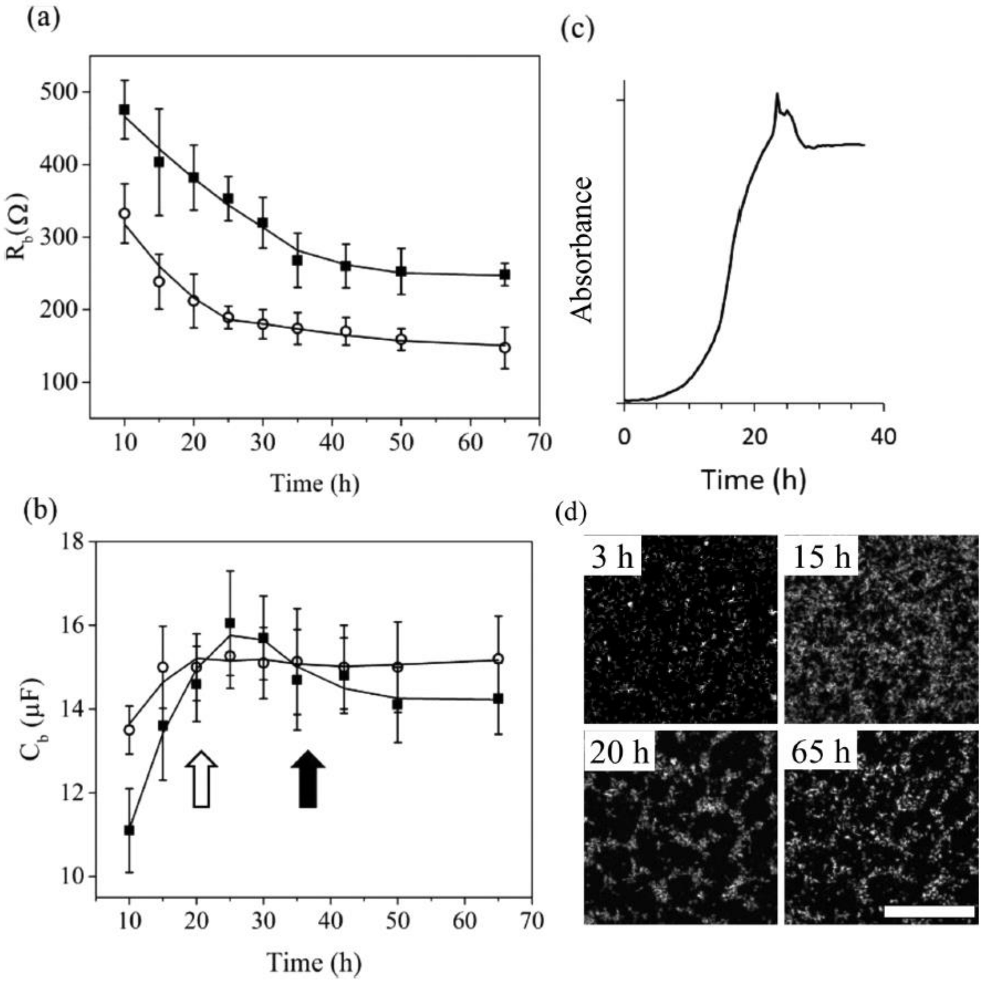

Figure 2.5 Trends of R_b **(a)** and C_b **(b)** during templated biofilm growth at the working electrode corner (■) and middle (○). Error bars were produced from the standard deviation of four measurements for each time point. $Q_C/Q_T = 0.5$ and $Q_C+Q_T = 1.2\ \mathrm{mL \cdot h^{-1}}$ for all measurements. Arrows mark the times from Figure 3 when exponential growth ends for corner (solid) and middle (hollow). **(c)** Normalized absorption signal from Amide II band in time for Pseudomonas sp. Visual confirmation of biofilm restructuring at the attachment surface in the channel middle by CLSM **(d)** after 3 h, 15 h, 20 h, and 65h using 40× objective. Scale bar (100 μm) in image at 65 h is representative of all images.

2.5.3 Biofilm resistance and capacitance under changing flow conditions

In order to understand the effect of changing flow conditions on surface-adhered biofilm segments, we compared R_b and C_b to optical microscopy results. Middle-templated growth was used in all experiments due to the higher and more uniform shear stress in that part of the channel, as well because no interfering effects could possibly occur from biofilm growth on the RE which was protected by a continuous flow of confinement solution at all times.[162] After 65 h of growth, the biofilm was subjected to different total flow rates in the range 0.6 $mL·h^{-1} < Q_{Tot} < 6$ $mL·h^{-1}$, corresponding to shear stresses in the range 5.35 mPa < τ < 53.5 mPa. Changes to Q_{Tot} preserved the flow rate ratio ($Q_C/Q_T = 2$), ensuring that the templating dimensions remained constant.[162] Immediately following each EIS measurement, the Q_{Tot} was increased and the system was left to stabilize for 10 minutes until the next measurement. Average values for R_b and C_b were obtained during three different experiments, conducted on separate samples prepared from separate inoculate. Both R_b and C_b increased with Q_{Tot} (Figure 2.6). At the highest flow rate (Q_{Tot} = 6 $mL·h^{-1}$), R_b and C_b had increased by about 10% over measured values at Q=0.6 $mL·h^{-1}$. Upon returning to the initial Q_{Tot}, no statistically significant hysteresis was measured in the R_b or C_b values. We confirmed that the fitted values of liquid-phase equivalence electrical elements remained constant during the shear stress cycling. This indicates that the fluctuation to R_b and C_b were related to changes in the properties of the biofilm directly, not liquid-phase interactions with the electrode surface. To better understand the connection between the biofilm microstructure at the attachment surface and the results obtained by EIS during flow rate cycling, a separate CLSM was conducted on biofilms prepared in exactly the same way as above. After 65 h following inoculation, we observed similar structured colonies as described above (Figure 2.5d). Next flow rates were cycled in the same range as above (0.6 $mL·h^{-1} < Q_{Tot} < 6$ $mL·h^{-1}$) for the same time intervals, and CLSM images were acquired before changing to the next flow rate. The results (sections 2.8.6 and 2.8.7) show that the colonies of GFP bacteria maintained their structure even at high flow rates, but under these conditions shifted by about 20 µm downstream under the applied shear force. After returning to lowest flow rate, the bacteria returned to nearly their original position. A slight difference in the initial and final positions (2-4 µm +/- 2 µm) may have been because of the application of elevated sheer forces for times exceeding the biofilm elastic relaxation time.[145] The fact that this displacement was largely reversible indicates that, despite the observed movement of the GFP bacteria, the anchoring point stays fixed upstream. Therefore we conclude that anchor is made from (non-fluorescent) extracellular polymer material (EPM), which is in line with the generally accepted model of biofilm attachment.[172]

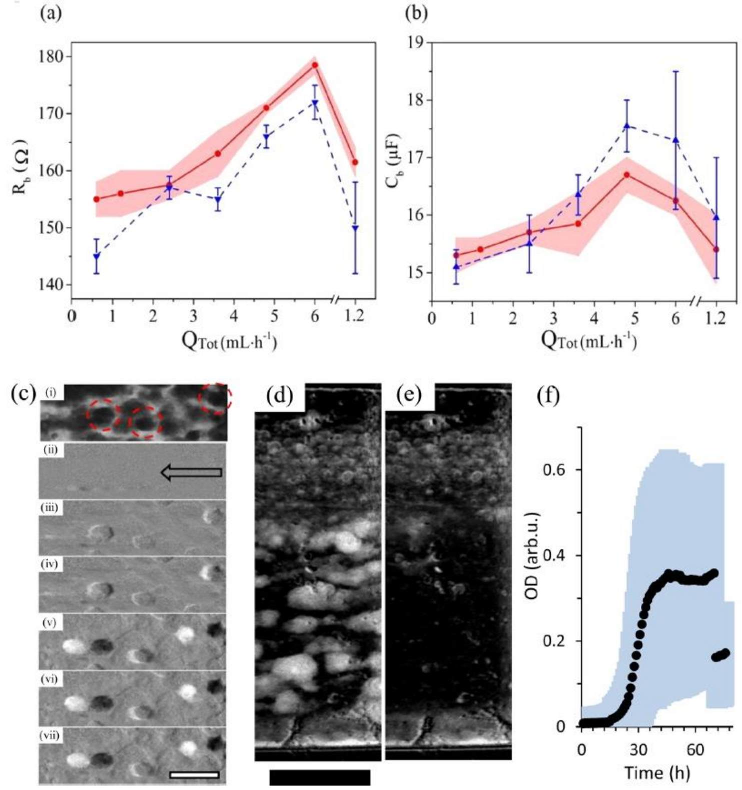

Figure 2.6 Flow rate dependency of fitted bioresistance **(a)** and biocapacitance **(b)** for 65 h old Pseudomonas sp. biofilm that had been cultured under Q_{Tot}= 1.2 mL·h^{-1} with flow rate ratio Q_C/Q_T =2. Red data points show the average values from three separate experiments, with error bands representing the standard deviation in their measurements. Blue triangles show the trend of resistance and capacitance changes with the same flow rates after shear-removal of significant portions of biofilm. **(c)** Optical micrographs showing typical long-range effects on biofilm due to changing shear forces. (i) Raw image in region of interest obtained at total flow rate Q_{tot}=1.2 mL·h^{-1}. Dashed red circles highlight the optically dense biofilm formations, which produced streamer formation under elevated flow in subsequent images. Background corrected images using (i) for the same region of interest at total flow (ii) Q_{tot}=0.6 mL·h^{-1}, (iii) Q_{tot}=2.4 mL·h^{-1}, (iv) Q_{tot}=3.6 mL·h^{-1}, (v) Q_{tot}=4.8 mL·h^{-1}, (vi) Q_{tot}=6 mL·h^{-1}, (vii) Q_{tot}=1.2 mL·h^{-1}. In all images, flow is from right to left as indicated by the arrow in (ii). A representative scale bar in (vii) is 250 μm. For all data in (a-c) measurements were obtained 10 min after Q_{Tot} was changed. Optical density mode images of biofilm growth at the electrode-containing microchannel surface before **(d)** and after **(e)** application of high shear stresses. Pixel intensities were calculated from OD = -log (I_t/I_0), where I_t was the time varying intensity from a specific pixel and I_0 is the intensity of the same pixel in the background image. Scale bar is 500 μm. Flow was from right to left. **(f)** OD vs. time plot of the biofilm growing in the electrode-containing channel during EIS measurements. Error band was obtained from the standard deviation of the pixel intensity from the 2000×610 μm microscope field of view shown in (d) and (e) at each time.

We believe that this resulted in temporary structural deformations such as biofilm stretching, thinning and/or modulation of distance between adjacent biofilm colonies, which could cause the observed reversible changes to R_b. Moreover, considering the largely static anchoring point, the shifting of the biofilm encased bacteria along the attachment surface, indicates sliding movement of the biofilm against the surface. This should temporarily increase the amount of biofilm in contact with the surface. This supports our observation that C_b increases under elevated flow rates, but returns to original values after flow rate is reduced. We compared EIS results to micrographs acquired from standard optical microscopy under the same conditions (Figure 2.6 c). After flow rate had increased to $Q_3 = 2.4$ $mL\cdot h^{-1}$, small differences were evident in the images relative to the background. These differences were the result of shifting biofilm density downstream, causing increases to OD on the downstream and decreases to OD on the upstream side of some features. At first, this effect was slight and reversible, probably being elastic in nature. However, at $Q_4=4.8$ $mL\cdot h^{-1}$, large and irreversible deformation of biofilm structure was observed in the form of streamers and changes to the surface texture. Streamer formation was attributed to a sudden partial detachment mechanism,[173] whereby portions of locally tall biofilm colonies became partially detached and dangled down-stream. Changes to biofilm texture were also observed and were likely related to the induced viscous flow in the biofilm due to the application of elevated shear forces for times exceeding the biofilm’s elastic relaxation time.[145] Therefore, while biofilms at the attachment surface demonstrated reversible changes under elevated bulk flow conditions, biofilm material further from the attachment surface were more susceptible to irreversible changes.

These results indicate that biofilm layers at the attachment surface are more resilient to shear flow, either because outer biofilm layers provided protection or because the inner layers were naturally more resilient, or both. To directly investigate the effect of prolonged application of shear force directly to surface-attached biofilm layers, we removed large portions of intervening layers and repeated the experiment. Biofilm removal was accomplished by applying a strong pulsing shear force by rapidly modulating the volumetric flow rate of syringe pump between Q=0 and 30 mL·h^{-1} for 10 s. The result was the removal of 50% biomass, mostly from the centre of the channel where the shear stress was the highest (Figure 2.6 e). Following biofilm removal, we observed that C_b values at all Q_{Tot} were statistically similar to measurements before removal (Figure 2.6 b). This indicated that the removal of outer biofilm layers did not affect the quantity of biofilm directly at the electrode surface. Also, the final C_b value after shear cycling against the exposed surface-adhered layers was not statistically different than after the cycling before their exposure. This indicated that the quantity of the surface-attached biofilm was also not affected by direct exposure to range and duration of elevated shear stresses for used here. This is not surprising because carbon electrodes are rough at the microscale, which enables strong attachment of biofilms.[174,175] In contrast, the average values for R_b were all reduced by about 5% compared to those measured before shear removal of outer biofilm segments. Considering that C_b measurements imply that the quantity of biofilm (and therefore the number of colonies) was not changed, the differences in R_b were likely due to changes in biofilm structure following shear removal. We also note that after cycling the shear stress directly against the exposed biofilm seed layers, R_b was reduced by 10% (Figure 2.6 a). This indicates that the structure of the exposed biofilm at the attachment surface was further modified by high flow rates. The nature of these changes should be investigated further, but likely involve the merging of formerly isolated attachment points under applied shear forces, thereby reducing the number of separate colonies.

2.6 Conclusion

A three-electrode microfluidic flow cell was designed for *in situ* EIS measurements of *Pseudomonas sp.* Measurements of biofilms confined to the channel corners or middle were accomplished by flow templated growth. With the use of an accepted electrical equivalence circuit for non-electroactive biofilms, bioresistance and biocapacitance were measured in time. Using EIS, biomass accumulation and a restructuring process at the surface were finished within the first 25 hours, whereas optical microscopy only showed continuous growth in the biofilm bulk until much later. Finally, we applied different shear stresses against middle-templated biofilms by cycling the total flow rates. The EIS results showed a strong, reversible correlation to the measured bioresistance and biocapacitance. Supporting measurements by CLSM suggest temporary stretching and spreading of the biofilm were responsible for the EIS observations. Regular optical measurements showed that cycling shear stress caused irreversible changes to bulk biofilm structure. Shear removal of the biofilm outer layers did not affect the amount of biofilm measured by EIS, but changes in bioresistance suggest that its structure at the attachment surface was changed and could be further modified by application of elevated shear stress directly against the exposed surface adhered layers.

2.7 Acknowledgments

The authors thank Professor Zhifeng Ding for helpful discussions about EIS concepts used in this work. This research was funded by grants to J.G. from Fonds de Recherche du Québec - Nature et Technologies (“nouveau chercheur” grant), Natural Sciences and Engineering Research Council of Canada (NSERC) Discovery grant and Canadian Foundation for Innovation (CFI) Leaders opportunity fund. S.J.C. is a research scholar from the Fonds de Recherche du Québec en Santé.

2.8 Supporting information

2.8.1 Calibration of the Au pseudo-reference electrode

In order to enhance compatibility with the microfabrication protocol used in this work, we used a planar gold electrode as a pseudo reference electrode. We calibrated its offset against a standard Ag/AgCl, KCl (3M) reference electrode by collecting CV curves for well-known potassium ferricyanide. In both cases the working and counter electrodes were both the same graphite material used in this study. As can be seen from Figure 2.7 the CV curves are nearly identical with the shift in position due to the reference electrode. By tracking the change in the midpoint (between reduction and oxidation peaks) from both curves it was determined that the pseudo gold reference resulted in a shift of 360 mV versus Ag/AgCl, KCl (3M). Furthermore, long-duration studies lasting over a month determined that there was no measureable shift in the position of CV curves, within the measurement accuracy of the instrument (+/- 0.5 mV). Therefore, the DC offset potential of 0 V versus the Au pseudo reference used in the EIS studies were, equivalent to 360 mV versus Ag/AgCl, KCl (3M). We note the sensibility of pseudo reference electrodes to environmental conditions. As explained in section 2.4.1, the set up used in the majority of the experiments in this work (mid-channel templating) protected the RE from biofilm growth due to its placement upstream of the WE/CE and its isolation from bacterial growth by fresh confinement solution (which did not support bacterial growth). In one experiment (corner-channel templating) inlets for nutrient and confinement solutions were switched, thereby exposing the RE to biofilm growth.

Literature reports using pseudo REs exposed to bacteria and biofilms did not note problems during EIS or other three-electrode experiments.[158,159] However, we cannot rule out the fact that some changes to the potential could occur, which would affect the polarization at the WE in time. If these changes were significant, then some effect on the structure could occur due to electrostatic interactions with the biofilm, as outlined before.[164] As outlined in the main paper, verification experiments by ATR-IR and CLSM show that the observed changes to EIS signals are most likely due to biological restructuring effects. Nevertheless, future studies of corner templated biofilms or other configurations where the RE is exposed to biofilm growth, would benefit from a stable RE.

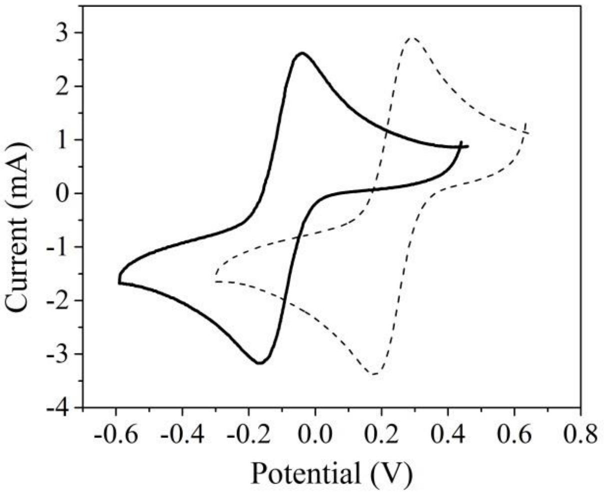

Figure 2.7 Cyclic voltammetry of potassium ferricyanide (10 mM) in biofilm growth medium using gold pseudo-reference (black line) and Ag/AgCl, KCl (3 M) reference electrode (dashed line).

2.8.2 Elements to the equivalent electrical circuits for biofilms on electrode surfaces

To extract physical meaning from Nyquist curves, we used a previously published equivalence circuit that was applied non-electroactive *Escherichia coli* biofilms grown in an ampicillin containing LB growth medium against indium-tin-oxide electrodes[157] (Figure 2.4). As discussed in the main paper and shown in Figure 2.5 d, this assumption is supported by CLSM data acquired at the attachment surface. Elements to the equivalent electrical circuit include:

R_S: Solution resistance,

R_b and **C_b**: Biomaterial resistance and capacitance, respectively.

CPE: Constant phase element of the solution-electrode interface, with impedance element given as, $Z_{\mathrm{CPE}} = \frac{1}{T(j\omega)^{\phi}}$, where T is a constant, j is the imaginary number ($j = \sqrt{-1}$), ω is the angular frequency (ω =2π*f*, *f* being the frequency) and φ expresses the deviation from ideal capacitor (φ=1) in an electrochemical system.

The double layer capacitor on the surface of the electrode often behaves like an imperfect capacitor. While there are several explanations for non-ideal behavior of the double layer such as non-uniform current distribution and surface roughness, we use CPE as an empirical constant without any specific physical basis, as is common for modeling this electrochemical phenomena.[176]

Z_d: Anomalous linear diffusion type Ib with reflecting boundary: This effect occurs when molecular diffusion is interrupted by static periods, usually due to a non-homogeneous environment, which creates a sub diffusion effect. An anomalous linear diffusion of type Ib with reflecting boundary impedance element can arise from physical and chemical interactions between particles and ions in the electrolyte and the biomaterial. This theory comes from continuous time random walk model in the macroscopic limit.[177]

2.8.3 A modified electrical equivalence circuit for biofilms consisting of separated colonies

As noted in section 2.5.2, a highly parallelized electrical equivalence model is beneficial to understand the behavior of the EIS results. Figure 2.8 shows a modified equivalence circuit compared to Figure 2.4 in the section of 2.5.2. Addition of more elements increases total capacitance, $C_{b,Tot} = C_{b,1} + C_{b,2} + \ldots + C_{b,n}$ which is the basis of the relationship between C_b and biomass. Total R_b, however adds as the inverse of each parallel element, $1/R_{b,Tot} = 1/R_{b,1} + 1/R_{b,2} + \ldots + 1/R_{b,n}$ which is the source of its measured reduction in time.

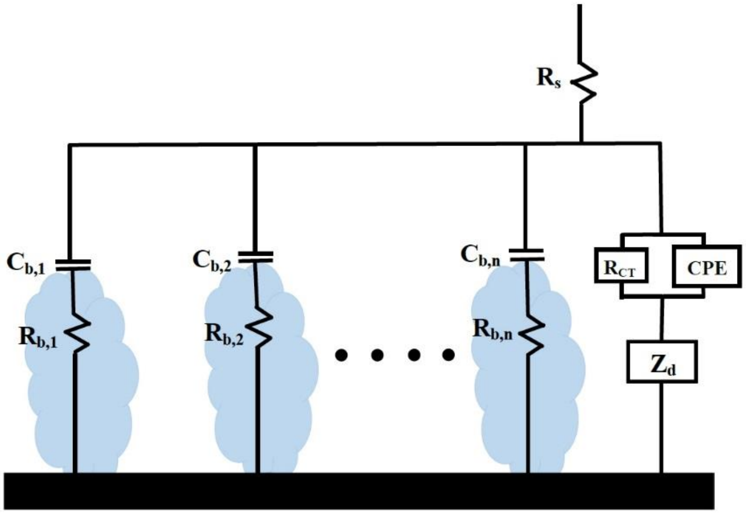

Figure 2.8 Parallelized electrical model to explain the respective reduction and augmentation of resistance and capacitance during biofilm growth. All electrical elements have the same meaning as described in section 2.8.2.

2.8.4 Expansion of templated growth region in time

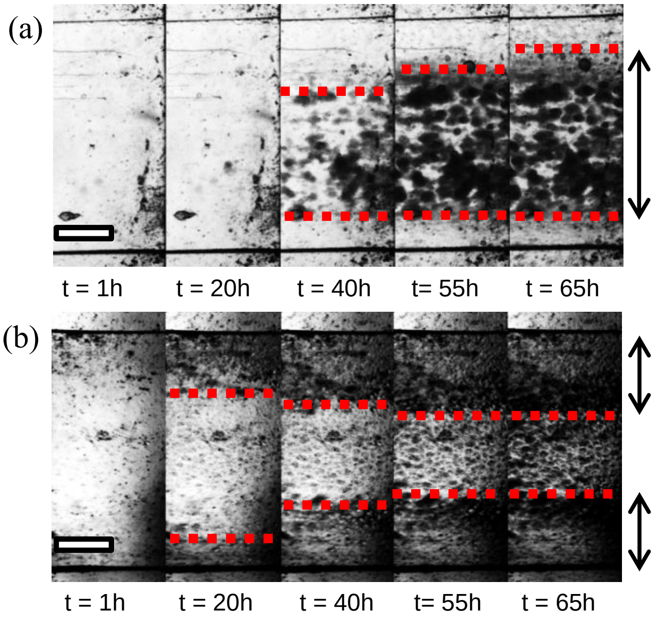

Figure 2.9 Biofilm-covered area versus time in **(a)** corner- and **(b)** middle-templated growth at different times. Red dotted lines show the approximate interface between template and confinement flow. Double-sided arrows show the region of templating. Scale bar in (a) and (b) are 450 µm.

As noted in the section of 2.5.2, we hypothesize that one of the contributing factors to the decrease of R_b in time was the physical expansion of the biofilm out of the original templated regions. This is believed to be the result of a relatively low, unoptimised Q_C/Q_T flow rate ratio ($Q_C/Q_T = 2$ in this study) compared to previous work ($Q_C/Q_T > 3$).[162] For corner templated growth images, we note that the appearance of biofilm in the channel center portion was likely due to growth on the glass slide, not the electrode-side of the channel. See Figure 2.2 b for more information.

2.8.5 ATR-IR experiments

A microfluidic device with the same dimensions as the one used for EIS was constructed to enclose an ATR-FTIR crystal (Figure 2.10). Here, an open microchannel (without electrode integration steps) was placed directly on the diamond ATR accessory. Since the crystal had the same width as the microchannel, it was possible to ensure that the crystal was centered in the microchannel without touching the PDMS wall. In order to avoid leakages, light pressure was applied on the PDMS device using a see-through anvil (View-Thru, Specac Ltd., London, UK). The anvil was pressed against a hard transparent intervening plastic plate to evenly distribute the pressure across the PDMS device. Positioning of the anvil relative to the ATR crystal was optimised for direct viewing the local biofilm by eye.

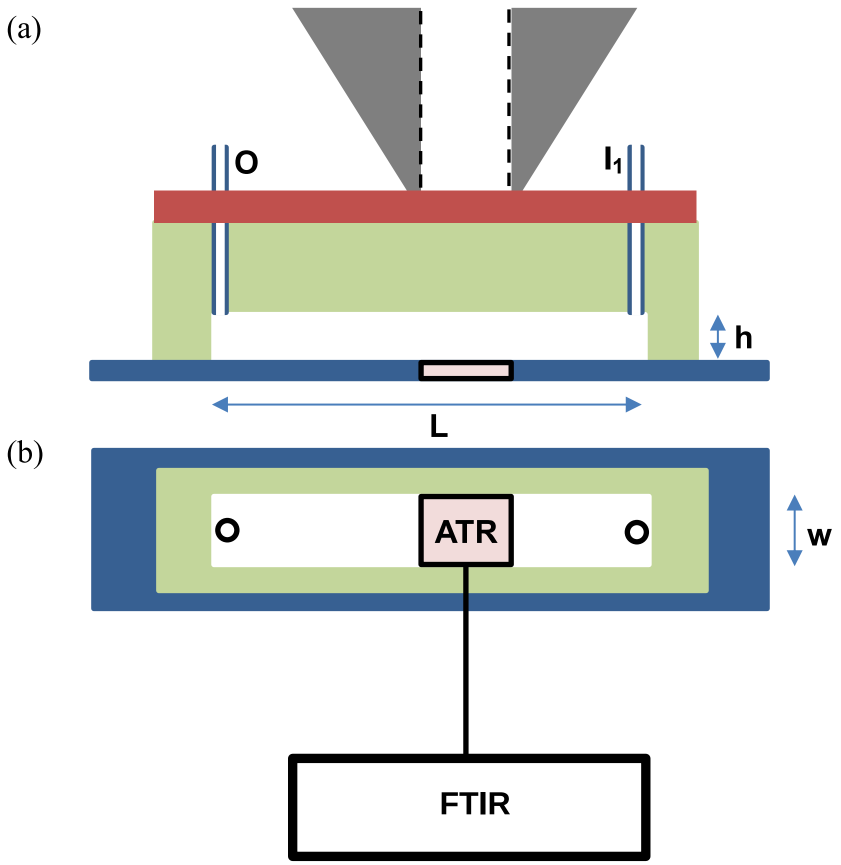

Figure 2.10 (a) and **(b)** show, respectively, the corresponding cross-section and bird’s eye views of the channel (same channel dimensions as above) containing an embedded diamond ATR-FTIR sensing element (2mm × 2mm). (a) The anvil with see-through optics (grey) is pressed against a hard transparent plastic plate (orange). Length, height and width were L=33 mm, h=300 µm and w=2 mm, respectively.

As explained in the main paper, ATR-IR experiments were conducted in nearly identical microchannels on *Pseudomonas sp.* biofilms exposed to the same hydrodynamic and nutrient conditions, except that biofilms were not templated to certain portions of the microchannel. This was done to verify that the reduction in C_b correlated to a reduction in biomass as measured by another surface sensitive technique. After a lag phase that lasted close to 5 hours, biofilm spectral absorbance bands grew for the next 15-20 hours, followed by a decrease before stabilization.

Representative data in Figure 2.6 a, showed these trends for the amide II band, which originates from N−H bending and C−N stretch, providing a good measure of protein content, a major molecular component of biofilms. The decrease in absorbance at 25 h matched the decrease in C_b intensity observed using EIS. The measurements also resembled other ATR-IR measurements that were previously conducted in non-microfluidic experiments on *Pseudomonas aeruginosa* PAO1 bacteria.[170] While ATR-FTIR reproduces similar effects to EIS regarding biomass growth and restructuring at the attachment surface, and even extends selectivity to the molecular constituents, structural information, such as that which is inferred from R_b measurements, is not available.

2.8.6 Quantifying the restructuring process at the attachment surface by CLSM measurements

Neither EIS nor ATR-FTIR provide spatially resolved information, whereas regular optical microscopy cannot strictly resolve biofilm structure at the attachment surface due to interference from other layers. Therefore, CLSM was used to visually verify biofilm restructuring at the attachment surface due to its ability to eliminate out of plane contributions to the image. We conducted a comprehensive experiment which obtained images at the attachment surface at regular 30 min intervals over the first 65 hours after inoculation. In section 2.5.2, we presented images corresponding to four different times to show bacteria distribution shortly after inoculation, followed by three images just before, shortly after and long after a discernible reorganization. This reorganization was characterized by the formation of interconnected structures (colonies) on the order of 10’s of µm. See the main paper for more details. While a comprehensive analysis of the complete time-series data set outside of the scope of this work, we do present trends in coefficient of variance (COV) as a measure of structural heterogeneity (Figure 2.11). Following inoculation, there is an initial rise in COV. After nearly 10 h some organization begins to occur, which is represented by a decrease in COV. After 15 h, CV reaches a local minimum before rising slightly for the next 5 h, followed by continuous decreases to CV for the duration of the experiment. The second COV peak at 20 h correlates to the onset of structures on the order of 10’s of µm, shown in the main paper after 20 h. Here we can see that the amount of bacteria at the surface decreases, presumably as a result of bacteria moving perpendicular to the surface as the biofilm thickens. We believe that this is the process that leads to decreases in the amount of biofilm as characterized by EIS and ATR-IR. It well-known that the interpretation of quantitative measurements of biofilm structure, such as COV, are complex and difficult to relate to physical properties.[178] As well, COV does not necessarily prioritize structural heterogeneity at the size scales identified here, nor does it visualize the extracellular material, which affect ATR and EIS measurements. Further work correlating biofilm structure at the attachment surface via high resolution microscopy to the results of surface sensitive techniques such as EIS will benefit from more sophisticated methods of structural quantification. For example, the ISA technique which quantifies textural entropy, homogeneity, energy, areal porosity, average horizontal and vertical run lengths, diffusion distance, and fractal dimension from digital biofilm images could be a valuable approach.[179]

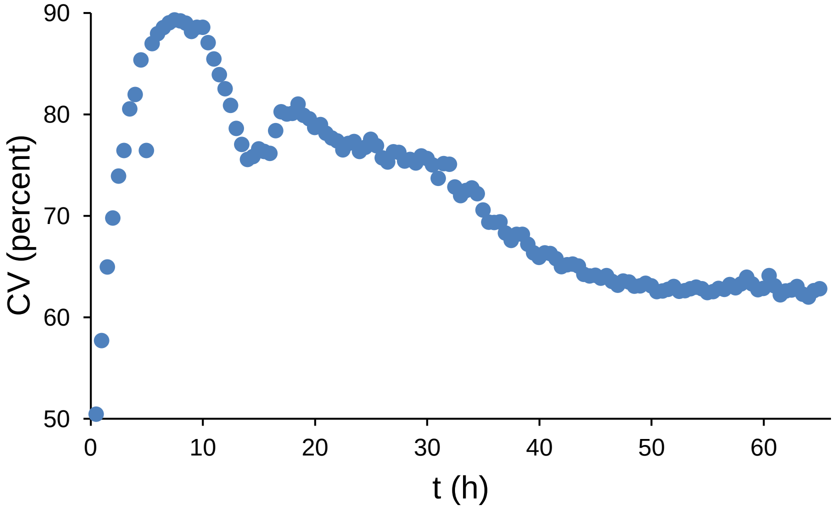

Figure 2.11 COV from analysis of continuous CLSM experiments conducted over a 65 h period following inoculation. COV was calculated from images of bacteria embedded in biofilms adhered to the glass slide of a microfluidic device. Acquisition was conducted using a 40× objective.

2.8.7 Measurement of shifting biofilm at the attachment surface using CLSM

In the section 2.5.3, it is proposed that the reversible increases to R_b and C_b are due to structural changes and higher contact of the biofilm with the electrode surface. The data in Figure 2.12 a shows the shifted biomass from the GFP bacteria before and after application of high flow rates. Secondly, in Figure 2.12 b shows the position of the biofilm biomass before application of high flow rates and after return to low flow rate following flow rate cycling. It can be seen that the biomass almost completely recovers its original position, proving that the biofilms colonies maintain a nearly static anchoring point upstream, even after being subjected to high flow rates.

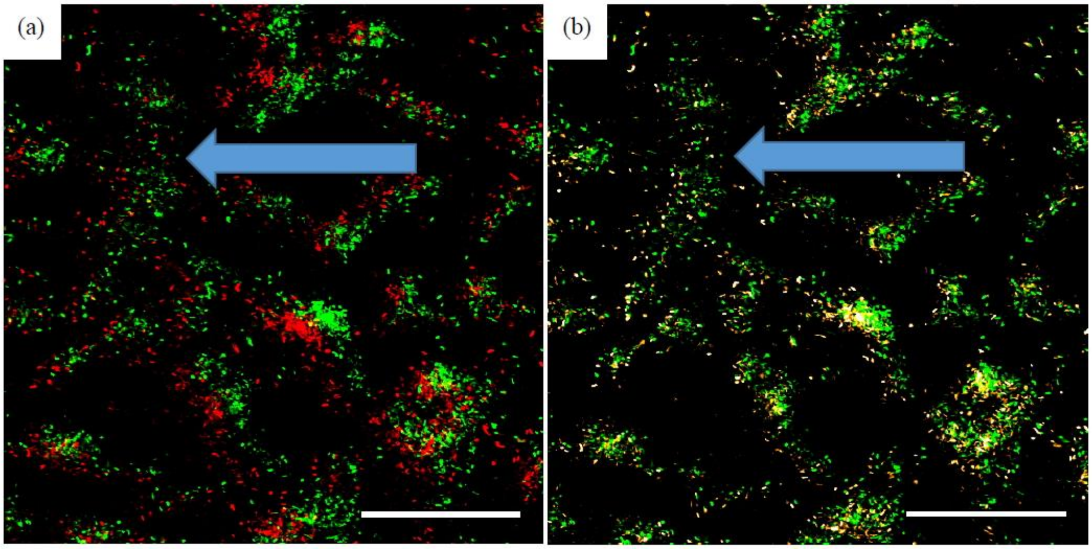

Figure 2.12 Shifting biofilm colonies at the attachment surface. **(a)** Position of GFP bacteria under cultivation flow conditions Q_{Tot}=1.2 mL·h^{-1} (green) and after reaching 6 mL·h^{-1} (red). **(b)** After position of the GFP bacteria after flow rate returns to initial flow conditions Q_{Tot}=1.2 mL·h^{-1} (yellow) compared to original positions before flow was increased (green). The green data in both (a) and (b) are identical.

Chapter 3. Flow-based deacidification of *Geobacter sulfurreducens* biofilms depends on nutrient conditions: A microfluidic bioelectrochemical study

Mir pouyan Zarabadi[1], Steve J. Charette[2,3,4], Jesse Greener[,1]*

[1]Département de Chimie, Faculté des sciences et de génie, Université Laval, Québec City, QC, Canada.

[2]Institut de Biologie Intégrative et des Systèmes, Pavillon Charles-Eugène-Marchand, Université Laval, Québec City, QC, Canada.

[3]Centre de recherche de l'Institut universitaire de cardiologie et de pneumologie de Québec, Québec City, QC, Canada.

[4]Département de biochimie, de microbiologie et de bio-informatique, Faculté des sciences et de génie, Université Laval, Québec City, QC, Canada.

Accepted manuscript online on 8 August 2018. Modifications on the numbering of the figures of the paper have been done in order to fit the sequence of the dissertation.

Published in *ChemElectroChem.* **2018**, *5*, 3645 – 3653.

3.1 Résumé

Les biofilms de la bactérie *Geobacter sulfurreducens* sont des matériaux prometteurs pour les nouveaux systèmes bioélectrochimiques. Pour améliorer les performances de tels systèmes, il convient de s’adresser aux limitations liées à l’acidification des biofilms. Cette recherche examine une hypothèse selon laquelle le flux de liquide peut désacidifier le pH du biofilm en améliorant le transport de la masse moléculaire dans les sous-domaines du biofilm. Un système électrochimique microfluidique a été utilisé pour mesurer les changements du pH du biofilm *in situ* tout en modulant avec précision les conditions hydrodynamiques lors d’un apport abondant (*turnover*), limité ou quasi nul en nutriments. Nous avons découvert qu’une augmentation des débits peut effectivement atténuer l’acidification des biofilms, mais pas en dessous des concentrations de turnovers, conditions habituellement utilisées dans ce type d’études. Cet effet est démontré par des observations selon lesquelles les augmentations de biocourant induites par le flux étaient relativement plus fortes pour les expériences menées à des concentrations limitées en éléments nutritifs par rapport aux concentrations de turnovers.

3.2 Abstract

Biofilms from *Geobacter sulfurreducens* are promising materials for new bioelectrochemical systems. To improve the performance of such systems, limitations related to biofilm acidification should be addressed. This work examines a long-held assumption that liquid flow can deacidify biofilm pH by enhancing molecular mass transport in the biofilm subdomain. A microfluidic electrochemical system was used to measure changes to biofilm pH in situ while accurately modulating hydrodynamic conditions under turnover, nutrient-limited and starvation conditions. We discovered that increased flow rates could indeed mitigate biofilm acidification, but not under turnover concentrations, the predominant conditions used in research studies. This effect is demonstrated with observations that flow-induced increases to bio-current were relatively stronger for experiments conducted under nutrient-limited concentrations compared to turnover concentrations.

3.3 Introduction

Biofilms from electro-active bacteria are a topic of intensive research as new biocatalysts for green chemistry with applications in waste remediation, energy production, and synthesis of chemical compounds and nanomaterials.[180,181,182] For electrode-adhered electro-active bacteria such as *Geobacter sulfurreducens*, substrate oxidation occurs in parallel with electron conduction through an extracellular bio-conductive network. *G. sulfurreducens* are among the most efficient species due to their direct electron transfer mechanism via conductive appendages and between redox groups within the densely packed biofilm.[67,73,183] This process is coupled with proton production to maintain electroneutrality, which can cause acidification in the biofilm due to reduced diffusivity. In turn, this acidification can limit bacterial metabolism and system performance. For example, biofilm acidification has been shown to reduce power output in microbial fuel cells (MFCs) and to limit the efficiencies of other bioelectrochemical systems.[77,79,184,185,186] In biofilms from *G. sulfurreducens*, complete metabolic inhibition can occur at pH values lower than 5.[76,187] Therefore, strategies that can reduce biofilm acidity in bio-electrochemical systems are an important goal. It has been proposed that flow-through systems might deliver performance improvements due to deacidification related to enhanced mass transfer of either acidic byproducts out of the biofilm[188] or deprotonated buffer molecules into the biofilm.[189] Similar claims have been made for bulk MFCs in the presence of stir-bar agitation[190] and for variable-speed rotating-disk electrode measurements.[77] However, to date, the hypothesis that flow can reduce biofilm acidity remains unproven experimentally. Moreover, even if flow can cause biofilm deacidification, its effect on current production compared with that of flux-enhanced nutrient availability should be explored. To address this question, strict control over flow and chemical concentrations should be implemented while conducting *in situ* measurement of pH changes.

The field of microfluidics has introduced new research opportunities to the life sciences and biotechnology due to its ability to precisely control culture conditions without exposure to ambient conditions. Specifically, flow rate and related hydrodynamic properties (shear stress, flow velocity, nutrient flux) can be manipulated over a large dynamic range while limiting the consumption of nutrient solutions and extending the experimental duration. Combined with the ability to rapidly adjust concentrations and other physiochemical parameters, complex multi-step experimental sequences can be devised. However, in situ measurements of changing pH within microchannels are not straightforward. Microfluidic designs that include embedded miniature pH electrodes have been demonstrated for measurement of liquid analytes,[191,192] but challenges include the fragility of typical porous glass materials used in these designs, mismatches in geometry with channel walls, and the likelihood of disruptions to local flow conditions. Moreover, long-term growth around the non-conductive tip of an embedded pH probe are not be representative of a typical electrode-adhered biofilm. pH-sensitive fluorophores have been used in characterisation of biofilms in MFCs, but they have only been demonstrated for short-term measurements following biofilm maturation,[187] likely due to problems associated with biocompatibility. Recently, nanoparticles capable of sensitive metal-enhanced florescence of embedded pH-sensitive fluorophores have been exploited for microfluidic studies of intact lactic acid-producing oral biofilms.[143] Covalent attachment of the nanoparticles to the biointerface prevented washout, and fluorophore confinement in a silica shell enhanced photo-stability, sensitivity and isolation from the biological environment, but use of this approach in the present application requires nanoparticle attachment to the electrode surface, which could interfere with electron transfer. Potentiostatic techniques, on the other hand, can be more promising for this application. First, the use of such techniques for in situ measurements in microfluidic channels is growing due to straightforward approaches to electrode miniaturization and integration, as well as a diversity of techniques that can be applied with the same experimental setup.[193] Second, the existing working electrode (WE) could also act as the probe surface, thereby avoiding the need for any foreign chemical probe molecules or additional sensors. In bulk liquid cells, cyclic voltammetry (CV) has been demonstrated as an effective technique for observing pH-induced shifts in the formal potential E_f (V) (arithmetic average of the cathodic and anodic redox peaks) for proton-involved redox processes (Eq. 3.1).[194,195]

$$[H_mRed] \rightleftharpoons [Ox] + ne^- + mH^+ \qquad \text{(Eq. 3.1)}$$

Where $[H_mRed]$ and $[Ox]$ are the respective concentrations of the initial redox species in its reduced and oxidized forms, with and n and m denoting the number of electrons and protons involved, respectively.[76,196,197] In metabolically active *Geobacter spp*. biofilms, redox changes to cytochromes c are coupled to other bioelectrochemical steps in bacterial respiration. Changes to E_f of cytochrome c groups involved in the electron transfer chain can be an indicator of the biofilm pH (pH_b) if they are coupled to H^+ production steps, such as in Eq. 3.1.[196,197,198] It is important to note that this technique is sensitive to net pH over the entire electroactive biofilm rather than local pH gradients within different layers.[76,199] In general, the dependence of E_f on pH for the redox reaction in Eq. 3.1 is given by the Nernst equation[195] or its simplified form (Eq. 3.2) when m = n:

$$E_f = E^0 - (0.059 \times pH) \qquad \text{(Eq. 3.2)}$$

where E^o (V) is the cytochrome c redox potential at pH = 0. Therefore, pH changes (ΔpH) can be quantitatively tracked by monitoring ΔE_f. In the present case, Eq. 3.2 indicates that E_f increases represent biofilm acidification and vice versa. Under hydrodynamic conditions, the combined effects of flow-controlled exchange of nutrient, buffer and acidic by-product molecules on the changes to biofilm pH (ΔpH_b) can be studied as a function of the flow rate of a typical acetate (Ac)-based nutrient solution. We note that although the flux of ions might affect, somewhat, the redox reaction kinetics, they do not affect E_f.[200,201]

3.4 Experimental section

3.4.1 Bacterial preparation

Frozen samples of *Geobacter sulfurreducens* (strain PCA, ATCC 51573) were cultured in an anaerobic glove box for 7 days and subcultured at least 2 times prior to injection into the electrochemical device. The glove box environment consisted of 10% H_2 and 10% CO_2 balanced with N_2. The *G. sulfurreducens* sub-culturing medium contained the following amounts per litre in distilled water: 1.5 g NH_4Cl, 0.6 g NaH_2PO_4, 0.1 g KCl, 2.5 g $NaHCO_3$, 0.82 g CH_3COONa (10 mM), 8 g $Na_2C_4H_2O_4$ (40 mM), 10 mL vitamin supplement ATCC® MD-VS™, and 10 mL trace mineral supplement ATCC® MD-TMS™. With the exception of sodium fumarate and vitamin/trace mineral supplements, all chemical compounds were dissolved in distilled water and autoclaved at 110 °C and 20 psi for 20 min. The *G. sulfurreducens* medium was transferred to the glove box, and the filtered sterilized sodium fumarate and vitamin/trace mineral supplements were added. The anaerobic nutrient medium was ready to use after overnight incubation in an anaerobic glove box. The pH of the medium was adjusted to 7 prior to sub-culturing in the glove box. For electrochemical growth of *G. sulfurreducens* in electrochemical cells, sodium fumarate and vitamins were excluded, and the pH was adjusted to 7.5. Sub-cultures that were transferred more than 8 times were discarded.[202]

3.4.2 Device fabrication and anaerobic environment

We followed a recent report that demonstrated the use of embedded electrodes at the bottom of a polydimethylsiloxane (PDMS) microchannel such that the transition to the electrode was seamless.[203] The device consisted of graphite WE and CE and a gold (Au) RE. Two graphite strips (GraphiteStore.com Inc., USA) with dimensions of 3 mm × 20 mm were embedded and used as the WE and CE. The surface area exposed to the solution for both electrodes after fabrication was 3 mm × 2 mm. The gold-coated polystyrene RE was fabricated via electroless deposition.

The electrode was subsequently cut into 3 × 20 mm strips and embedded into the microfluidic device in the same manner as in the WE and CE. A mixture of liquid polydimethylsiloxane (PDMS) and cross-linking agent Sylgard184 (Dow Corning, Canada) (10:1) was poured over the mould (FlowJEM Inc., Toronto, Canada) while the electrodes were placed on features of the mould with dimensions of 30 mm (L) × 2 mm (w) × 0.4 mm (h). After curing for 4 h at 70 °C, the device with embedded electrodes was removed from the mould. Cleaning and sterilization of the channel with a 70% ethanol solution and of the electrodes with 1 M HCl were conducted before sealing. The microfluidic electrochemical cell was sealed with a microscope slide by exposure to air plasma (PCD-001 Harrick Plasma, Ithaca, NY, USA). Because the microfluidic device was fabricated in PDMS, which is known to be porous to small molecules including O_2, an anaerobic enclosure (McIntosh and Filde's, 28029 Sigma-Aldrich) filled with anaerobic gas (20% CO_2 and 80% N_2) was used with a controlled temperature of 22 ±1 ^{o}C (Figure 3.8). The device was placed in the enclosure, and sterile perfluoroalkoxy connective tubing (PFA tube 1/16, Hamilton Inc., Canada) and electrical connections were attached via airtight feedthroughs in the enclosure cap. To minimize gas diffusion through the connective tubing outside of the enclosure, a layer of gas-impermeable tape (Loctite 249 Anaerobic Blue Threadlocker Tape, Medium Strength, Henkel Corp., Mississauga, Canada) was applied to the tubing, which was subsequently covered by epoxy glue. Electrical leads were fixed to the graphite WE and CE via alligator clips, and the gold RE was connected by solder with a protective coating of epoxy to physically stabilize the connection (Figure 3.8). The inlet tube was connected to a 50 mL glass syringe via connector assemblies (P-200x, P-658, IDEX, WA, USA). Syringe pumps (PHD 2000, Harvard Apparatus, Holliston, MA, USA) were used in controlled liquid injection. Before inoculation, the microfluidic channel and tubing were rinsed with sterile distilled water for 1 h at 1 $mL \cdot h^{-1}$. For calibration of the gold RE to a standard Ag/AgCl, 3M KCl RE and verification of cytochrome c formal redox potential pH dependency, a conventional three-electrode electrochemical cell was set up (see the section of 3.8.3 for details).

3.4.3 Electrochemical measurements

Electrochemical measurements included chronoamperometry (CA) and cyclic voltammetry (CV) performed using a commercially available potentiostat (Volta Lab PST006, Radiometer analytical, USA) controlled by the relevant software (Volta Master 4, Hach Radiometer Analytical, USA). Analysis was conducted using Origin Pro 2015.

3.4.4 Samples preparation for SEM imaging

Scanning electron microscopy (SEM) was performed after the experiment was completed to observe the bacteria attached to the WE (Figure 3.11). Before the electrode was removed from the microfluidic device, a fixation solution (2.5% glutaraldehyde in phosphate buffer) was flowed through the channel ($Q = 0.5\ mL \cdot h^{-1}$) for 2 h while the device remained under anaerobic conditions. The device was subsequently removed from the anaerobic enclosure and cut open to reveal and remove the working electrode. The biofilm-coated electrode was left exposed to the same fixation solution in a bath overnight. The next day, the electrode was transferred to a solution with 1% osmium tetroxide for 1.5 h and rinsed in phosphate buffer. Finally, the sample was sequentially dehydrated in 50, 75, 95 and 100% aqueous ethanol solutions for 15 min each, followed by drying at room temperature overnight. Prior to image capture, a thin layer of gold was sputtered on the biofilms and electrode (Model: Nanotech, SEM PREP 2). The images were collected with a JEOL JSM-6360 LV electron microscope.

3.5 Results and discussion

To better understand how the bulk flow of a typical Ac-based nutrient solution affects the pH_b of a *G. sulfurreducens* biofilm, a three-electrode microfluidic system was selected. The reader is directed to previous work that discusses the fabrication protocol to insert the electrodes flush against the microchannel wall in a similar device used for electrochemical impedance spectroscopy of non-electroactive biofilms.[203] Figure 3.1 a shows the device schematic, including placement of electrodes and direction of liquid flow. Figure 3.1 b shows an electron microscopy image of the orientation of a mature biofilm on the WE following an experiment. The flow rate and acetate concentrations ([Ac]) were controlled via programmable syringe pumps and upstream valves. To verify the stability of the gold pseudo reference electrode (RE) throughout the experiment, we collected cyclic voltammograms for a redox solution consisting of 10 mM potassium ferricyanide. The redox molecules were added to the same nutrient medium used in the remainder of the experiments to ensure that ions and support molecules were present during the test. The position of the redox peaks in the CV curves were unchanged during the two-week experiment, indicating the stability of the gold RE. Changes to the flow rate also did not affect the position of the redox peaks ($\Delta E_f = 0$), as expected, because proton concentration was not changed as part of the redox process involving ferricyanide (Figure 3.7). As discussed later, cytochrome c proteins in an inactive biofilm also had a value of $\Delta E_f = 0$ during flow rate cycling, as expected, because metabolic inactivity resulted in no proton production. In addition, changes to [Ac] did not affect RE performance. To ensure that the experimental conditions did not affect the microfluidic three-electrode flow cell performance, the RE was placed at the furthest upstream point such that it was always contacted by fresh nutrient solution. Byproducts from half-cell reactions at the WE and the counter electrode (CE) were carried downstream and did not contaminate the liquid environment around the RE because the upstream diffusion of H^+ was slower than the downstream convection (see Table 3.1 for mass transfer calculation results). The electrode configuration which placed the RE upstream were it could be exposed to a constant flux of fresh nutrient media has been shown previously as a method for achieving stable performance from an Au pseudo RE for non-electroactive bacteria and their biofilms.[203,204] For electroactive biofilms used here, the RE stability was enhanced because *G. sulfurreducens* bacteria could not complete the Krebs cycles via electrode respiration because no current is permitted to flow through REs. As a result, the RE remained completely free from bacterial contamination. This observation was verified by SEM and resonance

Raman spectroscopy following the experiments, as shown previously.[205] Thus, under regular experimental conditions (Q = 0.2 mL·h^{-1}, [Ac] = 10 mM), the measured E_f for cytochrome c was stable. We note that a different electrode arrangement may be required if the experiment involves changes to liquid phase chemistry during the experiment. For example, a three-electrode microfluidic microbial cell was recently demonstrated with a Ag/AgCl RE under a constant co-flow of electrolyte solution and the applied chemical changes being applied only to the WE, enabling excellent, long-term measurement stability of *G. sulfurreducens* biofilms.[133] However, care would have to be taken to ensure that the co-flow interface is stable during large changes to flow rate as we do here.

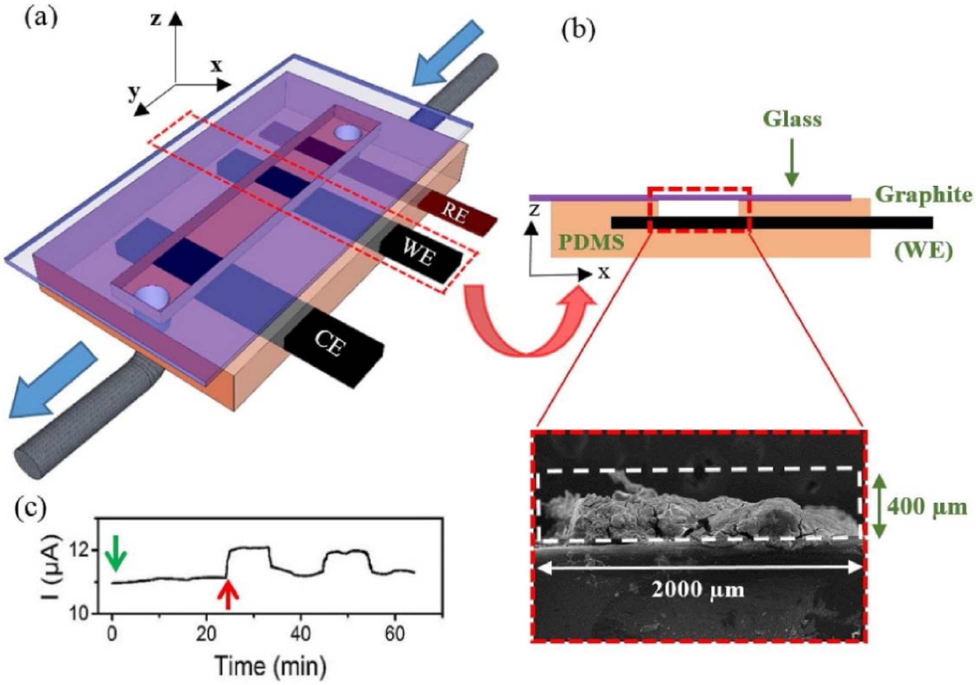

Figure 3.1 (a) Schematic of a three-electrode glass-sealed microfluidic flow cell with dimensions 2 mm width, 400 µm height and 30 mm length. The system consists of graphite working (WE) and counter-electrodes (CE) and a gold pseudo-reference electrode (RE). **(b)** Cross-sectional view of the microchannel with the sealing glass on top (purple) and an electrode on the bottom. Inset (below) shows an SEM image of the G. sulfurreducens biofilm at the downstream edge of the WE acquired after the end of an experiment. **(c)** Changes to current outputs (I) for biofilms subjected to solutions with [Ac] = 10 mM during modulations of their flow rates to between Q = 0.2 and Q = 1 mL·h^{-1} (green and red arrows, respectively, shown for the first flow cycle).

Inoculation of the microfluidic device was conducted by injection of the fumarate-containing *G. sulfurreducens* inoculum solution through the connective tubing using a 10 mL gastight glass syringe. The role of fumarate as a soluble electron acceptor allowed the bacteria to survive in planktonic form. Inoculum flowed for 3 h at Q = 0.5 $mL\cdot h^{-1}$ while the WE was held at 410 mV vs. Au, approximately 0 mV vs. Ag/AgCl (see Figure 3.6). This potential was sufficient to oxidize cytochrome c, thus enabling electrode respiration.[196] Subsequently, the source was changed to a 50 mL gastight syringe containing fumarate-free nutrient medium ([Ac] = 10 mM) solution flowing at Q=0.2 $mL\cdot h^{-1}$, without changing the potential at the WE. In the absence of dissolved fumarate, bacterial growth continued exclusively on the WE while the current was monitored via chronoamperometry (CA). Figure 3.2a is a typical dataset showing current increase collected using CA during the initial biofilm growth. We note from separate experiments that cycling between Q = 0.2 and 1 $mL\cdot h^{-1}$ at turnover concentrations ($[Ac]_{tn}$ = 10 mM), reproduced previous observations that variations in hydrodynamic conditions could affect the current output (Figure 3.1 C).[77]

After observing the expected response of the *G. sulfurreducens* biofilm in the microfluidic electrochemical flow cell, our next goal was to verify that changes in Q could only affect E_f for metabolically active biofilms. First, after an initial growth period of approximately 160 h, we changed the nutrient concentration to [Ac] = 0 mM from $[Ac]_{tn}$ (while maintaining Q = 0.2 $mL\cdot h^{-1}$) and the current began to drop (Figure 3.2 a, asterisk region). In separate experiments, the rate at which the current dropped was related to Q (data not shown), indicating a flow-dependent mechanism for the elimination of nutrient reserves trapped in the biofilm, which was likely enhanced by convection through the biofilm subdomain,[206,207,208] especially due to the head-on approach of the liquid.[209] After 6 h at Q = 0.2 $mL\cdot h^{-1}$, the current had decreased to nearly 15% of its pre-starvation value. We then began to acquire slow-scan cyclic voltammograms (CV_1 in Figure 3.2 a) to observe the effect of Q on redox potentials. A baseline subtraction protocol was applied to identify the cytochrome c formal redox potentials.[210] Two redox centres were identified with formal potentials of E_{f1} = -25 mV and E_{f2} = 55 mV vs. Au. Based on calibration measurements (Figure 3.6), these values matched the reported potentials for outer membrane cytochrome c groups (OmcB and OmcZ) and periplasmic cytochrome c (PpcA), with values of E_{f1} = -435 mV and E_{f2} = -355 mV vs. Ag/AgCl, respectively.[196] The separation of reduction and oxidation peaks for E_{f1} and E_{f2} produced values of 64 and 56 mV, respectively, demonstrating fully reversible electrochemical processes. Cycling Q during this time interval resulted in reversible changes to E_f (Figure 3.2 b). According to theory, changes to E_f should occur if the redox reaction involves a change to $[H^+]$, according to Eq. 3.1. This implies that the biofilm maintained some metabolic activity, even under starvation conditions. *G. sulfurreducens* biofilms are known to retain a certain amount of metabolic activity for similar durations following a switch to starvation conditions, due to limited nutrient reserves,[202] so temporary sensitivity of E_f to Q was not surprising. Exposure to [Ac] = 0 mM for another 16 h resulted in true biofilm starvation, including complete loss of metabolic activity and CV measurements (CV_2 in Figure 3.2 a) of E_f which were flow-independent (Figure 3.2 c). We concluded that flow-based changes to molecular mass transfer between the biofilm and the liquid phase could not cause changes to E_f unless the biofilm was metabolically active and H^+ production was coupled with the cytochrome c redox process as a part of the overall biofilm electron transfer chain. This result supports the previous observation that changes to hydrodynamic conditions did not affect measurements for an inactive *G. sulfurreducens* biofilm.[77] See the section of 3.8.7 for additional discussion of the differences between true starvation, temporarily reduced activity following a switch to nutrient-free conditions and nutrient-limited conditions. Finally, the system was returned to $[Ac]_{tn}$ ([Ac] = 10 mM), and the current slowly recovered to pre-starvation levels after 24 h, and continued growing after that (Figure 3.2 a).

The next goal was to quantify the flow-based changes to E_f from active biofilms under a typical nutrient solution with $[Ac]_{tn}$ and nutrient-limited Ac concentrations ($[Ac]_{ltd}$ = 0.3 mM). First cyclic voltammograms obtained under $[Ac]_{tn}$ displayed a sigmoidal shape (Figure 3.3 a), which is typical due to the large catalytic current.[196, 211] As expected, a first-derivative plot showed a single redox centre at E_f = 30 mV vs. Au (corresponding to -385 mV vs. Ag/AgCl), which was the average of E_{f1} and E_{f2} from above. Second, increasing the flow rate from Q = 0.2 $mL\cdot h^{-1}$ to Q = 1 $mL\cdot h^{-1}$ resulted in a small increase in the limiting current, but E_f remained constant (Figure 3.3 a, inset). We continued to increase Q until a slight but statistically significant shift to lower potential could be detected (ΔE_f = -18 mV) at Q=5 $mL\cdot h^{-1}$. According to Eq. 3.1, the shift to more negative potentials indicated biofilm deacidification of the biofilm. Third, the nutrient conditions were switched from $[Ac]_{tn}$ to $[Ac]_{ltd}$ using an upstream valve while maintaining the flow rate at Q = 0.2 $mL\cdot h^{-1}$. We acquired CVs after the system stabilized under the new nutrient conditions.

As shown in Figure 3.3 b, under $[Ac]_{ltd}$, E_f was easily reduced even with modest increases to Q, indicating increases in biofilm pH (pH_b). For example, changes as great as -125 mV at Q = 2 $mL\cdot h^{-1}$ were observed. The shift in E_f was reversible, returning to higher values when Q was reduced, thus indicating a return to relatively acidic conditions.

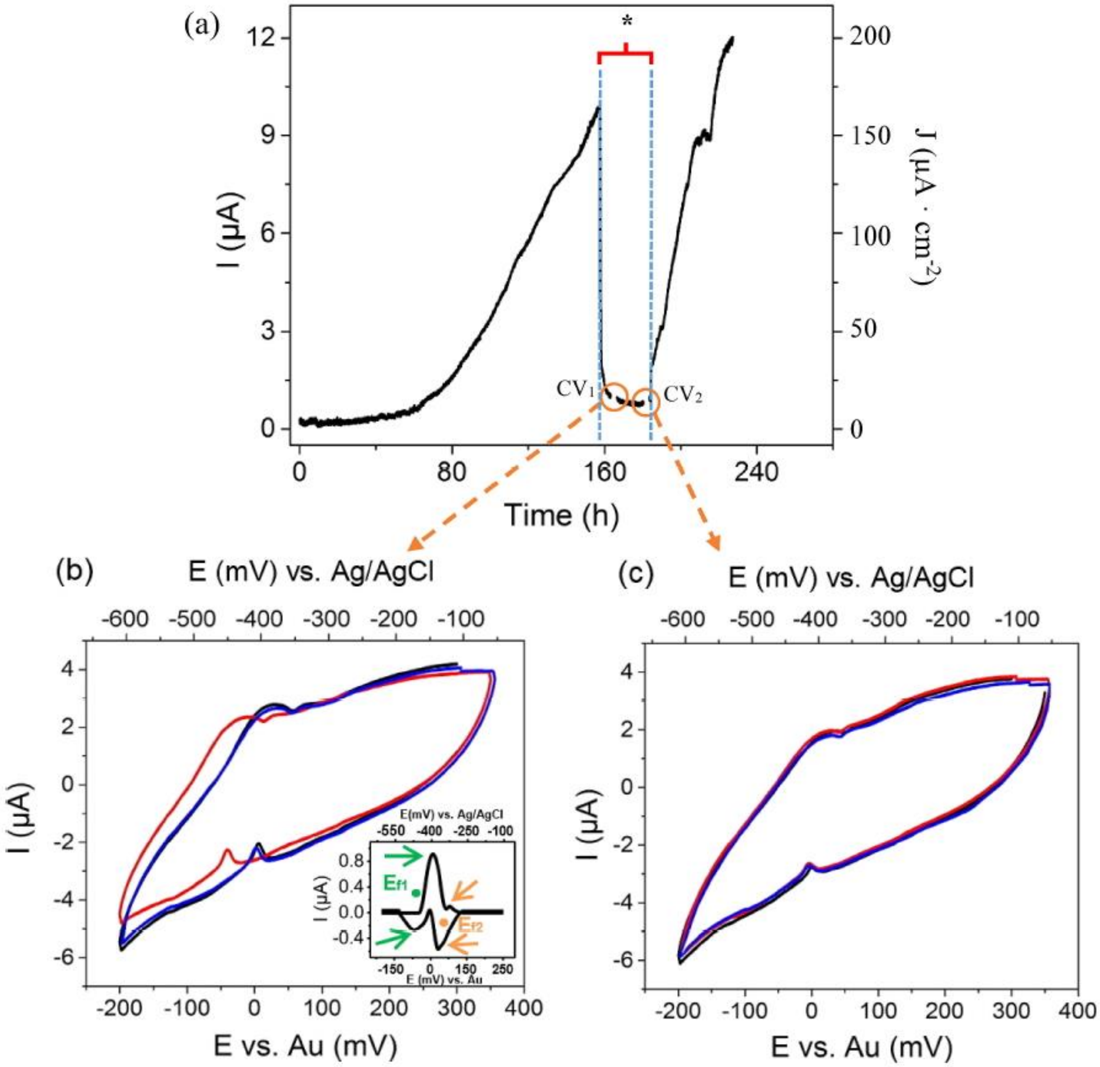

Figure 3.2 (a) CA of G. sulfurreducens during growth with [Ac] = 10 and 0 mM concentrations and Q = 0.2 mL·h^{-1}. The asterisk highlights the region of applied [Ac] = 0 mM. The encircled regions showing interrupted current indicate the times at which CVs were conducted (CV$_1$ and CV$_2$) under modulated Q. **(b)** CV of G. sulfurreducens biofilm 6 h after switching to [Ac] = 0 mM (marked CV$_1$ in (a)) and changing between Q = 0.2 (blue and black) and Q = 1 mL·h^{-1} (red). The inset shows baseline subtraction acquired at Q = 0.2 mL·h^{-1} to clarify the position of the electrochemical redox potentials. Green and orange arrows point to redox peaks associated with the first and second redox centers (E$_{f1}$ and E$_{f2}$), respectively. The positions of E$_{f1}$ and E$_{f2}$ (green and orange dots, respectively) were calculated using the arithmetic mean of the reduction and oxidation electrochemical potentials of each redox center. **(c)** Non-responsive formal potential under same flow rates as in (a) after continuation of starvation conditions for another 16 h (CV$_2$). In both (b) and (c), CVs were collected with scan rate (1 mV·s^{-1}) after a flow stabilization period of 15 min.

According to Eq. 3.2, changes to E_f under different values of Q could form the basis for study of the hydrodynamic effects on changes to pH_b (ΔpH_b). Thus, with the quantification of changes to E_f under different values of Q complete, we sought next to determine the corresponding changes to ΔpH_b. To verify the experimental changes to E_f for biofilms used here with the known pH of the solution (pH_s), we following the typical procedure reported in the literature.[196] Briefly, a 130 h biofilm grown under $[Ac]_{tn}$ was subsequently exposed to an Ac-free medium in a standard (bulk) electrochemical cell. After reaching 10% of the original current, the medium was switched to an Ac-free medium with specified pH_s values, and cyclic voltammograms were acquired. Under these conditions, the low current generated by the relatively young biofilm should have significantly limited the production and accumulation of H^+ in the biofilm, as reported previously. Therefore, pH_s and pH_b were expected to be nearly the same.[196,197] However, due to the temporary activity retained by the biofilm in the [Ac] = 0 mM solution, E_f still maintained pH_b dependency. As is typical for such calibration experiments, these were performed in a bulk (static) electrochemical cell to accommodate a Ag/AgCl probe, thereby maintaining a consistent reference as the solution-phase pH was adjusted. See the section of 3.8.1 for additional details on the electrochemical setup used in calibration measurements.

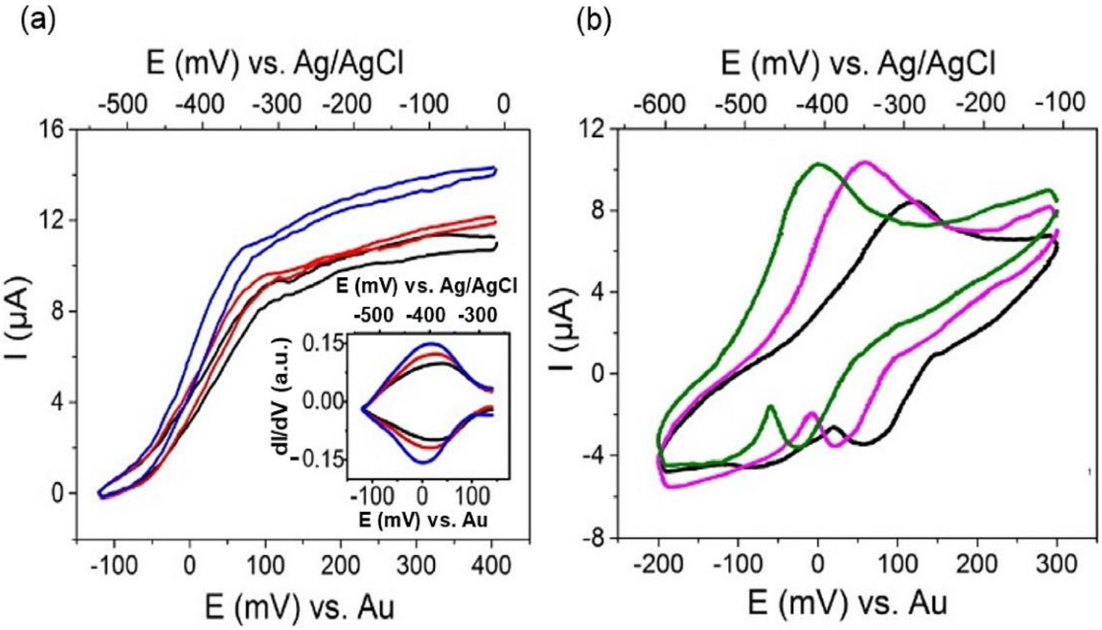

Figure 3.3 (a) CV of an electrode-adhered *G. sulfurreducens* biofilm exposed to turnover concentrations, $[\mathrm{Ac}]_{\mathrm{tn}}$ ([Ac] = 10 mM), with flow rates of Q = 0.2 (black curve), Q = 1 (red curve) and Q = 5 $\mathrm{mL \cdot h^{-1}}$ (blue curve). Inset shows first-derivative plot used to find the formal potential. **(b)** CV curves of an electrode-adhered *G. sulfurreducens* biofilm exposed to nutrient-limited concentrations, $[\mathrm{Ac}]_{\mathrm{ltd}}$ ([Ac] = 0.3 mM), with flow rates of Q = 0.2 (black), Q = 0.75 (pink) and Q = 2 $\mathrm{mL \cdot h^{-1}}$ (green). CVs of electrode-adhered *G. sulfurreducens* biofilm exposed to $[\mathrm{Ac}]_{\mathrm{tn}}$ acquired with a scan rate of 1 $\mathrm{mV \cdot s^{-1}}$ and exposed to $[\mathrm{Ac}]_{\mathrm{ltd}}$ with a scan rate of 5 $\mathrm{mV \cdot s^{-1}}$ (for easier identification of redox peaks). The biofilm age for (a) and (b) is 220 h.

Figure 3.4 a shows the CV curves, which shifted to lower potential with reduction of the imposed $\mathrm{pH_s}$ in the range of 6 to 8. From repeated experiments, the average E_f was obtained for each pH value, and a calibration plot was constructed. As shown in the inset of Figure 3.4 a, we observed a linear relationship between E_f and pH, as expected from Eq. 3.2. A linear fitting produced a slope of -52.5 ± 1.4 mV/pH unit. This value compares well with the predicted value of -59 mV/pH unit from the Nernst equation (i.e. Eq. 3.2) and the previous values measured using the same technique.[196,197] This result also reinforces our observations above that the electrochemical process was reversible. The slope of the calibration curve could be universally applied to accurately predict the changes in the net biofilm pH ($\Delta \mathrm{pH_b}$) based on ΔE_f values, independent of the choice of RE.

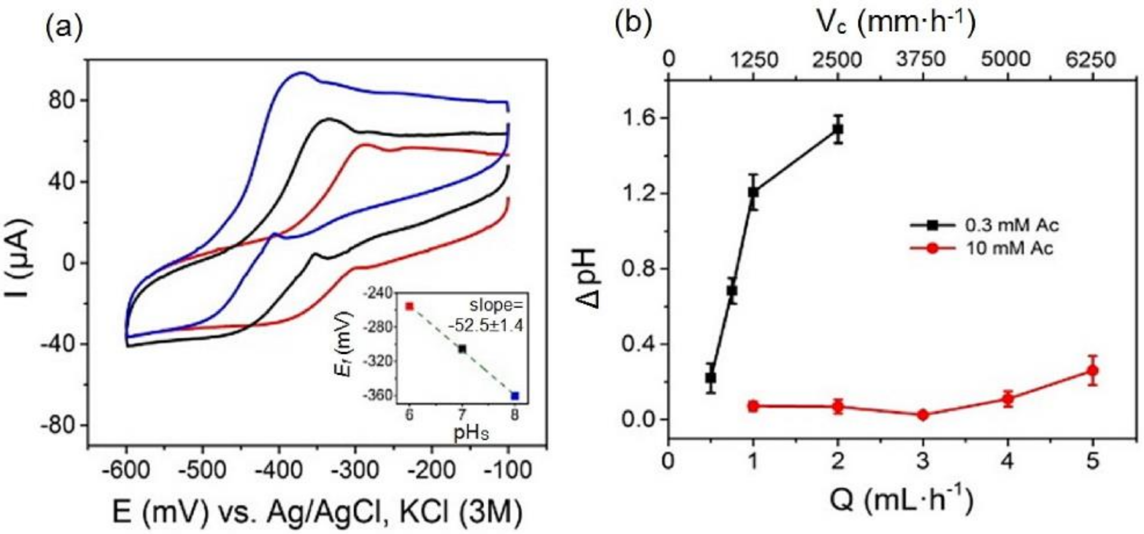

Figure 3.4 (a) Example CVs of *G. sulfurreducens* used to generate a calibration curve of formal potential at different pH_S. Scan rate (5 $mV \cdot s^{-1}$). Inset: Calibration curve of cytochrome c formal potential as a function of pH_S. The error bars resulting from 3 separate experiments are smaller than the data points. **(b)** Flow rate dependency of ΔpH_b under turnover ($[Ac]_{tn}$ = 10 mM) and nutrient-limited concentrations (and $[Ac]_{ltd}$ = 0.3 mM). Error bars show standard deviation in the measured ΔpH_b from 3 independent CV measurements.

We note that it has recently been shown that good correlation can be achieved between E_f of cytochrome c and net pH_b of a *G. sulfurreducens* biofilm in standard nutrient solution.[198] However, ΔpH_b was analysed in this work instead of pH_b to avoid possible complications arising from small measured offsets in the applied potentials with use of different gold REs from device to device or the possibility of slight differences between pH_S and pH_b during the calibration step described above.

Next, using Q = 0.2 $mL \cdot h^{-1}$ as a lower limit, ΔpH_b was determined from measured E_f values at different flow rates. Each experiment was repeated on separate days and consisted of the acquisition of three sequential CVs after flow stabilization. The E_f values from the second and third CVs from all three experiments were averaged together. Thus, data points and error bars (Figure 3.4 b) were result of a total of 6 cyclic voltammograms, acquired over three separate days. The results acquired matched other preliminary measurements that were conducted on separate biofilms. Figure 3.4 b shows the effect on ΔpH_b of Q cycling under turnover and nutrient-limited conditions. Under turnover conditions, pH_b was nearly unchanged over a wide range of flow rates, likely because the kinetics of acidic byproduct production were too fast to be washed out or neutralized by buffer molecules, even at elevated flow rates. In fact, increased flow rates could have actually increased the nutrient flux through the channel (J = Q×[Ac]) and the related nutrient availability, thus further increasing the H^+ production rate in parallel with higher measured electrical currents. On the contrary, increased flow rates did efficiently influence the pH_b, when the liquid medium was nutrient-limited. This was likely because the lower rate of H^+ production could more easily be washed out or neutralized by the higher influx buffer molecules. We note that the ΔpH_b of nearly 1.5 at high flow rate nearly matches the difference in pH measured previously between the nutrient solution and the mean pH_b.[198] Thus, we tentatively conclude that high flow rate of a nutrient-limited solution can almost completely de-acidify the biofilm.

Figure 3.5 summarizes the flow-based factors that might have caused the observed increase in current (ΔI) for different nutrient solution concentrations. For $[AC]_{tn}$, positive values of ΔI upon changing the flow rates (e.g. Figure 3.9) from low (Q_i) to high (Q_f) were not accompanied by obvious changes to biofilm pH ($\Delta pH_b \approx 0$). Therefore, in this case, ΔI was not due to increases to bacterial activity resulting from biofilm deacidification but was instead likely due to increases in Ac flux through the microchannel only ($\Delta J = (Q_f - Q_i)\cdot[Ac]_{tn}$). However, cycling the flow under $[Ac]_{ltd}$ conditions would have caused changes to both the nutrient availability via increases to Ac flux through the microchannel ($\Delta J = (Q_f - Q_i)\cdot[Ac]_{ltd} > 0$) and the biofilm deacidification ($\Delta pH_b > 0$). This dual effect could explain why ΔI values from Q cycling of nutrient-limited solutions were so similar to those obtained under turnover concentrations, despite having [Ac] and Ac flux that were nearly 30 times less (Figure 3.9). In fact, taken as a fraction of I at the slow flow rate (I_0), the $\Delta I/I_0$ was more than double for nutrient-limited conditions compared turnover conditions (see section 3.8.7 for more information). Therefore, we predict that bioelectrochemical systems based on *G. Sulfurreducens* and potentially other electroactive biofilms, could disproportionately benefit from operation under hydrodynamic conditions when nutrient concentrations are low. This could potentially open the way for a solution to poor performance of some bioelectrochemical systems at low concentrations.[212]

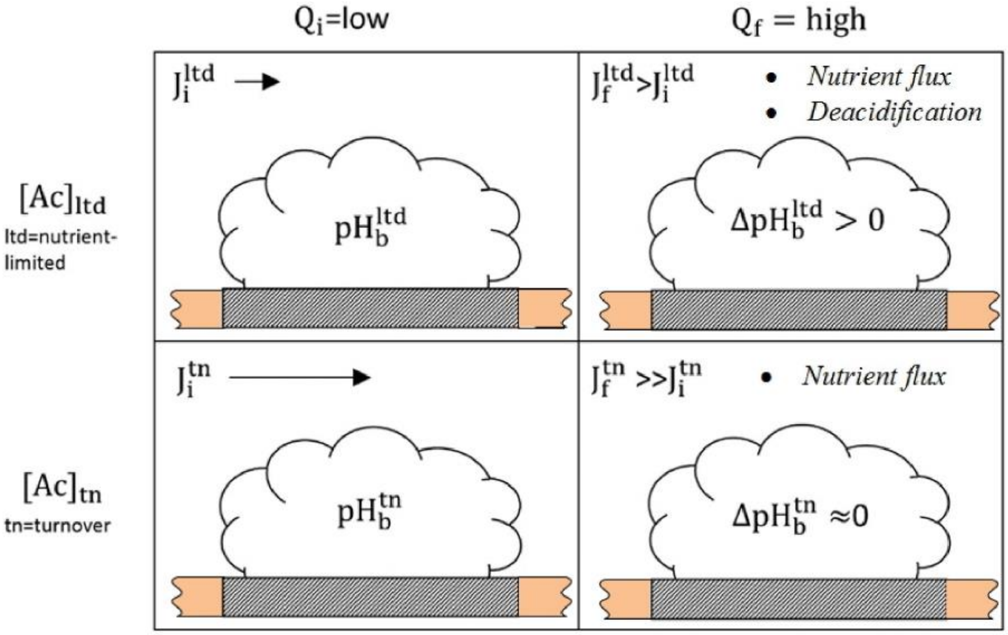

Figure 3.5 Summary of the effects of hydrodynamic cycling on ΔpH_b and proposed factors (italics) leading to a higher electrical current from electroactive biofilms in a microchannel. Deacidification is a general term that includes wash out of acidic by-products and increased neutralization by buffer molecules from the nutrient solution. The biofilm is shown protruding into the cross-flow stream from a continuous segment of the microchannel wall consisting of an embedded working electrode and the surrounding PDMS (cross-hatched and orange, respectively).

3.6 Conclusion

This work examined the role of bulk liquid hydrodynamic conditions and nutrient concentrations on changes to pH within electrode-adhered *G. sulfurreducens* biofilms. A three-electrode microfluidic flow system was used to accurately modulate the flow rates while conducting cyclic voltammetry measurements *in situ*. By following the pH-sensitive changes to the formal potential of cytochrome c, it was discovered that changes in hydrodynamic conditions could affect the acidity of *G. sulfurreducens* biofilms. However, flow rates were only effective in modulating acidity under nutrient-limited concentration conditions or temporarily, before the biofilm became completely inactive, after exposure to starvation conditions. Thus, previous assumptions that pH changes in electroactive biofilms could have contributed to higher current production when subjected to hydrodynamic conditions should be re-evaluated. Future studies should focus on the role of biofilm thickness, density and structural heterogeneity in preventing changes to pH with by elevated flow rates of nutrient solutions at turnover concentrations.

3.7 Acknowledgments

The authors thank Luc Trudel and Laurent Smith (U. Laval) for assistance with the culture of *G. sulfurreducens* and Richard Janvier (U. Laval) for technical assistance with SEM. J.G. is the recipient of an Early Researcher Award from the Fonds de recherche du Québec—nature et technologies (FRQNT). This research was supported by funding through the Natural Sciences and Engineering Research Council, Canada. J.G. and S.J.C. are supported by a joint FRQNT AUDACE grant (high risk, high reward) to study microbiological systems using microfluidics.

3.8 Supporting Information

3.8.1 Bulk electrochemical set-up

The graphite working electrode (WE) and counter electrode (CE) were cut into 0.5 cm × 0.5 cm for WE and 1 cm × 1 cm for CE. A hole was drilled and a wire was fasten and covered by epoxy glue. An Ag/AgCl, 3M KCl was used as a reference electrode. A 100 mL electrochemical cell chamber with 4-hole rubber cap was setup with three-electrode configuration set-up and a gas tube for purging with 20% CO_2 / 80% N_2. A 10 mM acetate growth medium, with no fumarate was used for *G. sulfurreducens* growth on the WE at 0 V vs. Ag/AgCl reference electrode. A pseudo reference gold electrode was replaced with Ag/AgCl reference electrode to verify ∆E between two reference electrodes of a 130 h old biofilm. Acetate-free medium with three different solution pH values (pH_s = 6, 7 and 8) was used for measurement of pH_b dependency of the formal potential of *G. sulfurreducens* cytochromes c.

3.8.2 Hydrodynamic calculations

The average velocity resulting from flowing liquid through the microchannel at a volumetric flow rate, Q ($mL \cdot h^{-1}$) was estimated based on Eq. 3.3

$$\bar{v}_c = Q/(w \cdot h) \qquad \text{(Eq. 3.3)}$$

Where w and h are the channel width (2 mm) and height (400 μm), respectively. The average applied shear stress at the wall $\bar{\tau}$ (Pa) is related to Q according to Eq. 3.4:

$$\bar{\tau} = 6 \cdot \mu \cdot Q/(w \cdot h^2) \qquad \text{(Eq. 3.4)}$$

Where μ is the liquid-phase viscosity (1×10^{-3} Pa·s). Table 3.1 shows the relation between Q, $\bar{v}_c$ and τ. As discussed in the next section, the only mode of mass transfer that can oppose convection is (upstream) diffusion, with average velocity, $\bar{v}_d$, given by Eq. 3.5:

$$\bar{v}_d = \frac{\bar{d}_d}{t} = \frac{\sqrt{2Dt}}{t} \qquad \text{(Eq. 3.5)}$$

Where *D* ($cm^2 \cdot s^{-1}$) is the diffusion coefficient. Taking t=1 s and the diffusion coefficient of a free proton as D_{H^+}=9.31 × 10^{-5} $cm^2 \cdot s^{-1}$,[213] we calculated the diffusion velocity to be approximately 2.2 $\mu m \cdot s^{-1}$ or 8 $mm \cdot h^{-1}$. Using the equations above, Table 3.1 summarized results for three flow rates used in the main paper.

Table 3.1 Velocities by convection and diffusion (of H^+) and shear stress based on typical flow conditions used in this study.

Q ($mL \cdot h^{-1}$)	$\bar{v}_{d^{H^+}}$ (constant) ($mm \cdot h^{-1}$)	$\bar{v}_c$ ($mm \cdot h^{-1}$)	Re	$\bar{\tau}$ (mPa)
0.2	8	250	0.028	1.04
1		1250	0.139	5.21
5		6250	0.693	26

As seen from Table 3.1, upstream diffusion of H^+ was calculated to be between 30 and 780 times slower than convection. In reality, the convection to diffusion ratio should be even higher, since effective proton diffusivity is lower inside the biofilm and for other chemical by-products. Periodic measurements of the nutrient solution pH (pH_s in the main paper) flowing into the device was 7.5 ± 0.1 throughout the experiment. Following experiments, scanning electron microscopy (SEM) was used to verify that bacterial growth did not occur on the RE, where electrode respiration was impossible.

3.8.3 Reference electrode calibration

A *G. sulfurreducens* biofilm was grown on graphite WE under 10 mM acetate nutrient solution in a bulk electrochemical cell at 0 V versus Ag/AgCl for 120 h. Then we added two Au REs, one which was clean and unused, and another that was extracted from a device which was used in a previous experiment (15 day duration). We were careful not to crack or otherwise damage the used Au RE during the extraction from the microfluidic device. Next CV was acquired (Figure 3.6) using the three REs: (i) Ag/AgCl (red), (ii) new Au (black) and (iii) the used Au RE (blue dashed). Comparing the raw results in Figure 3.6a the two curves for the Au RE electrodes were nearly the same. A closer look at the first derivative in (Figure 3.6b) showed that ΔE for cytochrome c groups in *G. sulfurreducens* between Ag/AgCl and a clean Au RE in our medium solution and condition was approximately 410 mV and 396 mV for the used Au RE. Similar experiments conducted with different clean Au RE usually resulted in a variation of approximately ±10 mV between separate devices. Thus, the difference of 14 mV may indicate a slight shift in the RE potential after use. Nevertheless, it is worth mentioning that a typical experiment consisting of cycling flow rates is normally completed in less than an hour. Therefore, any shifts in the RE potential over this time scale would likely have be unmeasurable.

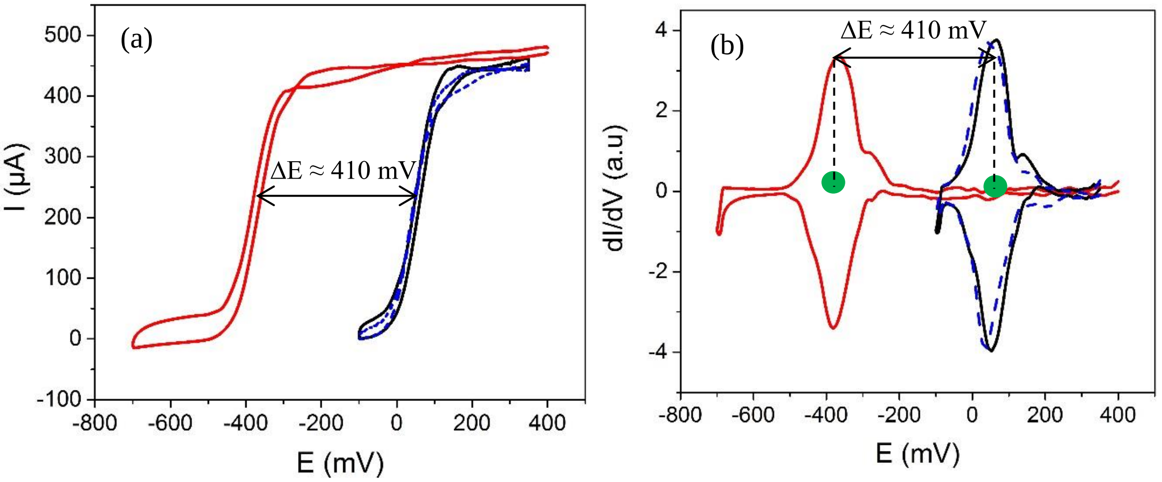

Figure 3.6 (a) CVs bulk experiments in 10 mM Ac with Ag/AgCl, 3M KCl (red), a clean Au RE (black), and a Au RE after being used for a 15 day G. sulfurreducens biofilm experiment (blue). **(b)** First derivative of bulk experiment CVs, which green circles marking the formal potential for the Ag/AgCl and clean Au RE. In each case a shift of E ≈ 410 mV was observed when using different REs. Therefore, E_f (vs. Ag/AgCl) = E_f (vs. clean Au) – 410 mV and -396 for the used Au RE.

3.8.4 Stability of formal potential under long durations and different flow rates

To verify stability of the electrochemical flow cell, formal potential of ferricyanide was measured for 2 weeks. During this time no obvious formal potential change was seen (Figure 3.7 a). We also used ferricyanide solution (10 mM added to a nutrient medium) to verify that formal potentials did not change with flow rate if the concentration of H^+ was not tied to the redox reaction. As explained in the main paper, the potassium ferricyanide was added to the same nutrient medium used in the rest of the work to ensure that ions and support molecules were present during the test. As seen in Figure 3.7 b, changing flow rate did not result in any changes in to formal potential of ferri/ferro redox couples, even at 10 mL·h^{-1}, which was higher than flow rates were used in biofilm measurement. The changes in CV shape match those predictions in the literature.[214] These experiments complement the ones conducted on metabolically inactive biofilms, which also showed no change in formal potential when flow rate was changed (main paper). These experiment can confirm functionality and stability of RE and device performance at different flow rate and long-term experiment. In addition, an experimental proof for flow rate independency of electrochemical formal potential in a pH-independent redox reaction of cytochrome c groups in the biofilm after reaching complete metabolic inactivity is also given in the main paper (Figure 3.2 c).

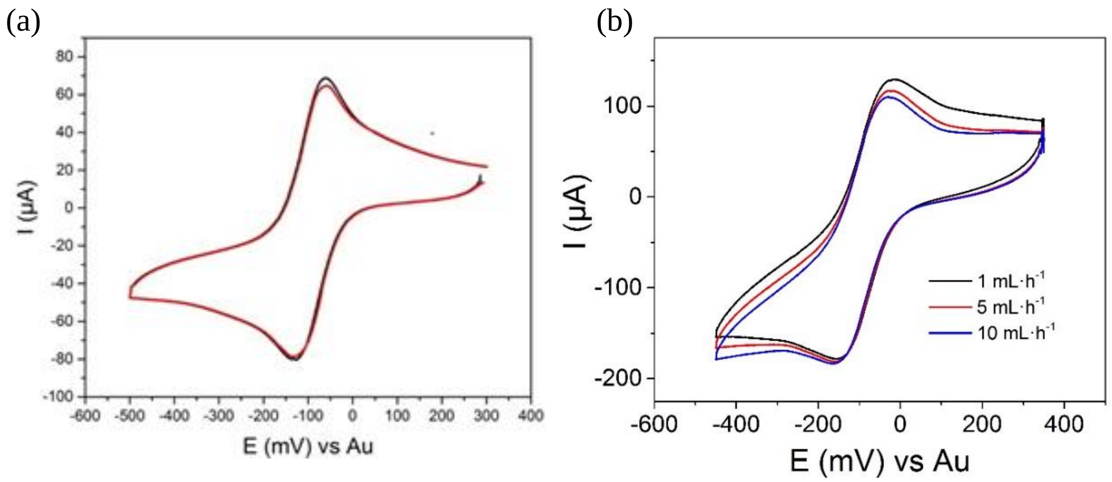

Figure 3.7 (a) Stability of the reference electrode measured by CV of ferricyanide in bacterial medium solution at time t=0 (black) and t=2 week (red). **(b)** Formal potential stability in flow for pH-independent redox reactions of 10 mM ferricyanide.

3.8.5 Set up of electrochemical microfluidic device and anaerobic container

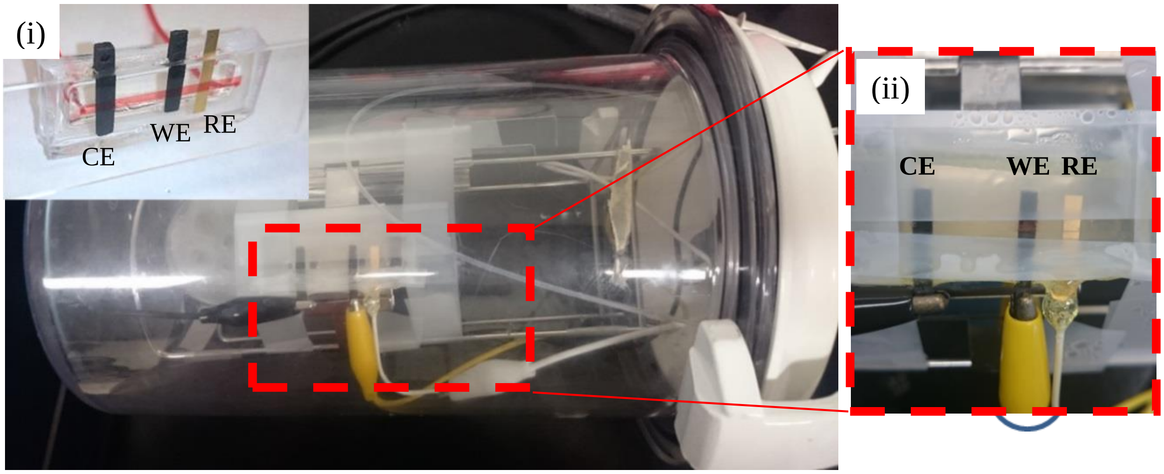

Figure 3.8 A three-electrode microfluidic device contained within the anaerobic enclosure with electrical, fluidic and gas connections via feedthroughs in the cap. Insets (i) and (ii) show the microfluidic device outside of the enclosure with red dye to show the channel relative to electrodes and (ii) inside the enclosure during the experiment, respectively. Small discolouration at the WE in inset (ii) is the accumulation of G. sulfurreducens (circled in blue).

3.8.6 Effect of starvation and nutrient-limited conditions

In this work the biofilms were exposed to either turnover concentrations ([Ac] = 10 mM), nutrient-limited concentrations ([Ac] = 0.3 mM) and starvation conditions ([Ac] = 0 mM). Depending on the time of exposure to certain concentrations, the biofilm metabolic state would change, which had effects on CA and CV measurements. In an equilibrium state under turnover conditions, biofilms would produce relatively high current, which could be modulated by flow rate. However, their E_f was only very weakly dependant on flow rate. In an equilibrium state under nutrient-limited concentrations, biofilm activity was reduced (as measured by reduced current output) and the E_f was highly sensitive to flow rate. We posit that sensitivity to flow rate is another indication that the biofilm was weakly active, because the H^+ production rate (proportional to current) was low enough to be modulated by flow.

This behaviour could be maintained indefinitely. Another indication that the biofilm was still somewhat active during exposure to nutrient-limited concentrations, ($[Ac]_{ltd}$ = 0.3 mM), was that return to turnover current occurred in just 5 minutes (e.g. green arrow in Figure 3.9 a), independent of the time of exposure to nutrient limited conditions. The biofilm behaviour under starvation conditions was more complex. Initially, biofilm activity, as measured by current, would be reduced, but still above the background. In this regime, E_f was sensitive to flow and return to turnover current was rapid (Figure 3.9 a). That is to say that the biofilm behaviour mirrored that of a biofilm exposed to nutrient-limited conditions. However, after long-term exposure to [Ac] = 0 mM, current reduced to background levels and the E_f were not modulated by flow rate, while the redox peaks became reduced in height (Figure 3.9 b). This is consistent with the loss of cytochrome c, likely due to biofilm degradation and cell death. Lastly, the difference in time to return to turnover conditions was much longer (> 1 day), likely due to a regrowth process to replace lost bacteria, as opposed to a reactivation process of existing low-activity bacteria.

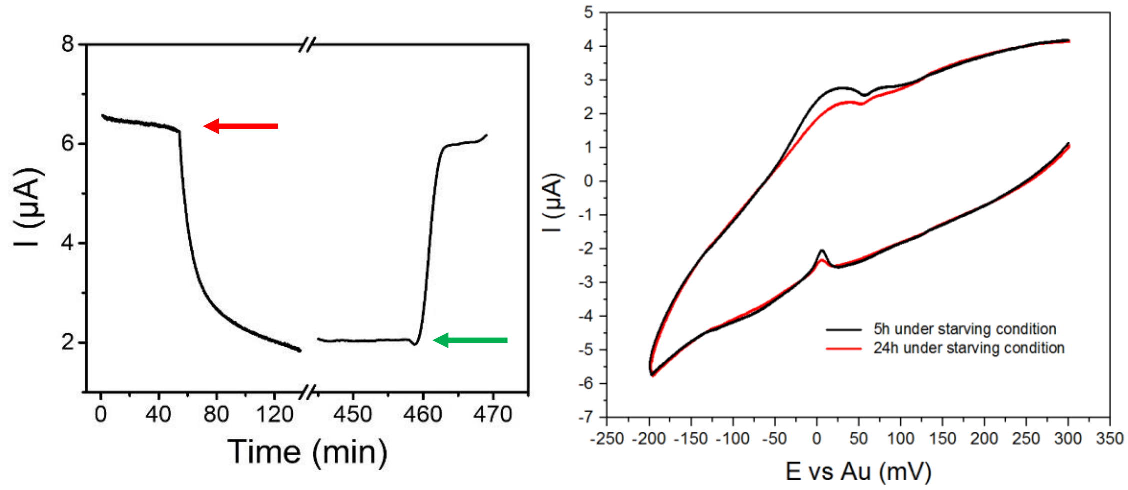

Figure 3.9 (a) Results from a separate experiment during switching from 10 to 0.3 mM acetate (red arrow). Resumption of 10 mM acetate conditions occurred at 460 min (green arrow) after CV measurements. **(b)** CV after subjecting samples to 5 h and 24 h of starvation ([Ac] = 0 mM) (1 $mV \cdot s^{-1}$ scan rate). In (a) t=0 h corresponds to biofilm age of 220 h. Flow rates were Q=0.2 $mL \cdot h^{-1}$ in both (a) and (b).

3.8.7 Biofilm activity and electric current for different [Ac] and Q

As discussed in the main paper, electric current (I) can be reversibly modulated by changes to volumetric flow rate (Q). To investigate the effect of Q on I for different concentrations used in this study, we subjected mature biofilms to Q between 0.2 mL·h^{-1} and 1 mL·h^{-1} at turnover, nutrient-limited and starvation conditions ([Ac] = 10, [Ac] = 0.3 and [Ac] = 0 mM, respectively). Figure 3.9 shows the results. At turnover concentrations cycling Q between Q = 0.2 and Q = 1 mL·h^{-1} resulted in large changes in current (approximately 7 µA). Cycling between the same flow rates at 0.3 mM acetate resulted in (only) slightly lower changes to current (5 µA). Thus, despite the approximately 30 times lower concentration, only a modest drop in ΔI was observed. Taken as a percentage of I at the slow flow rate (I_0), the $\Delta I/I_0$ was actually higher for nutrient-limited solutions (≈0.67) compared turnover conditions (0.27). We tentatively conclude that the reduction in biofilm acidity under increased flow rates of nutrient-limited solution may have contributed to biofilm electrocatalytic efficiency, over and above nutrient flux enhancements.

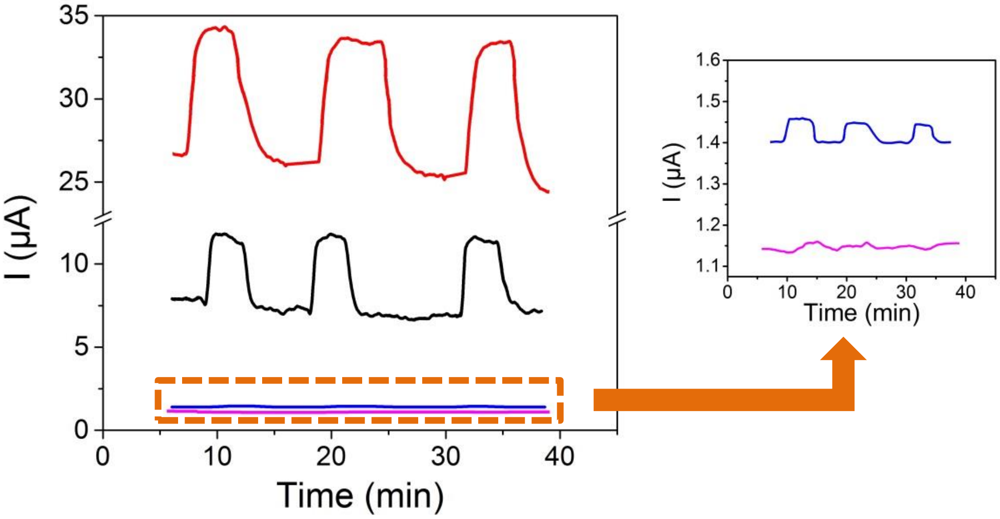

Figure 3.10 Flow rate effects on mature biofilm at 0.2 mL·h^{-1} (orange arrow) and 1 mL·h^{-1} (green arrow) for [Ac] = 10 mM (red curve) and [Ac] = 0.3 mM (black curve). Application of [Ac] = 0 mM with exposure time of 6 h (blue curve) and 24 h (pink curve) with 0.2 mL·h^{-1} flow rate.

Upon changing to an acetate-free solution (0 mM acetate), I became strongly diminished, but was still above the background value. Cycling Q still led to small and reversible changes to I during the first 5 h, following the switch to 0 mM acetate. However, after 24 h under starvation conditions, the current became non-responsive to flow (Figure 3.10 inset). This supports the observation made in the main paper that pH can change during flow cycling under starvation conditions, but only temporarily.

3.8.8 SEM Imaging

Figure 3.11 shows a close up on the same biofilm, such that individual bacteria are seen. From this image, it can be seen that the biofilm is comprised of cells, which are not surrounded by an obvious extracellular matrix. We note that the biofilm thickness varied between approximately 200 µm at the downstream edge of the electrode (Figure 3.1 b) to less than 60 µm at upstream positions (Figure 3.11 b).

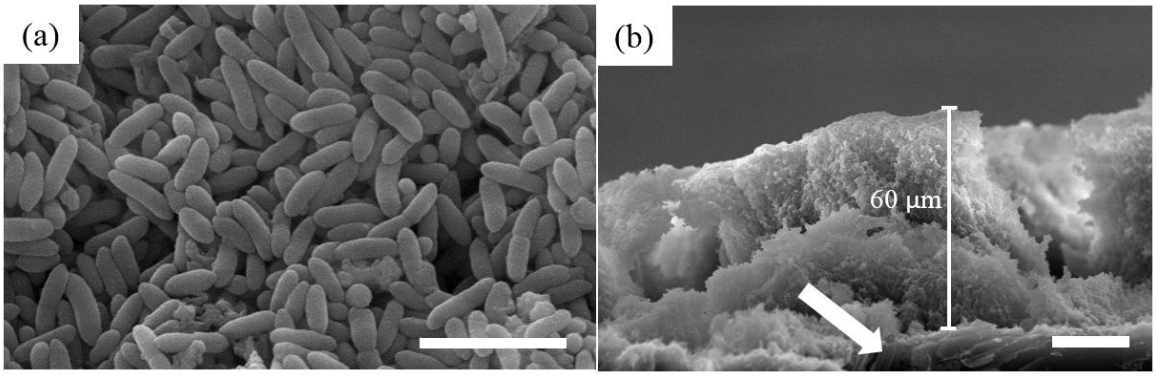

Figure 3.11 (a) Zoomed view of Figure 1a in main paper of G. sulfurreducens adhered to the WE via SEM using 30 keV, 3000× (scale bar 10 µm). **(b)** Side-view at an upstream position of the same biofilm shown in main paper Figure 3.1 b. Scale bar is 20 µm, arrow points to exposed graphite electrode at the biofilm base. The measurement of a 60 µm thick biofilm is shown.

Chapter 4. Toggling *Geobacter sulfurreducens* metabolic state reveals hidden behaviour and expanded applicability to sustainable energy applications

Mir pouyan Zarabadi[1], Steve J. Charette[2,3,4], Jesse Greener[,1]*

[1]Département de Chimie, Faculté des sciences et de génie, Université Laval, Québec City, QC, Canada.

[2]Institut de Biologie Intégrative et des Systèmes, Pavillon Charles-Eugène-Marchand, Université Laval, Québec City, QC, Canada.

[3]Centre de recherche de l'Institut universitaire de cardiologie et de pneumologie de Québec, Québec City, QC, Canada.

[4]Département de biochimie, de microbiologie et de bio-informatique, Faculté des sciences et de génie, Université Laval, Québec City, QC, Canada.

Accepted manuscript online on 01 May 2019. Modifications on the numbering of the figures of the paper have been done in order to fit the sequence of the dissertation.

Published in *Sustainable Energy & Fuels,* **2019**, DOI: 10.1039/C9SE00026G.

4.1 Résumé

Les biofilms électroactifs font l’objet d’un examen minutieux en raison de leur potentiel à permettre la mise au point de nouvelles technologies durables pour la production d’énergie et la biorestauration. Cependant, une activité métabolique fortement réduite à de faibles concentrations de nutriments constitue un obstacle à leur mise en œuvre. Une approche microfluidique a été utilisée pour des expériences de respiration en temps réel sur un biofilm de la bactérie *Geobacter sulfurreducens* afin de surmonter ces contraintes. Des changements précis dans les conditions de la solution ont permis une commutation rapide et réversible entre les états métaboliques du biofilm, ce qui a conduit aux découvertes suivantes. (i) Les réacteurs à écoulement peuvent maintenir l'activité du biofilm à des concentrations aussi faibles que 15 µM d’acétate; (ii) un état métabolique «pseudo-actif» sépare les états actif et inactif; et (iii) la conversion de l’acétate peut atteindre 90% pour les biofilms actifs au seuil de la pseudo-activité.

4.2 Abstract

Electroactive biofilms are under intense scrutiny due to their potential to enable new sustainable technologies for energy production and bioremediation. However, severely reduced metabolic activity at low concentrations is a barrier to their implementation. A microfluidic approach was used for real-time respiration experiments on a *Geobacter sulfurreducens* biofilm to overcome these constraints. Precise changes to solution conditions enabled rapid and reversible switching between biofilm metabolic states, leading to the following discoveries. (i) Flow reactors can maintain biofilm activity at concentrations as low as 15 µM; (ii) a “pseudo-active” metabolic state separates active and inactive states; and (iii) acetate conversion can be as high as 90 percent for active biofilms at the pseudo-activity threshold.

4.3 Introduction

Electroactive biofilms (EABs) have the potential to accelerate the development of new sustainable processes including the conversion of waste water to electricity.[215] [216] In addition EABs have been demonstrated for synthesis of chemical compounds and nanomaterials[217,218] and environmental remediation.[219] Moreover, new work is underway to understand and optimise their coupling with other microorganisms to expand functionality, via direct interspecies electron transfer.[217,220] EABs from *Geobacter sulfurreducens* are among the most studied because after the oxidation of an acetate molecule, electrons are efficiently conducted to external electron acceptors, such as an electrode via a direct externally electron transfer mechanism.[220,221] In studies using a microbial fuel cell (MFC) or a microbial electrolysis cell (MEC), the liquid phase typically contains high concentration of organic molecules, well in excess of 120 $mg \cdot L^{-1}$ (equivalent to 2 mM acetate). In contrast, far fewer studies have focused specifically on *Geobacter* performance at low concentrations, such as those occurring in selected natural environments where these organisms are found.[222,223] Recently, the importance of the low-concentration regime has been highlighted by a practical limitation that strongly reduces EAB current in MFCs at chemical oxygen demand (COD) levels between 100 to 200 $mg \cdot L^{-1}$ and outright at 50 $mg \cdot L^{-1}$.[224,212] The reason for this loss of activation is not known, but the impact is clear. In addition to poor performance at low concentrations, subsequent processing steps will be required to reduce final concentrations down to environmental discharge limits, adding another hurdle to implementation and increasing complexity.[225]

In the 1940's, Monod and others studied the effect of external influences such as nutrient concentrations on bacterial growth and metabolic activity.[226] Forty years later, detailed studies into nutrient mass transfer into biofilms and their effects on metabolism were conducted.[227] However, the difficulty in obtaining sufficient control over reaction parameters continues to limit studies of biofilm metabolic activity at low concentrations. For example, in bulk electrochemical cells, solution concentration continuously changes as acetate is oxidised and by-products are produced. To avoid concentration cycling, flow systems can be used to provide a continuous nutrient supply. Hydrodynamic conditions are also known to impact molecular transport via their effect on diffusion barriers around the EAB[228] and potentially from forced convection through voids, cavities and channel structures, as noted previously in non-electroactive biofilms.[229,206-210] It also appears that molecular transport into the highly active biofilm regions near the electrode surface plays a significant role under low-concentration conditions.[230] Taken together, well-controlled flow systems have a great potential for discovery and optimisation of EABs at low concentrations. A centimetre-scale flow system demonstrated the potential for studies of current generation at low concentrations.[231] However, dead volumes would limit response time and its demonstrated control in the range of 0 to 2.3 mM acetate is needed for the present study. Millifluidic systems can be easily constructed using standard machining techniques or even with standard flexible tubing. For example, respirometric studies of *Pseudomonas* biofilms using gas-permeable silicon tubing and a CO_2 detection system[232,233,234,235,236,237] could in principle be adapted for electrode-adhered anaerobic EABs, but the integration of electrodes within the tubing interior and the requirement of an oxygen-purged environment would present difficult challenges. Millifluidic systems and larger must also balance between reasonable solution volumes and limitations to attainable flow velocities or applied shear stresses. Alternatively, microfluidic approaches combine the advantages of low material consumption over a large range of applied hydrodynamic conditions, established methods for electrode integration and high control of chemical concentrations via on-chip dilution,[238,239] microvalves,[240] and formation of concentration gradients.[241] Increasingly, microfluidic flow cells are recognised as viable platforms for precision bioanalytical chemistry-based studies of biofilms, including hydrodynamic voltammetry.[99] For example, our group recently developed a robust three-electrode microfluidic flow cell for electrochemical measurements of bacterial biofilms from *Pseudomonas*[203] and *Geobacter* species.[242] Such a platform combines the benefits of direct and continuous measurements of bacterial metabolism[99] with standard microfluidic advantages such as unsurpassed control over solution-phase hydrodynamic and chemical properties, as well as low liquid consumption.[243] In addition, complex multi-step experimental sequences can be devised with vanishingly low latency, thus enabling more precise and rapid studies of microbiological systems than ever before.[244,245,246]

4.4 Results and discussion

In this work, we used a microfluidic three-electrode electrochemical flow cell to measure the current from *G.sulfurreducens* EABs via chronoamperometry, while low acetate concentrations were applied at well-defined flow rates. Using this setup, we identified threshold conditions that separated active, pseudo-active and inactive metabolic states. Moreover, these thresholds were dependent on flow rate. Figure 4.1a shows the schematic of the microfluidic system. The PCA strain of *G. sulfurreducens* was inoculated into the microchannel for 3 h with a 0.5 $mL\cdot h^{-1}$ flow rate. A three-way liquid mixer was placed between the microchannel inlet and three different air-tight glass syringes containing acetate concentrations of $[Ac]_1 = 10$, $[Ac]_2 = 0.2$ and $[Ac]_3 = 0$ mM. With the use of one-way stopcock valves at the inlet side of mixer inlets 1-3 (MI_1, MI_2, MI_3) and flow control via the syringe pumps, the final nutrient concentration could be determined from real-time dilutions in the range of 10 to 0 mM based on the formula:

$$[Ac] = ([Ac]_1 \times Q_1 + [Ac]_2 \times Q_2 + [Ac]_3 \times Q_3)/Q \qquad \text{(Eq. 4.1)}$$

where the total flow rate is given by $Q = Q_1 + Q_2 + Q_3$. Thus the average liquid velocity within the channel could be calculated from $v = Q/A$, where A is the channel cross-sectional area based on the channel height (h = 400 µm) and width (w = 2 mm). In this manner, rapid and precise changes in both [Ac] and Q could be generated on demand within a matter of seconds and maintained for durations ranging from seconds to tens of hours. After passing from the mixer to the microchannel, the liquid first flowed past a gold (pseudo) reference electrode (RE), followed by a graphite working electrode (WE), and finally a counter electrode

(CE). The surface area of all electrodes exposed to the liquid solution was 3 mm × 2 mm.

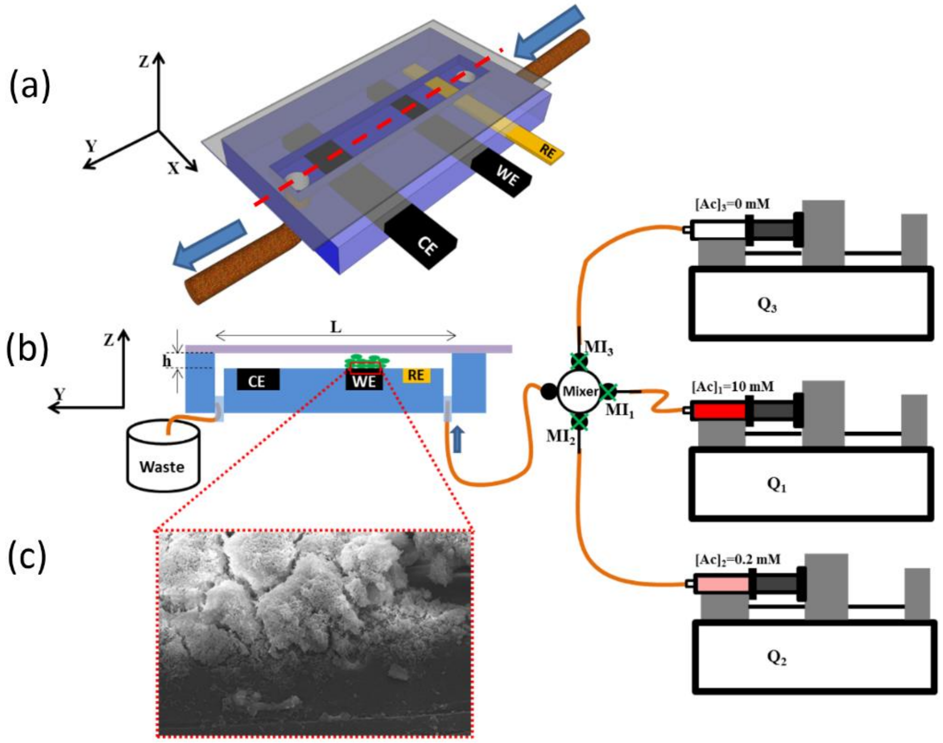

Figure 4.1 Experimental setup. (**a**) Three-dimensional schematic of a microfluidic electrochemical flow cell showing a gold reference electrode (RE) and graphite working and counter electrodes (WE, CE). Height, width and length were h = 400 µm, w=2000 µm and L = 3 cm, respectively. The exposed working electrode to the channel had the same width as the channel, and extended for 3000 µm along the channel length. The dashed line shows the position of the cross-section for (b). (**b**) 2D schematic of device cross-section (y-z plane), with three syringe pumps holding gas-tight syringes containing acetate nutrient solutions of 0, 0.2 and 10 mM. The outlet of each syringe was connected to one inlet of a mixing element via a one-way stopcock valve. The mixer outlet was connected to the device inlet. The inoculum syringe is not shown. (**c**) SEM image of G. sulfurreducens biofilm (>1000 h age) on the working graphite electrode following the experiments described in this work. All experiments were conducted at 22 °C.

Additional information on design and fabrication of the three-electrode microfluidic device can be found in our previous work[203,242] and in the Supporting Information. Because the electroactive *G. sulfurreducens* bacteria must externally transfer electrons to complete the tricarboxylic acid metabolic cycle,[248,53] their growth was strictly limited to the WE (Figure 4.1), where biofilm growth and acetate turnover rate was monitored directly via chronoamperometry. Placement of the RE in the upstream position ensured that by-products could not diffuse upstream with speed sufficient to overcome the downstream flow velocity (Section 4.6.1). Thus, contamination of the RE environment was stable for the duration of the experiment, as demonstrated previously.[99,203,242] The electric current is related to the overall biofilm metabolism based on the fact that oxidation of one mole of acetate ($\mathrm{mol_{Ac}}$) produces 8 moles of free electrons ($\mathrm{mol_e}$).[248,59] Therefore, the current, I ($\mathrm{C \cdot s^{-1}}$), can be converted to the acetate turnover rate, $\frac{\mathrm{dmol}_{Ac}}{\mathrm{dt}}$ ($\mathrm{mol_{Ac} \cdot s^{-1}}$), based on Equation 4.2:

$$\frac{\mathrm{dmol}_{Ac}}{\mathrm{dt}} = \frac{I}{8.F} \qquad \text{(Eq. 4.2)}$$

where F is Faraday's constant, $F = 9.6485 \times 10^4\ \mathrm{C \cdot mol_e^{-1}}$ and 8 is the proportionality constant for moles of electrons produced to moles of acetate oxidised. The combination of real-time control over [Ac] and Q together with instantaneous measurement of the acetate turnover rate presents a simple but powerful approach to study changes in EAB metabolism. In the remainder of this paper, we quantified the EAB metabolic activity via electric current.[247]

As shown in the Figure 4.1a, after channel inoculation and growth for approximately 300 h at [Ac] = 10 mM, the current reached 37.5 ± 0.75 µA (6.16 ± 0.12 $\mathrm{A \cdot m^{-2}}$). After this time, the current produced by the biofilm supplied with a nutrient medium of [Ac] = 10 mM at Q = 0.25 $\mathrm{mL \cdot h^{-1}}$ remained the same until the very end of the experiment, immediately before decommission of the flow cell. Therefore, we deduced that after 300 h the biofilm was mature and its thickness was constant.[248,249,250] SEM measurements of the biofilm at the end of the experiment showed that the biofilm had an average height of 80 µm. This resulted in a constriction in the flow channel, resulting in an average headspace above the biofilm of 320 µm. After verifying that the current was stable for another 210 h, the experiments were started.

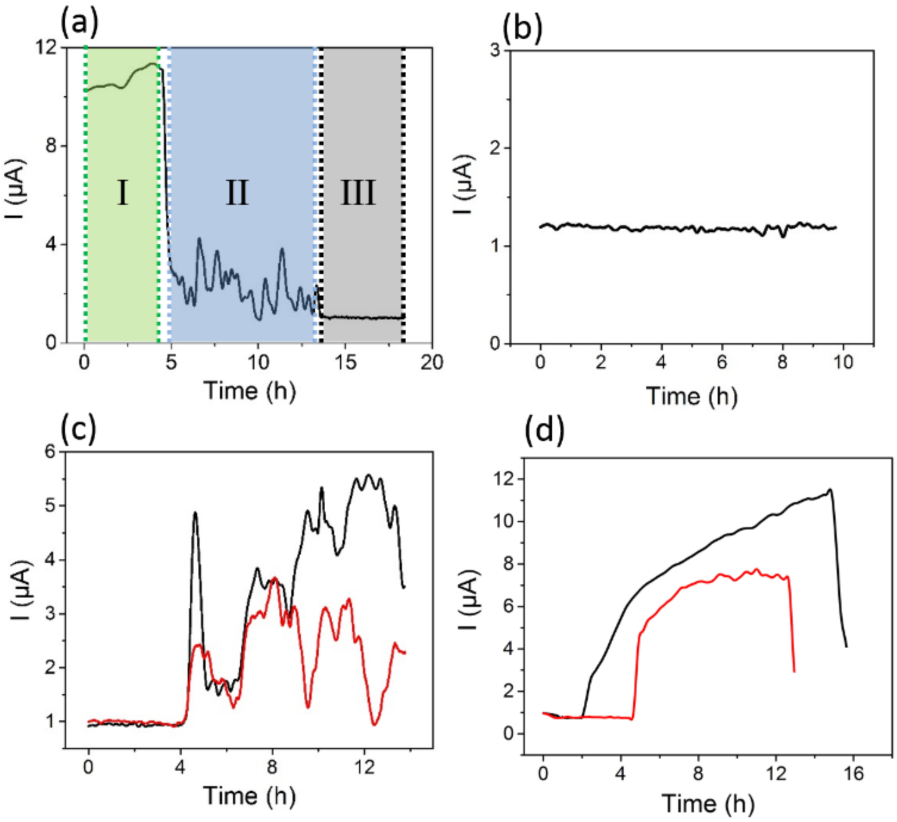

Figure 4.2 The effect of flow and nutrient concentration on current output of a fully mature G. sulfurreducens biofilm. (**a**) Current profiles due to changes in [Ac]. Region I shows an active biofilm exposed to [Ac] = 200 µM (green). Region II shows a pseudo-active biofilm with exposure to [Ac] = 140 µM acetate (blue). Region (III) shows an inactive biofilm after exposure to [Ac] = 80 µM (grey). In all cases, Q_T = 0.5 mL·h^{-1}. (**b**) Current recorded during increases to acetate concentration by 10 µM increments below $[Ac]_{PA}$. Flow rate was Q_T = 0.5 mL·h^{-1}. (**c**) Current output following two separate transitions from inactivity (at [Ac] = 0) to pseudo-activity via $[Ac]_{PA}$ = 160 µM with Q_T = 0.25 mL·h^{-1} (black curve) and $[Ac]_{PA}$ = 30 µM acetate at Q_T = 1 mL·h^{-1} (red curve). (**d**) Current output following two separate transitions from inactivity to full activity via $[Ac]_A$ = 200 µM acetate with 0.25 mL·h-1 flow rate (black line) and $[Ac]_A$ = 40 µM acetate with Q_T = 1 mL·h^{-1} flow rate (red line). Reduction in current in both data was the result of a switch to [Ac] = 0 M.

To test the response of a fully mature biofilm to different degrees of nutrient limitation, we switched the system to low-concentration mode by closing valve MI_1 and opening valves MI_2 and MI_3. In this step, we varied [Ac] between 0 and 0.2 mM

(200 µM) while maintaining Q = 0.25 mL·h^{-1} based on a simplified form of Eq. 4.1: $[Ac] = ([Ac]_2 \times Q_2 + [Ac]_3 \times Q_3)/Q$. The upper limit of 200 µM was chosen based on the lowest concentration which could maintain full EAB activity at the lowest flow rate used in this study (0.25 mL·h^{-1}). Switching to [Ac] = 200 µM resulted in an immediate reduction in current, which continued for nearly 1 h until a steady-state value of approximately 10 µA (1.67 A·m^{-2}) was reached (Figure 4.5b). Subsequently, we reduced [Ac] in a stepwise manner from 200 to 140 µM and eventually to 80 µM. As shown in Figure 4.2a, dropping the concentration to [Ac] = 140 µM resulted in an approximately 4 µA within the first few minutes. Unlike in other studies where current decreased monotonically to zero after applying zero concentration nutrient solutions,[242,251] or where a new lag phase was induced after a switching acetate for a complex carbon source,[252] the switch to the low, but non-zero acetate concentrations used here, induced a fluctuating current (region II). The fluctuating state could be maintained for up to 40 hours, as long as very low, but non-zero concentrations were applied (Figure 4.6c). Based on the power spectrum from a fast Fourier transform analysis of the time series data, the frequency component contributing to these oscillations could be as high as 2 h^{-1}. This is equivalent to periodicity of 30 mins. Thus, according to the Nyquist sampling theorem, the wave form was properly represented by the sampling rate which was 1/30 s (section 4.6.7). In contrast, the current profiles recorded during operation at nutrient concentrations at or above [Ac] = 200 µM featured nearly unobservable fluctuations in EAB current intensity and high frequency components that were 40 times slower than those in region II. Section 4.6.7 contains more information on the stark differences in current profiles between regions I and II. Switching to [Ac] = 80 µM while maintaining Q = 0.25 mL·h^{-1} resulted in a current reduction to a stable, non-fluctuating value of nearly 1 µA (region III), which matched the background current measured separately for the same setup. Further reduction of [Ac] had no effect on electrical current, indicating that the background current had indeed been achieved in the last step. Therefore, three distinct metabolic activity states could be selected based on [Ac] and from the EAB current

profiles: an active state (I), a pseudo-active state (II), and an inactive state (III) (Figure 4.2a).

Taking advantage of the ability to impose rapid, accurate changes in experimental conditions, an iterative screening procedure was developed to determine the exact transition concentrations that separated activity states I, II and III. This was accomplished via the application different [Ac] pulses while maintaining a constant Q. Specifically, in each iteration, concentration was cycled between [Ac] = 0 and an elevated concentration $[Ac]_i$ (where the subscript i is an index value for each iteration) until the EAB current increased above the background. The increase in concentration from one pulse to the next was $[Ac]_{i+1} - [Ac]_i = 10\ \mu M$. At concentrations too low to provoke a change from the metabolically inactive state, no deviation from the background current was observed (Figure 4.2b). In separate experiments, it was verified that the inactive state could be maintained for at least 20 h at such low, but non-zero concentrations (data not shown). With continued stepwise increases in $[Ac]_i$, a threshold concentration $[Ac]_{PA}$ was identified that resulted in the transition to the pseudo-active state. This transition was marked by an increase in current from background levels to the same fluctuating state observed in region II of Figure 4.2a. Continued increases to $[Ac]_i$ during subsequent iterations resulted in similar transitions to pseudo-activity until eventually, a new transition behaviour occurred in which the increase in current from background was smooth and asymptotically approached a maximum current I_{max}. At and above this concentration, the biofilm could achieve continuous metabolic activity, thus defining a second concentration threshold for fully active EABs, $[Ac]_A$.

As flow is known to affect the performance of *G. Sulfurreducens*,[248,129] measurements of $[Ac]_{PA}$ and $[Ac]_A$ were repeated in triplicate at 5 different total flow rates in the range of Q = 0.25 to 1.5 $mL \cdot h^{-1}$. This corresponded to flow velocities of approximately v = 5 to v = 30 $mm \cdot min^{-1}$ and τ = 1.2 to 7 mPa (see section 4.6.2, Table 4.1 for more information). Figures 4.2c and 4.2d show typical transitions following a switch from [Ac] = 0 to $[Ac]_{PA}$ and to $[Ac]_A$, respectively. In all cases, the threshold concentrations decreased as Q increased. Due to the unsteady nature of the pseudo-active metabolic state, we could not confirm whether the flow rate affected the current output profile after transitions from [Ac] = 0 µM to $[Ac]_{PA}$ (Figure 4.2c). However, as observed in Figure 4.2d, transitions from [Ac] = 0 to $[Ac]_A$ at different values of Q did showed differences in the current rise time and I_{max}. Specifically, for low $[Ac]_A$ at high Q, the rise time was short and I_{max} was low, whereas for higher $[Ac]_A$ at low Q, the rise time was slow, but I_{max} was larger. Increasing Q at any given $[Ac]_A$ resulted in shorter rise times and higher I_{max}. Thus Q appeared to control the rise time, whereas [Ac] and Q both affected I_{max}.

Figure 4.3 summarises the results from the experiments described above. In this case, three distinct biofilm metabolic activity states were separated by threshold concentrations $[Ac]_{PA}$ and $[Ac]_A$. Both threshold concentrations were reduced with increasing Q, with good repeatability in their measured values. To the best of our knowledge, the pseudo-active metabolic state separating the active and inactive states has never been observed before. Another major observation is that increasing Q can maintain metabolic activity at much lower [Ac] than in bulk conditions, paving the way for exploration of simple flow-based techniques to reduce the previously observed lower concentration limits. For example, the previously reported loss of EAB activity at nutrient concentrations of approximately 50 $mg \cdot L^{-1}$ COD (equivalent to 0.83 mM acetate)[212] is 30 and 55 higher than measured thresholds $[Ac]_A$ and $[Ac]_{PA}$ at high flow rate. It is noted that an exponential extrapolation of our results to static conditions ($Q = 0\ mL \cdot h^{-1}$) does predict $[Ac]_{PA}$ near 0.8 mM, confirming the pertinence of this work to previous studies. We also noted that the present measurements were conducted via chronoamperometry, which applies a constant potential throughout the experiment. This rules out a reduction in electrostatic-driven diffusion as the mechanism responsible for the loss of biofilm activity, which was proposed as a possible explanation for threshold concentrations in bulk microbial fuel cells.[212]

To better understand the role of flow in determining the loss of full metabolic activity, we converted the threshold concentration $[Ac]_A$ and the corresponding flow conditions to the threshold convective acetate flux through the channel:

$$J_A = [Ac]_A \times v_A \qquad \text{(Eq. 4.3)}$$

where v_A is the corresponding linear flow velocity to a specific $[Ac]_A$ value. As shown in the inset plot in Figure 4.3, J_A is nearly constant at 15.6 pmol·s^{-1}·mm^{-2} for all flow velocities.

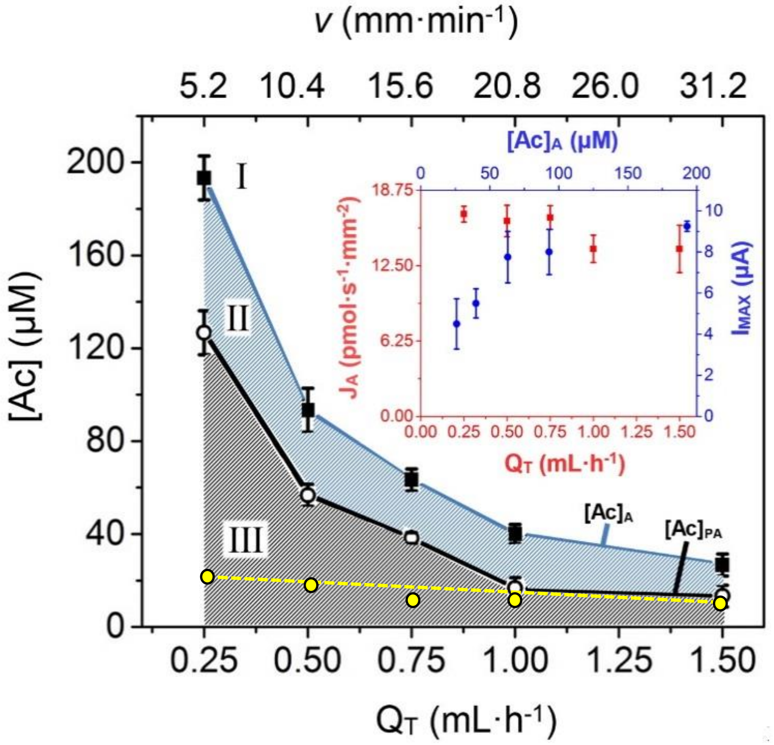

Figure 4.3 Dependency of concentration thresholds $[Ac]_{PA}$ (hollow circles) and $[Ac]_A$ (solid squares) on Q_T and equivalent flow velocity (v_A) for a fully mature biofilm from G. sulfurreducens bacteria. The upper portion of the plot labelled I (white) indicates [Ac], Q_T conditions resulting in active biofilms. The intermediate band labelled II (blue crosshatch) indicates [Ac], Q_T conditions resulting in pseudo-active biofilms. And the lower region of the plot labelled III (black crosshatch) indicated [Ac], Q_T conditions cause biofilm inactivity. Yellow circles and the respective trend line (dashed) are the calculated $[Ac]_f$ following acetate consumption at the WE. Error bars were not added as they were smaller than the data points. Inset: Nutrient flux threshold, J_A (pmol·s^{-1}), as a function of Q_T (red) and maximum current output, I_{max} (µA), as a function of $[Ac]_A$ (blue). Error bars for all points were generated from three separate experiments at the same flow rate.

Therefore, it is concluded that J_A is the influential parameter in determining the metabolic activity state and not independent values of [Ac] or v. We note that the range in the calculated velocity values in Figure 4.3 apply to an empty channel. However, both EAB and non-electroactive biofilm thicknesses are known to increase under imposed fluid flow shear, which could affect local flow velocity.[253,254] According to the SEM results discussed earlier, the reduced head space above the EAB, resulted in local velocities impinging on the upstream side of the biofilm being 18.7 $\mathrm{pmol \cdot s^{-1} \cdot mm^{-2}}$. Unlike J_A, it was noted that I_{max} was not constant over all v_A values. As observed in the Figure 4.3 inset, I_{max} increased with increasing $[Ac]_A$ (and lower v_A), similar to the observation related to Figure 4.2d. This is consistent with the expectation that solution-phase nutrient molecules should diffuse more rapidly into the EAB at high [Ac] because of higher concentration gradients between the bulk liquid and the depletion layer near the EAB surface.

The final acetate concentration, $[Ac]_f$, after catalytic oxidation by EABs is an important performance measure for MFCs and other bioelectrochemical systems for environmental remediation. Following liquid contact with the EAB, $[Ac]_f$ was determined for different initial acetate concentrations, $[Ac]_0$, and flow rates using Equation 4.4. Acetate conversion efficiency, ε_{Ac}, was determined by Eq. 4.5.

$$[Ac]_f = [Ac]_0 - (\frac{\mathrm{dmol_{Ac}}}{\mathrm{dt}} \ / \ Q) \qquad \text{(Eq. 4.4)}$$

$$\varepsilon_{Ac} = ([Ac]_0 - [Ac]_f)/[Ac]_0 \times 100\% \qquad \text{(Eq. 4.5)}$$

Here we evaluate $[Ac]_f$ and ε_{Ac} for different $[Ac]_A$ values shown in Figure 4.3. That is, we used Eqs. 4.4 and 4.5, with $[Ac]_0 = [Ac]_A$, I_{max} values obtained from data presented in Figure 4.3 (inset). Interestingly, the results for $[Ac]_f$ are plotted in Figure 4.3 were approximately 10-20 µM for all applied threshold concentrations, $[Ac]_A$. These corresponded to ε_{Ac} in the range of 60% (at high Q) to 90% (at low Q). We do not believe that relatively low ε_{Ac} at high Q is related to reduced contact time between the biofilm and the flowing liquid, as this would not explain why $[Ac]_f$ is nearly constant with Q, even slightly decreasing as Q increased. Instead, it appears that these final concentrations are approaching a lower limit, which may be either fundamental to the biological system or related to our setup. As a comparison, we conducted experiments at higher concentrations ranging from $[Ac]_0$ = 0.3 to $[Ac]_0$ = 10 mM in the same flow rate range used previously. In this case, the calculated ε_{Ac} values were much lower (section 4.6.8). Using average EAB currents achieved during $[Ac]_0 = [Ac]_{PA}$, ε_{Ac} was also determined to also be slightly worse than for $[Ac]_0 = [Ac]_A$, though still much better than for $[Ac] > [Ac]_A$. Therefore, it is concluded that the best conversion was achieved for $[Ac]_A$. See (section 4.6.8) for further discussion on this point, including an evaluation of the role of liquid/EAB contact time on ε_{Ac}. It is worth noting that the resulting final concentrations are equivalent to 0.65-1.25 $mg \cdot L^{-1}$, which is well-below the previously mentioned regulatory limits of 30 $mg \cdot L^{-1}$. The $[Ac]_f$ leaving the device were generally lower than the lower limit for biofilm pseudo-activity ($[Ac]_{PA}$), except at the highest flow rates where the two concentration profiles began to converge. The apparent contradiction that $[Ac]_f$ can be lower than $[Ac]_{PA}$ should be considered in the context of the experiment. The threshold $[Ac]_{PA}$ was the minimum concentration required to transition an inactive biofilm to pseudo-activity. In the current case, biofilms are supplied sufficient nutrients to establish some level of metabolic activity (i.e., $[Ac]_0 \geq [Ac]_{PA}$). Therefore, the observation that $[Ac]_f$ was generally lower than $[Ac]_{PA}$ is interpreted to mean that the entire biofilm could maintain its activity state, even in the downstream positions where concentrations were reduced by continuous acetate oxidation during the liquid/biofilm contact time. This is an interesting point that should be investigated further.

The present work opens the door to fundamental questions related to low activity thresholds and excellent acetate conversion in microflow conditions. In addition to a reduction in the diffusion barriers in flowing systems, other factors might play a role. For example, new evidence of flow-based biofilm deacidification[242] or the potential for convective flow through the biofilm to deliver nutrient molecules to deeper and more electrically active portions of the EAB may also play a role.[255] The root cause leading to loss of full activity should be also be investigated, with a particular focus on the mechanism causing the curious current oscillations in the pseudo-active metabolic state. The common $[Ac]_f$ for all $[Ac]_A$ threshold values (and their corresponding flow rates) should also be investigated. Simple modifications to the setup such as highly parallel channels and electrodes with greater surface areas and longer liquid/biofilm contact times should be investigated as approaches to potentially further reduce $[Ac]_f$ and improve current generation. In doing so, the true biological lower [Ac] limit to maintain activity may also be discovered. Finally, a microfluidic MFC should be tested at low-concentrations to determine the extent to which the excellent figures of merit for a microfluidic three-electrode device transfer to other bioelectrochemical systems.

4.5 Conclusion

A microfluidic electrochemical flow cell was used to study the metabolic state of electrode-adhered *Geobacter sulfurreducens* electroactive biofilms via chronoamperometry. The real-time current response to changes in acetate concentration and solution flow rate enabled the identification of three separate metabolic states: an active state, an inactive state and a newly identified pseudo-active state. In addition, flow conditions could strongly suppress loss of metabolic activity at low concentrations. Specifically, full biofilm activity could be maintained at concentrations as low as [Ac] = 25 µM, while pseudo-activity was maintained at concentrations as low as [Ac] = 15 µM with flow rates of 1.5 $mL \cdot h^{-1}$ (ca. 30 $mm \cdot min^{-1}$). This represents more than 50 times reduction in lowest usable Ac concentrations compared to bulk MFC studies. The final acetate concentrations leaving the device could reach as low as 10 µM or equivalently 0.65 $mg \cdot L^{-1}$ COD. Therefore, by extending previous flow studies to microscale flows of low concentration acetate solutions, this work paves the way for new approaches to optimisation and study of bioelectrochemical systems involving *Geobacter* and other electroactive biofilms.

4.6 Supporting information

4.6.1 Device fabrication and experiment methodology

In this work, a 3-electrode microfluidic flow cell was fabricated in a glass-sealed elastomeric chip which was housed in an anaerobic chamber. The working and counter electrodes were cut into 3 mm × 20 mm strips from a 10 cm x 10 cm graphite sheet. A gold pseudo reference electrode was made by electroless deposition on a polystyrene substrate and cut into 3 mm × 20 mm. A negative photoresist was used for device fabrication. The electrodes were placed on photoresist features and were covered with a mixture of liquid polydimethylsiloxane (PDMS) and cross-linking agent Sylgard184 (Dow Corning, Canada) in 10:1 ratio. After curing for 4 h at 70 °C, the device was taken from the mold and the electrodes and microchannel were cleaned and sterilized with 1M HCl and 70% EtOH, respectively. The inlet and outlet were punched and microchannel was sealed by a glass slide. The working, counter and reference electrode (WE, CE and RE, respectively) were connected to potentiostat and the sterile perfluoroalkoxy connective tubing (PFA tube 1/16, Hamilton Inc., Canada) was attached to the inlet and outlet of the device. As PDMS is known to be porous to gas molecules such as O_2, the microfluidic electrochemical device was placed in an anaerobic jar with 20% CO_2 and 80% N_2 (Figure 4.4). The tube inlet was connected to a mixer with 3 inlets from 3 different syringes with 10, 0.2, 0 mM acetate concentrations. Each of the 3 mixer inlets was connected to a one way stopcock valve to control the flow of liquid into the mixer. With flow control from syringe pumps holding gas-tight glass syringes, the nutrient concentrations were controlled based on the flow rate ratio between nutrient solutions containing different acetate concentration. To validate the ability of the setup to maintain anaerobic conditions during operation, an oxygen indicator (resazurin) was used based on the standard protocol.[256] The resazurin solution flowed into the jar, through the microfluidic device and off-chip into the waste container within the anaerobic jar. This experiment was conducted over 2 weeks without any indication of solution oxygenation. The high electrical current densities produced by the mature *Geobacter* biofilm matched the upper limits shown in the literature, thus supporting the conclusion that optimal anaerobic conditions were achieved.

Chronoamperometry and cyclic voltammetry were conducted using a commercial potentiostat (Volta Master 4, Hach Radiometer analytical, USA). All applied potentials were relative to a stable gold RE as demonstrated in previous work.[203,242] Chronoamperometry was conducted at an equivalent to 0 mV vs. Ag/AgCl. All current measurements by chronoamperometry were acquired every 2.7 seconds and a 10 point smoothing algorithm was conducted to reduce the file sizes. Thus time resolution of nearly 30 s. Solution velocity through the channel was determined based on the total volumetric flow rate. Acetate concentrations delivered to the microchannel were systematically changed to observe real-time effects on current outputs via chronoamperometry.

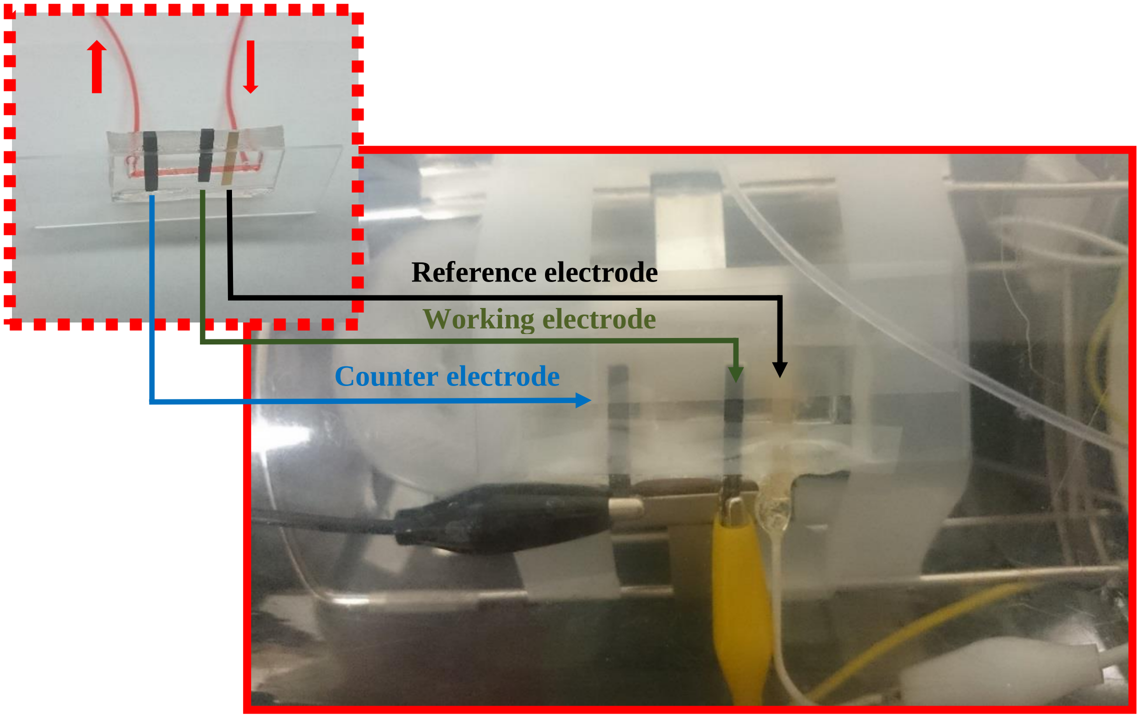

Figure 4.4 Microfluidic electrochemical cell with three-electrode setup and connections inside the anaerobic jar. Flow passes through the micro channel from inlet and touch RE, WE and CE, respectively. Inset: red solution is injected on to the device and withdrawn through connective tubing. The red liquid highlights the microfluidic channel.

4.6.2 Hydrodynamic considerations at and away from the working electrode

In general the flow velocity in the microchannel is calculated as

$$v = Q/(w \cdot h) \qquad \text{(Eq. 4.6)}$$

where h was the channel height (400 µm) and was the channel width (2 mm) and Q is the volumetric flow rate used. The growth of a biofilm on the working electrode (WE) surface will reduce the channel volume in the headspace above the electrode, which can change the local hydrodynamic properties. As discussed in the main paper the biofilm height after 300 h was assumed to be constant at 80 µm. Therefore, the channel height above the biofilm was h_b = 320 µm, 80% of the clean channel height. Therefore, average velocity above the electrode-adhered biofilm, v_b, at a volumetric flow rate, Q ($mL \cdot h^{-1}$) was estimated based on Eq. 4.6 and would have increased in proportion to the reduction free volume. Another outcome is the increase in the applied shear stress against the biofilm, compared to shear stress against the channel wall, τ_b and τ (Pa), respectively. Eq. 4.7a and 4.7b shows τ_b and τ as a function of flow rate:

$$\tau_{b\,=}\, 6 \cdot \mu \cdot Q/(w \cdot (h-h_b)^2) \qquad \text{(Eq. 4.7a)}$$

$$\tau_{\,=}\, 6 \cdot \mu \cdot Q/(w \cdot (h)^2) \qquad \text{(Eq. 4.7b)}$$

where µ is the liquid-phase viscosity (1×10^{-3} Pa·s) and $h-h_b$ is the headspace above the WE. Lastly, the Reynold's number was calculated both in the clean channel, Re, and above the biofilm, Re_b. Due to the competition between flow velocity and hydrodynamic diameter of the free volume in the clean and biofilm occupied portions of the channel, respectively, both Re and Re_b were the same for a given Q. In all cases, values well-below the threshold for laminar flow.

As discussed in previous work,[203, 242] the gold (pseudo) RE is accurate and stable if the liquid contacting it maintains constant physiochemical conditions, most importantly the pH. To ensure this was the case, we placed the RE upstream so that any metabolites or released biofilm flows downstream. We verify that upstream proton diffusion was slower than the downstream liquid velocity (*v*) by calculating the effective diffusion velocity, v_d, given by Eq. 4.8:

$$v_d = \frac{d_d}{t} = \frac{\sqrt{2D_{H^+}t}}{t} \qquad \text{(Eq. 4.8)}$$

where D_{H^+} ($\mathrm{cm^2 \cdot s^{-1}}$) is the proton diffusion coefficient in water (D_{H^+}=9.31 × 10^{-5} $\mathrm{cm^2 \cdot s^{-1}}$). Taking t=1 s and the diffusion coefficient of a free proton as,[257] we calculated v_d to be approximately 2.22 $\mathrm{\mu m \cdot s^{-1}}$ or 8.18 $\mathrm{mm \cdot h^{-1}}$. As this is 38 times slower than even the slowest channel flow velocity, no metabolites could reach the RE. Table 4.1 summarizes results for velocity, Reynold’s number and shear stress above and away from the WE and for five flow rates used in the main paper as well as the proton diffusion velocity.

To verify that pH did not in fact change at the source, periodic measurements of the nutrient solution pH flowing into the device determined that it was constant at 7 ± 0.1 throughout the experiment. Following experiments, scanning electron microscopy (SEM) was used to verify that bacterial growth did not occur on the RE, where electrode respiration was impossible.

Table 4.1 Hydrodynamic parameters in the clean portions of the channel (grey) and above the biofilm (orange) for typical flow conditions used in this study.

Q ($mL \cdot h^{-1}$)	$\bar{v}_{d^{H^+}}$ (constant) ($mm \cdot h^{-1}$)	v ($mm \cdot h^{-1}$)	Re	τ (mPa)	v_b ($mm \cdot h^{-1}$)	Re_b	τ_b (mPa)
0.25	8.2	312.5	0.065	1.159	390.6	0.065	1.811
0.5		625	0.130	2.318	781.3	0.130	3.622
0.75		937.5	0.195	3.476	1171.9	0.195	5.431
1		1250	0.260	4.636	1562.5	0.260	7.243
1.5		1875	0.390	6.952	2343.8	0.390	10.863

In summary, the RE remained sterile and the physiochemical properties of the fluid in contact with it were constant throughout the experiment, which explains its stable performance throughout the experiment, observed here and in previous work using a similar flow device.[203,242]

4.6.3 Bacterial preparation

G. sulfurreducens strain PCA (ATCC 51573) was cultured in our laboratory at 30 °C using an anaerobic medium containing the following per liter of distilled water: 1.5 g NH_4Cl, 0.6 g NaH_2PO_4, 0.1 g KCl, 2.5 g $NaHCO_3$, 0.82 g CH_3COONa (acetate, 10 mM), 8 g $Na_2C_4H_2O_4$ (fumarate, 40 mM), 10 mL vitamin supplements ATCC® MD-VS™, 10 mL trace mineral supplements ATCC® MD-TMS™. The filtered sterilized sodium fumarate, vitamin and trace mineral supplements were added after sterilization of all other materials at 110 °C, 20 psi pressure for 20 min at an autoclave. *G. sulfurreducens* were sub cultured in an anaerobic glove box containing the 10% H_2, 10% CO_2 and 80% N_2. Sub-culturing of *G. sulfurreducens* cells were done in an adjusted pH=7 nutrient medium in the glove box and 3th to 8th subculture samples were used at electrochemical cell. Sodium fumarate and vitamins were removed from the nutrient solution for biofilm growth in electrochemical mode.

4.6.4 Reference electrode calibration and stability

The gold reference electrode (RE) calibration and its stability during the experiments have been deeply studied in previous research[203,242] and compared to other microfluidic three-electrode cells with different electrode setups.[99] Briefly, a 10 mM acetate nutrient medium was used to measure formal potential of cytochrome c proteins in a *G. sulfurreducens* biofilm in a three-electrode bulk electrochemical cell via CV over the course of 120 h. When the standard Ag/AgCl RE was replaced with gold RE (new or used) a shift of 410 – 396 mV in the measured potential was recorded. To verify stability of the electrochemical flow cell featuring the gold RE, a 10 mM ferricyanide in medium solution was flowed for 2 weeks. During this time no obvious formal potential change was observed. In addition, changing flow rate did not result in any changes in to the measured formal potential of ferri/ferro redox couples, even at 10 $mL \cdot h^{-1}$, which was higher than flow rates were used in biofilm measurement. The details of experiment and discussion about flow stability can be found in previous study.

4.6.5 Device inoculation and growth

An inoculum solution containing *G. sulfurreducens* was first introduced to the microchannel through an upstream port in the mixer unit (not shown) for 3 h at $Q = 0.5\ mL \cdot h^{-1}$. The solution contained dissolved fumarate to enable extracellular electron transfer by planktonic bacteria. During inoculation, the WE was set to an oxidative electrochemical potential at 400 mV vs. Au, equivalent to 0 mV vs. Ag/AgCl, which also enabled electrode respiration for locally attached bacteria. After inoculation, the channel was exposed to a nutrient solution of [Ac] = 10 mM with no sodium fumarate, thereby ensuring the biofilm grew on the WE only. This was accomplished by opening valve MI_1 and setting $Q_1 = 0.25\ mL \cdot h^{-1}$, while the other pump flow rates for were set at $Q_2 = Q_3 = 0\ mL \cdot h^{-1}$ with valves MI_2 and MI_3 closed to prevent any back flow through the mixing unit. Under these conditions, the *G. sulfurreducens* bacteria could grow on the graphite-WE (Figure 4.1c) and a current was measured via chronoamperometry during the growth period (Figure

4.5a). As discussed in the main paper, the EAB was subjected to nutrient-limited growth media after approximately 500 h. Figure 4.5b, shows the reduction in current after switching from 10 mM to 0.2 mM in advance of the iterative process to find threshold concentrations. Due to the large difference in the time scale compared to Figure 4.5a the fluctuations appear to be lower, not due to any post-acquisition data processing (i.e. smoothing). The equilibrium current at 0.2 mM was approximately 10 µA, which was slightly above background current, proving that the EAB was still active.

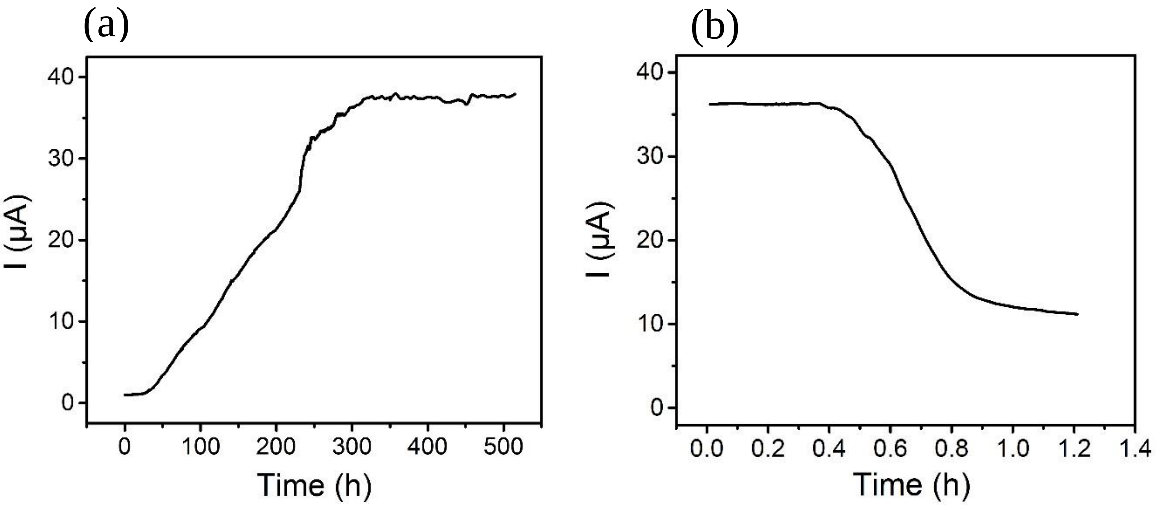

Figure 4.5 (a) G. sulfurreducens biofilm growth in microfluidic channel with 10 mM acetate nutrient and 0.2 mL·h^{-1} flow rate for 500 h. **(b)** Reduction of the current by switching from 10 mM nutrient medium to 0.2 mM Ac nutrient concentration.

4.6.6 Identification of cytochrome c formal potential by CV

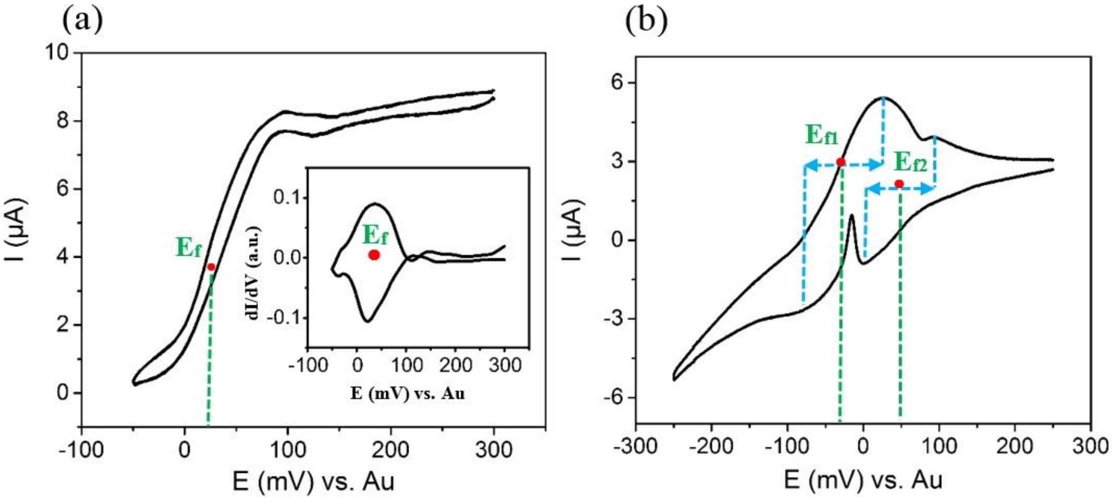

Figure 4.6 CV curve of *G. sulfurreducens* biofilm on the graphite WE at (**a**) turnover at 100 h and (**b**) non-turnover, recorded 5 hours after switching to a nutrient depleted solution. E_f is formal potential of cytochromes C of *G. sulfurreducens* biofilm. Scan rates were 1 $mV\cdot s^{-1}$ and 3 $mV\cdot s^{-1}$ for (a) and (b), respectively.

4.6.7 Fluctuations in electrical current for different metabolic activity regimes

We demonstrate fundamental differences in the current fluctuations of an active biofilm compared to those during pseudo-activity. Figure 4.7a shows a typical current profile for approximately the first 200 h hours following biofilm maturation. Note the narrow range in currents shown on the y-axis. As mentioned in Section 4.6.1, the time resolution for all chronoamperometry experiments was 30 s (1/120 h^{-1}). This was sufficient to observe frequency components as high as 60 h^{-1} according to the Nyquist sampling theorem. We used a fast Fourier transform algorithm on a typical 40 hour window (Figure 4.7b) compare the results to those in Figure 4.7c (fluctuations during pseudo-active state). A visual comparison is given via Figure 4.7c shows the transition to pseudo-activity after increasing acetate concentration above $[Ac]_{PA}$. The duration in both Figures 4.7b, c are 40 h to show the qualitative difference in oscillation periods. It is important to recognize that the y-axis scales between the two figures are very different.

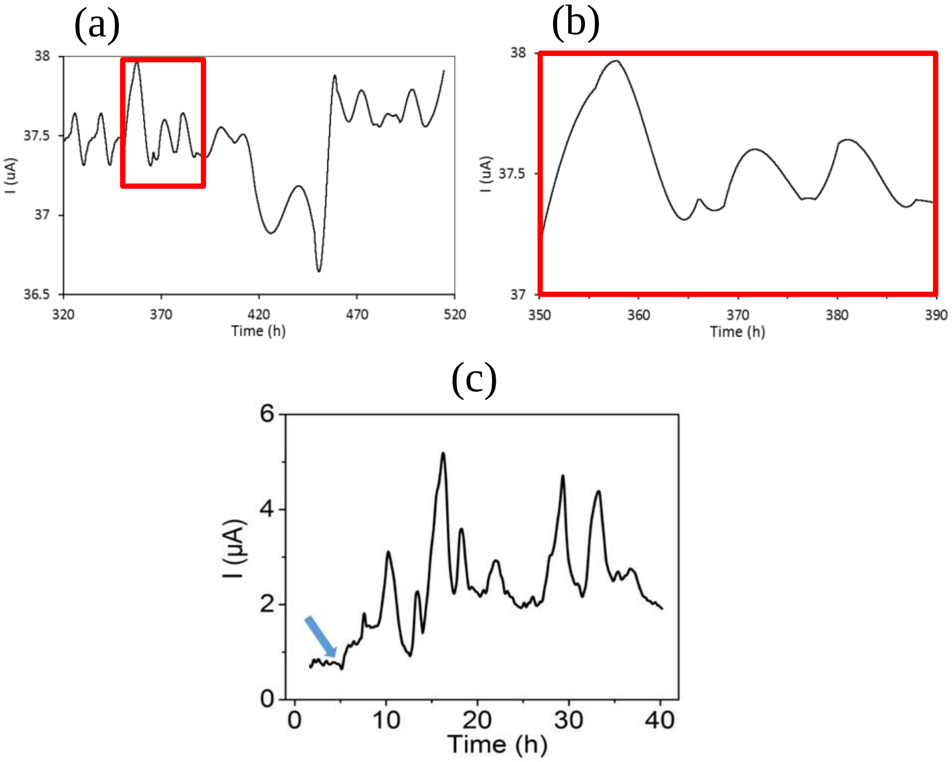

Figure 4.7 (a) CA of *G. sulfurreducens* biofilm profile for approximately the first 200 h hours following biofilm maturation. The red box shows the region of data shown in **(b)**. **(c)** Nutrient solution was switched to 80 µM acetate medium (blue arrow) while the flow rate was maintained constant at 0.5 mL·h^{-1}. G. sulfurreducens biofilm shows a fluctuating (pseudo-active) state after at 80 µm acetate in 40 h exposure time.

Table 4.2 quantitatively tabulates key observable differences for active biofilms (exposed to 10 mM acetate, Q_T=0.25 mLh^{-1}) and pseudo-active biofilms (exposed to a variety of conditions within Zone II shown in Figure 4.3). Observables included significant upper frequency components in the current fluctuations (f_{upper}), average current after background current (I_B) subtraction (I_{ave}-I_B) and a measurement of the absolute value of peak-to-peak (P2P) current as well as the P2P changes relative to the backgrounded adjusted average current. The results demonstrate very stark differences which can be summarized in two general observations: (1) current fluctuations from pseudo-active biofilms have high frequency components are that are approximately 40 times faster than those for active ones and (2) the relative intensity of the current fluctuations versus the average current output for pseudo-active is about 50 times higher than for active biofilms. Together these observations point to a fundamental difference in behaviour of biofilms in a pseudo-active state compared to the active state.

Table 4.2 Comparison of current fluctuations between active and pseudo-active biofilms.

			P2P fluctuations	
Biofilm state	**f_{upper} (h^{-1})**	**I_{ave}-I_B**	**Raw (μA)**	**Relative (%)**
Active	0.05	36.5	1.5	4.1
Pseudo active	2	2.6	5.4	207.7

4.6.8 Efficiency of acetate digestion

As noted in the main paper, when supplied concentrations at the activity threshold $[Ac]_A$, the final acetate concentration $[Ac]_f$ in the range of 10 to 20 μM indicated efficient oxidisation. This was notable because the supply concentrations were lower than in usable concentrations in bulk systems and as well because liquid/biofilm contact times were short, ranging from just 6 to 35 seconds, depending on the flow rate. Based on Eq. 4.5, (reproduced here as Equation 4.9) acetate conversion efficiency (ε_{Ac}) from initial concentration, $[Ac]_0$, to final concentration, $[Ac]_f$ is calculated:

$$\varepsilon_{Ac} = ([Ac]_0-[Ac]_f)/[Ac]_0\times100\% \qquad \text{(Eq. 4.9)}$$

Using data from the main Figure 4.3 for the different $[Ac]_A$, $[Ac]_f$ pairs for each Q value we obtained conversion efficiencies shown in Figure S5a.

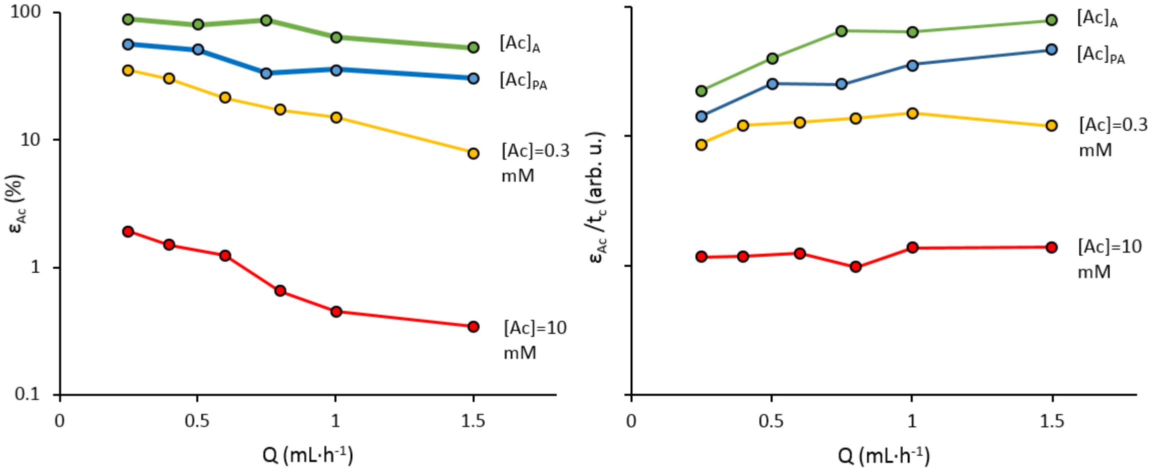

Figure 4.8. (a) Acetate conversion efficieny (ε_{Ac}) and (b) acetate conversion efficiency normalized by contact time (ε_{Ac}/t_C) as a function of Q for concentrations indicated. Exact values of $[Ac]_A$ and $[Ac]_{PA}$ are given in Figure 4.3. Both y-axes are plotted on a log-scale.

The same procedure was used to generate ε_{Ac} for $[Ac]_{PA}$ and for two higher concentrations, [Ac]=0.3 and 10 mM. It should be restated that the absolute concentration for the two thresholds $[Ac]_A$ and $[Ac]_{PA}$ changed with Q, whereas the tests at higher concentrations were held constant during changes to Q. Plotting ε_{Ac} versus Q in Figure 4.8a shows that acetate conversion is most efficient at activity threshold concentrations. This is expected for high concentration solutions above the traditional zero order concentration regimes because current does not increase in proportion to concentration and more time is required to reduce concentrations. However, even at the relatively low concentration of 0.3 mM, ε_{Ac} is notably worse than at either of the threshold concentrations. The general reduction in ε_{Ac} with increasing Q is expected since contact time reduced. We note that the time normalized efficiency actually increases with flow rate (Figure 4.8b). This is likely due to flow effects that both reduce the diffusion barrier around the biofilm and enable deeper penetration of the nutrient flow into the biofilm, effectively increasing accessibility of nutrients to bacteria in lower biofilm strata.

Chapter 5. A Generalized Kinetic Framework Applied to Whole-Cell Bioelectrocatalysis in Bioflow Reactors Clarifies Performance Enhancements for *Geobacter Sulfurreducens* Biofilms

Mir pouyan Zarabadi[1]*, Manon Couture*[2,4]*, Steve J. Charette*[2,3,4]*, Jesse Greener*[*,1,5]

[1]Département de Chimie, Faculté des sciences et de génie, Université Laval, Québec City, QC, Canada.

[2]Institut de Biologie Intégrative et des Systèmes, Pavillon Charles-Eugène-Marchand, Université Laval, Québec City, QC, Canada.

[3]Centre de recherche de l'Institut universitaire de cardiologie et de pneumologie de Québec, Québec City, QC, Canada.

[4]Département de biochimie, de microbiologie et de bio-informatique, Faculté des sciences et de génie, Université Laval, Québec City, QC, Canada.

[5]CHU de Québec, centre de recherche, Université Laval, 10 rue de l'Espinay, Québec, QC, Canada

Accepted manuscript online on 06 May 2019. Modifications on the numbering of the figures of the paper have been done in order to fit the sequence of the dissertation.

Published in *ChemElectroChem.* **2019**, *6*, 2715 – 2718.

5.1 Résumé

Une cinétique commune pour les études de catalyse à cellules entières est essentielle pour comprendre et optimiser les réacteurs en bioflux. Dans ce travail, nous démontrons l'applicabilité d'une version de la cinétique de Michaelis - Menten adaptée au flux dans le cas d’un biofilm bactérien électrocatalytique. Un réacteur en bioflux à trois électrodes a permis de mesurer des taux de constante catalytique jusqu’à 50% plus importants pour un biofilm de *Geobacter sulfurreducens* lorsque le débit variait. D’après les paramètres de la cinétique appliquée, les augmentations de la constante catalytique, de l'efficacité catalytique et de la capacité de réaction du dispositif induit par le flux pourraient être liées à une augmentation de la biomasse catalytique. Cette étude démontre qu'une cinétique normalisée est essentielle pour les mesures quantitatives de nouveaux systèmes catalytiques vivants dans les réacteurs à flux et pour l'analyse comparative de systèmes catalytiques des enzymes.

5.2 Abstract

A common kinetic framework for studies of whole-cell catalysis is vital for understanding and optimizing bioflow reactors. In this work, we demonstrate the applicability of a flow-adapted version of Michaelis-Menten kinetics to an electrocatalytic bacterial biofilm. A three-electrode microfluidic biofilm flow reactor measured increased turnover rates by as much as 50 % from a *Geobacter sulfurreducens* biofilm as flow rate was varied. Based on parameters from the applied kinetic framework, flow-induced increases to turnover rate, catalytic efficiency and device reaction capacity could be linked to an increase in catalytic biomass. This study demonstrates that a standardized kinetic framework is critical for quantitative measurements of new living catalytic systems in flow reactors and for benchmarking against well-studied catalytic systems such as enzymes.

5.3 Introduction

For centuries, whole-cell biotransformations have been used in the production of food and beverages. More recently, whole-cell biocatalysis has become an active area of research[258] due to its potential for low-cost synthesis of fine chemicals, including chiral molecules and pharmaceuticals,[259] natural food additives,[260] and applications in bioremediation and energy.[261] Whole-cell biocatalysis benefits from complex multi-enzyme reaction steps, applicability at ambient conditions, and attractive properties such as self-repair and regeneration. It can also be lower in cost compared with extracted enzymes because there is no need for isolation and purification steps and because cells produce their own enzyme co-factors.[262] Bacterial biofilms are promising for the same reasons, but include other benefits than make them candidates for industrial processes as well.[263,264] These include their preference for surface attachment, making them ideal for heterogeneous catalysis, their protective self-produced extracellular polymeric matrix, which can mitigate challenges related to toxicity, can lead to long-term productivity even under harsh conditions.[265,266] Promising areas of application include biodegradation and biochemical synthesis.[267]

Control over substrate concentration and reactor feeding strategy are the most important factors for optimisation of whole-cell biocatalysis.[268,269] Chemostat bioreactors can impose tunable concentrations against the biofilm and eliminate cyclic nutrient depletion and product accumulation between solution replenishment in bulk reactors.[270] However, latency in manipulations of reaction conditions during reaction optimization and fundamental research is a drawback. Microfluidic channels can address this problem because dead is space nearly zero. Combined with strictly laminar flow, microfluidic bioreactors also offer precise control of the shear forces and of diffusion barriers at the biofilm-liquid interface.[99] High surface-area-to-volume ratios result in efficient diffusive mass-transfer between the nutrient solution and the wall-adhered biofilm, even for short contact times at high flow velocities.[271] Due to the small volumes used in microfluidic bioreactors, liquid consumption is reduced and thus long-duration studies are possible under a large range of hydrodynamic conditions without the need for frequent refilling of reagent sources. With the proliferation of microfluidic bioanalytical tools for real-time *in situ* measurements of biofilms and their by-products, deeper scientific investigations are possible with better accuracy and repeatability.[99] In this work, we use microfluidic electrochemical flow cells to study whole-cell biofilm electrocatalysis under flow. The kinetic framework used connects whole-cell catalysis in flow systems to traditional Michaelis-Menten kinetics (Eq. 5.1) between a substrate molecule S and a catalytic bacteria in a biofilm, denoted by E, due to historical relation to enzyme kinetics.[272,273]

$$E + S \underset{k'_a}{\overset{k_a}{\rightleftharpoons}} ES \xrightarrow{k_{cat}} P + E \qquad \text{(Eq. 5.1)}$$

where k_a ($M^{-1}\cdot s^{-1}$) and k'_a (s^{-1}) are the forward and backward rate constants in the first reversible complexation step, and k_{cat} is the catalytic rate constant (s^{-1}) that irreversibly transforms the pre-equilibrated ES complex into the products. The irreversibility of the final transformation is a typical assumption for most biocatalytic systems but should be justified. The Michaelis-Menten constant K_M defines the substrate concentration that results in half-maximal activity. The reader is directed to the section 5.6.5 for more information.

Changes to certain reaction conditions can result in “apparent” or “effective” kinetics, which lead to the apparent Michaelis-Menten constants and efficiency parameters $K_{M(app)}$ and $\varepsilon_{(app)}$, respectively. In 1966, Lilly and Hornby developed a framework for enzyme kinetics that accounted for changes to hydrodynamic conditions in flow reactors[274] (Eq. 5.2).

$$P[S]_i = \frac{C}{Q} + K_{M(app)} \operatorname{Ln} (1 - P) \qquad \text{(Eq. 5.2)}$$

where $P = \frac{[S]_i - [S]_f}{[S]_i}$ is the substrate conversion fraction, and $C = k_{cat} [E] \beta$ is known as the device reaction capacity, which includes ratio of the reactor void volume to the total reactor volume, β. Assuming that k_{cat} and β are not sensitive to flow, changing C can supply evidence of forced convection through three-dimensional porous systems such as biofilms, a point that is often overlooked for reactive biofilms. Applied to enzyme catalysis, trends in $K_{M(app)}$ are often extrapolated to zero flow $K^0_{M(app)}$ to determine whether enzyme activity is only affected by mass transfer effects $K_M = K^0_{M(app)}$ or whether surface immobilization can also change the kinetics.[275,276,277] For enzymes in their native environment within whole cells or biofilms, it is expected that the K_M value measured during static experiments should be the same as $K^0_{M(app)}$ from flow reactors.

Although Michaelis-Menten kinetics have been applied to whole-cell catalysis, the Lilly-Hornby approach has not, limiting the advancement of whole-cell catalysis in flow reactors. To address this deficiency, the turnover rate ($\frac{d[P]}{dt} = -\frac{d[S]}{dt}$, Eq. 5.7) from surface-adhered cells or their biofilms should be measured while accurate control over flow rate and [S] are applied. An electroactive biofilm (EAB) from electrogenic bacteria, such as *Geobacter sulfurreducens* is an excellent choice because its ability to transfer electrons to an electrode during respiration,[99,278] enabling direct observations of instantaneous turnover rate using chronoamperometric measurements of electric current. For a monoculture EAB of *G. sulfurreducens* under anaerobic conditions, the turnover rate of an acetate substrate (Ac), namely $\frac{\mathrm{dmol_{Ac}}}{\mathrm{dt}}$ ($\mathrm{mol_{Ac}{\cdot}s^{-1}}$), is calculated from the electrical current I ($\mathrm{C{\cdot}s^{-1}}$) using Eq. 5.3:

$$\frac{\mathrm{dmol}_{Ac}}{\mathrm{dt}} = \frac{I}{8.F} \qquad \text{(Eq. 5.3)}$$

where F is Faraday's constant or $F = 9.6485 \times 10^4\ \mathrm{C{\cdot}mol_e^{-1}}$, and 8 is the proportionality constant for the number of moles of electrons produced for each mole of Ac oxidized. The irreversible final transformation in Eq. 5.1 is a good assumption for chronoamperometry experiments on electrode-adhered EABs due to the application of an electrode potential, which can quickly and efficiently conduct electrons away from the reaction site.

5.4 Results and discussion

In this work, we conducted real-time measurements of the instantaneous turnover rates from EAB of *G. sulfurreducens* bacteria in a microfluidic three-electrode flow cell under controlled reaction conditions. Figure 5.1a presents the top- and side-view schematics of the device, including the sequential placement of the electrodes. Figure 1b shows a typical scanning electron microscopy image of a mature biofilm on the WE following an experiment. The reader is directed to the section 5.6.2 for additional details on device fabrication, operating conditions, and preparation of *G. sulfurreducens*. The reader is also directed to section 5.6.6 for a justification that electron transfer kinetics are not rate limiting under different flow conditions. Thus turnover rate can be interpreted substrate conversion via a modified version of Michaelis-Menten kinetics.[279]

$$I = I_{max} \frac{[\mathrm{Ac}]}{K_{M(app)} + [\mathrm{Ac}]} \qquad \text{(Eq. 5.4)}$$

where I_{max} is the maximum current output when the substrate [Ac] is much larger than $K_{M(app)}$.

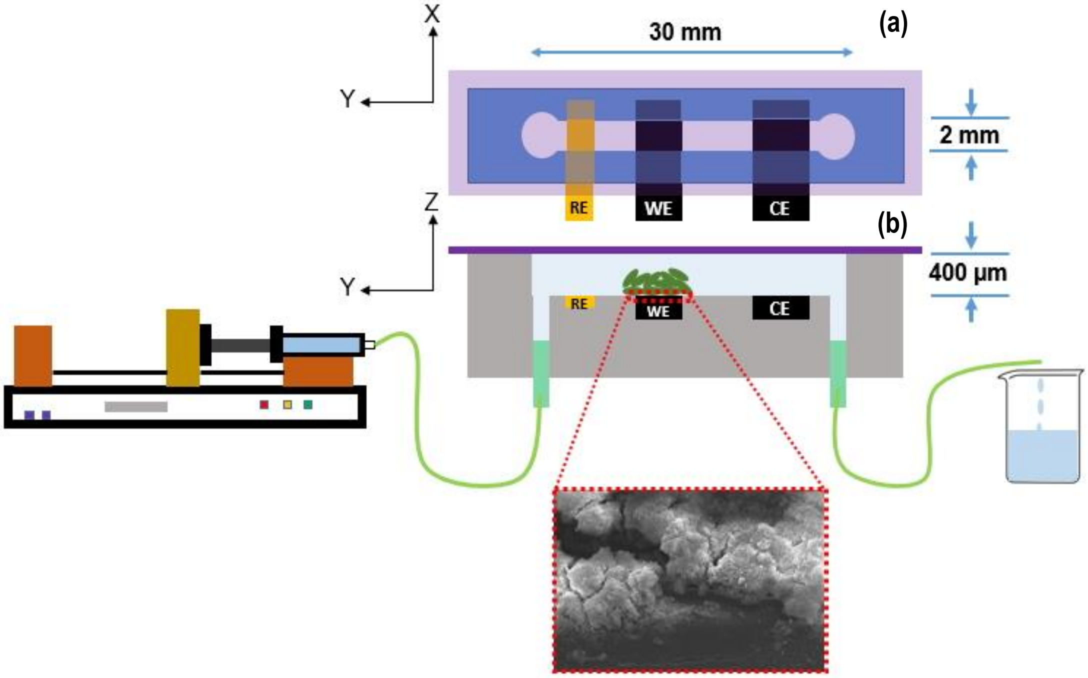

Figure 5.1 Schematic of a 3-electrode glass-sealed electrochemical microfluidic cell with dimensions 2 mm (w) × 0.4 mm (h) × and 30 mm (L). RE, WE and CE represent pseudo reference electrode (gold), the working electrode (graphite) and the counter electrode (graphite), respectively. **(a)** Top view of the microchannel with the sealing glass on top (violet) with one inlet (next to RE) and one outlet (next to CE). The dark blue part shows PDMS which is used for microchannel fabrication. **(b)** Side view of microfluidic electrochemical cell. The inlet of microfluidic channel is connected to a glass gas-tight syringe with 10 mM acetate concentration and 0.2 mL·h^{-1} flow rate. The *G. sulfurreducens* cells were grown on the surface of graphite working electrode. The red box shows SEM image (z-y orientation) of mature *G. sulfurreducens* biofilm on the graphite electrode.

The chronoamperometry data in Figure 5.2 show peaks in the current I over a background signal of approximately 20 µA as flow pulses ranging from Q = 0.4 to 3 mL·h^{-1} were applied over a background flow rate of Q = 0.2 mL·h^{-1}. The Figure 5.2 inset plot presents the averaged I vs. Q results from four different measurements on different days. Flow rate of Q = 3 mL·h^{-1} resulted in a 24% increase in current measurements over those acquired at Q = 0.4 mL·h^{-1}. Enhancements could not be compared with direct measurements under static conditions (Q = 0) because continuous Ac depletion in small microchannel volume around the electrode would prevent stable measurements of current. However, an extrapolation to Q = 0 using current values in the linear region from Q = 0.2 to Q = 1 $mL \cdot h^{-1}$ gave an estimated zero flow current value of I = 18.25 μA (3 $A \cdot m^{-2}$), which is in the normal range (1-10 $A \cdot m^{-2}$) for other reported experiments under static conditions. Therefore, we estimated that the turnover rate at 3 $mL \cdot h^{-1}$ was more than 50% higher than that under static conditions. Based on the electric current obtained for each flow rate Q, the [Ac] conversion was calculated for different initial acetate concentrations $[Ac]_i$ in the range of 0.3 to 10 mM using the formula in Eq. 5.5:

$$P \cdot [Ac]_i = [Ac]_i - [Ac]_f = \frac{dmol_{Ac}}{dt} / Q \qquad \text{(Eq. 5.5)}$$

where P is defined for Eq. 5.2, and $[Ac]_f$ is the final Ac concentration after biocatalytic oxidation. Figure 5.3a shows separate plots of the change in [Ac] as a function of Q for the different applied $[Ac]_i$. According to Eq. 5.2, as $[Ac]_i$ is varied, the plot of $P \cdot [Ac]_i$ vs. – Ln (1-P) should result in a straight line with slope - $K_{M(app)}$ and intercept C/Q. Such a linear plot was obtained for the five different flow rates used in this work (Figure 5.3b).

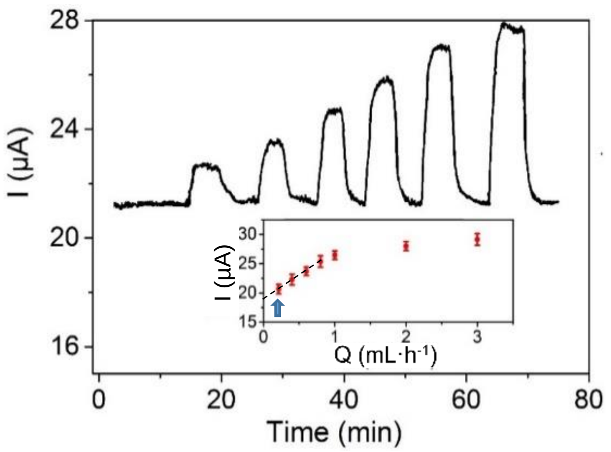

Figure 5.2 Flow rate modulation from Q = 0.2 $mL \cdot h^{-1}$ (base flow) to elevated values, Q = 0.4, 0.6, 0.8, 1, 2 and 3 $mL \cdot h^{-1}$ for a 600 h old *G. sulfurreducens* biofilm exposed to [Ac] = 10 mM. Inset: average I vs. Q during for a mature biofilm (> 600 h) conducted 4 times on four consecutive days. Error bars represent standard deviation of averaged measurements. The blue arrow points to data at Q = 0.2 mL/h that were acquired from background current measurements, whereas the other values were acquired from peak current values in the main figure. The dashed line extrapolates the linear portion of the inset figure to Q = 0 conditions.

Figure 5.3c shows the values of $K_{M(app)}$ obtained from the slopes in Figure 5.3b. The trends in $K_{M(app)}$ are discussed after validation of the technique by comparison to the conventional K_M constant from static experiments. First, we extrapolated to Q = 0, obtaining $K^0_{M(app)}$ = 0.59 mM. Then, direct measurements of K_M were collected from a *G. sulfurreducens* biofilm in a bulk 3-electrode system under similar conditions (bacterial age, graphite electrode material and nutrient solution). Electric currents were obtained immediately after stabilization following replacement with a new nutrient solution with a different [Ac] (Figure 5.9b). Plotting I vs. [Ac] produced a standard Michaelis-Menten profile (Figure 5.3d) and a Lineweaver-Burk plot of 1/I vs. 1/[Ac] yielded the expected straight line (Figure 5.3d inset). A fitting algorithm applied to either curve in Figure 5.3d yielded a value of K_M = 0.62 mM. The similarity between K_M and $K^0_{M(app)}$ for the present system also matched the K_M = 0.60 mM reported previously for bulk measurements.[279]

The implications of reduced $K_{M(app)}$ with increasing Q are examined next. Applied Ac concentrations of 10 mM are considered to lie in the "substrate saturated" regime[280] ([Ac] >> K_M), and should be described by Eq. 5.3 (equivalently $I=k_{cat}[E]$). Therefore, an increase in either or both of k_{cat} or [E] could explain the peak I values (Figure 5.2), which increased by 24% when Q was increased from 0.4 to 3 $mL \cdot h^{-1}$. Despite previous suggestions that accelerated turnover under flow could be the result of EAB deacidification,[281] a likely route to increases in k_{cat}, pH was recently shown not to change for similar conditions at [Ac] = 10 mM.[242] Alternatively, flow-induced increases to current might be at least partially related to changes to [E]. In this vein, consider the measurements of device reaction capacity (C), which increased by 19% when increasing flow from Q = 0.4 to Q = 3 $mL \cdot h^{-1}$ (Table 5.1 and Figure 5.10). Taking into account that C depends only on [E], k_{cat}, and the physical dimensions implicit in β (Eq. 5.2), flow-related increases to C support the likelihood of increases to [E], assuming that k_{cat} and β remain largely constant. Flow-based increases to [E] could result from better contact between the acetate molecules and the catalytic bacteria at different strata within the biofilm due to forced convective flow through the porous biofilm, as noted previously for non-electroactive biofilms.[207,208]

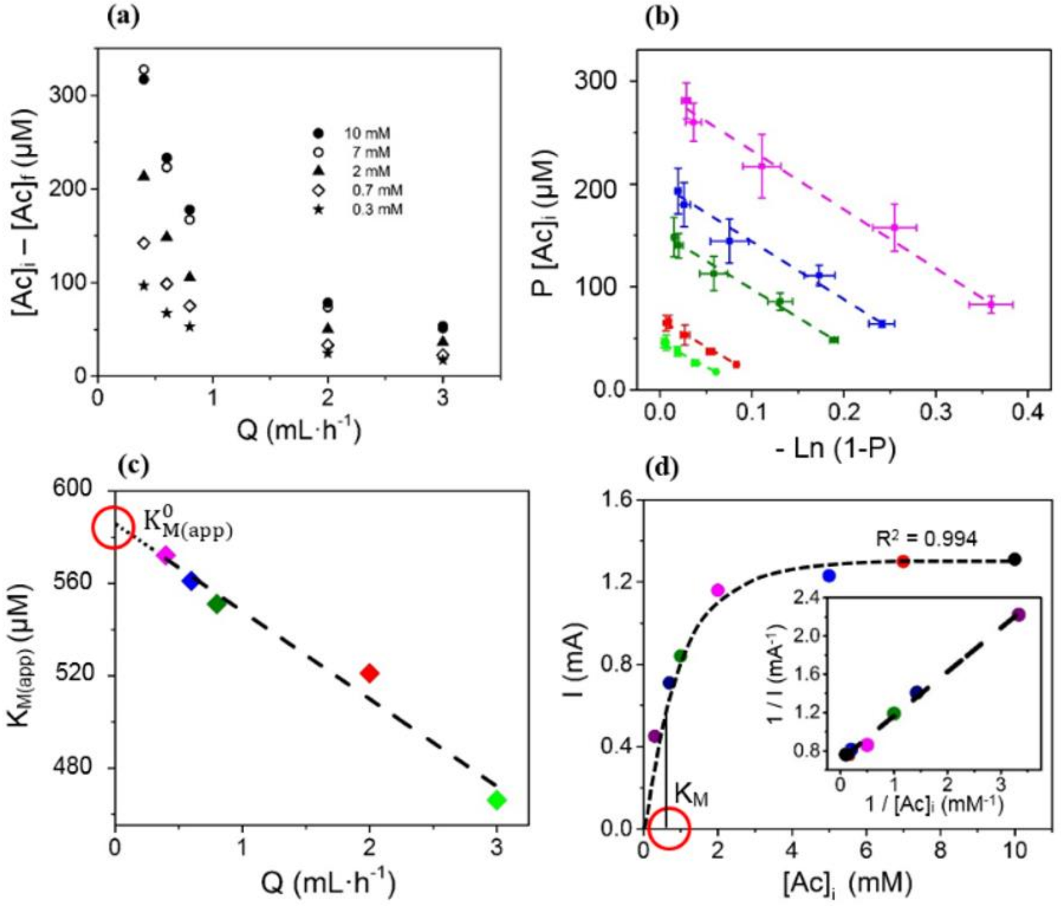

Figure 5.3 (a) Plots of the concentration of acetate nutrient converted for respiration vs. flow rate as a function of the initial acetate concentration. **(b)** Plots of P $[Ac]_i$ vs. – Ln(1 - P). The modulated flow rates were Q = 0.4 mL·h^{-1} (pink), 0.6 mL·h^{-1} (blue), 0.8 mL·h^{-1} (dark green), 2 mL·h^{-1} (red) and 3 mL·h^{-1} (green). **(c)** Plot of $K_{M(app)}$ vs. Q. The intercept on the vertical axis (red circle) yields a zero-flow $K_{M(app)}$ value ($K^0_{M(app)}$) of 0.59 mM. **(d)** Current vs. initial acetate concentrations in the bulk experiment for 10 mM (black), 7 mM (red), 5 mM (blue), 2 mM (pink), 1 mM (dark green), 0.7 mM (dark blue) and 0.3 mM (purple). The curve was fitted to Eq. 5.4 to find $K_{M(app)}$. Inset: The Lineweaver-Burk plot of the reciprocal current output vs. the reciprocal acetate concentration demonstrates the expected linear profile for systems applicable to Michaelis-Menten kinetics.

The implication of additional *G. sulfurreducens* bacteria contributing to biocatalysis combined with reduced diffusion barriers around the biofilm at higher flow rates, can be exploited for improvement to device performance in future flow-based bioelectrochemical applications. Global improvements in performance under flow are expressed by increases to (apparent) catalytic efficiency $\varepsilon_{(app)} = k_{cat}/K_{M(app)}$, by replacing K_M with $K_{M(app)}$ in Eq. 5.4. Notably, increases to $\varepsilon_{(app)}$ were calculated to be 19% as Q increased from 0.4 to 3 $mL \cdot h^{-1}$, which correspond closely to measured changes to I and C and proposed changes in [E] for the same flow rate range.

As applied to the study of *G. sulfurreducens* biofilms, a flow-adapted version of the Michaelis-Menten equation was used for the first time to understand and develop whole-cell catalysis while leveraging the advantages of microfluidic flow cells. Various applications can be envisioned, especially those related to synthetic biology and metabolic engineering in which cells are effectively considered as units of production for valuable products of bulk and fine chemicals.[270] In addition, characterization of enzymes within their native (cellular) environment is an important goal in the field of enzymology.[282]

5.5 Conclusion

Our work shows that measurements of kinetic parameters such as K_M, $\varepsilon_{(app)}$, and [E] as a function of flow for whole-cell catalysts is feasible microorganisms immobilized within a microfluidic chamber. Generalization of this approach together with the application of different detection modes for non-electroactive biofilms appears a desirable next step.

5.6 Supporting information

5.6.1 Bacterial preparation

Frozen samples of *Geobacter sulfurreducens* (strain PCA, ATCC 51573) were cultured at 30 °C using an anaerobic medium in an anaerobic chamber with 10% H_2 and 10% CO_2 balanced with N_2 for 7 days and sub-cultured at least 2 times prior to injection into the electrochemical device. The medium contained the following (per liter of distilled water): 1.5 g NH_4Cl, 0.6 g NaH_2PO_4, 0.1 g KCl, 2.5 g $NaHCO_3$, 0.82 g CH_3COONa (acetate, 10 mM), 8 g $Na_2C_4H_2O_4$ (fumarate, 40 mM), 10 mL vitamin supplements ATCC® MD-VS™, 10 mL trace mineral supplements ATCC® MD-TMS™. With the exception of sodium fumarate and vitamin/trace mineral supplements that were added after filter sterilization into final nutrient medium, all chemical compounds were dissolved in distilled water and sterilize by autoclaving at 110 °C and 20 psi for 20 min. The nutrient medium was adjusted to pH = 7 and *G. sulfurreducens* were sub-cultured 3 to 8 times. Sodium fumarate and vitamins were added in the aqueous nutrient solution only for biofilm growth of planktonic bacteria, whereas they were removed to encourage electrode respiration.

5.6.2 Microfluidic device fabrication, anaerobic environment and inoculation

The microfluidic device fabrication, anaerobic condition, inoculation and bacterial preparation have been explained in previous publications,[203,242] and are briefly reviewed here with emphasis on the present context.

Device fabrication (electrodes): The microfluidic electrochemical cell used in this study included a three-electrode configuration, consisting of graphite working (WE) and counter (CE) electrodes and a gold pseudo reference electrode (RE). The WE and CE were cut from a commercial source (GraphiteStore.com Inc., USA) into

3×20 and 4×20 mm strips, respectively. The pseudo reference electrode (RE) was created by Au electroless deposition on a polystyrene support material and was subsequently cut into 3×20 mm strips.

Device fabrication (electrodes integration): a typical silicon master mould with SU8 features (FlowJEM Inc., Toronto, Canada) defined the channel length, width, height dimensions being 30 (L), 2 (w), 0.4 mm (h). Electrodes were wrapped entirely with tape to prevent PDMS from directly contacting any portion of the electrodes. Then, electrodes were embedded into the microchannel by first placing them flush against the top of the channel feature on the silicon master mould and held in place with double-sided tape. A mixture of liquid polydimethylsiloxane (PDMS) and cross-linking agent Sylgard184 (Dow Corning, Canada) (ratio 10:1) was poured over the mould with the electrodes in place. After curing the PDMS for 4 h at 70 °C, the electrodes were embedded at the bottom of the channel and the device was removed from the mould. The residual tape was cut from all the electrode surfaces. Before sealing the channel, graphite electrodes were swabbed 2 M HCl to remove any debris following the channel fabrication. Then the entire channel was cleaned and sterilized using a 70% ethanol solution and autoclaved distilled water. The microfluidic electrochemical cell was then sealed with a microscope slide by exposure to air plasma (PCD-001 Harrick Plasma, Ithaca, NY, USA). Electrical connections were made to the exposed parts of electrodes outside of the device. The gold RE was connected by solder and a protective coating of epoxy was added to physically stabilize the connection. The electrical connections to the graphite electrodes were accomplished with alligator clips. The finalized microfluidic device is shown in Figure 5.4 (inset).

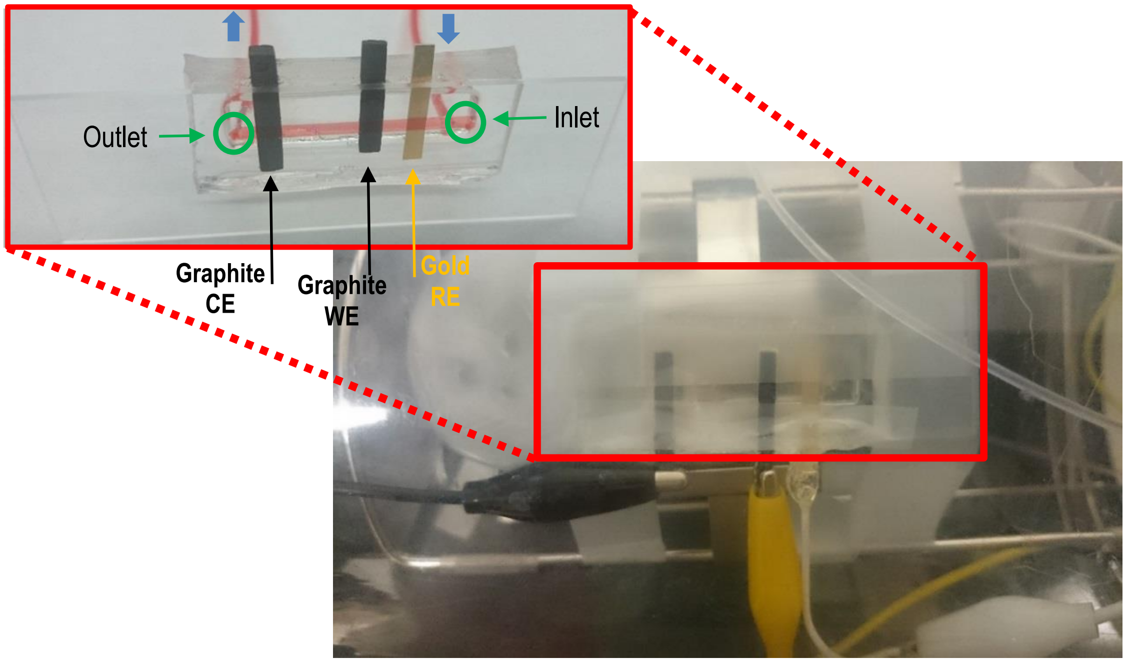

Figure 5. 4 Image of the three-electrode device after installation within the anaerobic enclosure. Electrical connections to the counter electrode and working electrode are shown via black and yellow alligator clips. The epoxy-protected solder connection to the gold reference electrode is shown with the white wire. Inset: close up of the microfluidic device before installation and electrical connections with the red dye aqueous solution being passed through the channel for contrast.

Anaerobic enclosure: The PDMS polymer enables diffusion of small molecules including O_2 through it. Therefore, the microfluidic device was housed within a small anaerobic enclosure (McIntosh and Filde's, 28029 Sigma-Aldrich) and filled with an anaerobic gas (20% CO_2 and 80% N_2). A feedthrough port in the enclosure enabled electrical connections between electrodes and potentiostat and the sterile perfluoroalkoxy connective tubing (PFA tube 1/16, Hamilton Inc., Canada) between the device liquid connectors and syringe pumps. The port was sealed using epoxy glue to prevent air exchange with the ambient conditions. A layer of epoxy glue with gas-impermeable tape was applied on the tubing to minimize gas diffusion through the connective tubing outside of the enclosure. The inlet tube was connected to a 50 mL glass syringe and 10 mL for inoculations via connector assemblies (P-200x, P-658, IDEX, WA, USA). Syringe pumps (PHD 2000, Harvard

Apparatus, Holliston, MA, USA) were used in controlled liquid injection. Temperature control of 23 ± 0.5 ^{o}C was verified by a local temperature probe. A picture of the microfluidic device installed in the anaerobic chamber, is shown in Figure 5.4.

Inoculation: Before inoculation, the microfluidic channel and tubing were rinsed with sterile distilled water for 1 h at 1 $mL \cdot h^{-1}$. All inoculation and subsequent biofilm growth was conducted in a, in a 20:80 CO_2:N_2 gas purged system ensuring constant anaerobic conditions. A 1.5 mL inoculum aqueous solution containing *G. sulfurreducens* was first introduced to the microchannel through for 3 h at Q = 0.5 $mL \cdot h^{-1}$. The medium aqueous solution contained dissolved fumarate to enable extracellular electron transfer by planktonic bacteria. During inoculation, an oxidative electrochemical potential was applied to the working electrode (400 mV vs. Au, equivalent to 0 mV vs. Ag/AgCl)[242] which enabled electrode respiration for sessile bacteria. After 3 h inoculation process, the inoculum syringe was exchanged for a 50 mL air-tight syringe containing acetate nutrient medium with no sodium fumarate or vitamins, with flow rate Q = 0.2 $mL \cdot h^{-1}$. Exclusion of fumarate (and to a less important degree, vitamins) ensured that external electron transfer could only occur at the WE, which remained poised at 400 mV vs. Au. The system was maintained under these growth conditions, with periodic replacement of the nutrient syringe for the duration of the experiment. The current output was monitored by chronoamperometry during growth of *G. sulfurreducens* electroactive biofilm.

5.6.3 Flow rate vs. time

The Figure 5.5 shows flow rate vs. time to correspond to I vs. t data in the main part of Figure 5.2.

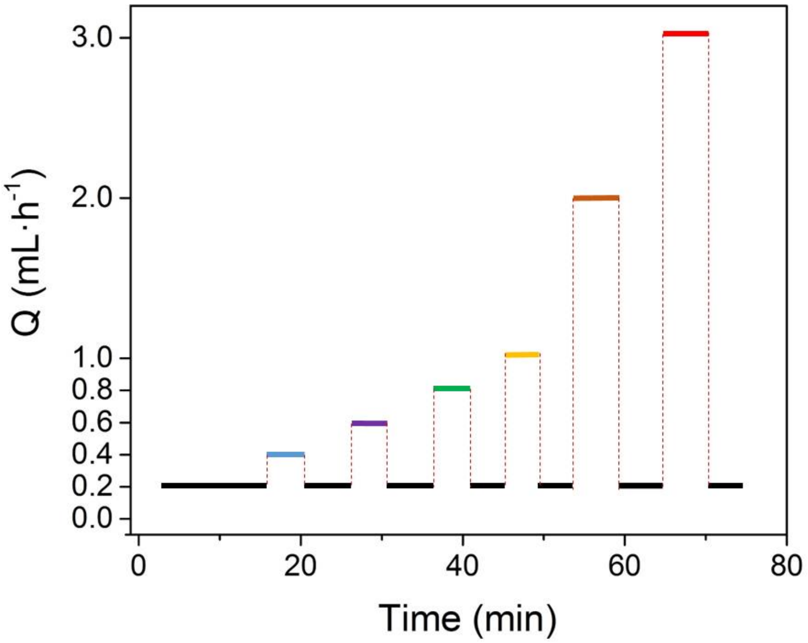

Figure 5.5 The changes of flow rate in function of time of acquisition. The black lines shows the time in which the flow rate is 0.2 mL·h^{-1} and blue, purple, green, yellow, brown and red lines are 0.4, 0.6, 0.8, 1, 2 and 3 mL·h^{-1}, respectively.

5.6.4 SEM sample preparation

Scanning electron microscopy (SEM) was conducted after the experiment finished with the objective to observe the bacteria attached to the WE (Figure 5.1b). Before the electrode was removed from the microfluidic device, a fixation aqueous solution (2.5 % glutaraldehyde in 0.1M phosphate buffer, pH = 7.4) was applied to channel (Q = 0.5 mL·h^{-1}) for 2 h while the device was still under anaerobic conditions. Then, the device was removed from the anaerobic enclosure and cut open to expose and remove the WE. The biofilm coated electrode was then left exposed to the same fixation solution in a bath overnight. The next day the electrode was then transferred to a solution with 1 % osmium tetroxide for 1.5 h and rinsed in 0.1M phosphate buffer, pH = 7.4. Finally, the sample was sequentially dehydrated in 50, 75, 95 and 100% aqueous ethanol solutions for 15 min, respectively, followed by room temperature drying overnight. Before acquiring images, a thin layer of gold was sputtered on the biofilms and electrode (Model: Nanotech, SEM PREP 2). The images were captured with JEOL JSM-6360 LV electron microscope imaging platform.

5.6.5 The Michaelis-Menten and Lilly-Hornby kinetics

This section contains information relating the classic Michaelis-Menten equation and its flow variant, Lilly-Hornby. A key parameter in the Michaelis-Menten equation is the Michaelis-Menten constant K_M, otherwise known as the half-saturation concentration. K_M is calculated in based on the individual rate constants from Eq. 5.1 based on Eq. 5.6:

$$K_M = \frac{k_a' + k_{cat}}{k_a} \qquad \text{(Eq. 5.6)}$$

In the application of this model to whole-cell kinetics, each reaction step is complex and consists of several sequential biochemical enzymatic reactions, e.g., in the tricarboxylic acid cycle or TCA cycle, as well as molecular diffusion steps. Nevertheless, the Michaelis-Menten model gives a useful framework for understanding overall kinetics, which can be described by the rate equation in Eq. 5.7:

$$\frac{d[P]}{dt} = \left.\frac{d[P]}{dt}\right|_{max} \frac{[S]}{K_M + [S]} \qquad \text{(Eq. 5.7)}$$

where $\frac{d[P]}{dt}$ ($mol \cdot L^{-1} \cdot s^{-1}$) is the rate of product production or equivalently, the turnover rate. When [S] = K_M, the reaction proceeds at half-maximal rate ($\frac{1}{2}\left.\frac{d[P]}{dt}\right|_{max}$) and tends to a maximum ($\left.\frac{d[P]}{dt}\right|_{max}$), often referred to as the maximum velocity, when [S] >> K_M. Under these conditions, the maximum rate is related to k_{cat} and [E] via Eq. 5.8:

$$\left.\frac{d[P]}{dt}\right|_{max} = k_{cat}[E] \qquad \text{(Eq. 5.8)}$$

Finally, the reaction efficiency ε can be estimated from Eq. 5.9:

$$\varepsilon = \frac{k_{cat}}{K_M} \qquad \text{(Eq. 5.9)}$$

Lilly and Hornby obtained Eq. 5.2 (main paper) by integrating the Michaelis-Menten rate equation with the boundary conditions for substrate concentrations at the inlet $[S]_i$ and outlet $[S]_f$, thereby yielding Eq. 5.10:

$$([S]_i - [S]_f) - K_{M(app)} \operatorname{Ln} \frac{[S]_f}{[S]_i} = k_{cat} \left(\frac{[E]}{Q}\right)(\beta) \qquad \text{(Eq. 5.10)}$$

where β is the ratio of the reactor void volume to the total reactor volume. With knowledge of the reactor conditions, Eq. 5.10 can be written in the form shown in Eq. 5.11 to describe $K_{M(app)}$ as a function of the flow rate, Q ($mL \cdot s^{-1}$).[274]

$$([Ac]_i - [Ac]_f) - K_{M(app)} \operatorname{Ln} \frac{[Ac]_f}{[Ac]_i} = k_{cat} \left(\frac{[E]}{Q}\right)(\beta) \qquad \text{(Eq. 5.11)}$$

Equation 5.11 is equivalent to the Eq. 5.2, based on the definition of substrate conversion fraction, $P = \frac{[S]_i - [S]_f}{[S]_i}$, and the device reaction capacity, $C = k_{cat}[E]\,\beta$.

5.6.6 Verification of efficient electron transfer kinetics

To attribute the changes in electric current to Michaelis-Menten kinetics during manipulations of flow, the electron transfer rate must not be rate-limiting compared with the nutrient conversion step. In addition to the use of graphite WE and CE to improve charge transfer and efficient oxygen reduction reactions over long experimental durations,[283] a direct evaluation of the role of electron transfer kinetics was undertaken. Blending the the Nernst and Michaelis–Menten equations has been used to model the steady-state kinetics of an enzyme/electrode redox systems, including for electroactive biofilms.[81] For such a system where $[Ac] \gg K_M$, Michaelis-Menten kinetics result in a maximum current, I_{max}, yielding Eq. 5.12, which shows the role of applied potential (E) on the current.

$$I = I_{max}\left\{\frac{1}{1+\exp\left[-\frac{F}{RT}(E-E_{KA})\right]}\right\} \qquad \text{(Eq. 5.12)}$$

where R is the ideal gas constant (8.3145 $J.mol^{-1}.K^{-1}$), F is the Faraday constant (9.6485 $x10^{4}$ $C.mol^{-1}$), T is the temperature (K), and E_{KA} (V) is related to the standard reduction potential of proteins associated with respiration. Applying a potential $E=E_{KA}$ gives the half maximum activity, resulting in $I=1/2\cdot I_{max}$ somewhat similar to the role of K_M for concentration in the Michaelis-Menten kinetics. Under ideal behaviour, current should follow the typical S-curve generated by the Nernst term in Eq. 5.6. Moreover, if $E>>E_{KA}$, the electron transfer is rapid and not limiting, causing the term to reduce to 1. In this case the metabolic turnover of Ac is the rate limiting process, and the Michaelis-Menten kinetics can be used to describe the catalytic process.

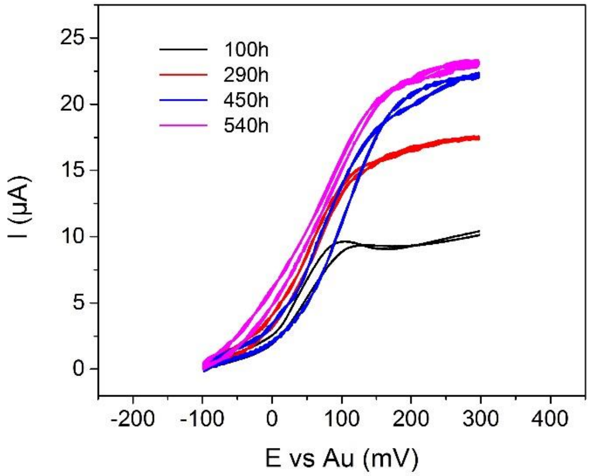

Figure 5.6 CV curves of G. sulfurreducens biofilm during growth for 100 h (black curve), 290 h (red curve), 450 h (blue curve) and 540 h (pink curve) after inoculation.

As observed in Figure 5.6, S-shape curves were produced, with E_{KA} being measured between near 30 to 50 mV vs. Au. The characteristic S-shape cyclic voltammograms showed a limiting current at high applied potentials between 150 and 250 mV vs. Au. The values of the limiting current increased with age of the biofilm before and during maturity, as expected. As electron transfer in the limiting current portion of the voltammogram indicate efficient electron transfer, 400 mV vs. Au was applied during all chronoamperometry experiments to ensure operation in the current limiting window. In this case the Nernst factor in the Nernst-Michalis-Menten kinetics[81] reduced to 1 (Eq. 5.12) and manipulation of [Ac] during chronoamperometry should be described by the modified Michaelis-Menten equation (Eq. 5.4).

In addition, to the above, we verified the flow independence of the EAB discharge rate as an indicator of flow sensitivity to electron transfer. This is important since flow-dependant conditions, i.e., shear stress, can change by over 10 times in the flow conditions used in this work (See Table 5.1, section 5.6.9). To accomplish this, we looked at the discharge rate for mature biofilms under different flow rates after 10 min exposure to open circuit voltage (OCV) for [Ac] = 0.3 and 10 mM. Immediately following reconnection to chronoamperometic conditions (400 mV vs. Au), current jumped to a maximal value, followed by an exponential decline (Figure 5.7). The nearly identical discharge curves under different flow rates demonstrated that electron transfer kinetics are not altered during the manipulation of flow and Michaelis–Menten kinetics remain relevant for the description of the rate limiting metabolic turnover of Ac.

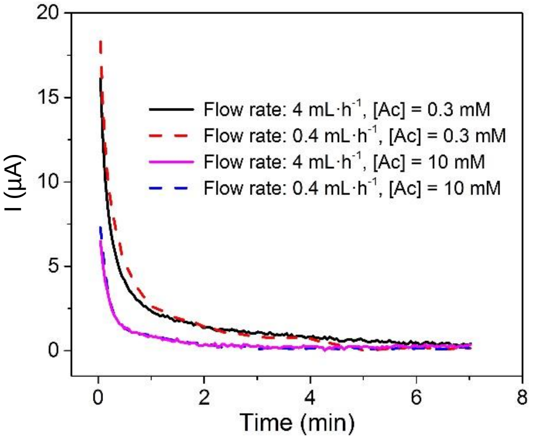

Figure 5.7 Discharge curves on mature biofilm (540 h growth) at 2 different flow rates and nutrient concentrations following 10 min of charging under OCV conditions. Current acquisition was conducted after switching from OCV to 400 mV vs. Au.

5.6.7 Initial biofilm growth in microfluidic electrochemical cell

Initial electrochemical growth of *G. sulfurreducens* is continuously monitored by CA electrochemical technique from 0 to 140 h (Figure 5.8). After lag-phase, a rapidly increasing anodic (oxidation) current was measured indicating *G. sulfurreducens* biofilm growth at the WE. The WE was poised on an oxidative potential of 400 mV vs Au (0 V vs. Ag/AgCl). *G. sulfurreducens* biofilm growth in microfluidic electrochemical cell and pseudo-reference electrode studies (stability, electrochemical potential vs. Ag/AgCl and consistency with flow) has been reported before.[242]

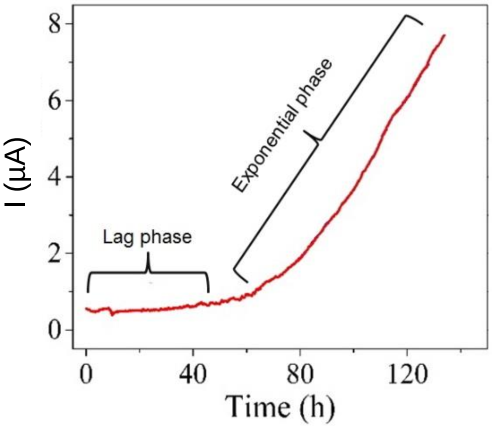

Figure 5.8 Initial electrochemical growth of *G. sulfurreducens.*

5.6.8 Bulk set-up for bacterial growth and measurements of K_M

Figure 5.9a shows growth curves for *G. sulfurreducens* electroactive biofilm on graphite WE in bulk 3-electrode cells. Bulk experiments were done in an electrochemical cell inside an anaerobic chamber. The graphite working electrode (WE) and counter electrode (CE) were cut into 0.5 cm × 0.5 cm for WE and 1 cm × 1 cm for CE. A hole was made by a drill press and a wire was looped and fastened through it and covered by epoxy glue. An Ag/AgCl, 3M KCl was used as a reference electrode. A 100 mL electrochemical cell chamber with 4-hole rubber cap was setup with 3-electrode configuration set-up and a gas tube for purging with

20% CO_2 / 80% N_2. A 10 mM acetate growth medium, with no fumarate was used for *G. sulfurreducens* growth on the WE at 0 V vs. Ag/AgCl reference electrode. This potential was verified to be the same as 400 mV vs. Au, which was used for microfluidic experiments. After maturation with a steady state current output for 2 days, the nutrient aqueous solution was changed with different acetate concentration solutions and the current was recorded for approximately 90 min.

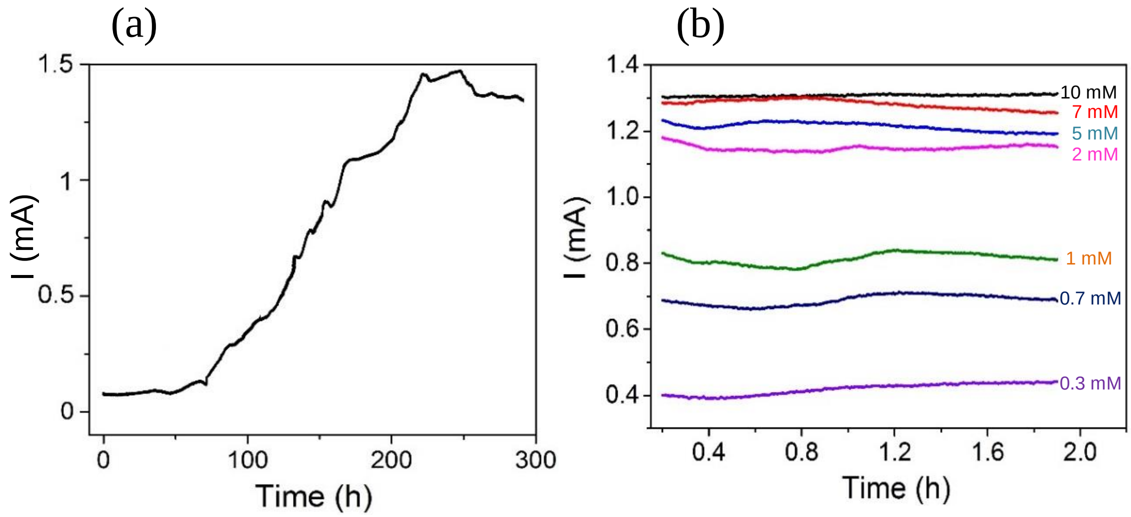

Figure 5.9 (a) CA curve of *G. sulfurreducens* biofilm growth in an electrochemical cell chamber with 10 mM acetate nutrient (WE potential: 0 V vs Ag/AgCl), **(b)** CA curves of *G. sulfurreducens* biofilm at different acetate concentrations. The current output from G. sulfurreducens biofilm has been recorded after reaching to steady state conditions for around 90 min.

5.6.9 Influence of flow on reactor parameters

Table 5.1 lists several parameters as a function of flow rate, Q. First the average linear channel flow velocity ($\bar{v}_c$) is compared with the average proton diffusion velocity ($\bar{v}_{d_{H^+}}$). This shows that upstream diffusion of protons from the WE where they are generated, is always slower than the average flow velocity. Therefore, the pH at the RE is never affected by down-stream oxidation process, since proton diffusion is faster than any other by-products. The reader is directed to other works using a similar microfluidic electrochemical flow cell, where this point is discussed in more detail.[209,242] Second, calculation of the Reynold's number (Re) shows that flow is strictly laminar at all flow rates in this work. Third, the average shear stress ($\bar{\tau}$) quantifies tangential forces against the electrode-adhered *G. sulfurreducins* biofilm. Finally, the apparent Michaelis-Menten constant, $K_{M(app)}$, and the device reaction capacity, C, are given. These are the result of linear fitting of curve in Figure 5.3b, resulting from the Lilly-Hornby equation (Eq. 5.2). Calculations for $K_{M(app)}$ and C are derived from the peak I values (Figure 5.2), not from the baseline flow rates (Q = 0.2 mL/h).

Table 5.1. Tabulation of changes to mean proton diffusion velocity ($\bar{v}_{d^{H^+}}$), channel flow velocity ($\bar{v}_c$), Reynolds number (Re), shear stress ($\bar{\tau}$), Apparent Michaelis-Menten constant ($K_{m(app)}$) and device reaction capacity (C).

Q ($mL \cdot h^{-1}$)	$\bar{v}_{d^{H^+}}$ (constant) ($mm \cdot h^{-1}$)	$\bar{v}_c$ ($mm \cdot h^{-1}$)	Re	$\bar{\tau}$ (mPa)	$K_{m(app)}$ (µM)	C (nmol/h)
0.2	8	250	0.028	1.04	N/A	N/A
0.4		500	0.056	2.08	572	116
0.6		750	0.083	3.13	561	120
0.8		1000	0.111	4.17	551	123
2		2500	0.278	10.42	521	136
3		3750	0.417	15.63	466	138

5.6.10 Trends in the device reaction capacity

The device reaction capacity, C (mol/h) relates the catalytic rate constant (k_{cat}), biocatalytical concentration ([E]) and void fraction ratio β, via $C = k_{cat} \cdot [E] \cdot \beta$. As explained in the main paper, assuming invariability of k_{cat} and β, flow-induced changes to C can be interpreted as changes to [E], the amount of involved bacterial catalyst in contact with the nutrient aqueous solution. Figure 5.10 plots values of C from Table 5.1 against Q. Non-linear increases to C with Q demonstrate increases to [E]. It is hypothesized that this is due to forced convection through the biofilm. Calculating the Δ[C]/[C]×100% at Q=0.4 to Q=3, an increase of 22% is noted. Extrapolation backwards to Q=0 is not obvious due to the non-linear nature of C, but an estimation of 109 nmol/h is obtained using the three data points from the lowest flow rates, in the linear portion of the figure. Thus C=138 at 3 mL/h marks an increase of approximately 27% over estimated Q=0 values, and an equivalent increase in contacted *G. sulfurreducens* by the nutrient solution. With the assumption that changes in C are the result of changes in [E] we estimate that elevated flow rates of Q=3 mL·h^{-1} increased [E] by 22% and 27% over Q = 0.4 and static conditions, respectively.

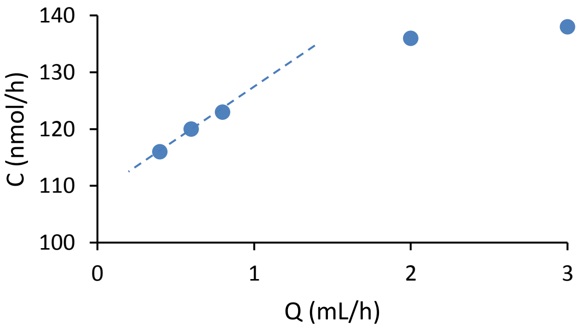

Figure 5.10 Changes in device reaction capacity with flow rate, using data from Table 5.1. The blue dotted line extrapolates backwards the trends from the linear portion of the curve to static flow conditions at Q=0.

5.6.11 Trends in $K_{M(app)}$ and reaction mechanisms

The reaction mechanism for this work can be clarified based on the Michaelis-Menten kinetic model. For example, considering Eq. 5.1 in the main paper, flow-induced reductions to $K_{M(app)}$ indicate a progressive increase in the complex ES with increasing Q. In other words, higher local concentrations of Ac availability at the biofilm/liquid interface can occur due to increased convective flux and related reductions in diffusion barriers, which can result in more efficient Ac capture by the bacteria and rapid complexation with cell-bound enzymes, followed by a final oxidation to electrons and other by-products. Thus, the reason for the increased peak current values in Figure 5.2 is understood to be the result of higher catalytic reaction rate in Eq. 1, i.e., $d[P] / dt = k_{cat} [ES]$. The use of the Lilly-Hornby model demonstrates both similar and dissimilar trends from other literature examples using flow channels packed with microbead-immobilized enzymes.[274,87,88] In assaying the effect of flow rate on $K_{M(app)}$ for enzyme systems, less emphasis has been placed on the implications of the underlying reaction mechanisms. For example, other studies have shown that $K_{M(app)}$ becomes reduced with increasing flow rate.[283] This could be because under diffusion-limited conditions flow-induced reductions to diffusion barriers can result in increased concentration near the enzyme and increase the associated enhancement of substrate-enzyme complexation. For those studies in which $K_{M(app)}$ increases with Q, it is probably because reduced liquid/biofilm contact times and the observed accumulation of deposited substrate at the support surface, resulted in less formation ES.[81] We suggest that this observation might be due to slow preliminary complexation (low k_a) or fast decomplexation (high k'_a). In other studies, $K_{M(app)}$ was observed to remain unchanged with flow,[88] indicating that substrate binding was not rate-limiting.

Chapter 6. Perspectives and future works

6.1 Master curve of {flow rate – nutrient concentration – bacterial activity} in *G. sulfurreducens* biofilm

During research on *G. sulfurreducens* biofilms in microfluidic electrochemical cells, several new discoveries were made regarding biofilm activity under precise flow and nutrient medium concentrations which require further studies. Our broad goal is to devise a comprehensive map that relates both flow rate and nutrient concentrations to electroactive biofilm activity for the first time. The work in Chapter 4 is a starting point a low concentrations, but it should be extended into higher concentrations to provide a more comprehensive picture. As a preliminary overview a series of nutrient concentration changes were applied on mature *G. sulfurreducens* biofilm at different flow rates using a microfluidic electrochemical cell. The changes of flow rates for reactivation procedure of a mature biofilm after temporary exposure to 0 mM acetate by exposure to higher concentrations: 20, 10, 7, 2, 0.85, 0.7 and 0.2 mM of nutrient (acetate) were plotted. Trends were observed by analysing the details data during the reactivation of a dormant biofilm via analysis of current vs. time profiles An example of the effect of flow rates on activation of *G. sulfurreducens* biofilm in high (10 mM) and low (0.2 mM) nutrient concentration was shown at Figure 6.1 a. Plotting current output during biofilm reactivation and extracting an exponential growth constant (via exponential fitting) resulted in a universal master curve. Figure 6.1 b demonstrates 2 examples of 0.25 mL·h^{-1} flow rate in 10 mM acetate nutrient (solid line) and 0.2 mM (dash line) with exponential growth constant (k) values.

Figure 6.1 c shows the curve of constant growth, k (μA·h^{-1}), (which were calculated by exponential fitting of current – time curve in different flow rates and nutrient concentration) vs. flow rate. By extrapolating the curves, two concentrations (0.2 and 0.7 mM) have positive x-axe value which can be referred to minimum flow rate requirement for reactivation of mature *G. sulfurreducens* biofilm and higher concentrations can reactive the biofilm at zero flow rate (static) condition.

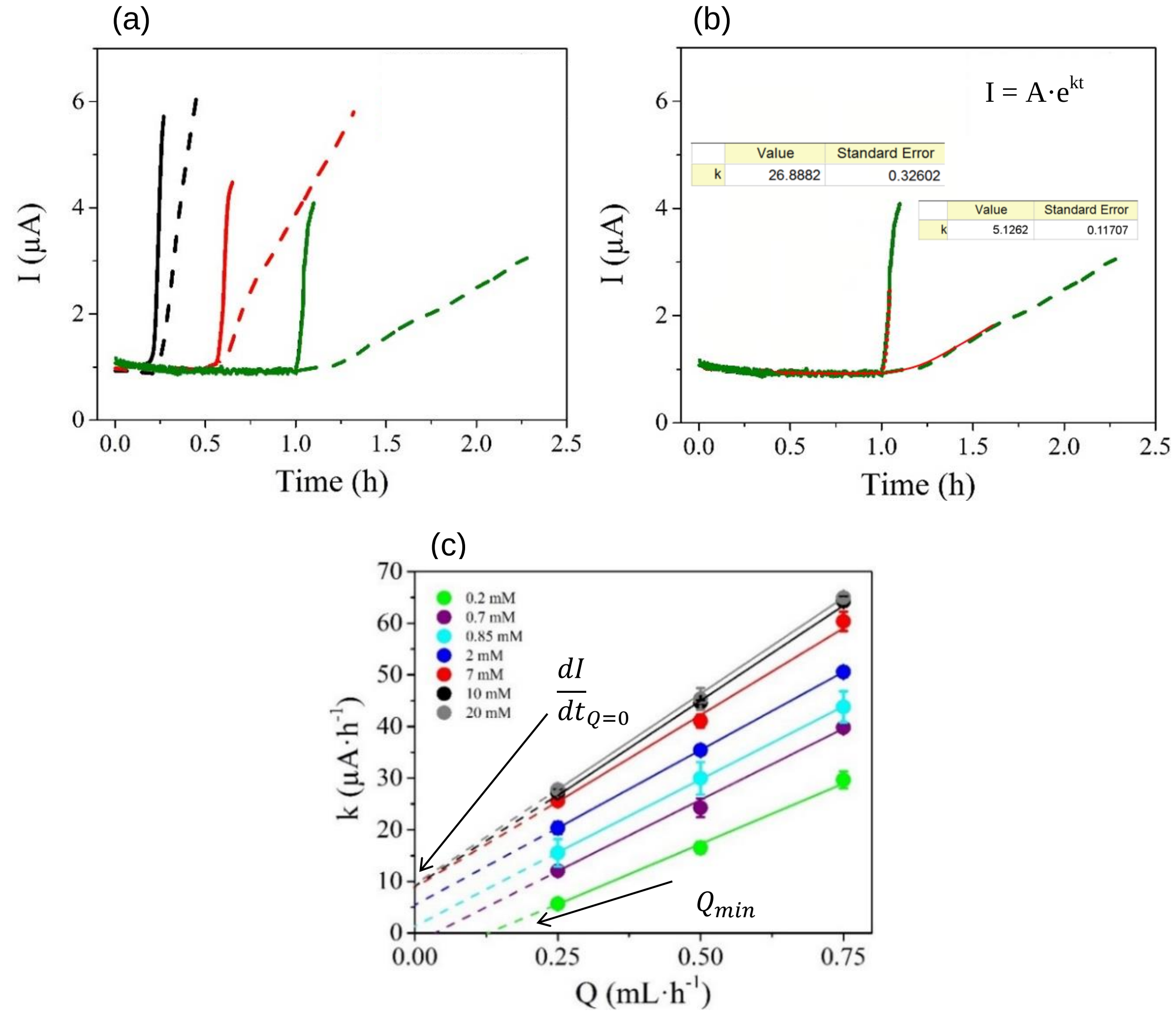

Figure 6.1 (a) Initial current versus time plots for reactivation of a mature G. sulfurreducens biofilm upon switching from [Ac]=0 mM to [Ac]=10 mM (solid lines) and [Ac]=0.2 mM (dash lines) nutrient solution at Q=0.75 mL·h^{-1} (black), Q=0.5 mL·h^{-1} (red), Q= 0.25 mL·h^{-1} (green). The time t=0 was the time of switching to the Ac containing solution and the delay in the increase to the current was due to the time required for the new solution to reach the biofilm. **(b)** Two examples of 0.25 mL·h^{-1} flow rate in 10 mM acetate nutrient (solid line) and 0.2 mM (dash line) with exponential growth constant (k) values. Red lines shows fitting curves for exponential growth. **(c)** Trends in the reactivation growth constant (μA·h^{-1}) vs. Q (mL·h^{-1}) after switching to 20 mM (gray), 10 mM (black), 7 mM (red), 2 mM (blue), 0.85 mM (blue light), 0.7 mM (purple) 0.2 mM (green) from [Ac]=0 mM conditions. Error bars were acquired from at least three separate experiments and were smaller than the data points in many cases. The dashed lines show linear fit for each data set, which were extrapolated backward to obtain predicted minimum the reactivation growth constant, dI/dt$_{min}$ (at Q=0) and the minimum flow rate, Q$_{min}$, required achieve a biofilm reactivation for [Ac]=0.2 mM.

On the other hand, in high concentrations (7 – 20 mM), k constants reached to similar values. This complex curve needs more studies for better understanding of different aspects of flow rate and nutrient concentration for reactivation of mature electroactive biofilm.

6.2 Spectroelectrochemistry for electroactive bacteria studies

A second new direction that can follow from this thesis can include new analytical platforms for spectroelectrochemistry of EABs. Spectroelectrochemistry combines spectroscopy with electrochemistry while this is correlated with the changes in the spectral signature, generally from IR to UV range, of electroactive compounds above an electrode posed at a selected (oxidative or reductive) potential.[284] The first related reports of using spectroelectrochemical techniques date back to approximately 30 years ago, where it was used to identify the redox state of metalloproteins such as heme-containing cytochromes in purified proteins.[285] This technique subsequently been used monitor the redox state of similar proteins in EABs. For example, a UV/VIS spectroelectrochemical experiment on c-type cytochromes of *Shewanella loihica* PV-4 (a well-known electroactive bacteria)[286] and a study on the redox state of c-type cytochromes on *G. sulfurreducens* cells attached to gold electrodes by applying attenuated total reflection surface enhanced infrared absorption spectroscopy (ATR-SEIS) have been reported before.[287] These spectroelectrochemical experiments are getting attention of researchers for measurement of live cells (EABs) to better understand of the bacterial outer membrane/electrode interaction. Figure 6.2 shows a proposed setup for an ATR-IR electrochemical cell for IR-spectroelectrochemical measurements.

A microfluidic electrochemical cell can easily provide measurements for FTIR spectroscopy and simultaneous electrochemical analysis during biofilm growth and after maturation with manipulation of flow rates and nutrient concentrations. Together such an approach holds the potential to open a new information-dense approach for better understanding of bioelectrochemical processes in living microbial systems.

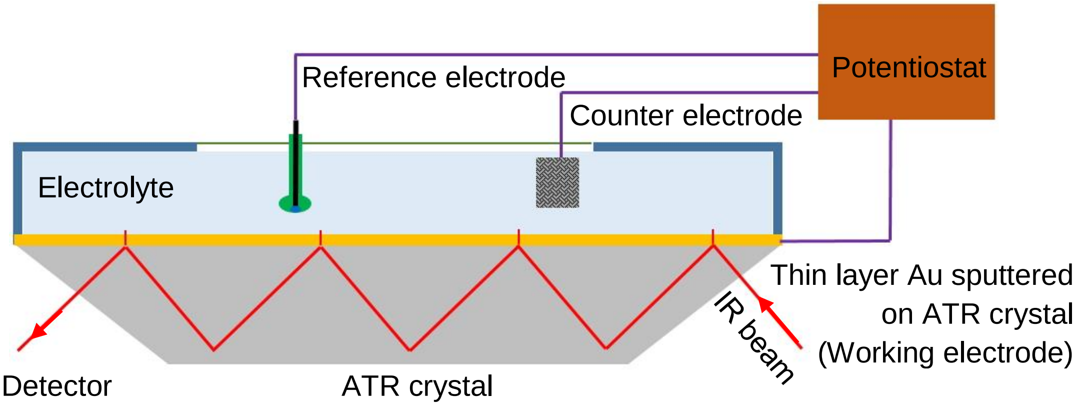

Figure 6.2 A schematic of ATR-IR electrochemical cell for which can be used for IR-spectroelectrochemical studies of *G. sulfurreducens* cells.

6.3 Direct interspecies electron transfer (DIET)

Direct interspecies electron transfer (DIET) is a recently discovered EET strategy where cell-to-cell electron transfer occurs between syntrophic (cross-feeding) microbial species.[288] DIET can be engineered via the addition of various non-biological conductive materials such as graphite and inert metals for improvement DIET process or study of EET between different species.[289,290] In recent years, understanding and optimization of the DIET process has increased which has led to improvements of anaerobic digestion.[291] Generally, metabolic capabilities of microorganisms can use chemically diverse, soluble organic substrates for their growth. Recently several high-profile studies have been conducted on different bacterial co-culture such as *Prosthecochloris aestuarii* / *Geobacter Sulfurreducens*,[292] *Desulfovibrio vulgaris* / *Clostridium acetobutylicum*[293] and *C. methanogenesis* microorganisms.[294,295,296] A tight association with the two species is formed in a bacterial aggregation. It seems that DIET can be also facilitated by an exchange of electron carrier proteins, such as ferredoxin[293] based on an observation of *Desulfovibrio vulgaris* and *Clostridium acetobutylicum* growth in co-culture.[293] All proposed DIET mechanisms need to be studied deeply in order to resolve the numerous questions that remain about the process and how to exploit it for new BES.

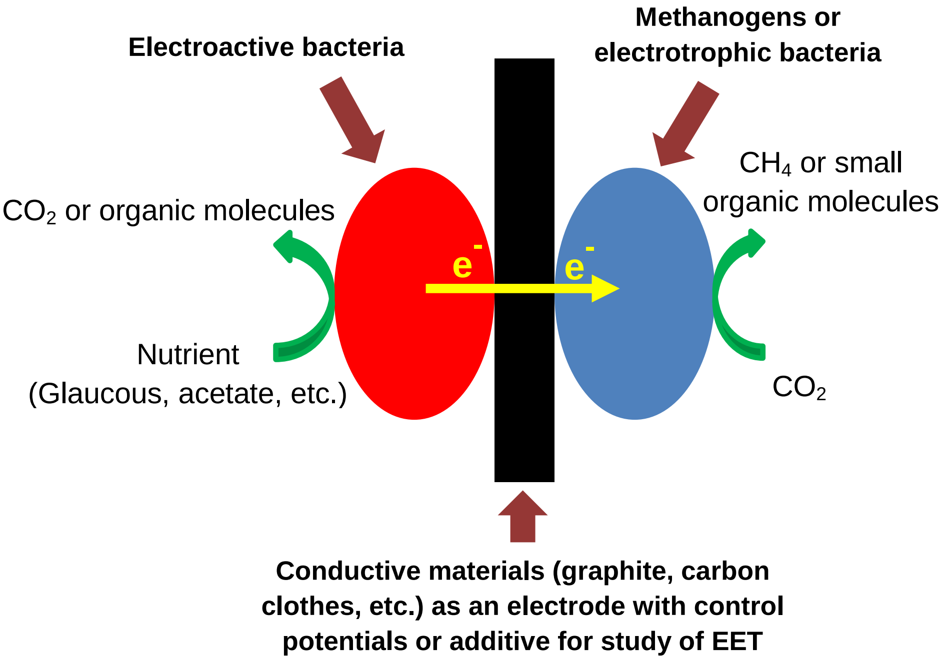

Figure 6.3 A simple proposed set up for DIET studies with different kind of microorganisms. By applying microfluidic tools can have an environment control or inputs and outputs of the system for EET investigation.

DIET also has the potential to drive more standard processes, such as those involving Methanogens (microbes known to produce methane), which have been getting increased attention in the last ten years.[297,298,299] Methanogens are strictly anaerobic microorganisms that do not grow using fermentation or alternative electron acceptors for respiration. They generate methane as the final product of metabolism by reducing CO_2 to CH_4.[297,300] Supplying the electrical conditions required for methanogens by electroactive bacteria, can result in a fully self-sufficient biological electrochemical system, with no external power requirements.[291] Generally, in most of anaerobic methanogenic environments, *Methanosaeta* species are predominant microbes.[301] *Methanogens* have been identified only from the domain archaea which are morphologically similar to bacteria but genes possession and metabolic pathways are more closely related to those of eukaryotes.[301] Several studies demonstrated that *Methanosaeta* species can engage in DIET in anaerobic digesters treating brewery waste.[302,303] Recently, in a co-culture of *Geobacter metallireducens* and *Methanosaeta*, directly transferred electrons from *G. metallireducens* to *Methanosaeta* for the reduction of CO_2 to CH_4 has been observed.[297] Also, it is believed that *Methanosarcina* species could accept electrons from non-biological extracellular surfaces as well as attached *Methanosarcina barkeri* onto granular activated carbon (GAC), which served as a mediator for electron transfer between *M. barkeri* and *G. metallireducens*.[304]

By using a microfluidic electrochemical cell, several research directions can be envisaged to enable better understanding and optimization of DIET. As a simple example, Figure 6.3 proposed a DIET between electroactive bacteria and two kinds of microorganisms (methanogens and electrode-oxidizing bacteria). By using a specific design of microfluidic electrochemical cell, we are able to manipulate EET between selected cultures. The behavior of microorganisms in different well-defined electrochemical potentials and shear stress can be precisely studied.

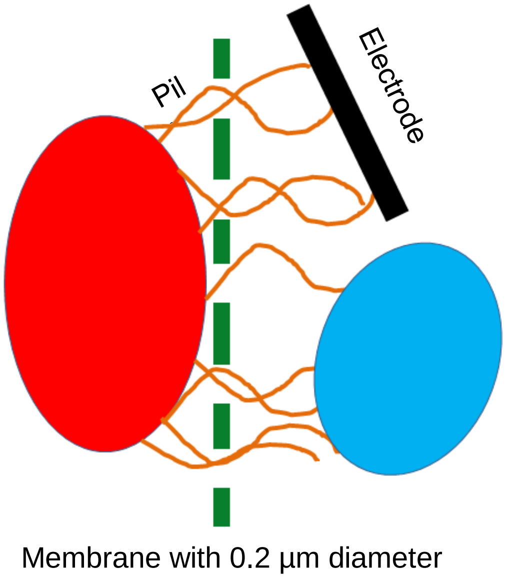

Figure 6.4 A simple proposed set up for pili separation from bacteria for DET or DIET studies with different kind of microorganisms.

As another example, Figure 6.4 shows a proposed setup for EET between electroactive bacteria and an electrode or another bacteria as DET or DIET via pili while there is no physical contact between cell membrane and electrode or electron acceptor bacteria. Preliminary tests conducted using a membrane (filter) with cylindrical channels having a diameter of under 0.2 µm showed promise as an approach to allow the pili nanowires be expanded through the membrane while the cell body remains isolated. Studies of EET through pili nanowires without involving the bacteria’s membrane cytochromes c can reveal valuable information about the nature of the pili attached to a living cell, thus complementing and moving beyond previous studies involving isolated pili. This can open the door for improvement of EET for future MFCs or better understanding DIET mechanism.

As a final thought, future members of our group can find comfort in this statement: *G. sulfurreducens* showed very good performance in microfluidic electrochemical cell (3-electrode configuration) and they can improve the device for being compatible with DIET experiments. The gold reference electrode is now well characterized in *G. sulfurreducens* growth medium and other electrodes demonstrated very good functionality. The others can modify it for a spectroelectrochemical measurement with ATR-IR or other spectroscopies such as Raman or UV-Vis. Several questions are unknown related to the triangle of nutrient concentration, metabolic activity and flow rate of nutrients in microchannel and for answering these questions; they should do some experiments to find the effects of hydrodynamic (mass transfer) through the mature biofilm.

Conclusion

This thesis has provided the details on the fabrication and use of a new 3-electrode configuration microfluidic electrochemical cell for electrochemical analysis of both electroactive and non-electroactive biofilms. In some cases, these were supported by measurements by microscopy and spectroscopic techniques. After an introduction to electrochemistry, bioelectrochemistry, microbiology and microfluidics in Chapter 1, Chapter 2 featured *in situ* EIS measurements of *Pseudomonas* sp., confined to the microchannel corners or middle by flow templated growth. The bioresistance and biocapacitance were defined and measured in different growth time. Optical microscopy, CLSM and ATR-IR verified and extended the electrochemical results. The effects of shear stresses applied to biofilms templated in the middle of the channel and their correlation with biocapacitance and bioresistance were revealed.

Chapter 3 presented studies of hydrodynamic effects and nutrient concentrations on changes to pH within electrode-adhered *G. sulfurreducens* electroactive biofilms. It was discovered that changes in hydrodynamic conditions could affect the acidity of *G. sulfurreducens* biofilms by mitigation of biofilm acidification, but not under turnover concentrations, which are the conditions used in most research studies. Nevertheless, the effect of flow-based deacidification was profound at low concentrations. As discussed below, this poses some interesting possibilities for optimization of BES performance in a wider range of relevant conditions.

Chapter 4 and 5 are the extension of the project, related to hydrodynamic and nutrient concentration manipulations, described in Chapter 3. In Chapter 4, we demonstrated flow – nutrient concentration dependency in generally low nutrient concentrations in a mature biofilm. Real-time current responses to concentration and flow rate changes enabled the identification of three separate metabolic states: active, inactive and a pseudo-active state. The latter was identified by our work for the first time. This work opens the door to new micro flow-based approaches to the optimisation of BESs involving *Geobacter* species, and may be instructive for other electroactive biofilm species as well.

In Chapter 5, we presented the compatibility of the Lilly-Hornby enzymatic reaction kinetic equation with live microorganisms for the first time. The Lilly-Hornby equation makes the link between the Michaelis constant, K_M, and its sensitivity to flow rate of the nutrient solutions. Specifically, this was accomplished for controlled flow conditions against an electrode-adhered *G. sulfurreducens* electroactive biofilm via measurements of the current produced under a constant applied electrochemical potential. This study can provide a straightforward method to verify kinetic constants in electroactive bacteria, with potential for improvements to MFC and other BES applications.

Bibliographie

---

[1] Bard, A. J.; Faulkner, L. R.; Leddy, J.; Zoski, C. G., *Electrochemical methods: fundamentals and applications*. wiley New York: 1980; Vol. 2.

[2] Metters, J. P.; Kadara, R. O.; Banks, C. E., New directions in screen printed electroanalytical sensors: an overview of recent developments. *Analyst* **2011,** *136* (6), 1067-1076.

[3] Palacin, M. R., Recent advances in rechargeable battery materials: a chemist's perspective. *Chemical Society Reviews* **2009,** *38* (9), 2565-2575.

[4] Carrette, L.; Friedrich, K.; Stimming, U., Fuel cells–fundamentals and applications. *Fuel cells* **2001,** *1* (1), 5-39.

[5] Schlesinger, M.; Paunovic, M., *Modern electroplating*. John Wiley & Sons: 2011; Vol. 55.

[6] Gibilaro, M.; Massot, L.; Chamelot, P.; Cassayre, L.; Taxil, P., Electrochemical extraction of europium from molten fluoride media. *Electrochimica Acta* **2009,** *55* (1), 281-287.

[7] Roberge, P. R., *Handbook of corrosion engineering*. McGraw-Hill: 2000.

[8] Logan, B. E.; Call, D.; Cheng, S.; Hamelers, H. V.; Sleutels, T. H.; Jeremiasse, A. W.; Rozendal, R. A., Microbial electrolysis cells for high yield hydrogen gas production from organic matter. *Environmental science & technology* **2008,** *42* (23), 8630-8640.

[9] Logan, B. E., *Microbial fuel cells*. John Wiley & Sons: 2008.

[10] Atanassov, P.; Apblett, C.; Banta, S.; Brozik, S.; Barton, S. C.; Cooney, M.; Liaw, B. Y.; Mukerjee, S.; Minteer, S. D., Enzymatic biofuel cells. *Interface-Electrochemical Society* **2007,** *16* (2), 28-31.

[11] Rabaey, K.; Rozendal, R. A., Microbial electrosynthesis—revisiting the electrical route for microbial production. *Nature Reviews Microbiology* **2010,** *8* (10), 706.

[12] Nguyen, N.-T.; Wereley, S. T.; Wereley, S. T., *Fundamentals and applications of microfluidics*. Artech house: 2002.

[13] Bockris, J. O. M.; Conway, B. E.; White, R. E., *Modern aspects of electrochemistry*. Springer Science & Business Media: 2012; Vol. 22.

[14] Lasia, A., Electrochemical impedance spectroscopy and its applications. In *Modern aspects of electrochemistry*, Springer: 2002; pp 143-248.

---

[15] Barsoukov, E.; Macdonald, J. R., *Impedance spectroscopy: theory, experiment, and applications*. John Wiley & Sons: 2018.

[16] Alkire, R. C.; Kolb, D. M.; Lipkowski, J., *Bioelectrochemistry: fundamentals, applications and recent developments*. John Wiley & Sons: 2011; Vol. 13.

[17] Guo, C. X.; Zheng, X. T.; Lu, Z. S.; Lou, X. W.; Li, C. M., Biointerface by cell growth on layered graphene–artificial peroxidase–protein nanostructure for in situ quantitative molecular detection. *Advanced Materials* **2010,** *22* (45), 5164-5167.

[18] Grieshaber, D.; MacKenzie, R.; Voeroes, J.; Reimhult, E., Electrochemical biosensors-sensor principles and architectures. *Sensors* **2008,** *8* (3), 1400-1458.

[19] Wang, J., Electrochemical biosensors: towards point-of-care cancer diagnostics. *Biosensors and Bioelectronics* **2006,** *21* (10), 1887-1892.

[20] Hamelers, H. V.; Ter Heijne, A.; Sleutels, T. H.; Jeremiasse, A. W.; Strik, D. P.; Buisman, C. J., New applications and performance of bioelectrochemical systems. *Applied microbiology and biotechnology* **2010,** *85* (6), 1673-1685.

[21] Ronkainen, N. J.; Halsall, H. B.; Heineman, W. R., Electrochemical biosensors. *Chemical Society Reviews* **2010,** *39* (5), 1747-1763.

[22] Krikstolaityte, V.; Kuliesius, J.; Ramanaviciene, A.; Mikoliunaite, L.; Kausaite-Minkstimiene, A.; Oztekin, Y.; Ramanavicius, A., Enzymatic polymerization of polythiophene by immobilized glucose oxidase. *Polymer* **2014,** *55* (7), 1613-1620.

[23] Daniels, J. S.; Pourmand, N., Label-free impedance biosensors: Opportunities and challenges. *Electroanalysis* **2007,** *19* (12), 1239-1257.

[24] Hernandez-Vargas, G.; Sosa-Hernández, J.; Saldarriaga-Hernandez, S.; Villalba-Rodríguez, A.; Parra-Saldivar, R.; Iqbal, H., Electrochemical biosensors: a solution to pollution detection with reference to environmental contaminants. *Biosensors* **2018,** *8* (2), 29.

[25] Yang, L.; Bashir, R., Electrical/electrochemical impedance for rapid detection of foodborne pathogenic bacteria. *Biotechnology advances* **2008,** *26* (2), 135-150.

[26] Ou, Y.; Buchanan, A. M.; Witt, C. E.; Hashemi, P., Frontiers in electrochemical sensors for neurotransmitter detection: towards measuring neurotransmitters as chemical diagnostics for brain disorders. *Anal. Methods* **2019,** 11, 2738-2755.

[27] Wang, J., Electrochemical glucose biosensors. *Chemical reviews* **2008,** *108* (2), 814-825.

[28] Heller, A.; Feldman, B., Electrochemical glucose sensors and their applications in diabetes management. *Chemical reviews* **2008,** *108* (7), 2482-2505.

[29] Dong, J.; Zhou, X.; Zhao, H.; Xu, J.; Sun, Y., Reagentless amperometric glucose biosensor based on the immobilization of glucose oxidase on a ferrocene@ NaY zeolite composite. *Microchimica Acta* **2011,** *174* (3-4), 281-288.

[30] Martín-Yerga, D.; Costa-García, A., Towards a blocking-free electrochemical immunosensing strategy for anti-transglutaminase antibodies using screen-printed electrodes. *Bioelectrochemistry* **2015,** 105, 88-94.

[31] Amiri, M.; Bezaatpour, A.; Jafari, H.; Boukherroub, R.; Szunerits, S., Electrochemical methodologies for the detection of pathogens. *ACS sensors* **2018,** *3* (6), 1069-1086.

[32] Katz, E.; Willner, I., Probing biomolecular interactions at conductive and semiconductive surfaces by impedance spectroscopy: routes to impedimetric immunosensors, DNA-sensors, and enzyme biosensors. *Electroanalysis: An International Journal Devoted to Fundamental and Practical Aspects of Electroanalysis* **2003,** *15* (11), 913-947.

[33] Knichel, M.; Heiduschka, P.; Beck, W.; Jung, G.; Göpel, W., Utilization of a self-assembled peptide monolayer for an impedimetric immunosensor. *Sensors and Actuators B: Chemical* **1995,** *28* (2), 85-94.

[34] Rickert, J.; Göpel, W.; Beck, W.; Jung, G.; Heiduschka, P., A ‘mixed’self-assembled monolayer for an impedimetric immunosensor. *Biosensors and Bioelectronics* **1996,** *11* (8), 757-768.

[35] Luo, X.; Davis, J. J., Electrical biosensors and the label free detection of protein disease biomarkers. *Chemical Society Reviews* **2013,** *42* (13), 5944-5962.

[36] Santos, A.; Davis, J. J.; Bueno, P. R., Fundamentals and applications of impedimetric and redox capacitive biosensors. *J. Anal. Bioanal. Tech* **2014,** *7* (016), 1-15.

[37] Alfonta, L.; Katz, E.; Willner, I., Sensing of acetylcholine by a tricomponent-enzyme layered electrode using faradaic impedance spectroscopy, cyclic voltammetry, and microgravimetric quartz crystal microbalance transduction methods. *Analytical chemistry* **2000,** *72* (5), 927-935.

[38] Patolsky, F.; Zayats, M.; Katz, E.; Willner, I., Precipitation of an insoluble product on enzyme monolayer electrodes for biosensor applications: characterization by faradaic impedance spectroscopy, cyclic voltammetry, and microgravimetric quartz crystal microbalance analyses. *Analytical chemistry* **1999,** *71* (15), 3171-3180.

[39] Fletcher, M.; Savage, D. C., *Bacterial adhesion: mechanisms and physiological significance*. Springer Science & Business Media: 2013.

[40] Flemming, H.-C.; Wingender, J., The biofilm matrix. *Nature reviews microbiology* **2010,** *8* (9), 623.

---

[41] Renner, L. D.; Weibel, D. B., Physicochemical regulation of biofilm formation. *MRS bulletin* **2011,** *36* (5), 347-355.

[42] Peterson, B. W.; He, Y.; Ren, Y.; Zerdoum, A.; Libera, M. R.; Sharma, P. K.; Van Winkelhoff, A.-J.; Neut, D.; Stoodley, P.; Van Der Mei, H. C., Viscoelasticity of biofilms and their recalcitrance to mechanical and chemical challenges. *FEMS microbiology reviews* **2015,** *39* (2), 234-245.

[43] Oliver, S. P.; Jayarao, B. M.; Almeida, R. A., Foodborne pathogens in milk and the dairy farm environment: food safety and public health implications. *Foodbourne Pathogens & Disease* **2005,** *2* (2), 115-129.

[44] Li, N.; Brahmendra, A.; Veloso, A. J.; Prashar, A.; Cheng, X. R.; Hung, V. W.; Guyard, C.; Terebiznik, M.; Kerman, K., Disposable immunochips for the detection of Legionella pneumophila using electrochemical impedance spectroscopy. *Analytical chemistry* **2012,** *84* (8), 3485-3488.

[45] Brosel-Oliu, S.; Uria, N.; Abramova, N.; Bratov, A., Impedimetric sensors for bacteria detection. In *Biosensors-Micro and Nanoscale Applications*, InTech: 2015.

[46] Ista, L. K.; Mendez, S.; Lopez, G. P., Attachment and detachment of bacteria on surfaces with tunable and switchable wettability. *Biofouling* **2010,** *26* (1), 111-118.

[47] Kang, J.; Kim, T.; Tak, Y.; Lee, J.-H.; Yoon, J., Cyclic voltammetry for monitoring bacterial attachment and biofilm formation. *Journal of Industrial and Engineering Chemistry* **2012,** *18* (2), 800-807.

[48] Wang, Y.; Ye, Z.; Ying, Y., New trends in impedimetric biosensors for the detection of foodborne pathogenic bacteria. *Sensors* **2012,** *12* (3), 3449-3471.

[49] Kim, T.; Kang, J.; Lee, J.-H.; Yoon, J., Influence of attached bacteria and biofilm on double-layer capacitance during biofilm monitoring by electrochemical impedance spectroscopy. *Water research* **2011,** *45* (15), 4615-4622.

[50] Bekir, K.; Barhoumi, H.; Braiek, M.; Chrouda, A.; Zine, N.; Abid, N.; Maaref, A.; Bakhrouf, A.; Ouada, H. B.; Jaffrezic-Renault, N., Electrochemical impedance immunosensor for rapid detection of stressed pathogenic Staphylococcus aureus bacteria. *Environmental Science and Pollution Research* **2015,** *22* (20), 15796-15803.

[51] Ruan, C.; Yang, L.; Li, Y., Immunobiosensor chips for detection of Escherichia c oli O157: H7 using electrochemical impedance spectroscopy. *Analytical Chemistry* **2002,** *74* (18), 4814-4820.

[52] Bajracharya, S.; Sharma, M.; Mohanakrishna, G.; Benneton, X. D.; Strik, D. P.; Sarma, P. M.; Pant, D., An overview on emerging bioelectrochemical systems

(BESs): technology for sustainable electricity, waste remediation, resource recovery, chemical production and beyond. *Renewable Energy* **2016,** *98*, 153-170.

[53] Harnisch, F.; Freguia, S., A basic tutorial on cyclic voltammetry for the investigation of electroactive microbial biofilms. *Chemistry–An Asian Journal* **2012,** *7* (3), 466-475.

[54] Sevda, S.; Yuan, H.; He, Z.; Abu-Reesh, I. M., Microbial desalination cells as a versatile technology: functions, optimization and prospective. *Desalination* **2015,** *371*, 9-17.

[55] Schröder, U., Anodic electron transfer mechanisms in microbial fuel cells and their energy efficiency. *Physical Chemistry Chemical Physics* **2007,** *9* (21), 2619-2629.

[56] Wang, H.; Ren, Z. J., Bioelectrochemical metal recovery from wastewater: a review. *Water research* **2014,** *66*, 219-232.

[57] Borole, A. P.; Reguera, G.; Ringeisen, B.; Wang, Z.-W.; Feng, Y.; Kim, B. H., Electroactive biofilms: current status and future research needs. *Energy & Environmental Science* **2011,** *4* (12), 4813-4834.

[58] Babauta, J.; Renslow, R.; Lewandowski, Z.; Beyenal, H., Electrochemically active biofilms: facts and fiction. A review. *Biofouling* **2012,** *28* (8), 789-812.

[59] Bond, D. R.; Lovley, D. R., Electricity production by *Geobacter sulfurreducens* attached to electrodes. *Applied and environmental microbiology* **2003,** *69* (3), 1548-1555.

[60] Kim, H. J.; Park, H. S.; Hyun, M. S.; Chang, I. S.; Kim, M.; Kim, B. H., A mediator-less microbial fuel cell using a metal reducing bacterium, *Shewanella putrefaciens*. *Enzyme and Microbial technology* **2002,** *30* (2), 145-152.

[61] Rabaey, K.; Verstraete, W., Microbial fuel cells: novel biotechnology for energy generation. *TRENDS in Biotechnology* **2005,** *23* (6), 291-298.

[62] Zhao, J.; Li, X. F.; Ren, Y. P.; Wang, X. H.; Jian, C., Electricity generation from Taihu Lake cyanobacteria by sediment microbial fuel cells. *Journal of Chemical Technology & Biotechnology* **2012,** *87* (11), 1567-1573.

[63] Speers, A. M.; Reguera, G., Electron donors supporting growth and electroactivity of *Geobacter sulfurreducens* anode biofilms. *Appl. Environ. Microbiol.* **2012,** *78* (2), 437-444.

[64] Caccavo, F.; Lonergan, D. J.; Lovley, D. R.; Davis, M.; Stolz, J. F.; McInerney, M. J., Geobacter sulfurreducens sp. nov., a hydrogen-and acetate-oxidizing dissimilatory metal-reducing microorganism. *Applied and environmental microbiology* **1994,** *60* (10), 3752-3759.

---

[65] Lloyd, J. R.; Leang, C.; Myerson, A. L. H.; Coppi, M. V.; Cuifo, S.; Methe, B.; Sandler, S. J.; Lovley, D. R., Biochemical and genetic characterization of PpcA, a periplasmic c-type cytochrome in Geobacter sulfurreducens. *Biochemical Journal* **2003,** *369* (1), 153-161.

[66] Inoue, K.; Leang, C.; Franks, A. E.; Woodard, T. L.; Nevin, K. P.; Lovley, D. R., Specific localization of the c-type cytochrome OmcZ at the anode surface in current-producing biofilms of *Geobacter sulfurreducens*. *Environmental Microbiology Reports* **2011,** *3* (2), 211-217.

[67] Richter, H.; McCarthy, K.; Nevin, K. P.; Johnson, J. P.; Rotello, V. M.; Lovley, D. R., Electricity generation by Geobacter sulfurreducens attached to gold electrodes. *Langmuir* **2008,** *24* (8), 4376-4379.

[68] Zhou, M.; Jin, T.; Wu, Z.; Chi, M.; Gu, T., Microbial fuel cells for bioenergy and bioproducts. In *Sustainable Bioenergy and Bioproducts*, Springer: 2012; pp 131-171.

[69] Bonanni, P. S.; Schrott, G. D.; Busalmen, J. P., A long way to the electrode: how do Geobacter cells transport their electrons? Portland Press Limited: 2012.

[70] Leang, C.; Coppi, M. V.; Lovley, D., OmcB, a c-type polyheme cytochrome, involved in Fe (III) reduction in *Geobacter sulfurreducens*. *Journal of Bacteriology* **2003,** *185* (7), 2096-2103.

[71] Malvankar, N. S.; Vargas, M.; Nevin, K. P.; Franks, A. E.; Leang, C.; Kim, B.-C.; Inoue, K.; Mester, T.; Covalla, S. F.; Johnson, J. P., Tunable metallic-like conductivity in microbial nanowire networks. *Nature nanotechnology* **2011,** *6* (9), 573.

[72] Steidl, R. J.; Lampa-Pastirk, S.; Reguera, G., Mechanistic stratification in electroactive biofilms of *Geobacter sulfurreducens* mediated by pilus nanowires. *Nature communications* **2016,** *7*, 12217.

[73] Malvankar, N. S.; Tuominen, M. T.; Lovley, D. R., Lack of cytochrome involvement in long-range electron transport through conductive biofilms and nanowires of *Geobacter sulfurreducens*. *Energy & Environmental Science* **2012,** *5* (9), 8651-8659.

[74] Rabaey, K.; Boon, N.; Höfte, M.; Verstraete, W., Microbial phenazine production enhances electron transfer in biofuel cells. *Environmental science & technology* **2005,** *39* (9), 3401-3408.

[75] Freguia, S.; Masuda, M.; Tsujimura, S.; Kano, K., Lactococcus lactis catalyses electricity generation at microbial fuel cell anodes via excretion of a soluble quinone. *Bioelectrochemistry* **2009,** *76* (1-2), 14-18.

[76] Babauta, J. T.; Nguyen, H. D.; Harrington, T. D.; Renslow, R.; Beyenal, H., pH, redox potential and local biofilm potential microenvironments within *Geobacter sulfurreducens* biofilms and their roles in electron transfer. *Biotechnology and bioengineering* **2012,** *109* (10), 2651-2662.

[77] Babauta, J. T.; Beyenal, H., Mass transfer studies of *Geobacter sulfurreducens* biofilms on rotating disk electrodes. *Biotechnology and bioengineering* **2014,** *111* (2), 285-294.

[78] Torres, C. I.; Marcus, A. K.; Lee, H.-S.; Parameswaran, P.; Krajmalnik-Brown, R.; Rittmann, B. E., A kinetic perspective on extracellular electron transfer by anode-respiring bacteria. *FEMS microbiology reviews* **2010,** *34* (1), 3-17.

[79] Bonanni, P. S.; Bradley, D. F.; Schrott, G. D.; Busalmen, J. P., Limitations for current production in Geobacter sulfurreducens biofilms. *ChemSusChem* **2013,** *6* (4), 711-720.

[80] Richter, H.; Nevin, K. P.; Jia, H.; Lowy, D. A.; Lovley, D. R.; Tender, L. M., Cyclic voltammetry of biofilms of wild type and mutant Geobacter sulfurreducens on fuel cell anodes indicates possible roles of OmcB, OmcZ, type IV pili, and protons in extracellular electron transfer. *Energy & Environmental Science* **2009,** *2* (5), 506-516.

[81] Rimboud, M.; Desmond-Le Quemener, E.; Erable, B.; Bouchez, T.; Bergel, A., Multi-system Nernst–Michaelis–Menten model applied to bioanodes formed from sewage sludge. *Bioresource technology* **2015,** *195*, 162-169.

[82] Rimboud, M.; Pocaznoi, D.; Erable, B.; Bergel, A., Electroanalysis of microbial anodes for bioelectrochemical systems: basics, progress and perspectives. *Physical Chemistry Chemical Physics* **2014,** *16* (31), 16349-16366.

[83] Pham, T. H.; Aelterman, P.; Verstraete, W., Bioanode performance in bioelectrochemical systems: recent improvements and prospects. *Trends in biotechnology* **2009,** *27* (3), 168-178.

[84] Dunn, G., Michaelis–Menten Equation. *Wiley StatsRef: Statistics Reference Online* **2014**.

[85] Seong, G. H.; Heo, J.; Crooks, R. M., Measurement of enzyme kinetics using a continuous-flow microfluidic system. *Analytical chemistry* **2003,** *75* (13), 3161-3167.

[86] Lilly, M.; Hornby, W.; Crook, E., The kinetics of carboxymethylcellulose-ficin in packed beds. *Biochemical Journal* **1966,** *100* (3), 718.

[87] Lloret, L.; Eibes, G.; Moreira, M.; Feijoo, G.; Lema, J.; Miyazaki, M., Improving the catalytic performance of laccase using a novel continuous-flow microreactor. *Chemical engineering journal* **2013,** *223*, 497-506.

---

[88] Halim, A. A.; Szita, N.; Baganz, F., Characterization and multi-step transketolase-ω-transaminase bioconversions in an immobilized enzyme microreactor (IEMR) with packed tube. *Journal of biotechnology* **2013,** *168* (4), 567-575.

[89] Whitesides, G. M., The origins and the future of microfluidics. *Nature* **2006,** *442* (7101), 368.

[90] Stone, H. A.; Stroock, A. D.; Ajdari, A., Engineering flows in small devices: microfluidics toward a lab-on-a-chip. *Annu. Rev. Fluid Mech.* **2004,** *36*, 381-411.

[91] Beebe, D. J.; Mensing, G. A.; Walker, G. M., Physics and applications of microfluidics in biology. *Annual review of biomedical engineering* **2002,** *4* (1), 261-286.

[92] Ong, S.-E.; Zhang, S.; Du, H.; Fu, Y., Fundamental principles and applications of microfluidic systems. *Front Biosci* **2008,** *13* (7), 2757-2773.

[93] Stone, H. A.; Kim, S., Microfluidics: basic issues, applications, and challenges. *AIChE Journal* **2001,** *47* (6), 1250-1254.

[94] Elvira, K. S.; i Solvas, X. C.; Wootton, R. C., The past, present and potential for microfluidic reactor technology in chemical synthesis. *Nature chemistry* **2013,** *5* (11), 905.

[95] Karimi, A.; Karig, D.; Kumar, A.; Ardekani, A., Interplay of physical mechanisms and biofilm processes: review of microfluidic methods. *Lab on a Chip* **2015,** *15* (1), 23-42.

[96] Atencia, J.; Beebe, D. J., Controlled microfluidic interfaces. *Nature* **2004,** *437* (7059), 648.

[97] Mehling, M.; Tay, S., Microfluidic cell culture. *Current opinion in Biotechnology* **2014,** *25*, 95-102.

[98] Maltezos, G.; Gomez, A.; Zhong, J.; Gomez, F. A.; Scherer, A., Microfluidic polymerase chain reaction. *Applied Physics Letters* **2008,** *93* (24), 243901.

[99] Pousti, M.; Zarabadi, M. P.; Abbaszadeh, A. M.; Paquet-Mercier, F.; Greener, J. Microfluidic bioanalytical flow cells for biofilm studies: a review. *The Analyst* **2018,** 144, 68-86.

[100] Esch, E. W.; Bahinski, A.; Huh, D., Organs-on-chips at the frontiers of drug discovery. *Nature reviews Drug discovery* **2015,** *14* (4), 248.

[101] Yi, C.; Zhang, Q.; Li, C.-W.; Yang, J.; Zhao, J.; Yang, M., Optical and electrochemical detection techniques for cell-based microfluidic systems. *Analytical and bioanalytical chemistry* **2006,** *384* (6), 1259-1268.

---

[102] Demello, A. J., Control and detection of chemical reactions in microfluidic systems. *Nature* **2006,** *442* (7101), 394-402.

[103] Cygan, Z. T.; Cabral, J. T.; Beers, K. L.; Amis, E. J., Microfluidic platform for the generation of organic-phase microreactors. *Langmuir* **2005,** *21* (8), 3629-3634.

[104] Poelma, C.; Van der Heiden, K.; Hierck, B.; Poelmann, R.; Westerweel, J., Measurements of the wall shear stress distribution in the outflow tract of an embryonic chicken heart. *Journal of The Royal Society Interface* **2010,** *7* (42), 91-103.

[105] Bennett, M. R.; Hasty, J., Microfluidic devices for measuring gene network dynamics in single cells. *Nature Reviews Genetics* **2009,** *10* (9), 628.

[106] Hof, L. A.; Guo, X.; Seo, M.; Wüthrich, R.; Greener, J., Glass imprint templates by spark assisted chemical engraving for microfabrication by hot embossing. *Micromachines* **2017,** *8* (1), 29.

[107] Carlborg, C. F.; Haraldsson, T.; Öberg, K.; Malkoch, M.; van der Wijngaart, W., Beyond PDMS: off-stoichiometry thiol–ene (OSTE) based soft lithography for rapid prototyping of microfluidic devices. *Lab on a Chip* **2011,** *11* (18), 3136-3147.

[108] Greener, J.; Li, W.; Ren, J.; Voicu, D.; Pakharenko, V.; Tang, T.; Kumacheva, E., Rapid, cost-efficient fabrication of microfluidic reactors in thermoplastic polymers by combining photolithography and hot embossing. *Lab on a Chip* **2010,** *10* (4), 522-524.

[109] Debono, M.; Voicu, D.; Pousti, M.; Safdar, M.; Young, R.; Kumacheva, E.; Greener, J., One-step fabrication of microchannels with integrated three dimensional features by hot intrusion embossing. *Sensors* **2016,** *16* (12), 2023.

[110] Goral, V. N.; Hsieh, Y.-C.; Petzold, O. N.; Faris, R. A.; Yuen, P. K., Hot embossing of plastic microfluidic devices using poly (dimethylsiloxane) molds. *Journal of Micromechanics and Microengineering* **2010,** *21* (1), 017002.

[111] Martinez-Duarte, R.; Madou, M., SU-8 photolithography and its impact on microfluidics. *Microfluidics and Nanofluidics Handbook* **2011**, 231-268.

[112] Sollier, E.; Murray, C.; Maoddi, P.; Di Carlo, D., Rapid prototyping polymers for microfluidic devices and high pressure injections. *Lab on a Chip* **2011,** *11* (22), 3752-3765.

[113] Berthier, E.; Young, E. W.; Beebe, D., Engineers are from PDMS-land, Biologists are from Polystyrenia. *Lab on a Chip* **2012,** *12* (7), 1224-1237.

[114] Tang, Z.; Akiyama, Y.; Itoga, K.; Kobayashi, J.; Yamato, M.; Okano, T., Shear stress-dependent cell detachment from temperature-responsive cell culture surfaces in a microfluidic device. *Biomaterials* **2012,** *33* (30), 7405-7411.

---

[115] Hong, S. H.; Hegde, M.; Kim, J.; Wang, X.; Jayaraman, A.; Wood, T. K., Synthetic quorum-sensing circuit to control consortial biofilm formation and dispersal in a microfluidic device. *Nature communications* **2012,** *3*, 613.

[116] Culotti, A. and Packman, A.I., *Pseudomonas aeruginosa* promotes Escherichia coli biofilm formation in nutrient-limited medium. *PLoS One* **2014,** 9, p.e107186.

[117] Persat, A.; Nadell, C. D.; Kim, M. K.; Ingremeau, F.; Siryaporn, A.; Drescher, K.; Wingreen, N. S.; Bassler, B. L.; Gitai, Z.; Stone, H. A., The mechanical world of bacteria. *Cell* **2015,** *161* (5), 988-997.

[118] Wang, H.-Y.; Bernarda, A.; Huang, C.-Y.; Lee, D.-J.; Chang, J.-S., Micro-sized microbial fuel cell: a mini-review. *Bioresource technology* **2011,** *102* (1), 235-243.

[119] Mukherjee, S.; Su, S.; Panmanee, W.; Irvin, R. T.; Hassett, D. J.; Choi, S., A microliter-scale microbial fuel cell array for bacterial electrogenic screening. *Sensors and Actuators A: Physical* **2013,** *201*, 532-537.

[120] Bester, E.; Wolfaardt, G. M.; Aznaveh, N. B.; Greener, J., Biofilms' role in planktonic cell proliferation. *International journal of molecular sciences* **2013,** *14* (11), 21965-21982.

[121] Park, A.; Jeong, H.-H.; Lee, J.; Kim, K. P.; Lee, C.-S., Effect of shear stress on the formation of bacterial biofilm in a microfluidic channel. *BioChip Journal* **2011,** *5* (3), 236.

[122] Mosier, A. P.; Kaloyeros, A. E.; Cady, N. C., A novel microfluidic device for the in situ optical and mechanical analysis of bacterial biofilms. *Journal of microbiological methods* **2012,** *91* (1), 198-204.

[123] Pousti, M.; Joly, M.; Roberge, P.; Abbaszadeh Amirdehi, M.; Bégin-Drolet, A.; Greener, J., Linear scanning ATR-FTIR for chemical mapping and high-throughput studies of Pseudomonas sp. biofilms in microfluidic channels. *Analytical chemistry* **2018**, 90 (24), 14475–14483.

[124] Pousti, M.; Greener, J., Altered biofilm formation at plasma bonded surfaces in microchannels studied by attenuated total reflection infrared spectroscopy. *Surface Science* **2018,** *676*, 56-60.

[125] Pousti, M.; Lefèvre, T.; Amirdehi, M. A.; Greener, J., A surface spectroscopy study of a Pseudomonas fluorescens biofilm in the presence of an immobilized air bubble. *Spectrochimica Acta Part A: Molecular and Biomolecular Spectroscopy* **2019,** *222*,117163**.**

[126] Asayesh, F.; Zarabadi, M. P.; Greener, J., A new look at bubbles during biofilm inoculation reveals pronounced effects on growth and patterning. *Biomicrofluidics* **2017,** *11* (6), 064109.

[127] Asayesh, F.; Zarabadi, M. P.; Aznaveh, N. B.; Greener, J., Microfluidic flow confinement to avoid chemotaxis-based upstream growth in a biofilm flow cell reactor. *Analytical Methods* **2018,** *10* (37), 4579-4587.

[128] Estrada-Leypon, O.; Moya, A.; Guimera, A.; Gabriel, G.; Agut, M.; Sanchez, B.; Borros, S., Simultaneous monitoring of Staphylococcus aureus growth in a multi-parametric microfluidic platform using microscopy and impedance spectroscopy. *Bioelectrochemistry* **2015,** *105*, 56-64.

[129] Yang, Y.; Ye, D.; Li, J.; Zhu, X.; Liao, Q.; Zhang, B., Microfluidic microbial fuel cells: from membrane to membrane free. *Journal of Power Sources* **2016,** *324*, 113-125.

[130] ElMekawy, A.; Hegab, H. M.; Dominguez-Benetton, X.; Pant, D., Internal resistance of microfluidic microbial fuel cell: challenges and potential opportunities. *Bioresource technology* **2013,** *142*, 672-682.

[131] Yang, Y.; Ye, D.; Li, J.; Zhu, X.; Liao, Q.; Zhang, B., Biofilm distribution and performance of microfluidic microbial fuel cells with different microchannel geometries. *International Journal of Hydrogen Energy* **2015,** *40* (35), 11983-11988.

[132] Qian, F.; Morse, D. E., Miniaturizing microbial fuel cells. *Trends in biotechnology* **2011,** *29* (2), 62-69.

[133] Li, F.; Zheng, Z.; Yang, B.; Zhang, X.; Li, Z.; Lei, L., A laminar-flow based microfluidic microbial three-electrode cell for biosensing. *Electrochimica Acta* **2016,** *199*, 45-50.

[134] Billings, N.; Birjiniuk, A.; Samad, T. S.; Doyle, P. S.; Ribbeck, K., Material properties of biofilms—a review of methods for understanding permeability and mechanics. *Reports on Progress in Physics* **2015,** *78* (3), 036601.

[135] Rittman, B. E., The effect of shear stress on biofilm loss rate. *Biotechnology and Bioengineering* **1982,** *24* (2), 501-506.

[136] Molobela, I.; Ho, W., Impact of shear stress on the formation and structure of microbial biofilms: a review. **2011**.

[137] Van Loosdrecht, M.; Heijnen, J.; Eberl, H.; Kreft, J.; Picioreanu, C., Mathematical modelling of biofilm structures. *Antonie van Leeuwenhoek* **2002,** *81* (1-4), 245-256.

---

[138] Stoodley, P.; Dodds, I.; Boyle, J. D.; Lappin-Scott, H., Influence of hydrodynamics and nutrients on biofilm structure. *Journal of applied microbiology* **1998,** *85* (S1), 19S-28S.

[139] Liu, Y.; Tay, J. H., Metabolic response of biofilm to shear stress in fixed-film culture. *Journal of Applied Microbiology* **2001,** *90* (3), 337-342.

[140] Ai, H.; Xu, J.; Huang, W.; He, Q.; Ni, B.; Wang, Y., Mechanism and kinetics of biofilm growth process influenced by shear stress in sewers. *Water Science and Technology* **2016,** *73* (7), 1572-1582.

[141] Mbaye, S.; Séchet, P.; Pignon, F.; Martins, J., Influence of hydrodynamics on the growth kinetics of glass-adhering Pseudomonas putida cells through a parallel plate flow chamber. *Biomicrofluidics* **2013,** *7* (5), 054105.

[142] Peyton, B. M., Effects of shear stress and substrate loading rate on Pseudomonas aeruginosa biofilm thickness and density. *Water Research* **1996,** *30* (1), 29-36.

[143] Gashti, M. P.; Asselin, J.; Barbeau, J.; Boudreau, D.; Greener, J., A microfluidic platform with pH imaging for chemical and hydrodynamic stimulation of intact oral biofilms. *Lab on a Chip* **2016,** *16* (8), 1412-1419.

[144] Rittmann, B. E.; Stilwell, D.; Ohashi, A., The transient-state, multiple-species biofilm model for biofiltration processes. *Water Research* **2002,** *36* (9), 2342-2356.

[145] Shaw, T.; Winston, M.; Rupp, C. J.; Klapper, I.; Stoodley, P., Commonality of elastic relaxation times in biofilms. *Physical review letters* **2004,** *93* (9), 098102.

[146] Evans, L. V., *Biofilms: recent advances in their study and control*. CRC press: 2003.

[147] Lewis, K., Riddle of biofilm resistance. *Antimicrobial agents and chemotherapy* **2001,** *45* (4), 999-1007.

[148] Stewart, P. S., Diffusion in biofilms. *Journal of bacteriology* **2003,** *185* (5), 1485-1491.

[149] De Beer, D.; Stoodley, P.; Roe, F.; Lewandowski, Z., Effects of biofilm structures on oxygen distribution and mass transport. *Biotechnology and bioengineering* **1994,** *43* (11), 1131-1138.

[150] Allison, D. G.; Maira-Litran, T.; Gilbert, P., *Antimicrobial resistance of biofilms*. Harwood Academic Publishers: Amsterdam, The Netherlands: 2000.

[151] Schlafer, S.; Meyer, R. L., Confocal microscopy imaging of the biofilm matrix. *Journal of microbiological methods* **2017,** *138*, 50-59.

[152] Abadian, P. N.; Goluch, E. D., Surface plasmon resonance imaging (SPRi) for multiplexed evaluation of bacterial adhesion onto surface coatings. *Analytical Methods* **2014,** *7* (1), 115-122.

[153] Paquet-Mercier, F.; Aznaveh, N. B.; Safdar, M.; Greener, J., A microfluidic bioreactor with in situ SERS imaging for the study of controlled flow patterns of biofilm precursor materials. *Sensors* **2013,** *13* (11), 14714-14727.

[154] Beyenal, H.; Babauta, J. T., *Biofilms in bioelectrochemical systems: from laboratory practice to data interpretation*. John Wiley & Sons: 2015.

[155] Dheilly, A.; Linossier, I.; Darchen, A.; Hadjiev, D.; Corbel, C.; Alonso, V., Monitoring of microbial adhesion and biofilm growth using electrochemical impedancemetry. *Applied microbiology and biotechnology* **2008,** *79* (1), 157-164.

[156] Ward, A. C.; Connolly, P.; Tucker, N. P., Pseudomonas aeruginosa can be detected in a polymicrobial competition model using impedance spectroscopy with a novel biosensor. *PloS one* **2014,** *9* (3), e91732.

[157] Ben-Yoav, H.; Freeman, A.; Sternheim, M.; Shacham-Diamand, Y., An electrochemical impedance model for integrated bacterial biofilms. *Electrochimica Acta* **2011,** *56* (23), 7780-7786.

[158] Laczka, O.; Maesa, J.-M.; Godino, N.; del Campo, J.; Fougt-Hansen, M.; Kutter, J. P.; Snakenborg, D.; Muñoz-Pascual, F.-X.; Baldrich, E., Improved bacteria detection by coupling magneto-immunocapture and amperometry at flow-channel microband electrodes. *Biosensors and Bioelectronics* **2011,** *26* (8), 3633-3640.

[159] Estrada-Leypon, O.; Moya, A.; Guimera, A.; Gabriel, G.; Agut, M.; Sanchez, B.; Borros, S., Simultaneous monitoring of Staphylococcus aureus growth in a multi-parametric microfluidic platform using microscopy and impedance spectroscopy. *Bioelectrochemistry* **2015,** *105*, 56-64.

[160] Liu, H.; Crooks, R. M., Highly reproducible chronoamperometric analysis in microdroplets. *Lab on a Chip* **2013,** *13* (7), 1364-1370.

[161] Wolfaardt, G.; Hendry, M.; Birkham, T.; Bressel, A.; Gardner, M.; Sousa, A.; Korber, D.; Pilaski, M., Microbial response to environmental gradients in a ceramic-based diffusion system. *Biotechnology and bioengineering* **2008,** *100* (1), 141-149.

[162] Aznaveh, N. B.; Safdar, M.; Wolfaardt, G.; Greener, J., Micropatterned biofilm formations by laminar flow-templating. *Lab on a Chip* **2014,** *14* (15), 2666-2672.

[163] Bakke, R.; Kommedal, R.; Kalvenes, S., Quantification of biofilm accumulation by an optical approach. *Journal of Microbiological Methods* **2001,** *44* (1), 13-26.

[164] Stoodley, P.; Lappin-Scott, H., Influence of electric fields and pH on biofilm structure as related to the bioelectric effect. *Antimicrobial agents and chemotherapy* **1997,** *41* (9), 1876-1879.

[165] Vafai, K., *Porous media: applications in biological systems and biotechnology*. CRC Press: 2010.

[166] Bester, E.; Kroukamp, O.; Wolfaardt, G. M.; Boonzaaier, L.; Liss, S. N., Metabolic differentiation in biofilms as indicated by carbon dioxide production rates. *Applied and environmental microbiology* **2010,** *76* (4), 1189-1197.

[167] Tolker-Nielsen, T.; Brinch, U. C.; Ragas, P. C.; Andersen, J. B.; Jacobsen, C. S.; Molin, S., Development and dynamics of Pseudomonassp. biofilms. *Journal of bacteriology* **2000,** *182* (22), 6482-6489.

[168] Klausen, M.; Aaes-Jørgensen, A.; Molin, S.; Tolker-Nielsen, T., Involvement of bacterial migration in the development of complex multicellular structures in Pseudomonas aeruginosa biofilms. *Molecular microbiology* **2003,** *50* (1), 61-68.

[169] Pink, J.; Smith-Palmer, T.; Chisholm, D.; Beveridge, T.; Pink, D., An FTIR study of Pseudomonas aeruginosa PAO1 biofilm development: interpretation of ATR–FTIR data in the 1500–1180 cm− 1 region. *Biofilms* **2005,** *2* (3), 165-175.

[170] Pink, J.; Smith-Palmer, T.; Beveridge, T.; Pink, D., An FTIR study of Pseudomonas aeruginosa PAO1 biofilm growth and dispersion. An improved ATR method for studying biofilms: the C–H stretch spectral region. *Biofilms* **2004,** *1* (3), 157-163.

[171] Pereira, M. O.; Kuehn, M.; Wuertz, S.; Neu, T.; Melo, L. F., Effect of flow regime on the architecture of a Pseudomonas fluorescens biofilm. *Biotechnology and bioengineering* **2002,** *78* (2), 164-171.

[172] Wingender, J.; Flemming, H., The biofilm matrix. *Nature Rev Microbiol* **2010,** *8*, 623-633.

[173] Parvinzadeh Gashti, M.; Bellavance, J.; Kroukamp, O.; Wolfaardt, G.; Taghavi, S. M.; Greener, J., Live-streaming: Time-lapse video evidence of novel streamer formation mechanism and varying viscosity. *Biomicrofluidics* **2015,** *9* (4), 041101.

[174] Scheuerman, T. R.; Camper, A. K.; Hamilton, M. A., Effects of substratum topography on bacterial adhesion. *Journal of colloid and interface science* **1998,** *208* (1), 23-33.

[175] Fox, P.; Suidan, M. T.; Bandy, J. T., A comparison of media types in acetate fed expanded-bed anaerobic reactors. *Water Research* **1990,** *24* (7), 827-835.

[176] Jorcin, J.-B.; Orazem, M. E.; Pébère, N.; Tribollet, B., CPE analysis by local electrochemical impedance spectroscopy. *Electrochimica Acta* **2006,** *51* (8-9), 1473-1479.

[177] Bisquert, J.; Compte, A., Theory of the electrochemical impedance of anomalous diffusion. *Journal of Electroanalytical Chemistry* **2001,** *499* (1), 112-120.zn

[178] Beyenal, H.; Lewandowski, Z.; Harkin, G., Quantifying biofilm structure: facts and fiction. *Biofouling* **2004,** *20* (1), 1-23.

[179] Yang, X.; Beyenal, H.; Harkin, G.; Lewandowski, Z., Quantifying biofilm structure using image analysis. *Journal of microbiological methods* **2000,** *39* (2), 109-119.

[180] Logan, B. E., Exoelectrogenic bacteria that power microbial fuel cells. *Nature Reviews Microbiology* **2009,** *7* (5), 375.

[181] Cheng, S.; Xing, D.; Call, D. F.; Logan, B. E., Direct biological conversion of electrical current into methane by electromethanogenesis. *Environmental science & technology* **2009,** *43* (10), 3953-3958.

[182] Tan, Y.; Adhikari, R. Y.; Malvankar, N. S.; Pi, S.; Ward, J. E.; Woodard, T. L.; Nevin, K. P.; Xia, Q.; Tuominen, M. T.; Lovley, D. R., Synthetic biological protein nanowires with high conductivity. *Small* **2016,** *12* (33), 4481-4485.

[183] Lovley, D. R., Live wires: direct extracellular electron exchange for bioenergy and the bioremediation of energy-related contamination. *Energy & Environmental Science* **2011,** *4* (12), 4896-4906.

[184] Aracic, S.; Semenec, L.; Franks, A. E., Investigating microbial activities of electrode-associated microorganisms in real-time. *Frontiers in microbiology* **2014,** *5*, 663.

[185] Torres, C. I.; Kato Marcus, A.; Rittmann, B. E., Proton transport inside the biofilm limits electrical current generation by anode-respiring bacteria. *Biotechnology and Bioengineering* **2008,** *100* (5), 872-881.

[186] Zhao, Z.; Li, Y.; Quan, X.; Zhang, Y., New Application of Ethanol-Type Fermentation: Stimulating Methanogenic Communities with Ethanol to Perform Direct Interspecies Electron Transfer. *ACS Sustainable Chemistry & Engineering* **2017,** *5* (10), 9441-9453.

[187] Franks, A. E.; Nevin, K. P.; Jia, H.; Izallalen, M.; Woodard, T. L.; Lovley, D. R., Novel strategy for three-dimensional real-time imaging of microbial fuel cell communities: monitoring the inhibitory effects of proton accumulation within the anode biofilm. *Energy & Environmental Science* **2009,** *2* (1), 113-119.

[188] Ye, D.; Yang, Y.; Li, J.; Zhu, X.; Liao, Q.; Deng, B.; Chen, R., Performance of a microfluidic microbial fuel cell based on graphite electrodes. *International journal of hydrogen energy* **2013,** *38* (35), 15710-15715.

[189] Ren, H.; Torres, C. I.; Parameswaran, P.; Rittmann, B. E.; Chae, J., Improved current and power density with a micro-scale microbial fuel cell due to a small characteristic length. *Biosensors and Bioelectronics* **2014,** *61*, 587-592.

[190] Liu, Y.; Kim, H.; Franklin, R.; Bond, D. R., Gold line array electrodes increase substrate affinity and current density of electricity-producing *G. sulfurreducens* biofilms. *Energy & Environmental Science* **2010,** *3* (11), 1782-1788.

[191] Greener, J.; Tumarkin, E.; Debono, M.; Kwan, C.-H.; Abolhasani, M.; Guenther, A.; Kumacheva, E., Development and applications of a microfluidic reactor with multiple analytical probes. *Analyst* **2012,** *137* (2), 444-450.

[192] Greener, J.; Tumarkin, E.; Debono, M.; Dicks, A. P.; Kumacheva, E., Education: a microfluidic platform for university-level analytical chemistry laboratories. *Lab on a Chip* **2012,** *12* (4), 696-701.

[193] Kjeang, E.; Roesch, B.; McKechnie, J.; Harrington, D. A.; Djilali, N.; Sinton, D., Integrated electrochemical velocimetry for microfluidic devices. *Microfluidics and Nanofluidics* **2007,** *3* (4), 403-416.

[194] Medintz, I. L.; Stewart, M. H.; Trammell, S. A.; Susumu, K.; Delehanty, J. B.; Mei, B. C.; Melinger, J. S.; Blanco-Canosa, J. B.; Dawson, P. E.; Mattoussi, H., Quantum-dot/dopamine bioconjugates function as redox coupled assemblies for in vitro and intracellular pH sensing. *Nature materials* **2010,** *9* (8), 676.

[195] Walczak, M. M.; Dryer, D. A.; Jacobson, D. D.; Foss, M. G.; Flynn, N. T., pH dependent redox couple: An illustration of the nernst equation. *Journal of chemical education* **1997,** *74* (10), 1195.

[196] Katuri, K. P.; Kavanagh, P.; Rengaraj, S.; Leech, D., Geobacter sulfurreducens biofilms developed under different growth conditions on glassy carbon electrodes: insights using cyclic voltammetry. *Chemical Communications* **2010,** *46* (26), 4758-4760.

[197] Patil, S. A.; Harnisch, F.; Koch, C.; Hübschmann, T.; Fetzer, I.; Carmona-Martínez, A. A.; Müller, S.; Schröder, U., Electroactive mixed culture derived biofilms in microbial bioelectrochemical systems: the role of pH on biofilm formation, performance and composition. *Bioresource technology* **2011,** *102* (20), 9683-9690.

[198] Hou, J.; Liu, Z.; Zhou, Y.; Chen, W.; Li, Y.; Sang, L., An experimental study of pH distributions within an electricity-producing biofilm by using pH microelectrode. *Electrochimica Acta* **2017,** *251*, 187-194.

[199] Bond, D. R.; Strycharz-Glaven, S. M.; Tender, L. M.; Torres, C. I., On electron transport through Geobacter biofilms. *ChemSusChem* **2012,** *5* (6), 1099-1105.

[200] Moya, A.; Illa, X.; Prats-Alfonso, E.; Zine, N.; Gabriel, G.; Errachid, A.; Villa, R. In *Flexible microfluidic bio-lab-on-a-chip multi-sensor platform for electrochemical measurements*, SENSORS, 2014 IEEE, IEEE: 2014; pp 1018-1021.

[201] Snowden, M. E.; Unwin, P. R.; Macpherson, J. V., Single walled carbon nanotube channel flow electrode: hydrodynamic voltammetry at the nanomolar level. *Electrochemistry Communications* **2011,** *13* (2), 186-189.

[202] Marsili, E.; Sun, J.; Bond, D. R., Voltammetry and growth physiology of *Geobacter sulfurreducens* biofilms as a function of growth stage and imposed electrode potential. *Electroanalysis: An International Journal Devoted to Fundamental and Practical Aspects of Electroanalysis* **2010,** *22* (7-8), 865-874.

[203] Zarabadi, M. P.; Paquet-Mercier, F. o.; Charette, S. J.; Greener, J., Hydrodynamic Effects on Biofilms at the Biointerface Using a Microfluidic Electrochemical Cell: Case Study of *Pseudomonas sp. Langmuir* **2017,** *33* (8), 2041-2049.

[204] Laczka, O.; Maesa, J.; Godino, N.; del Campo, J.; Fougt-Hansen, M.; Kutter, J., D. 517 Snakenborg, FX Muñoz-Pascual, E. Baldrich, Improved bacteria detection by 518 coupling magneto-immunocapture and amperometry at flow-channel 519 microband electrodes. *Biosens. Bioelectron* **2011,** *26*, 3633-3640.

[205] Abbaszadeh Amirdehi, M.; Saem, S.; Zarabadi, M. P.; Moran-Mirabal, J. M.; Greener, J., Microstructured Anodes by Surface Wrinkling for Studies of Direct Electron Transfer Biofilms in Microbial Fuel Cells. *Advanced Materials Interfaces* **2018**, 1800290.

[206] Brito, A.; Melo, L., Mass transfer coefficients within anaerobic biofilms: effects of external liquid velocity. *Water Research* **1999,** *33* (17), 3673-3678.

[207] De Beer, D.; Stoodley, P.; Lewandowski, Z., Liquid flow and mass transport in heterogeneous biofilms. *Water Research* **1996,** *30* (11), 2761-2765.

[208] Nguyen, V. T.; Morgenroth, E.; Eberl, H., A mesoscale model for hydrodynamics in biofilms that takes microscopic flow effects into account. *Water science and technology* **2005,** *52* (7), 167-172.

[209] Eberl, H.; Picioreanu, C.; Heijnen, J.; Van Loosdrecht, M., A three-dimensional numerical study on the correlation of spatial structure, hydrodynamic conditions, and mass transfer and conversion in biofilms. *Chemical Engineering Science* **2000,** *55* (24), 6209-6222.

[210] Fourmond, V.; Hoke, K.; Heering, H. A.; Baffert, C.; Leroux, F.; Bertrand, P.; Léger, C., SOAS: A free program to analyze electrochemical data and other one-dimensional signals. *Bioelectrochemistry* **2009,** *76* (1-2), 141-147.

[211] Fricke, K.; Harnisch, F.; Schröder, U., On the use of cyclic voltammetry for the study of anodic electron transfer in microbial fuel cells. *Energy & Environmental Science* **2008,** *1* (1), 144-147.

[212] He, W.; Wallack, M. J.; Kim, K.-Y.; Zhang, X.; Yang, W.; Zhu, X.; Feng, Y.; Logan, B. E., The effect of flow modes and electrode combinations on the performance of a multiple module microbial fuel cell installed at wastewater treatment plant. *Water research* **2016,** *105*, 351-360.

[213] Wraight, C. A., Chance and design—proton transfer in water, channels and bioenergetic proteins. *Biochimica et Biophysica Acta (BBA)-Bioenergetics* **2006,** *1757* (8), 886-912.

[214] Adesokan, B. J.; Quan, X.; Evgrafov, A.; Heiskanen, A.; Boisen, A.; Sørensen, M. P., Experimentation and numerical modeling of cyclic voltammetry for electrochemical micro-sized sensors under the influence of electrolyte flow. *Journal of Electroanalytical Chemistry* **2016,** *763*, 141-148.

[215] Logan, B., Microbial fuels for the future. *Nature* **2008,** *454* (7207), 943.

[216] Tan, Y.; Adhikari, R. Y.; Malvankar, N. S.; Pi, S.; Ward, J. E.; Woodard, T. L.; Nevin, K. P.; Xia, Q.; Tuominen, M. T.; Lovley, D. R., Synthetic biological protein nanowires with high conductivity. *Small* **2016,** *12* (33), 4481-4485.

[217] Lovley, D. R., Syntrophy goes electric: direct interspecies electron transfer. *Annual review of microbiology* **2017,** *71*, 643-664.

[218] Zhao, Z.; Zhang, Y.; Wang, L.; Quan, X., Potential for direct interspecies electron transfer in an electric-anaerobic system to increase methane production from sludge digestion. *Scientific reports* **2015,** *5*, 11094.

[219] Cologgi, D. L.; Speers, A. M.; Bullard, B. A.; Kelly, S. D.; Reguera, G., Enhanced uranium immobilization and reduction by *Geobacter sulfurreducens* biofilms. *Applied and environmental microbiology* **2014**, AEM. 02289-14.

[220] Lovley, D. R.; Ueki, T.; Zhang, T.; Malvankar, N. S.; Shrestha, P. M.; Flanagan, K. A.; Aklujkar, M.; Butler, J. E.; Giloteaux, L.; Rotaru, A.-E., *Geobacter*: the microbe electric's physiology, ecology, and practical applications. In *Advances in microbial physiology*, Elsevier: 2011; Vol. 59, pp 1-100.

[221] Lovley, D. R., Bug juice: harvesting electricity with microorganisms. *Nature Reviews Microbiology* **2006,** *4* (7), 497.

---

[222] Crevecoeur, S.; Vincent, W. F.; Comte, J.; Lovejoy, C., Bacterial community structure across environmental gradients in permafrost thaw ponds: methanotroph-rich ecosystems. *Frontiers in microbiology* **2015,** *6*, 192.

[223] Bottos, E. M.; Vincent, W. F.; Greer, C. W.; Whyte, L. G., Prokaryotic diversity of arctic ice shelf microbial mats. *Environmental microbiology* **2008,** *10* (4), 950-966.

[224] Zhang, X.; He, W.; Ren, L.; Stager, J.; Evans, P. J.; Logan, B. E., COD removal characteristics in air-cathode microbial fuel cells. *Bioresource technology* **2015,** *176*, 23-31.

[225] Ahn, Y.; Logan, B. E., Effectiveness of domestic wastewater treatment using microbial fuel cells at ambient and mesophilic temperatures. *Bioresource technology* **2010,** *101* (2), 469-475.

[226] Jannasch, H. W.; Egli, T., Microbial growth kinetics: a historical perspective. Springer: 1993.

[227] Williamson, K.; McCarty, P. L., Verification studies of the biofilm model for bacterial substrate utilization. *Journal (Water Pollution Control Federation)* **1976**, 281-296.

[228] Liu, Y.; Kim, H.; Franklin, R.; Bond, D. R., Gold line array electrodes increase substrate affinity and current density of electricity-producing *G. sulfurreducens* biofilms. *Energy & Environmental Science* **2010,** *3* (11), 1782-1788.

[229] Costerton, J. W.; Stewart, P. S.; Greenberg, E. P., Bacterial biofilms: a common cause of persistent infections. *science* **1999,** *284* (5418), 1318-1322.

[230] Ren, H.; Tian, H.; Gardner, C. L.; Ren, T.-L.; Chae, J., A miniaturized microbial fuel cell with three-dimensional graphene macroporous scaffold anode demonstrating a record power density of over 10000 W m^{-3}. *Nanoscale* **2016,** *8* (6), 3539-3547.

[231] Tront, J. M.; Fortner, J.; Plötze, M.; Hughes, J.; Puzrin, A. M., Microbial fuel cell biosensor for in situ assessment of microbial activity. *Biosensors and Bioelectronics* **2008,** *24* (4), 586-590.

[232] Kroukamp, O.; Wolfaardt, G. M., CO2 production as an indicator of biofilm metabolism. *Applied and environmental microbiology* **2009,** *75* (13), 4391-4397.

[233] Dumitrache, A.; Wolfaardt, G. M.; Allen, D. G.; Liss, S. N.; Lynd, L. R., Tracking the cellulolytic activity of Clostridium thermocellum biofilms. *Biotechnology for biofuels* **2013,** *6* (1), 175.

[234] Jackson, L.; Kroukamp, O.; Wolfaardt, G., Effect of carbon on whole-biofilm metabolic response to high doses of streptomycin. *Frontiers in microbiology* **2015,** *6*, 953.

[235] Stone, W.; Kroukamp, O.; Moes, A.; McKelvie, J.; Korber, D. R.; Wolfaardt, G. M., Measuring microbial metabolism in atypical environments: Bentonite in used nuclear fuel storage. *Journal of microbiological methods* **2016,** *120*, 79-90.

[236] Stone, W.; Kroukamp, O.; McKelvie, J.; Korber, D.; Wolfaardt, G., Microbial metabolism in bentonite clay: saturation, desiccation and relative humidity. *Applied Clay Science* **2016,** *129*, 54-64.

[237] Stone, W.; Kroukamp, O.; Korber, D. R.; McKelvie, J.; Wolfaardt, G. M., Microbes at surface-air interfaces: the metabolic harnessing of relative humidity, surface hygroscopicity, and oligotrophy for resilience. *Frontiers in microbiology* **2016,** *7*, 1563.

[238] Lee, K.; Kim, C.; Kim, Y.; Ahn, B.; Bang, J.; Kim, J.; Panchapakesan, R.; Yoon, Y.-K.; Kang, J. Y.; Oh, K. W., Microfluidic concentration-on-demand combinatorial dilutions. *Microfluidics and nanofluidics* **2011,** *11* (1), 75-86.

[239] Voicu, D.; Scholl, C.; Li, W.; Jagadeesan, D.; Nasimova, I.; Greener, J.; Kumacheva, E., Kinetics of multicomponent polymerization reaction studied in a microfluidic format. *Macromolecules* **2012,** *45* (11), 4469-4475.

[240] Unger, M. A.; Chou, H.-P.; Thorsen, T.; Scherer, A.; Quake, S. R., Monolithic microfabricated valves and pumps by multilayer soft lithography. *Science* **2000,** *288* (5463), 113-116.

[241] Keenan, T. M.; Folch, A., Biomolecular gradients in cell culture systems. *Lab on a Chip* **2008,** *8* (1), 34-57.

[242] Zarabadi, M. P.; Charette, S. J.; Greener, J., Flow-Based Deacidification of Geobacter sulfurreducens Biofilms Depends on Nutrient Conditions: a Microfluidic Bioelectrochemical Study. *ChemElectroChem* **2018,** *5* (23), 3645-3653.

[243] Squires, T. M.; Quake, S. R., Microfluidics: Fluid physics at the nanoliter scale. *Reviews of modern physics* **2005,** *77* (3), 977.

[244] Liu, Y.; Lu, H., Microfluidics in systems biology—hype or truly useful? *Current opinion in biotechnology* **2016,** *39*, 215-220.

[245] Zhang, Z.; Boccazzi, P.; Choi, H.-G.; Perozziello, G.; Sinskey, A. J.; Jensen, K. F., Microchemostat—microbial continuous culture in a polymer-based, instrumented microbioreactor. *Lab on a Chip* **2006,** *6* (7), 906-913.

[246] Balagaddé, F. K.; You, L.; Hansen, C. L.; Arnold, F. H.; Quake, S. R., Long-term monitoring of bacteria undergoing programmed population control in a microchemostat. *Science* **2005,** *309* (5731), 137-140.

[247] Snider, R. M.; Strycharz-Glaven, S. M.; Tsoi, S. D.; Erickson, J. S.; Tender, L. M., Long-range electron transport in *Geobacter sulfurreducens* biofilms is redox gradient-driven. *Proceedings of the National Academy of Sciences* **2012**, 201209829.

[248] Sun, D.; Chen, J.; Huang, H.; Liu, W.; Ye, Y.; Cheng, S., The effect of biofilm thickness on electrochemical activity of *Geobacter sulfurreducens*. *International journal of hydrogen energy* **2016,** *41* (37), 16523-16528.

[249] Marsili, E.; Rollefson, J. B.; Baron, D. B.; Hozalski, R. M.; Bond, D. R., Microbial biofilm voltammetry: direct electrochemical characterization of catalytic electrode-attached biofilms. *Applied and environmental microbiology* **2008,** *74* (23), 7329-7337.

[250] Jana, P. S.; Katuri, K.; Kavanagh, P.; Kumar, A.; Leech, D., Charge transport in films of *Geobacter sulfurreducens* on graphite electrodes as a function of film thickness. *Physical Chemistry Chemical Physics* **2014,** *16* (19), 9039-9046.

[251] Li, Z.; Zhang, Y.; LeDuc, P. R.; Gregory, K. B., Microbial electricity generation via microfluidic flow control. *Biotechnology and bioengineering* **2011,** *108* (9), 2061-2069.

[252] You, J.; Walter, X. A.; Greenman, J.; Melhuish, C.; Ieropoulos, I., Stability and reliability of anodic biofilms under different feedstock conditions: Towards microbial fuel cell sensors. *Sensing and bio-sensing research* **2015,** *6*, 43-50.

[253] Pham, H. T.; Boon, N.; Aelterman, P.; Clauwaert, P.; De Schamphelaire, L.; Van Oostveldt, P.; Verbeken, K.; Rabaey, K.; Verstraete, W., High shear enrichment improves the performance of the anodophilic microbial consortium in a microbial fuel cell. *Microbial biotechnology* **2008,** *1* (6), 487-496.

[254] Blauert, F.; Horn, H.; Wagner, M., Time-resolved biofilm deformation measurements using optical coherence tomography. *Biotechnology and bioengineering* **2015,** *112* (9), 1893-1905.

[255] Jain, A.; Gazzola, G.; Panzera, A.; Zanoni, M.; Marsili, E., Visible spectroelectrochemical characterization of Geobacter sulfurreducens biofilms on optically transparent indium tin oxide electrode. *Electrochimica Acta* **2011,** *56* (28), 10776-10785.

[256] Jiang, D.; Li, B., Novel electrode materials to enhance the bacterial adhesion and increase the power generation in microbial fuel cells (MFCs). *Water Science and Technology* **2009,** *59* (3), 557-563.

[257] Agmon, N., The grotthuss mechanism. *Chemical Physics Letters* **1995,** *244* (5-6), 456-462.

[258] Domach, M. M., Perspectives and Prospects for Whole Cell Catalysis. *Catalysis Letters* **2015,** *145* (1), 346-359.

---

[259] Chartrain, M.; Greasham, R.; Moore, J.; Reider, P.; Robinson, D.; Buckland, B., Asymmetric bioreductions: application to the synthesis of pharmaceuticals. *Journal of Molecular Catalysis B: Enzymatic* **2001,** *11* (4-6), 503-512.

[260] Dasgupta, D.; Bandhu, S.; Adhikari, D. K.; Ghosh, D., Challenges and prospects of xylitol production with whole cell bio-catalysis: a review. *Microbiological research* **2017,** *197*, 9-21.

[261] Santoro, C.; Arbizzani, C.; Erable, B.; Ieropoulos, I., Microbial fuel cells: from fundamentals to applications. A review. *Journal of power sources* **2017,** *356*, 225-244.

[262] Robinson, P. K., Enzymes: principles and biotechnological applications. *Essays in biochemistry* **2015,** *59*, 1-41.

[263] Halan, B.; Buehler, K.; Schmid, A., Biofilms as living catalysts in continuous chemical syntheses. *Trends in biotechnology* **2012,** *30* (9), 453-465.

[264] Rosche, B.; Li, X. Z.; Hauer, B.; Schmid, A.; Buehler, K., Microbial biofilms: a concept for industrial catalysis? *Trends in biotechnology* **2009,** *27* (11), 636-643.

[265] Li, X. Z.; Webb, J. S.; Kjelleberg, S.; Rosche, B., Enhanced benzaldehyde tolerance in Zymomonas mobilis biofilms and the potential of biofilm applications in fine-chemical production. *Appl. Environ. Microbiol.* **2006,** *72* (2), 1639-1644.

[266] Gross, R.; Hauer, B.; Otto, K.; Schmid, A., Microbial biofilms: new catalysts for maximizing productivity of long-term biotransformations. *Biotechnology and bioengineering* **2007,** *98* (6), 1123-1134.

[267] Maksimova, Y. G., Microbial biofilms in biotechnological processes. *Applied biochemistry and microbiology* **2014,** *50* (8), 750-760.

[268] Çelik, D.; Bayraktar, E.; Mehmetoğlu, Ü., Biotransformation of 2-phenylethanol to phenylacetaldehyde in a two-phase fed-batch system. *Biochemical engineering journal* **2004,** *17* (1), 5-13.

[269] Hacka, C.; Woodley, J.; Lilly, M.; Liddell, J., Design of a control system for biotransformation of toxic substrates: toluene hydroxylation by Pseudomonas putida UV4. *Enzyme and microbial technology* **2000,** *26* (7), 530-536.

[270] Lin, B.; Tao, Y., Whole-cell biocatalysts by design. *Microbial cell factories* **2017,** *16* (1), 106.

[271] Zarabadi, M. P.; Charette, S. J.; Greener, J., Toggling *Geobacter sulfurreducens* metabolic state reveals hidden behaviour and expanded applicability to sustainable energy applications. *Sustain. Energ. Fuels* **2019,** *DOI: 10.1039/C9SE00026G*

---

[272] Villahermosa, D.; Corzo, A.; Garcia-Robledo, E.; González, J. M.; Papaspyrou, S., Kinetics of Indigenous Nitrate Reducing Sulfide Oxidizing Activity in Microaerophilic Wastewater Biofilms. *PloS one* **2016,** *11* (2), e0149096.

[273] Longmuir, I., Respiration rate of bacteria as a function of oxygen concentration. *Biochemical Journal* **1954,** *57* (1), 81.

[274] Lilly, M.; Hornby, W.; Crook, E., The kinetics of carboxymethylcellulose-ficin in packed beds. *Biochemical Journal* **1966,** *100* (3), 718.

[275] Halim, A. A.; Szita, N.; Baganz, F., Characterization and multi-step transketolase-ω-transaminase bioconversions in an immobilized enzyme microreactor (IEMR) with packed tube. *Journal of biotechnology* **2013,** *168* (4), 567-575.

[276] Wang, J.; Gu, S.-S.; Cui, H.-S.; Yang, L.-Q.; Wu, X.-Y., Rapid synthesis of propyl caffeate in ionic liquid using a packed bed enzyme microreactor under continuous-flow conditions. *Bioresource technology* **2013,** *149*, 367-374.

[277] Seong, G. H.; Heo, J.; Crooks, R. M., Measurement of enzyme kinetics using a continuous-flow microfluidic system. *Analytical chemistry* **2003,** *75* (13), 3161-3167.

[278] Torres, C. I.; Marcus, A. K.; Lee, H.-S.; Parameswaran, P.; Krajmalnik-Brown, R.; Rittmann, B. E., A kinetic perspective on extracellular electron transfer by anode-respiring bacteria. *FEMS microbiology reviews* **2010,** *34* (1), 3-17.

[279] Zhu, X.; Tokash, J. C.; Hong, Y.; Logan, B. E., Controlling the occurrence of power overshoot by adapting microbial fuel cells to high anode potentials. *Bioelectrochemistry* **2013,** *90*, 30-35.

[280] Bonanni, P. S.; Schrott, G. D.; Robuschi, L.; Busalmen, J. P., Charge accumulation and electron transfer kinetics in Geobacter sulfurreducens biofilms. *Energy & Environmental Science* **2012,** *5* (3), 6188-6195.

[281] Ye, D.; Yang, Y.; Li, J.; Zhu, X.; Liao, Q.; Deng, B.; Chen, R., Performance of a microfluidic microbial fuel cell based on graphite electrodes. *international journal of hydrogen energy* **2013,** *38* (35), 15710-15715.

[282] Khosla, C., Quo vadis, enzymology? *Nature chemical biology* **2015,** *11* (7), 438.

[283] Li, S.; Cheng, C.; Thomas, A., Carbon-Based Microbial-Fuel-Cell Electrodes: From Conductive Supports to Active Catalysts. *Advanced Materials* **2017,** *29* (8), 1602547.

[284] Khan, M. M.; Ansari, S. A.; Lee, J.-H.; Lee, J.; Cho, M. H., Mixed culture electrochemically active biofilms and their microscopic and spectroelectrochemical studies. *ACS Sustainable Chemistry & Engineering* **2013,** *2* (3), 423-432.

---

[285] Walker, F. A.; Emrick, D.; Rivera, J. E.; Hanquet, B. J.; Buttlaire, D. H., Effect of heme orientation on the reduction potential of cytochrome b5. *Journal of the American Chemical Society* **1988,** *110* (18), 6234-6240.

[286] Jain, A.; Connolly, J. O.; Woolley, R.; Krishnamurthy, S.; Marsili, E., Extracellular electron transfer mechanism in Shewanella loihica PV-4 biofilms formed at indium tin oxide and graphite electrodes. *International Journal of Electrochemical Science* **2013**, *8*, 1778-1793.

[287] Busalmen, J. P.; Esteve-Nuñez, A.; Berná, A.; Feliu, J. M., ATR-SEIRAs characterization of surface redox processes in *G. sulfurreducens*. *Bioelectrochemistry* **2010,** *78* (1), 25-29.

[288] Summers, Z. M.; Fogarty, H. E.; Leang, C.; Franks, A. E.; Malvankar, N. S.; Lovley, D. R., Direct exchange of electrons within aggregates of an evolved syntrophic coculture of anaerobic bacteria. *Science* **2010,** *330* (6009), 1413-1415.

[289] Liu, F.; Rotaru, A.-E.; Shrestha, P. M.; Malvankar, N. S.; Nevin, K. P.; Lovley, D. R., Promoting direct interspecies electron transfer with activated carbon. *Energy & Environmental Science* **2012,** *5* (10), 8982-8989.

[290] Chen, S.; Rotaru, A.-E.; Shrestha, P. M.; Malvankar, N. S.; Liu, F.; Fan, W.; Nevin, K. P.; Lovley, D. R., Promoting interspecies electron transfer with biochar. *Scientific reports* **2014,** *4*, 5019.

[291] Rotaru, A.-E.; Shrestha, P. M.; Liu, F.; Shrestha, M.; Shrestha, D.; Embree, M.; Zengler, K.; Wardman, C.; Nevin, K. P.; Lovley, D. R., A new model for electron flow during anaerobic digestion: direct interspecies electron transfer to Methanosaeta for the reduction of carbon dioxide to methane. *Energy & Environmental Science* **2014,** *7* (1), 408-415.

[292] Ha, P. T.; Lindemann, S. R.; Shi, L.; Dohnalkova, A. C.; Fredrickson, J. K.; Madigan, M. T.; Beyenal, H., Syntrophic anaerobic photosynthesis via direct interspecies electron transfer. *Nature communications* **2017,** *8*, 13924.

[293] Benomar, S.; Ranava, D.; Cárdenas, M. L.; Trably, E.; Rafrafi, Y.; Ducret, A.; Hamelin, J.; Lojou, E.; Steyer, J.-P.; Giudici-Orticoni, M.-T., Nutritional stress induces exchange of cell material and energetic coupling between bacterial species. *Nature communications* **2015,** *6*, 6283.

[294] Kato, S.; Hashimoto, K.; Watanabe, K., Methanogenesis facilitated by electric syntrophy via (semi) conductive iron-oxide minerals. *Environmental microbiology* **2012,** *14* (7), 1646-1654.

[295] Tang, J.; Zhuang, L.; Ma, J.; Tang, Z.; Yu, Z.; Zhou, S., Secondary mineralization of ferrihydrite affects microbial methanogenesis in *Geobacter-Methanosarcina* cocultures. *Appl. Environ. Microbiol.* **2016,** *82* (19), 5869-5877.

---

[296] Yamada, C.; Kato, S.; Ueno, Y.; Ishii, M.; Igarashi, Y., Conductive iron oxides accelerate thermophilic methanogenesis from acetate and propionate. *Journal of bioscience and bioengineering* **2015,** *119* (6), 678-682.

[297] Morita, M.; Malvankar, N. S.; Franks, A. E.; Summers, Z. M.; Giloteaux, L.; Rotaru, A. E.; Rotaru, C.; Lovley, D. R., Potential for direct interspecies electron transfer in methanogenic wastewater digester aggregates. *MBio* **2011,** *2* (4), e00159-11.

[298] Lee, J.-Y.; Lee, S.-H.; Park, H.-D., Enrichment of specific electro-active microorganisms and enhancement of methane production by adding granular activated carbon in anaerobic reactors. *Bioresource technology* **2016,** *205*, 205-212.

[299] Cruz Viggi, C.; Rossetti, S.; Fazi, S.; Paiano, P.; Majone, M.; Aulenta, F., Magnetite particles triggering a faster and more robust syntrophic pathway of methanogenic propionate degradation. *Environmental science & technology* **2014,** *48* (13), 7536-7543.

[300] Villano, M.; Aulenta, F.; Ciucci, C.; Ferri, T.; Giuliano, A.; Majone, M., Bioelectrochemical reduction of CO2 to CH4 via direct and indirect extracellular electron transfer by a hydrogenophilic methanogenic culture. *Bioresource technology* **2010,** *101* (9), 3085-3090.

[301] Smith, K. S.; Ingram-Smith, C., Methanosaeta, the forgotten methanogen? *Trends in microbiology* **2007,** *15* (4), 150-155.

[302] Baek, G.; Kim, J.; Cho, K.; Bae, H.; Lee, C., The biostimulation of anaerobic digestion with (semi) conductive ferric oxides: their potential for enhanced biomethanation. *Applied microbiology and biotechnology* **2015,** *99* (23), 10355-10366.

[303] Zhao, Z.; Zhang, Y.; Li, Y.; Dang, Y.; Zhu, T.; Quan, X., Potentially shifting from interspecies hydrogen transfer to direct interspecies electron transfer for syntrophic metabolism to resist acidic impact with conductive carbon cloth. *Chemical Engineering Journal* **2017,** *313*, 10-18.

[304] Rotaru, A.-E.; Shrestha, P. M.; Liu, F.; Markovaite, B.; Chen, S.; Nevin, K. P.; Lovley, D. R., Direct interspecies electron transfer between Geobacter metallireducens and Methanosarcina barkeri. *Appl. Environ. Microbiol.* **2014,** *80* (15), 4599-4605.